




**ADVERTIMENT.** L'accés als continguts d'aquesta tesi queda condicionat a l'acceptació de les condicions d'ús establertes per la següent llicència Creative Commons:  <https://creativecommons.org/licenses/?lang=ca>

**ADVERTENCIA.** El acceso a los contenidos de esta tesis queda condicionado a la aceptación de las condiciones de uso establecidas por la siguiente licencia Creative Commons:  <https://creativecommons.org/licenses/?lang=es>

**WARNING.** The access to the contents of this doctoral thesis it is limited to the acceptance of the use conditions set by the following Creative Commons license:  <https://creativecommons.org/licenses/?lang=en>

Facultat de Ciències

Departament de Física

**Fabrication and characterization of FeMn alloys  
with antibiofilm properties for biodegradable  
implant applications**

**PhD Thesis**

Programa de doctorat en Ciència de Materials

**Aleksandra Bartkowska**

**Directors:**

Jordi Sort Viñas

Eva Pellicer Vilà

Carme Nogués Sanmiquel

2023







Memòria presentada per aspirar al Grau de Doctor per

**Aleksandra Bartkowska**

Vist i plau

Jordi Sort Viñas

Eva Pellicer Vilà

Carme Nogués Sanmiquel

Bellaterra, 20 de setembre de 2023



El **Dr. Jordi Sort Viñas**, professor ICREA del Departament de Física de la Universitat Autònoma de Barcelona,  
i la **Dra. Eva Pellicer Vilà**, professora catedràtica del Departament de Física de la Universitat Autònoma de Barcelona,  
i la **Dra. Carme Nogués Sanmiquel**, professora catedràtica del Departament de Biologia Cel·lular, de Fisiologia i d'Immunologia de la Universitat Autònoma de Barcelona,

CERTIFIQUEN:

Que **Aleksandra Bartkowska** ha realitzat sota la seva direcció el treball d'investigació que s'exposa a la memòria titulada «Fabrication and characterization of FeMn alloys with antibiofilm properties for biodegradable implant applications» per optar al grau de **Doctor per la Universitat Autònoma de Barcelona**.

Que el disseny dels experiments, síntesi de mostres, llur caracterització, l'anàlisi dels resultats, la redacció dels articles i d'aquesta memòria són fruit del treball d'investigació realitzat per Aleksandra Bartkowska.

I perquè així consti, signen el present certificat,

Jordi Sort Viñas

Eva Pellicer Vilà

Carme Nogués Sanmiquel

Bellaterra, 20 de setembre de 2023



You cannot hope to build a better world without improving the individuals. To that end, each of us must work for his own improvement, and at the same time share a general responsibility for all humanity, our particular duty being to aid those to whom we think we can be most useful.

Maria Skłodowska-Curie



This project has received funding from the European Union's Horizon 2020 research and innovation programme under the Marie Skłodowska-Curie grant agreement No. 861046







# Acknowledgments

First and foremost I am deeply thankful to my supervisors - Jordi, Eva and Carme for giving me this opportunity and believing I will be a good candidate to handle that challenging project. I am very grateful for the trust, support and autonomy I have been given over the last three years and for caring about my overall professional success. *Merci!*

I would like to thank my collaborators, Adam, Ludovico, Andreu and Oriol for helping me with experiments that I could not have done alone. To Pau for constant support in various technical problems that I stumbled upon during my lab life, and for being such a cheerful person during that (no complaints!). To all my work colleagues, especially Konrad, Michael, Tan, Christina, Sofia, Ma, Monalisha and Irena for sharing the work time and nice scientific (and non) conversations. To Jordi M for his valuable help in bureaucracy. To the Microscopy Service at UAB, especially to Cristina and Marti, for always being ready to help. To Aliona for her support, great advices and for making me feel less homesick.

To the BIOREMIA community for creating this wonderful family of young and senior scientists where we are always welcome. To all seniors and our great coordinator, Mariana, for creating this amazing group. To all my Bioremia colleagues for this incredible journey together full of laughs and support. To my Bioremia best friends, Paula, Adam, Ludovico and Kirti for a great time together, many board games and trips. I am always looking forward to seeing you again.

To my new/old friends from CERN for welcoming me again and being very helpful and kind at the time. To Lucia, Joao and Deepti for making me feel as if I have never left. To Alice for the warm welcome since day 1 of work. Special thanks to my incredible friend Maria, for always finding solutions to make my life easier, for introducing me to the Spanish culture and for making my move to France much easier than it could be.

As I am extremely lucky to have met just the right people in my life I would like to list all my amazing friends without whom I would certainly not have succeeded in this tough PhD journey (and managed to keep

---

the long-distance relationship) - to Pelc, Konieczko, Magda F., Filip and Madzia Z. for keeping up with me since high school and being extremely supportive throughout the years; to Mateusz for always being there for me with a cup of delicious coffee; to Monika and Kinga for always willing to meet whenever I arrive in Poland. To my fantastic Barcelona friends who kept me sane during these last months - Ignacio and Olga (and of course Bubuś and Birra).

To my brother, for believing in me since I was a kid and always encouraging me to push more. Without you, I would not get where I am.

Szczególne podziękowania kieruję do moich rodziców, którzy zawsze starali się zrozumieć moje szalone pomysły o przenoszeniu się na drugi koniec Europy, mimo że nie do końca byli z nich zadowoleni. Dziękuję za miłość którą mi zawsze okazywaliście, za naukę ciężkiej pracy i wytrwałości oraz sprawienie że czułam się wystarczająca. Bez was to nie byłoby możliwe. I na koniec nie mogę nie wspomnieć naszego najwspalniejszego domownika, Aleksia.

Thank you all! Dziękuję Wam wszystkim! Gracias a todos!

# Abstract

Biodegradable implants constitute a new generation of biomedical materials that are being developed to assist in tissue healing processes and gradually degrade *in vivo* after their function is fulfilled. In recent years, Fe-Mn alloys have been studied as potential candidates for biodegradable implant materials because of their excellent mechanical properties and improved corrosion rate. In addition, the incorporation of antimicrobial elements, such as Ag and ZnO, is being studied to develop a material with antibiofilm properties that will lead to a decreased risk of implant-associated infections.

In this thesis, porous equiatomic Fe-Mn alloys disks were fabricated via powder metallurgy by ball-milling and vacuum sintering. The first field of study covered the incorporation of antibacterial Ag into the Fe<sub>50</sub>Mn<sub>50</sub> base alloy by the mechanical alloying of metallic powders to form uniformly dispersed Ag-rich precipitates within the FeMn matrix. The second field of study covered the deposition of a ZnO coating onto the porous FeMn disk by the dip-coating method. The addition of Ag and ZnO was aimed at accelerating the degradation rate and simultaneously decreasing the biofilm formation. A variety of methods were employed to characterize the properties of the synthesized materials, including scanning electron microscopy, transmission electron microscopy and X-ray diffraction for microstructural characterization, while nanoindentation and compression tests were used to assess the mechanical properties. Biodegradability was investigated by immersing the specimens in Hank's Balanced Salt Solution (HBSS). The release of Fe, Mn and Ag/Zn ions was quantified to assess the degradation rate. The magnetic properties were studied using vibrating sample magnetometry before and after immersion in HBSS. Studies on cytocompatibility towards Saos-2 cells, inflammatory cytokine responses, and biofilm formation of *Staphylococcus aureus* have also been conducted.

The results revealed that porous, non-cytotoxic, FeMn-based biomaterials can be fabricated by powder metallurgy. The phase composition of porous FeMn(-xAg) alloys changes with increasing Ag content from fully austenitic to a dual phase comprising austenite and martensite, which

---

also leads to a higher mechanical strength of the Ag-containing alloys. The immersion tests, conducted up to 84 days for FeMn(-xAg) samples revealed that Mn release is higher than that of Fe. Formation of degradation products enriched in O, Ca, P and Cl was observed.

The deposition of ZnO coatings significantly improved the degradation rate of the FeMn alloys, with a significant increase in ion release up to 28 days of immersion. The formation of secondary phases during the fabrication process was observed, which contributed to accelerating degradation. Both groups of materials showed good cytocompatibility towards Saos-2 cells. Moreover, the addition of both Ag and ZnO leads to a reduction in *S. aureus* biofilm formation when compared to the base FeMn alloy.

## Resumen

Els implants biodegradables constitueixen una nova generació de materials biomèdics l'objectiu dels quals és ajudar en els processos de cicatrització dels teixits i degradar-se gradualment *in vivo* una vegada complerta la seva funció. En els darrers anys, els aliatges de Fe-Mn s'han postulat com a candidats per a implants biodegradables gràcies a les seves excel·lents propietats mecàniques i una velocitat de corrosió adequada. A més, la incorporació d'elements antimicrobians, com ara Ag i ZnO, s'està avaluant per tal de desenvolupar un material amb propietats anti biofilm que faci disminuir el risc d'infeccions associades a implants.

En aquesta tesi, es van fabricar aliatges porosos equiatòmics de Fe-Mn en forma de disc mitjançant pulvimetal·lúrgia per molta en un molí de boles i posterior sinterització al buit. En el primer estudi es va abordar la incorporació de Ag amb capacitat anti bactericida a l'aliatge Fe<sub>50</sub>Mn<sub>50</sub> mitjançant aliat mecànic de pols metàl·liques per formar precipitats rics en Ag uniformement dispersos dins de la matriu de FeMn. El segon estudi es va enfocar en la deposició d'un recobriment de ZnO sobre el disc porós de FeMn mitjançant el mètode de recobriment per immersió (dip-coating). La introducció d'Ag i ZnO tenia com a objectiu accelerar la velocitat de degradació del material i, simultàniament, dificultar la formació de biopel·lícules. Es van emprar diverses tècniques per caracteritzar les propietats dels materials sintetitzats, incloent-hi la microscòpia electrònica de rastreig, la microscòpia electrònica de transmissió, i la difracció de raigs X per a la caracterització de la microestructura, mentre que es van dur a terme assajos de nanoindentació i compressió per avaluar-ne les propietats mecàniques. La biodegradabilitat es va investigar tot submergint les mostres en una solució de Hank's (HBSS). Així, es va quantificar l'alliberament d'ions de Fe, Mn i Ag/Zn per avaluar la velocitat de degradació. Les propietats magnètiques es van estudiar per magnetometria de mostra vibrant abans i després de la immersió en HBSS. També es van dur a terme estudis de citocompatibilitat en cèl·lules Saos-2, de les respostes inflamatòries de les citocines, i de la formació de biopel·lícules de *Staphylococcus aureus*.

---

Els resultats van revelar que és factible fabricar biomaterials porosos, no citotòxics, de base FeMn mitjançant pulvimetal·lúrgia. Es va observar que la microestructura dels aliatges porosos de FeMn(-xAg) canvia amb l'augment del contingut de Ag, des d'una única fase austenítica fins a la coexistència de fases austenita i martensita, cosa que també condueix a una major resistència mecànica dels aliatges que contenen Ag. Les proves d'immersió de FeMn(-xAg), realitzades fins a 84 dies, van revelar que l'alliberament de Mn és més gran que el de Fe. Es va observar la formació de productes de degradació enriquits en O, Ca, P i Cl. D'altra banda, el recobriment dels discs de FeM amb ZnO va permetre millorar significativament la velocitat de degradació del material, observant-se un augment significatiu de l'alliberament d'ions fins als 28 dies d'immersió. Es va observar la formació de fases secundàries durant el procés de fabricació de les mostres, fet que podia explicar l'increment observat en la velocitat de degradació. Tots dos grups de materials van mostrar bona citocompatibilitat en cèl·lules Saos-2. A més, l'addició d'Ag i ZnO conduïa a una reducció en la formació de biopel·lícules de *S. aureus* en comparació amb l'aliatge de base FeMn.

# Glossary

**AM** Additive manufacturing

**bcc** Body-centred cubic

**BMs** Biodegradable metals

**CR** Corrosion rate

**CFU** Colony forming units

**EDS** Energy dispersive X-ray spectroscopy

**EPS** Extracellular polymeric substances

**E<sub>r</sub>** Reduced Young's modulus

**FBR** Foreign body reaction

**fcc** Face-centred cubic

**GIXRD** Grazing incidence X-ray diffraction

**H** Hardness

**HBSS** Hank's balanced salt solution

**hcp** Hexagonal close-packed

**HUVEC** Human umbilical vein endothelial cells

**IAI** Implant-associated infections

**ICP** Inductively coupled plasma (spectroscopy)

**MEA** monoethanolamine

**MRI** Magnetic resonance imaging

**NDE** Negative difference effect

**PBS** Phosphate-buffered saline



---

**PEEK** Polyetheretherketone

**PGA** Polyglycolic acid

**PLLA** Poly(L-lactic acid)

**PM** Powder metallurgy

**PVA** Polyvinyl alcohol

**RMA** Relative metabolic activity

**SBF** Simulated body fluid

**SHE** Standard hydrogen electrode

**SLM** Selective laser melting

**SAED** Selective area electron diffraction

**SEM** Scanning electron microscopy

**STEM** Scanning transmission electron microscopy

**TEM** Transmission electron microscopy

**TWIP** Twinning-induced plasticity (steel)

**VSM** Vibrating sample magnetometer

**XRD** X-ray diffraction

# Preface

This thesis is structured into the following chapters:

- |                                      |  |
|--------------------------------------|--|
| <b>1 Introduction</b>                | An overview of biodegradable Fe-based alloys is presented, exploring the underlying reasons for pursuing this research. The fundamentals of biodegradable alloys, methods to enhance their performance, and the evaluation of their biocompatibility are all discussed. Furthermore, this chapter addresses the issue of biofilm-associated infections and presents potential solutions for addressing this concern. |
| <b>2 Objectives</b>                  | The main objectives and aims of this work.   |
| <b>3 Experimental</b>                | A detailed description of the experimental techniques employed to fabricate and characterize FeMn-based biodegradable materials performed within this work.  |
| <b>4 Results</b>                     | Main findings obtained as a part of this work presented in the form of a compilation of articles.  |
| <b>5 General discussion</b>          | Broader discussion of the aspects not fully addressed in the articles.   |
| <b>6 Conclusions and future work</b> | Main conclusions derived from the thesis and aspects that can be tackled as a continuation of this work.   |

# Contents

<b>Acknowledgments</b>	<b>i</b>
<b>Abstract</b>	<b>iii</b>
<b>Resumen</b>	<b>v</b>
<b>Glossary</b>	<b>vii</b>
<b>Preface</b>	<b>ix</b>
<b>1 Introduction</b>	<b>1</b>
1.1 Biodegradable metals . . . . .	2
1.1.1 Degradation mechanism of biodegradable metals . .	4
1.1.2 Mg-based biodegradable metals . . . . .	8
1.1.3 Zn-based biodegradable metals . . . . .	10
1.1.4 Fe-based biodegradable metals . . . . .	11
1.2 Fe-Mn biodegradable alloys . . . . .	14
1.2.1 Degradation mechanism . . . . .	16
1.2.2 Alloying . . . . .	18
1.2.3 Processing methods . . . . .	19
1.2.4 Porous structures . . . . .	19
1.2.5 Surface modifications . . . . .	20
1.3 Biocompatibility of Fe-based biodegradable metals . . . . .	22
1.3.1 <i>In vitro</i> cytotoxicity assessment . . . . .	24
1.3.2 <i>In vitro</i> biocompatibility of Fe-Mn alloys . . . . .	26
1.4 Antibacterial and antibiofilm materials . . . . .	29
1.4.1 Biofilm formation . . . . .	31
1.4.2 Design strategies of antibacterial and antibiofilm materials . . . . .	32
1.4.3 Degradable versus non-degradable biomaterials - infection resistance . . . . .	34
1.5 Antibacterial and antibiofilm Fe-based biodegradable alloys	34
<b>2 Objectives</b>	<b>38</b>

<b>3</b>	<b>Experimental techniques</b>	<b>40</b>
3.1	Processing techniques . . . . .	41
3.1.1	Powder metallurgy . . . . .	41
3.1.2	Surface modification of FeMn alloy by dip-coating of ZnO . . . . .	42
3.2	Characterization techniques . . . . .	44
3.2.1	Biodegradability . . . . .	44
3.2.2	Physical properties . . . . .	46
3.2.3	Cytotoxicity tests and cell proliferation assays . . .	49
3.2.4	Assesment of bacterial adhesion and viability . . . .	50
	<b>Bibliography</b>	<b>53</b>
<b>4</b>	<b>Results as a compilation of articles</b>	<b>73</b>
4.1	Paper 1: Biodegradable porous FeMn (-xAg) alloys: As- sessment of cytocompatibility, mechanical, magnetic and antibiofilm properties . . . . .	74
4.2	Paper 2: Silver-induced $\gamma \rightarrow \epsilon$ martensitic transformation in FeMn alloys: An experimental and computational study	95
4.3	Paper 3: Accelerated biodegradation of FeMn porous al- loy coated with ZnO: effect on cytocompatibility and an- tibiofilm properties . . . . .	112
<b>5</b>	<b>General discussion</b>	<b>132</b>
<b>6</b>	<b>Conclusions and future perspectives</b>	<b>138</b>
	<b>List of Figures</b>	<b>141</b>
	<b>List of Tables</b>	<b>143</b>



# 1 Introduction

Nowadays, we face increasing life expectancy and, at the same time, people wish to maintain the highest quality of life during ageing. As a perfect machine, the human body can self-heal when injured. However, as the expected life span increases, the human body may reach a state when it can no longer repair the injuries naturally. Fortunately, this naturally irreparable damage can be rebuilt by the surgical implantation of biomaterials, which will assist in tissue regeneration and healing. Implants are materials made of various metals, polymers, and ceramics, and interest in developing new and better materials for implants is increasing every year. When load-bearing applications are significant, metals are the most suitable group due to their high mechanical strength and fracture toughness [1].

In most cases, ordinary implants made of titanium and stainless steel must be removed after a certain period posterior to implantation, which involves a secondary implant removal operation, and thus increases the cost of medical treatment and the risk of infection. Moreover, they cause undesirable phenomena such as stress shielding and the release of toxic metallic ions, which can negatively influence patients' health.

Fortunately, in the last two decades, the concept of biodegradable materials has been conceived to avoid implant removal surgery. This class of biodegradable implants performs its function for a limited period, promoting the healing process, and then gradually dissolves *in vivo* until it is completely degraded. The first comprehensively studied biodegradable implant materials were polymers, as their biodegradability could be well adjusted, and the degradation products could be predicted. Polymers such as polyetheretherketone (PEEK) [2]–[4], poly(L-lactic acid) (PLLA) [5]–[7], polyglycolic acid (PGA) were tested and commercially applied. However, owing to their poor mechanical properties, they cause several problems, such as large implant sizes needed to achieve the necessary mechanical stability and load-bearing capacity, thrombosis, inflammation, or delayed arterial healing.

Taking into account the superior mechanical properties of metals compared to polymers, researchers have proposed a new idea, *i.e.* to apply metallic materials as biodegradable materials. Table 1.1 compares the mechanical properties of the most commonly studied biodegradable polymer (PLLA) and degradable metals. Mg- and Fe-based materials are the most intensively studied groups of degradable metals. In the last few years, another group of Zn-based alloys has been extensively investigated. Pure Mg possesses the lowest mechanical strength (with a tensile strength of 86 MPa) and elongation, while pure Fe - the highest, with a tensile strength of 200 MPa. The mechanical strength of Zn lies between Mg and Fe, with a value of tensile strength of 150 MPa. For comparison, PLLA has a tensile strength of 70 MPa, which is lower than all mentioned metals.

Table 1.1: Comparison of mechanical properties of the most commonly studied biodegradable materials

Material	Young's modulus (GPa)	Yield strength (MPa)	Tensile strength (MPa)	Elongation (%)	Ref.
Pure Mg	41	20	86	13	[8]
Pure Zn	94	150	150	20.5	[9]
Armco Fe	200	150	200	40	[8]
PLLA	3.1	-	70	6	[10]

### 1.1 Biodegradable metals

Even though the common trend in the field of metallic biomaterials is to improve their corrosion resistance, recently a new group emerged – biodegradable metals, where the paradigm is turned around and faster corrosion becomes an advantage. The definition of biodegradable metals, proposed by Zheng *et al.* [11] is as follows: *Biodegradable metals (BMs) are metals expected to corrode gradually in vivo, with an appropriate host response elicited by released corrosion products, then dissolve completely upon fulfilling the mission to assist with tissue healing with no implant residues.* The main component of BMs should be a metallic element essen-

tial to human body, that has the ability to be metabolized or assimilated by cells and tissues [11].

Biodegradable metals, compared to inert implants, are considered bioactive, *i.e.* they evoke a biological response at the biomaterial/tissue interface, which results in bond formation [12]. Degradable metals have found increasing interest in the last two decades when the vast majority of scientific papers were published. The paradigm of degradable implant materials is that they gradually degrade *in vivo* until their role is fulfilled, without the need for a revision surgery. Three main groups of alloys emerged, namely Mg-, Zn- and Fe-based alloys. All those elements are essential for the human body and are considered promising as biodegradable metals.

Fig. 1.1 shows schematically the degradation process and changes in the mechanical integrity of biodegradable metals during the bone fracture healing process, which involves inflammation, repair and remodelling phases. Soft callus forms during the first 2-3 weeks post-fracture. Then, the mineralization progresses to transform a soft callus into a hard callus, possessing enough strength and rigidity to withstand low-impact exercise. The period of healing depends on the location of the fracture, the patient's age and health, and the condition of adjacent soft tissues. It is generally thought that mechanical support should be kept within 12-24 weeks, depending on the factors mentioned earlier. In the case of Mg alloys, the loss of mechanical integrity occurs earlier, thus their degradation should be slowed down to extend their functionality. For Fe-based alloys, the good mechanical integrity is kept for an exceedingly large period, thus the degradation should be accelerated [11].

The widespread use of biodegradable metals in clinical applications still requires further investigation. Many factors should be taken into account, *e.g.* age and condition of the patient, type of fracture, risk of infection, *etc.* One of the steps to allow the broad use of biodegradable implants is to adjust their mechanical properties and carefully study the degradation process, both *in vitro* and *in vivo*.



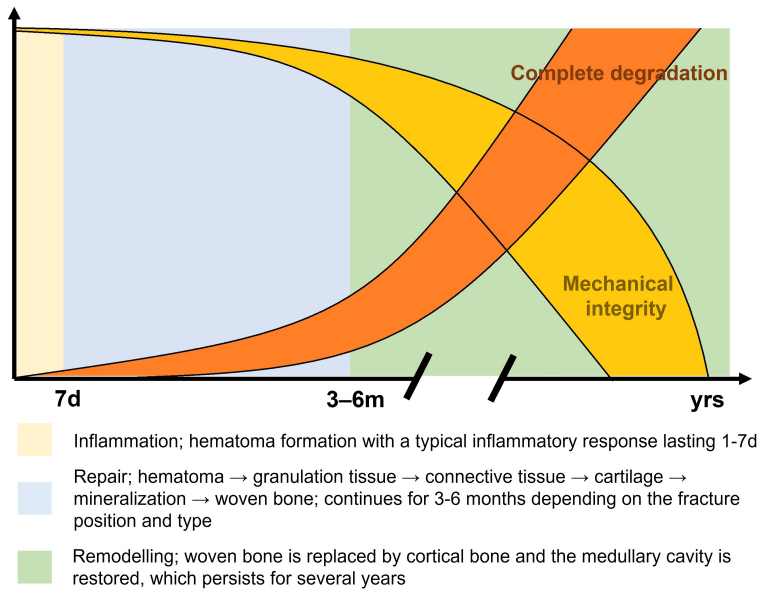
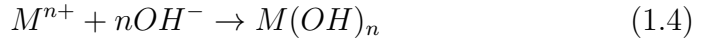


Figure 1.1: Schematic mechanism of the degradation process and changes in the mechanical integrity of biodegradable metals during bone healing process. Reproduced from [11]. Copyrights Elsevier 2014.

### 1.1.1 Degradation mechanism of biodegradable metals

Biodegradable metals should degrade in the physiological environment of the human body and the degradation rate should match the healing period. The generalized mechanism of degradation occurs by an electrochemical reaction with electrolyte (physiological solutions or body fluids). Oxides, hydroxides, phosphates, hydrogen gas and other compounds can be produced as a result of the degradation. Fig. 1.2 shows the schematic process of degradation in body fluids. When the degradation process occurs in a nearly neutral environment, the reactions comprise the anodic dissolution of the metal (Eq. 1.1) and varying cathodic reaction (Eq. 1.2 or Eq. 1.3). As soon as the metal is in contact with body fluids, it is oxidized into metallic cations, according to Eq. 1.1 and Fig. 1.2a. Then the electrons generated by anodic reactions are consumed in cathodic reactions, which for Mg alloys corresponds to water reduction (Eq. 1.2) and for Fe and Zn alloys - dissolved oxygen reaction (Eq. 1.3). According to Fig. 1.2a,b the cathodic and anodic reactions will be accompanied by adsorption of organic molecules, such as proteins, amino acids and

lipids. A layer of degradation products will form on the surface, according to Eq. 1.4 and Fig. 1.2b, which then can be broken down by the presence of chlorides on its surface, leading to pitting corrosion (Fig. 1.2c). Further degradation is followed by the deposition of calcium phosphates (*i.e.*, apatite-like precipitates) on the surface, as well as cell adhesion. As implantation time increases, the cells will proliferate to form tissues. Meanwhile, the degraded metal will disintegrate in the form of particles, which will be discharged into the surrounding media (Fig. 1.2d).



### Biodegradability testing

Biodegradability testing *in vitro* is aimed to simulate the *in vivo* degradation process and is usually performed in physiological solutions such as the well-known Hank's balanced salt solution (HBSS), the simulated body fluid (SBF) and the phosphate-buffered saline (PBS). Table 1.2 lists the ion concentration in blood plasma and the most commonly used physiological solutions. Biodegradability tests are typically performed at a body temperature of around 37°C. Methods such as static and dynamic immersion, potentiodynamic corrosion testing and others are usually applied. The static immersion test is based on the ASTM-G31-72 standard, where the specimens are simply immersed in a physiological solution with a given surface-to-solution ratio for a desired period of time (usually up to one month). Then the samples can be analyzed for weight loss and the media can be used to examine the concentrations of released ions. Both of those values can be later used to estimate the corrosion rates, according to Eq. 1.5 [13] and Eq. 1.6 [14]. Removing corrosion products in the

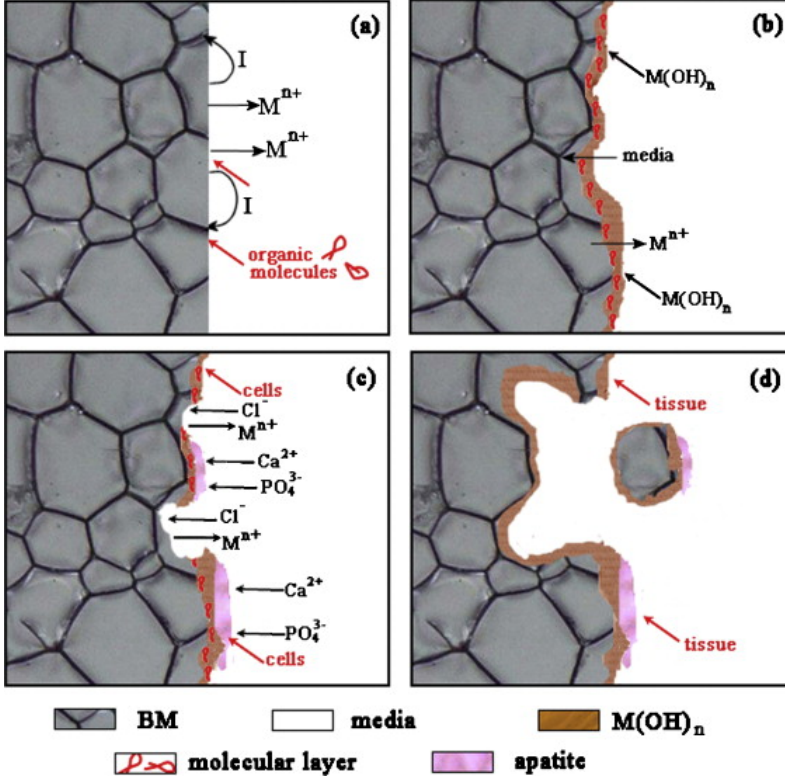


Figure 1.2: Schematic mechanism of the degradation process of biodegradable metals in body fluids. Reproduced with permission [11]. Copyright 2014, Elsevier.

mass-loss measurements is crucial, otherwise, it can lead to a negative corrosion rate (mass gain) [14], [15]. This removal of corrosion products might be difficult for porous materials due to the accumulation of products inside the pores. Hence, for porous materials other methods, such as ion release determination might be more appropriate.

$$CR = 8.76 \times 10^4 * W / (A * t * \rho) \quad (1.5)$$

Where  $CR$  is the corrosion rate in millimetres per year ( $\text{mm year}^{-1}$ ),  $W$  is the weight loss (g),  $A$  is the specimen area ( $\text{cm}^2$ ),  $t$  is the exposure time (h) and  $\rho$  is the density ( $\text{g cm}^{-3}$ ). Another way to express the corrosion rate is by using the released ion concentration, as expressed by Eq. 1.6:

$$CR = cV/St \quad (1.6)$$

Where  $CR$  is the corrosion rate given in  $\text{g/m}^2/\text{day}$ ,  $c$  is the ion release concentration ( $\text{g/L}$ ),  $V$  is the volume of solution used in the immersion

test (L),  $S$  is the initial surface area exposed to the corrosive solution ( $\text{m}^2$ ) and  $t$  is the exposure time (days).

Moravej *et al.* [16] proposed a dynamic degradation test with a test bench designed for this purpose. In a dynamic test, the samples are exposed to the circulation of the testing solution. The dynamic solution flow can partially remove the degradation products and the calculated degradation rate obtained through a dynamic test is generally higher than in the static one, as the passive layer of corrosion products forms later.

Another method used to estimate the corrosion rate is the potentiodynamic polarization test. The corrosion rate in that test is calculated according to the Eq. 1.7. It is a very efficient way of studying the corrosion behaviour of biodegradable alloys. However, these tests are performed in a short testing time, with an accelerated corrosion process, which does not directly simulate the real corrosion process *in vivo*.

$$CR = (3.27 \times 10^{-3} * i_{corr} EW) / \rho \quad (1.7)$$

Where  $CR$  is the corrosion rate in millimeters per year ( $\text{mm year}^{-1}$ ),  $i_{corr}$  is the corrosion current density ( $\mu\text{Acm}^{-2}$ ),  $EW$  is the equivalent weight of the material and  $\rho$  is its density ( $\text{gcm}^{-3}$ ).

Table 1.2: Compositions of blood plasma and most commonly used pseudo-physiological solutions [17]

Ions (mg/L)	Blood plasma	0.9M NaCl	HBSS	SBF	PBS
$\text{Na}^+$	3000-3400	5425	3258	3265	3519
$\text{K}^+$	130-210	-	227	195	162
$\text{Cl}^-$	3400-3750	3518	5043	5275	4947
$\text{HCO}_3^-$	1100-2400	-	254	256	-
$\text{HPO}_4^{2-}$	270-450	-	75	96	920
$\text{Ca}^{2+}$	84-110	-	-	100	-
$\text{Mg}^{2+}$	15-30	-	-	36	-
$\text{SO}_4^{2-}$	5-15	-	-	-	-
D-glucose	600-1100	-	1000	-	-
Albumin	35000-50000	-	-	-	-

### 1.1.2 Mg-based biodegradable metals

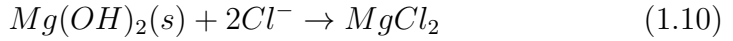
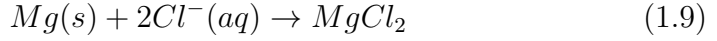
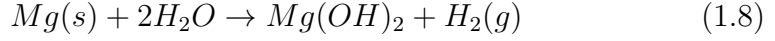
Magnesium is one of the essential elements in the human body, being naturally found in bone tissue. It is involved in the activation of enzymes and numerous physiological processes, such as bone formation, neuromuscular stability and muscle contractility [1], [18].

Mg-based alloys have been widely studied as structural materials thanks to their low density ( $1.738 \text{ g/cm}^3$ ) and adjustable mechanical properties. These alloys are of particular interest for industries where low density is an important factor, such as the automotive [19]–[22] and aerospace industries [23]–[26]. Regarding their application as implant material, Mg alloys are also attractive due to their low weight, relatively high fracture toughness, and elastic modulus and compressive strength close to that of human bone [27]–[29]. The low elastic modulus (15–30 GPa) of Mg is favourable as it can reduce the so-called stress shielding effect during the load transfer at the bone-implant interface [27]. Moreover, Mg is one of the least noble metals in the electrochemical series, with a corrosion potential of  $-2.372 \text{ V}$  vs. the standard hydrogen electrode (SHE) [30].

Mg and its alloys have been used for over 100 years in numerous clinical applications, such as cardiovascular, musculoskeletal and general surgeries [11] due to their good biocompatibility and mechanical properties close to that of human bone. Various Mg implants have been used, including fixation pins, wires, nails, screws, plates, sheets and others. Due to several factors, such as uncontrollable corrosion rates and accumulation of hydrogen gas bubbles as well as simultaneous developments in stainless steel-based implants, the research on Mg implants was abandoned and it was resumed again only two decades ago [31], when the idea of biodegradable metallic stents emerged.

One of the biggest challenges in using Mg and its alloys is their high degradation rate and abnormal hydrogen release upon degradation in physiological pH (7.4–7.6) [1], which is referred to as the Negative Difference Effect (NDE). In a standard atmosphere, unprotected magnesium corrodes with developing magnesium hydroxide  $\text{Mg}(\text{OH})_2$ , slightly soluble in water. However, when the corrosion takes place in an aqueous physiological solution containing chloride ions ( $\text{Cl}^-$ ), the degradation process is severe,

as the  $Mg(OH)_2$  reacts with  $(Cl^-)$  to create soluble magnesium chloride and hydrogen gas, as shown in the Eqs. 1.8, 1.9, 1.10,:



Premature degradation of the implant does not provide long enough mechanical support, as the implant corrodes before the new tissues can develop enough to withstand the applied mechanical load. Moreover, the generation of hydrogen gas, forming as bubbles on the surface of Mg, can cause undesirable effects, such as the penetration of the bloodstream with  $H_2$  gas [31] and inflammation around the implant.

Other limitations of Mg, possessing a hexagonal close-packed (hcp) structure, are its poor mechanical properties and low ductility. To date, researchers have published numerous reports on changes and improvements in the chemical composition, microstructure and fabrication processes to produce new alloys with more suitable degradation rates. Alloying can furnish a material with a chemical composition able to provide increased corrosion resistance and appropriate mechanical properties and at the same time, improve the formability of the material. There are two main groups of Mg-based alloys, namely those containing 2-10% of Al with trace additions of Zn and Mn, providing controlled degradation rate and improved mechanical properties, and those involving rare earth elements combined with Zn, Y, Ag and small additions of Zr, that provides refined structure and better mechanical properties [1]. The most important condition regarding alloying is that the alloying element is not causing toxicity.

Different approaches to improve the properties of Mg-based alloys involve studying coatings to control the degradation rate and improve the biocompatibility or bioactivity of implants [32]–[34]. Coatings such as calcium phosphate [35]–[37] can help to control the degradation process

by simply delaying the initiation of corrosion. Biodegradable polymers used as coatings are also a suitable approach to slow down the corrosion process [38]–[40].

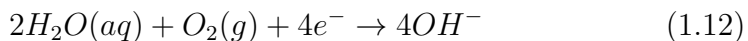
To sum up, Mg-based alloys constitute promising materials for biodegradable implant applications. The main strategy to improve their properties is to increase their corrosion resistance in physiological conditions by altering their composition and coating deposition.

### 1.1.3 Zn-based biodegradable metals

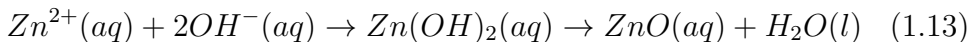
The fabrication of Zn-based biodegradable metals emerged recently as a new research interest in the field of biomaterials. Zn, similar to Mg and Fe, is an important nutrient element in the human body, regulating gene expressions, being a catalyst for over 50 enzymes and stimulating bone formation [41]. The daily intake of Zn is between 6-10 mg [9]. Zinc has been one of the most studied alloying elements for biodegradable Mg-based alloys and it is currently studied as the main element in Zn-based biodegradable alloys. It possesses a suitable degradation rate, between that of Mg (-2.372 V vs. SHE) and Fe (-0.447 V vs. SHE), with a standard electrode reduction potential of -0.762 V vs. SHE [30], making it a very attractive candidate for biodegradable implant applications. Moreover, Zn is susceptible to corrosion in neutral pH in aqueous environments [42]. The anodic reaction for Zn in aqueous solutions is:



The cathodic reaction comprises the formation of hydroxide ions:



The hydroxide ions react with the  $\text{Zn}^{2+}$  cations to yield  $\text{Zn}(\text{OH})_2$ , which later evolves to ZnO and water:



The main limitation of pure Zn results from its poor mechanical properties, as in the case of Mg. Zn is a metal with a hcp crystalline structure and low melting point, which provides a high driving force for dynamic recovery [43].

As a result, the dislocation density does not increase significantly during plastic deformation, contributing to its limited strength and plasticity [44]. Moreover, Zn undergoes strain softening, *i.e.* its strength decreases with plastic deformation [44]–[46]. While biomedical devices should have stable mechanical properties, strain softening could deprive the materials of their sufficient mechanical characteristics [41].

Efforts have been made to improve the mechanical properties of Zn-based alloys and limit the strain-softening effect. One of the most popular approaches is by alloying with soluble elements, such as Mg [47], [48], Al [49], Cu [50], Li [51], Ca [52], Sr [52]. Alloying with Mg led to an improved cytocompatibility [48] and strength, however, the ductility remained low, reaching the highest value of 15% for Zn-0.15Mg alloy [47] and the strain softening effect remained. Similar results were obtained for Zn-Al alloy [49]. Alloying with other elements also did not limit the strain-softening effect. Recently, relevant results have been achieved upon alloying Zn with Ag [53], [54], which helped to limit the strain softening and improved the strength and ductility. Furthermore, the Zn-Ag alloy showed good cytocompatibility [54].

Overall, Zn is a new, promising "rising star" of biodegradable metals. Several challenges are currently being solved to apply the material as an implant, the most challenging being its poor mechanical properties. Unfortunately, due to its low mechanical strength, the application of Zn-based alloys as implant materials might be only limited to coronary arteries.

#### 1.1.4 Fe-based biodegradable metals

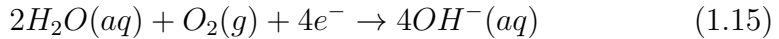
The earth is rich in iron ore, as it forms around 5% of Earth's crust. Fe as a pure metal or a main element of steels has found countless applications in construction materials [55], [56], in the automotive industry [57]–[59] and many others. The most common group of alloys using iron as the major alloying element are steels.

Fe is a key element in the human body, as it is an essential component of hemoglobin and myoglobin. Hemoglobin is responsible for the transportation of oxygen from the lungs to the rest of the body, while

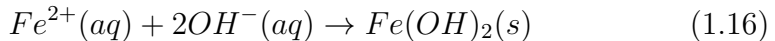


myoglobin provides oxygen to the muscles, supporting muscle metabolism. Moreover, Fe is crucial for physical growth, hormone synthesis, cellular functions and neurological development. The daily intake of Fe for adults is between 10-20 mg, but it depends on the age, sex, and type of diet. The upper limit of Fe intake is around 45 mg for adults.

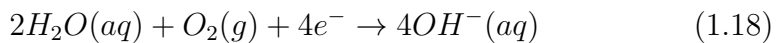
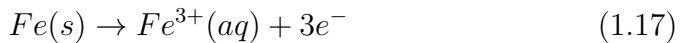
The application of Fe-based metals as an implant material is not new, as stainless steels have been already widely applied as load-bearing permanent implants in clinical applications. Iron has high mechanical strength, ductility, and formability and shows good biocompatibility. The combination of good mechanical parameters and formability has unique benefits such as the possibility of fabricating thinner and smaller products and producing complicated shapes such as foils, struts and foams. Moreover, the advantage of Fe over Mg is that it does not show any hydrogen gas evolution upon corrosion. However, Fe has the highest corrosion potential among the standard biodegradable metals (Mg, Zn and Fe), namely -0.447 V vs. SHE [30], which makes it less prone to corrosion. The main challenge in its application as a biodegradable metal is the need to accelerate its slow degradation rate. According to the Pourbaix diagram for Fe [60], it is susceptible to corrosion in neutral pH in aqueous environments, which can be described by the following anodic and cathodic reactions:



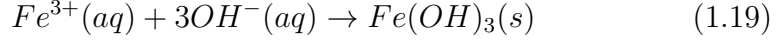
The general corrosion reaction can be described as:



Fe can also oxidize to the III oxidation state, as described by the following anodic and cathodic reactions:



The general corrosion reaction, in this case, can be described as follows:



The oxidation state of Fe can affect the long-term cytocompatibility of the implant. It was observed that when Fe is oxidized to  $Fe^{3+}$  rather than  $Fe^{2+}$ , the degradation products induce higher cytotoxicity [61]–[64].

Physiological fluids are composed of water, metallic and non-metallic ions and proteins that are not described by the above corrosion reactions. Because of the complex composition of physiological solutions, apart from oxides and hydroxides, several different degradation products can form as Fe reacts with the ions present in physiological solutions. As a result, degradation products such as iron phosphates ( $FePO_4$ ) and carbonates ( $FeCO_3$ ) can form. Moreover, Fe-free species such as calcium carbonates ( $CaCO_3$ ), phosphates and proteins can be adsorbed on the surface.

The mechanical properties of Fe such as ultimate strength, ductility and yield strength are much higher than those of Mg and Zn. Contrary to Mg and Zn, which possess the hcp structure, Fe possesses a body-centred cubic (bcc) structure. The bcc structure is characterized by a higher number of slip systems, which can be activated to accommodate plastic deformation.

The main limitations of Fe result from its low corrosion rate and ferromagnetism of pure Fe. Ferromagnetism can lead to misplacement of the stent during implantation and limit the post-implantation checks by magnetic resonance imaging (MRI). The corrosion rate of Fe-based biodegradable alloys has been improved through alloying with various elements such as Mn [65]–[67], Ga [68], through the creation of porous structures [69], surface grain refinement [70], ion implantation with Zn [71], Ta [72], Pt [73] and Au [74], etc.

An antiferromagnetic Fe-based alloy can be formed by alloying with high amounts of Mn, as established in the breakthrough study by Hermawan [65], [75]. The high content of Mn is also used to stabilize austenite ( $\gamma$ -Fe) at room temperature, reduce the corrosion potential of the system to increase the degradation rate, and promote higher ductility. Thus,

Fe-Mn alloys constitute a very promising biomaterial of choice and will be discussed in detail in the next section.

### 1.2 Fe-Mn biodegradable alloys

Manganese is currently the most studied alloying element for biodegradable Fe-based alloys. As mentioned above, it provides a number of advantages such as stabilization of austenitic  $\gamma$ -Fe, eliminating or significantly decreasing strong ferromagnetism of pure Fe, and improving mechanical properties due to solid solution strengthening, which allows for higher ultimate tensile strength and elongation to failure. Moreover, Fe-Mn alloys possess a higher corrosion rate than pure Fe and show good biocompatibility.

Fe-Mn alloys as biodegradable implant materials were first proposed by Hermawan *et al.* in a study from 2007 [75]. The Fe-35Mn (wt.%) alloy was proposed due to its low magnetic susceptibility, good mechanical properties and satisfactory corrosion behaviour. Securing the non-magnetic behaviour of Fe-Mn alloys is of utmost importance, as it makes the alloy compatible with MRI.

Fig. 1.3a shows the phase diagram for the Fe-Mn system, in which many different phases can form, depending on the temperature and Mn content [66]. The Fe-Mn phase diagram consists typically of three main phases:  $\alpha$  ferrite of bcc structure,  $\gamma$  austenite with face-centred cubic (fcc) structure and  $\sigma$  phase with tetragonal structure. The two most common phases are bcc- $\alpha$  and fcc- $\gamma$ . The  $\alpha$  (ferrite) phase is a solid solution of Mn in Fe, with a bcc structure, formed at low temperatures with low Mn content. It is a strongly ferromagnetic phase. The  $\gamma$  austenite phase has an fcc structure, it is stable at higher temperatures and contains more Mn. The presence of a sufficient amount of Mn stabilizes the austenitic structure of the system at room temperature.

Fig. 1.3b shows constituent phases forming in cast Fe-Mn alloys. Apart from the phases shown on the phase diagram in panel (a), the hexagonal  $\epsilon$  and  $\alpha'$  phases can also form. The  $\epsilon$ -martensite formation can occur under specific conditions by transformation from austenitic phase [77], [78]. Austenite has low stacking fault energy, hence during plastic

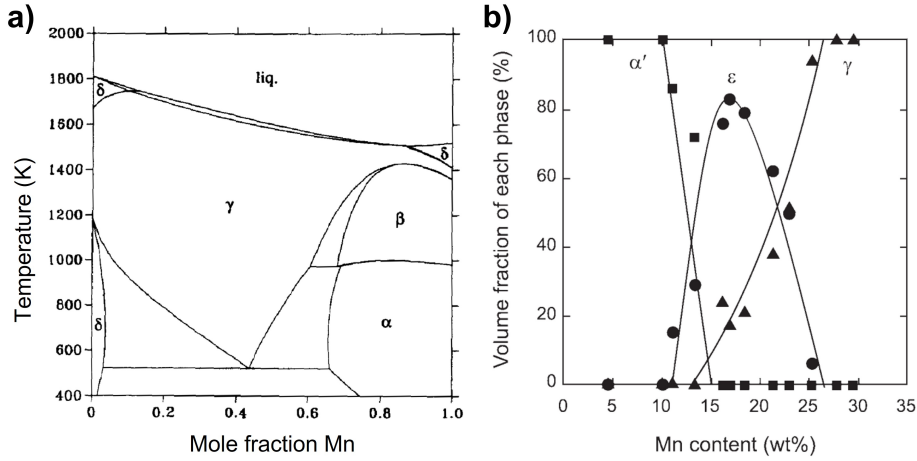


Figure 1.3: (a) Phase diagram of Fe-Mn system and (b) volume fraction of phases depending on Mn content in Fe-Mn alloys obtained through casting. Reproduced with permission [76].

deformation and rapid cooling, it can undergo phase transformation to form  $\epsilon$  martensite [79]. By applying stacking faults on the alternate close pack (111) planes of austenite, the hexagonal  $\epsilon$  martensite phase can form and the transformation takes place via dislocation glide [79], [80]. The  $\epsilon$  phase, similarly to austenite, has antiferromagnetic properties. This phase is known for its exceptional mechanical properties, and alloys exhibiting the phase transformation have been widely applied where superior mechanical properties are of need.

Owing to their exceptional mechanical properties and excellent formability, the Fe-Mn alloys gained great interest in the field of biodegradable metals [65], [66], [81]. Among this group, those comprising more than 20 wt.% Mn have garnered significant attention due to their non-magnetic character, and favourable balance between strength and degradability [75], [82]. While *in vitro* studies demonstrated that the corrosion of Fe-Mn alloys surpasses that of pure Fe, *in vivo* investigations have revealed that their corrosion rate remains inadequately slow [83]. Consequently, novel strategies and solutions are currently under development to accelerate the corrosion rate of Fe-Mn alloys [84]–[86]. In the next subsections, various strategies implemented so far to improve the properties of Fe-Mn-based implant materials are discussed.

### 1.2.1 Degradation mechanism

Manganese is less noble than Fe in the electrochemical series, having a standard reduction potential of  $-1.185\text{V}$  vs. SHE [30], for the reduction of  $\text{Mn}^{2+}$ . As it is fully soluble in Fe, a decreased corrosion potential of the alloy is expected, as confirmed by various investigations. Manganese, similarly as Fe, can interact with other species present in the physiological fluids to form various degradation products, such as carbonates ( $\text{MnCO}_3$ ) [87].

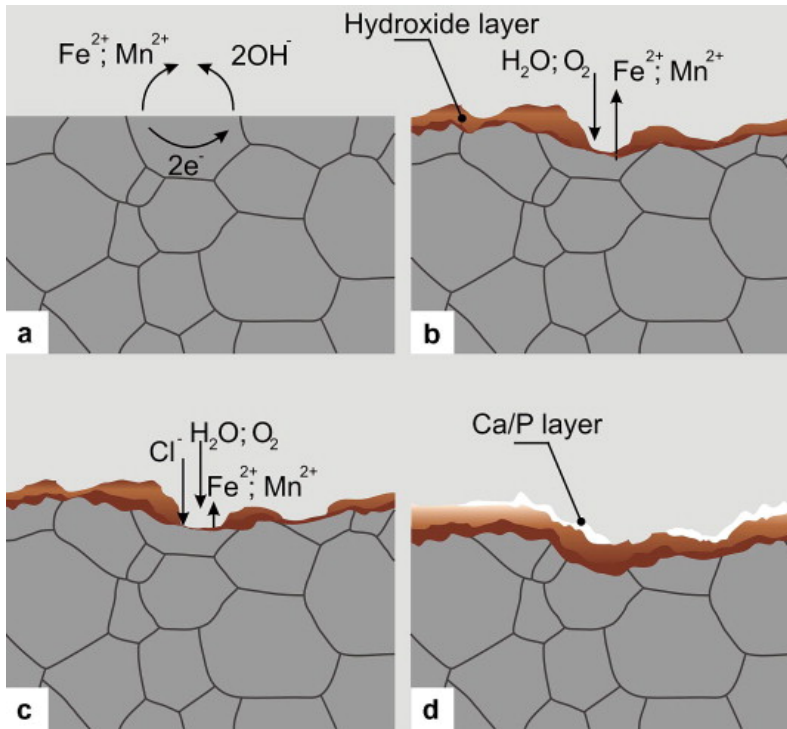
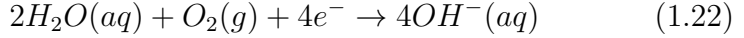
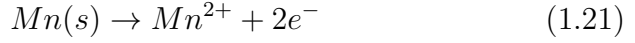


Figure 1.4: Schematic of generalized degradation mechanism of Fe-Mn alloys. Reproduced with permission [65]. Copyright 2010, Elsevier.

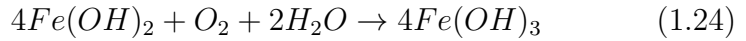
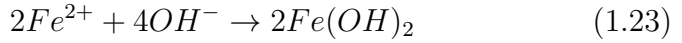
Fig. 1.4 illustrates the corrosion mechanism of Fe-Mn alloys. According to Hermawan *et al.* [65], four steps can be distinguished:

1. **Initial corrosion reaction (Fig. 1.4a):** As soon as the alloy is immersed in the test physiological solution, it is oxidized to metallic ions, as described by reactions 1.20 and 1.21. The electrons produced in the anodic reaction are consumed in a cathodic reaction, according

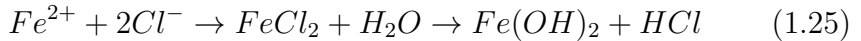
to reaction equation 1.22. These anodic and cathodic reactions occur over the entire surface, at grain and phase boundaries, in places where there is a difference in corrosion potential.



2. **Formation of hydroxide layers (Fig. 1.4b):** The released metallic ions and the hydroxyl ion ( $OH^{-}$ ) react to produce insoluble hydroxides, as described by Eqs. 1.23 and 1.24.



3. **Formation of pits (Fig. 1.4c):** The hydroxide layers do not completely cover or protect the surface, hence the  $Cl^{-}$  ions present in physiological solutions are able to penetrate beneath the hydroxide layer and form a metal chloride, followed by its hydrolyzation by water to the corresponding hydroxide and free acid, as established by Eq. 1.25. As a result, the local pH value inside the as-formed pits is lowered, while the global solution remains neutral. The pits can then grow to become wider and deeper.



4. **Formation of calcium/phosphorus layer (Fig. 1.4d):** The last step in the degradation mechanism consists of the formation of a new layer of degradation products containing Ca and P, with a mineral-like morphology. The presence of those precipitates can eventually lead to the formation of hydroxyapatite, a biocompatible and bioactive compound, with a chemical composition similar to that of the bone.

### 1.2.2 Alloying

Alloying relies upon introducing additional elements into a primary metal to adjust their properties through compositional changes. This process has the capability to transform the microstructure, chemical, and phase composition of metals, leading to adjustments in mechanical properties, corrosion behaviour, and biocompatibility. Furthermore, alloying has the potential to impact the corrosion kinetics of biodegradable metals by influencing their electrochemical behaviour and degradation rate. In the realm of improving the properties of biodegradable Fe-Mn-based alloys, alloying stands out as the primary solution [81], [84].

The most studied alloys so far are standard Fe-Mn with varying amounts of Mn, Fe-Mn-Si and Fe-Mn-C alloys. Twinning-induced plasticity steels (TWIP), consisting of Fe, Mn and C, provide suitable degradation combined with high strength, which makes them perfect candidates for biodegradable stents [88]. The standard TWIP steels contain Fe as the base element, C, high amounts of Mn (18-30 wt.%), and sometimes traces of Al and N [89]. Biodegradable TWIP steels are of interest as they combine attractive mechanical properties, good formability and biocompatibility [88], [90], [91]. Fe-Mn-C alloys have a better corrosion rate than pure Fe [91]–[93]. Additions of Si to form Fe-Mn-Si constitute also a very interesting approach, as a shape memory alloy can be formed [94], [95].

Recently, alloying FeMn with noble metals such as Ag, Pt and Pd was proposed to induce the formation of well-dispersed particles that can act as a cathode against the Fe-Mn matrix. The resulting micro-galvanic corrosion sites can lead to an improved degradation rate of the alloys [84]. Specifically, Fe-Mn-Pd alloy was proposed by Schinhammer *et al.* [96] and proved to significantly increase the corrosion rate of FeMn in SBF. Further studies have demonstrated that this ternary alloy is a promising candidate for biodegradable implant applications [89], [97], [98]. On the other hand, Fe-Mn-Cu alloys were reported by Mandal *et al.* [99], [100] and showed a 6 times higher corrosion rate than Fe-Mn alloy. Fe-Mn-Ag alloys significantly improved the corrosion rate when compared to Fe-Mn and pure Fe [101], [102]. Moreover, additions of Cu and Ag not only improve the properties of the alloys but also inhibit bacterial growth [101].

### 1.2.3 Processing methods

Well-chosen processing methods can change the properties of Fe-Mn alloys by modifying their microstructure, grain size, crystallographic orientation, defect density and even phase composition. The processing methods used in the fabrication of Fe-Mn alloys can have a direct impact on their mechanical properties, corrosion behavior, degradation rate, and biocompatibility. Pathways such as powder metallurgy (PM), casting, plastic deformation and additive manufacturing (AM) have been used.

Powder metallurgy is a processing method that involves the fabrication of biodegradable metal implants from powders. PM techniques, such as simple pressing and sintering, can alter the microstructure and properties of biodegradable metals. For example, powder compaction parameters, such as compaction pressure and temperature, can influence the porosity, density, and mechanical properties of the final implant [103], [104]. Additive manufacturing, one of the branches of PM, is getting increasing attention for the processing of metallic biodegradable alloys thanks to its ability to create complex shapes for a wide range of applications. Technologies used in the AM of metals include selective laser melting (SLM) and laser powder-bed fusion (LPBF), which allowed for successful fabrication of Fe-Mn [105], [106] and Fe-Mn-Ag [105], [107], [108] alloys. These works proved the AM to be an effective method to fabricate both porous and dense materials with reduced corrosion resistance.

Needless to say, two alloys of the same composition can have different properties due to the processing route chosen, for example, cast and wrought FeMnSi alloys possess different phase compositions and corrosion rates [109]. The annealing and aging treatments can also change the microstructure of the material, by affecting the phase composition and precipitation growth [89], [110].

### 1.2.4 Porous structures

Designing porous structures is a successful approach to improve the corrosion rate of Fe-Mn alloys. Basically, increasing the effective surface area of the material leads to enhanced degradation. One of the explanations is that the high surface area obtained by creating pores and voids provides



a substantial number of corrosion sites allowing for the oxidation reaction [111], [112].

Apart from increasing the corrosion rate, porous structures might be useful as artificial scaffolds for bone tissues, as the porosity can enhance tissue integration and vascularization [113]. Moreover, porous structures provide space necessary for cell growth, adhesion and proliferation, thus assisting tissue-oriented endogenous growth [114]. Also, the porous structures can decrease the risks associated with stress shielding and create a durable bone-implant interface, as the mechanical properties of porous implants will be closer to that of bone.

To date, several studies have reported on the fabrication of porous Fe-Mn structures with varying levels of porosity [115], [116]. One of the most effective methods is AM, which allows for complex shapes fabrication. For instance, a porous Fe-Mn bone scaffold was fabricated by SLM and proved to have higher corrosion rate than pure Fe fabricated using the same approach. Fig. 1.5 presents Fe-Mn foams obtained through the polymeric sponge replication method, *i.e.* by dipping the polymeric sponge (template) into the powder slurry followed by drying, template removal and sintering to obtain porous foams which replicate the initial shape of a template [115]. This method is a very effective way to obtain porous structures with desired shapes, high porosity and similar pore shape to that of cancellous bone. Besides Fe-Mn, it has been already applied to other materials for implant applications such as Ti [117]–[120], Mg [114] and hydroxyapatite [121], [122].

### 1.2.5 Surface modifications

Surface modifications, as opposed to other approaches, can alter the properties of biodegradable metals by acting on the surface of the material instead of the bulk. Due to surface modifications, properties of the materials such as degradation behaviour, mechanical properties, biocompatibility, and corrosion resistance can be changed. Changing the surface roughness, and deposition of coatings onto the material or creating surface patterns can allow controlling the corrosion rate of Fe-Mn alloys, both by increasing and decreasing it [85], [123]. For instance, surface texturing and roughening can accelerate the degradation rate of biodegradable metals

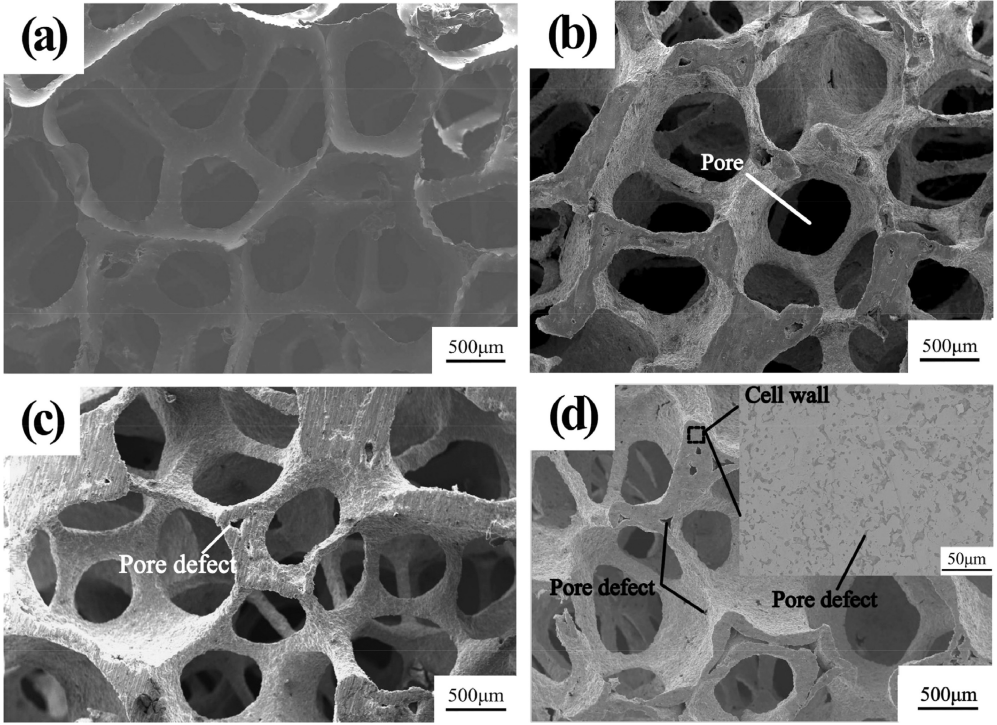


Figure 1.5: Fe-Mn foams fabricated by replica method. Reproduced with permission from [115]. Copyright 2020, Elsevier.

by increasing the surface area and promoting faster corrosion. Donik *et al.* [85] proposed a laser-texturing method to modify the surface topography of Fe-Mn alloy. Thanks to the resulting tooth comb profile at the surface, the laser-textured Fe-Mn alloy exhibits a 10 times higher degradation rate than the Fe-Mn alloy. Fig. 1.6 shows the as-prepared laser textured sample and sample after immersion for 3 days. Very clear signs of degradation can be observed just after 3 days of immersion.

Surface modifications can also influence the mechanical properties of biodegradable metals, such as their strength, ductility, and toughness. For example, the deposition of hard and wear-resistant coating can improve the wear resistance of a biodegradable metal implant in load-bearing applications. Reports on the deposition of hydroxyapatite coating by electrodeposition on Fe-Mn substrate revealed suitable mechanical properties, good adhesion to the underlying metallic material and tunable degradation behaviour [124], [125].

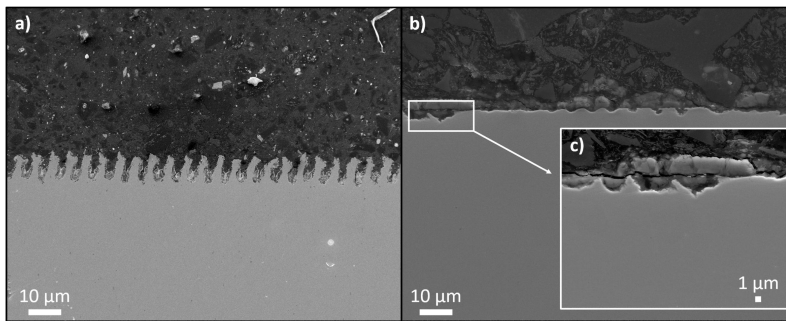


Figure 1.6: SEM images of surface topography of laser-textured Fe-Mn samples (a) after 3 days of immersion (b) and (c). Reproduced with permission from [85]. Copyright 2018, Elsevier

Another advantage of surface modifications is the possibility of enhancing the biocompatibility of Fe-Mn alloys by creating a surface that is more prone to cell adhesion, proliferation, and tissue integration. Coatings made of biocompatible materials, such as hydroxyapatite [125] and collagen [123] can be applied onto the surface of biodegradable metals to improve their biocompatibility and promote tissue healing. On the other hand, dealloying of Fe-Mn and Fe-Mn-Zn alloys was designed to enhance the initial cell attachment and improve the tissue/implant interface adhesion by creating nano topographies on the surface [126].

In summary, surface modifications play a critical role in altering the properties of biodegradable metals, allowing for the customization of their degradation behaviour, mechanical properties, biocompatibility, and corrosion resistance to meet specific application requirements. When combined with a suitable processing route and composition, a new, improved Fe-Mn alloy can be obtained.

### 1.3 Biocompatibility of Fe-based biodegradable metals

**Biocompatibility** is the capability of an implant material to fulfil its supportive function without evoking any harmful effects in the tissues. Fe-based biodegradable alloys have been investigated for their potential use as biodegradable implants due to their unique combination of good mechanical properties, formability and biodegradability. Fe-Mn alloys have been studied for potential applications as orthopaedic implants, car-

diovascular stents, and tissue scaffolds, with promising results in terms of tissue integration and healing. When considering the biocompatibility of Fe-based biodegradable metals, key aspects such as cytotoxicity, cell proliferation, biodegradability kinetics, non-toxicity of the corrosion products, and inflammatory response should be taken into account.

As for any other biodegradable material, Fe-based alloys should have low cytotoxicity. **Cytotoxicity** is considered as the ability of a substance or agent to cause cell death or damage. Cytotoxic substances cover chemicals, toxins, radiation, drugs, *etc.* Exposure of cells to cytotoxic agents can result in DNA damage, membrane damage, mitochondrial dysfunction and others that can lead to cell death. The toxicity can be described through a relationship between the concentration of a cytotoxic substance in a living organism and the resulting biological response, *i.e.* cell growth or death [127]. The toxicity of a given element or substance can be characterized by the upper intake level, which is the maximum daily amount that can be taken without causing any risk of adverse health problems [128], [129], which is strongly connected with the concentration of ions released by corroding metal. To point out, small concentrations of poisonous elements can have no toxic effect and at the same time, excessive amounts of nutritious substances can result in an adverse response. Fe and its main alloying elements such as Mn and C are crucial elements for the human body, but elevated concentrations can cause toxicity. Moreover, different cell types are affected differently by the same ion concentration. Fe-based alloys have been studied using a variety of cell types, such as fibroblasts, osteoblasts and endothelial cells without causing significant cytotoxicity. The toxicity of biodegradable Fe-based alloys is determined mainly by the toxicity of the alloying elements and that of the degradation products [16].

The corrosion behaviour and released degradation products should not be harmful or cause undesired effects. On the one hand, the degradation products can be internalized by cells and also affect their viability. On the other hand, pH changes associated with the corrosion of Fe can be expected at the biomaterial/tissue interface. Schinhammer *et al.* [91] showed that the oxidation state of Fe, which was related to the pH of the ions-containing solution, can also affect cytocompatibility. Namely, human umbilical vein endothelial cells (HUVEC) were more sensitive to

$\text{Fe}^{3+}$  ions than to  $\text{Fe}^{2+}$ , which was attributed to a lower pH found in the  $\text{Fe}^{3+}$  ions solutions. Cells are pH-sensitive, and a more acidic pH can affect their viability. Recall that degradation is a complex process that yields both metallic ions and insoluble products. The ion release level has to be controlled to minimize its potentially harmful effect on surrounding tissues. The released degradation products have to be biocompatible and should be safely released or absorbed and metabolized by the human body.

### 1.3.1 *In vitro* cytotoxicity assessment

Prior to discussing the methods employed for assessing *in vitro* biocompatibility, it is essential to provide an explanation of several key parameters:

- Cell proliferation is an action of cell division and multiplication, which results in an increasing number of cells or tissues over time. It involves several stages such as DNA replication, formation of new cell membranes and organelles and separation of the duplicated DNA into two daughter cells by mitosis. Cell proliferation should be regulated to maintain tissue homeostasis and prevent the uncontrolled growth of cells, which can result in the development of tumours and cancer.
- Cell adhesion to the implant is important, as it enables the attachment of cells to its surface. It can be divided into (i) cell attachment, (ii) spreading and (iii) focal adhesion formation, *i.e.* powerful interaction between cells and biomaterial surface [130]. Cell adhesion depends on the surface state and it prefers surfaces with more hydrophilic properties. Specifically modified surfaces can allow for better cell attachment, for example by introducing roughness or porosity.
- The inflammatory response happens when the immune system of the human body is activated as a response to an infection or injury. However, the implantation of a foreign body is also one of the factors triggering the inflammatory response, known as foreign body reaction (FBR). FBR can be divided into five phases: (i) protein absorption, (ii) acute and (iii) chronic inflammation, (iv) foreign body giant cell

formation and (v) fibrosis [131]. Macrophages are the main character in all of these phases, apart from protein absorption, as they are one of the first cells to arrive at the implant site. Macrophages can engulf and digest degradation products through a process known as phagocytosis. Regarding the long-term response to implant, macrophages can form a layer of cells around the implant surface, called foreign body giant cell, which isolates the material from surrounding tissues. Inflammatory cell response is an important component of the immune system to fight against infection and injury, however, prolonged inflammation can cause tissue damage and chronic diseases.

*In vitro* cytotoxicity is studied as a first step to evaluate the biocompatibility of a newly synthesized material. Those tests are aimed to mimic the *in vivo* conditions. The cell line used in the evaluation of cytocompatibility should be chosen according to the aimed implant application, *i.e.* materials for bone implants should be tested with osteoblastic cells, while materials for stents should be evaluated for their compatibility with endothelial cells as well as blood cells. The *in vitro* tests can be divided into direct and indirect studies [132]. Through the cytotoxicity evaluation, factors such as cell damage, cell growth and specific aspects of cellular metabolism can be addressed. The cytotoxicity can be determined both qualitatively and quantitatively. Qualitative tests consist of microscopical examination of cells, using staining if desired. From this analysis, different grades of cytotoxicity can be obtained, from none, where no reduction of cell growth is observed through mild, where not more than 50% of growth inhibition is noticed up to severe toxicity, where nearly complete or complete destruction of cells is detected. Quantitative tests measure cell death, inhibition of cell growth and cell proliferation. Reduction of cell viability by more than 30% is considered a cytotoxic effect, as described by ISO 10993-5:2009. In the interpretation of the quantitative results, a statistical analysis should be performed to correctly compare the samples.

The direct *in vitro* tests consist of direct cell exposure to the tested material and allow for both qualitative and quantitative assessment of cytotoxicity. Direct methods are usually used to examine the potentially harmful effects of the material on living cells. Cells are seeded on the

surface of the tested material and cultured for the desired period, usually between 24h to 7 days. Control samples should be always used to compare and validate the results. The control refers to a group/condition that serves as a reference point for comparison and is essential for the correct experimental design. It helps to evaluate the effects of different variables under study. The most common direct testing methods are cell viability and proliferation assays. The cell viability assays assess the ability of cells to preserve their capacity to remain alive (*i.e.* viability).

Indirect tests involve cells' exposure to conditioned media or extracts obtained from the tested material. The extracting conditions should exaggerate the clinical use conditions so that the potential toxicological hazard can be identified. Prior to the extraction sample should be sterilized and the extraction itself should be performed in sterile conditions, following the ISO 10993-12:2007 standard. The first step in indirect testing consists of extract preparation, where the tested material is exposed to an extraction vehicle for a desired period of preparation (usually 24h at 37°C). The extraction vehicle can be culture media with serum, physiological saline solution or another suitable vehicle. The preferable extraction vehicle is the culture media with serum, due to its ability to support cellular growth. The culture media used for conditioning should be sterile. After the desired period of conditioning, the sample is withdrawn from the media and the conditioned media is used to culture the cells for further studies. Additional experiments can be conducted utilizing either the original extract alone or a series of diluted extracts, where the original extract serves as the diluent. This indirect testing approach is useful in examining the cytotoxicity of biodegradable metals, as it can identify if the material releases toxic substances, corrosion products or ions in the surrounding biological environment. Through indirect testing, inflammatory cytokine response can be also examined. However, the experiment should be well-designed, taking into account the extraction conditions, duration of conditioning and the appropriate controls.

### 1.3.2 *In vitro* biocompatibility of Fe-Mn alloys

Several studies have reported that Fe-based BMs show good biocompatibility *in vitro*. Fe is an essential element for the human body and high

concentrations are needed to induce toxicity *i.e.* between 350-500  $\mu\text{g}/\text{dl}$  in serum [65]. Transferrin bounds the extracellular Fe, which keeps iron soluble and non-toxic [133]. The excess of Fe is detoxified by sequestration to iron-storing protein, ferritin [133]. As noted by Hermawan *et al.* [65], those two properties lead to a low inhibition of the metabolic activity of 3T3 mouse fibroblast cell line exposed to iron at ranges of concentrations (up to 16  $\text{mg}/\text{ml}$ ).

On the other hand, although manganese is also an essential trace element for the human body, it exhibits potential toxicity, as the concentration of 3-5.6  $\mu\text{g}/\text{dl}$  can result in neurologic symptoms. The toxic effect of Mn relies upon targeting mitochondria and increasing the level of lactic acid [134]. Overdosage of Mn could lead to neurotoxicity and intoxication [135].

When Fe is alloyed with Mn to form a solid solution with austenitic fcc crystal structure, the alloy has different properties than the forming elements, *i.e.* bcc Fe and bcc Mn. Therefore, the biocompatibility of the resulting alloy is expected to be different to that of the constituents, *i.e.* to be less toxic than pure Mn [65].

The initial assessment of the biocompatibility of Fe-Mn alloys for stent application was first published in the pioneering work by Hermawan *et al.* [65], [66], [75], [81], where the Fe-Mn alloys were fabricated by powder metallurgy. The authors showed that alloying Fe with Mn allowed for accelerating the corrosion rate and improved the MRI compatibility due to the formation of a fully austenitic structure when Mn content was over 29 wt.%. Cell viability studies were performed using a 3T3 mouse fibroblast cell line (3T3) on alloys containing 20-35 wt.% Mn. When alloyed, variation in manganese content in the Fe-Mn alloys did not show any significant differences in the relative metabolic activity (RMA). However, when a simple, non-alloyed mixture of Fe and Mn powders was analyzed, the results showed a decrease in the RMA, which was attributed to Mn toxicity. Thus, alloying to form a solid solution seems to be important to obtain a non-toxic material.

The effect of additions of noble elements, aimed at increasing the degradation rate by creating micro galvanic cells was also addressed. The biocompatibility of Fe-Mn alloy with additions of Cu was studied by



Mandal *et al.* [99], [100]. Thanks to the addition of Cu, a cytocompatible, austenitic alloy with antibacterial properties and increased degradation rate was obtained. Moreover, addition of 10 wt.% of Cu improved the proliferation of MG-63 cells. Studies conducted on TWIP steels with additions of noble Pd showed good cytocompatibility as long as the ion release was below the cytotoxicity threshold [136]. Fe-Mn-Cu alloy Fe-Mn-Ag alloys also showed an increased degradation rate, good biocompatibility and a potential antibacterial effect [99], [100], [137]. In further studies on Fe-Mn-Ag alloys, their good hemocompatibility (*i.e.* compatibility with blood cells) and cytocompatibility were confirmed [138]. *In vitro* tests show that no chronic toxicity was observed in Fe-35Mn and Fe-35Mn-1Ag alloy [139], with the higher inflammatory response obtained for the Ag-containing alloys.

The *in vitro* biocompatibility of highly porous Fe-Mn foams fabricated through the replica method revealed improved cell proliferation after direct culture for 7 days with osteoblastic MC3T3-E1 cells [115]. The cytotoxicity studies on porous Fe-Mn-Si-Pd alloys showed that a high level of porosity can decrease cell viability, which was attributed to higher ion release from the highly porous alloys [97]. Similar results were obtained on Fe30Mn alloys with 0, 5, 10 and 60 % volume porosity [140]. The results showed that although the alloy with the highest level of porosity shows the highest degradation, it also experiences the lowest cell viability, as the cells do not adhere well to the surface. Thus, it is important to control the porosity levels to avoid too high degradation rates.

To summarize, the biocompatibility of Fe-Mn alloys can be affected by various factors such as alloy composition, microstructure, surface state, porosity levels and implant design. The cytocompatibility of Fe-based alloys depends on the released ion concentration level, which should be kept within tolerable limits [136]. Although *in vitro* methods are valuable in the initial assessment of biocompatibility, further *in vivo* studies should be conducted to correctly assess both the degradation rate and biocompatibility. Moreover, the potential application of the studied material should be considered before designing the experiments in order to choose the correct cell line. In the case of Fe-Mn alloys, the most common potential application is either as a stent or orthopaedic material.

## 1.4 Antibacterial and antibiofilm materials

The National Institutes of Health reported that as much as 80% of human bacterial infections are caused by hard-to-cure bacterial biofilms [141], [142]. Biofilm-associated infections are a type of infection that originated from the formation of biofilms. Biofilms are complex communities of microorganisms embedded in a matrix of extracellular polymeric substances (EPS), that can adhere to various surfaces, such as those of medical devices as well as natural surfaces, for example, teeth and mucosal membranes. Biofilms can form on the surfaces of implanted medical devices, such as orthopaedic implants and cardiovascular devices. Biofilms are resilient and problematic to eradicate, which makes them an enormous threat causing severe infections. Biofilm-associated infections can include catheter-associated urinary tract infections [143]–[145], dental biofilm-associated infections [146]–[148], respiratory biofilm-associated infections [149], [150] and implant-associated infections (IAI) [151]–[153].

The IAI occur on both permanent and temporary medical implantable devices that are aimed to support or restore human functions. They became one of the most severe complications in orthopaedic surgeries. When the infection occurs, it requires secondary operation and antibacterial therapy, which not only has a stressful effect on the patient but also significantly increases the cost of medical treatment. IAI are predominantly caused by bacteria coming from surgical procedures or occur through bloodstream and open wounds [154]. The implant surface is a substrate for bacterial adhesion and biofilm formation. Without an implant, considered as a foreign body, the contamination by pathogens is usually cleaned by host immune defences. However, when considering IAI, the foreign body (implant) provokes a local tissue response (comprising acute and chronic inflammation, granulation tissue formation and fibrous encapsulation) and induces bacterial colonization and infection. The standard treatment for bacterial infections is antibiotics and antimicrobial agents. However, the bacteria growing in a biofilm are between 100 and 1000 times less sensitive to antimicrobials than planktonic bacteria [155]. Post-operative infections and insufficient osteogenesis are the two most common reasons for implant failure. The expression *race for the surface* was proposed by Gristina *et al.*[156], which describes the 'fight' between

cell integration and bacterial adhesion on the implant's surface. The hope is that host tissue cells will win this contest. Therefore, new solutions must be established to design materials resistant to biofilm formation and at the same time, when needed, allow for tissue integration.

Fig. 1.7 shows the possible effects taking place after a technically correct implant surgery [152]. Almost immediately after the surgery, infection resulting from early postoperative contamination can be observed. However, the clinical signs of infections may be delayed and not appear for many years. The IAI can occur as a result of contamination coming from routine dental treatment or wounds. In this case, the implant is protected only when integrated into host tissues and a when a standard host tissue response is obtained at the implant site.

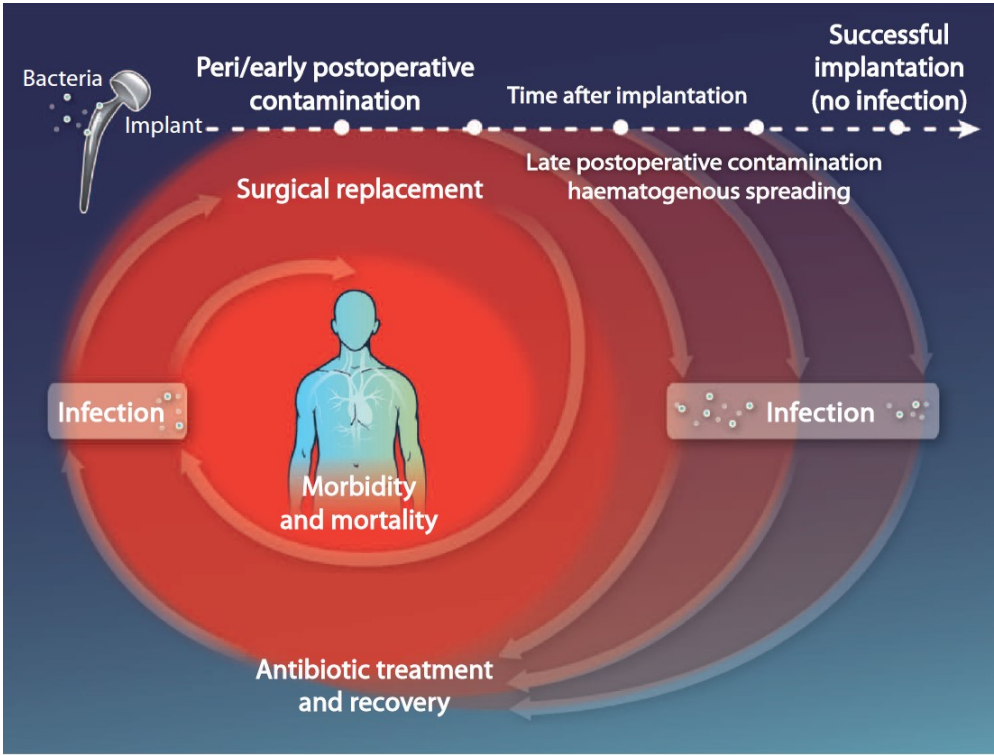


Figure 1.7: Risk factors of patients undergoing implant surgery regarding biomaterial-associated infections. From [152]. Reprinted with permission from AAAS.

### 1.4.1 Biofilm formation

The formation of biofilms consists of five stages, as shown in Fig. 1.8. The initiation of biofilm formation, *i.e.* the reversible attachment occurs due to contact of the surface with single planktonic cells. During the reversible attachment, the biofilm matrix components are produced. The bacterial adhesion depends on several factors, such as the type of pathogen and physiological fluids, the surface topography and the physiochemical properties of the material [157]–[159]. During the maturation of biofilm, the bacteria clusters of several bacteria thicknesses appear that are embedded in the EPS matrix (Maturation I), which then fully mature into microcolonies (Maturation II stage). The last step, namely dispersion, consists of the reduction and degradation of biofilm matrix components [160]. In this stage, the cells are mobile, protecting them from shear stress, antimicrobial agents or host immune responses. Moreover, the EPS matrix promotes communication among the microorganisms, which allows them to function as a community with collective behaviours, such as enhanced resistance to antibiotics and host immune responses.

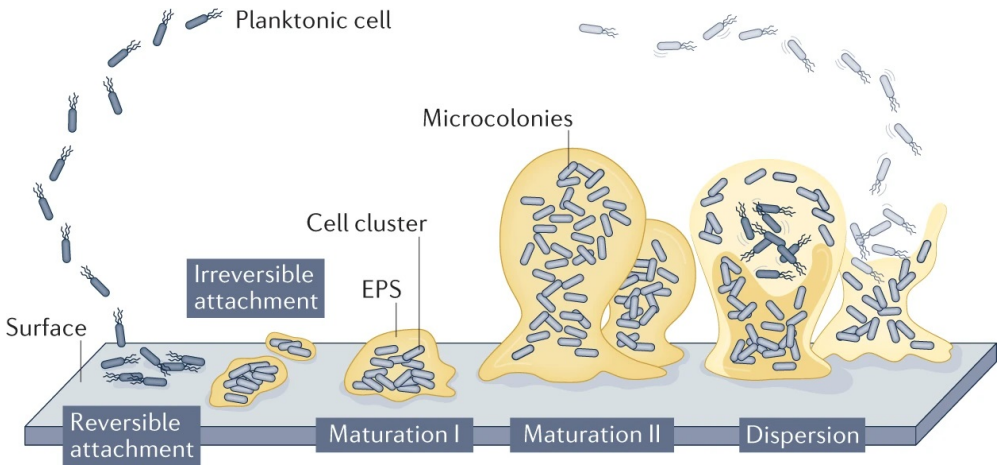


Figure 1.8: The schematic representation of biofilm formation and development. Reproduced from [160]. Copyright 2022, Springer Nature.

Biofilm-associated infections pose significant challenges in clinical practice, as they can be resistant to conventional antimicrobial treatments, including antibiotics and antiseptics. The protective nature of the biofilm matrix and the cooperative behavior of microorganisms within the biofilm

can confer increased tolerance to antimicrobial agents, as well as hinder immune responses. Additionally, biofilms can undergo structural changes that can further enhance their resistance to treatments. Therefore, effective strategies for preventing and managing biofilm-associated infections often require a multidisciplinary approach, involving a combination of antimicrobial therapies, biofilm prevention measures, and strategies to disrupt or remove biofilms from infected surfaces.

### 1.4.2 Design strategies of antibacterial and antibiofilm materials

There is a growing body of literature that recognises the importance of developing biofilm-resistant implant materials, as practically all biomaterials can be affected by microbial contamination during implantation. Several solutions have been proposed to limit biofilm-associated infections, such as the fabrication of antibacterial metallic alloys, containing Ag, Cu or Zn; photosensitive or UV-activable antibacterial surfaces such as TiO<sub>2</sub>, drug-loaded surfaces containing antibiotics, *etc.* Fig. 1.9 proposes an overview of surfaces for antibacterial materials. The left side includes the factors preventing bacterial adhesion such as surface charge, stiffness, adhesion points, wettability and mechanical interactions. On the right, factors preventing biofilm formation are present: nanostructures, roughness, geometry, cations and antimicrobial peptides. The upper part proposes complex antibacterial systems for clinical applications such as triggered killing, capturing, long-term antifouling, self-cleaning and targeting [161]. The most popular design strategies are tackling the process of biofilm development and include [157]:

1. Anti-adhesion surfaces, inhibiting bacterial adhesion,
2. Anti-colonization surfaces, inhibiting bacterial colonization,
3. Anti-biofilm surfaces, inhibiting the formation of biofilm,
4. Anti-proliferation surfaces, inhibiting the proliferation of bacteria.

The chosen type of surface should depend on the device application, *i.e.* temporary implants such as urinary and vascular catheters or feeding tubes do not require tissue integration, hence in these devices, anti-adhesive,

antibiotic-releasing, silver-impregnated and contact-killing coatings would solve the problem of potential implant infection [152]. In the case of materials for internal implants, which are aimed to favour the host tissue integration, the race for the surface has to be considered. Surfaces aimed to enhance cell adhesion, proliferation and growth are also attracting microorganisms. Contrarily, surfaces and coating preventing bacterial adhesion might not adequately integrate with host cells and tissues. Thus, the perfect surface would repel and kill bacteria, while simultaneously promoting tissue-cell adhesion [152].

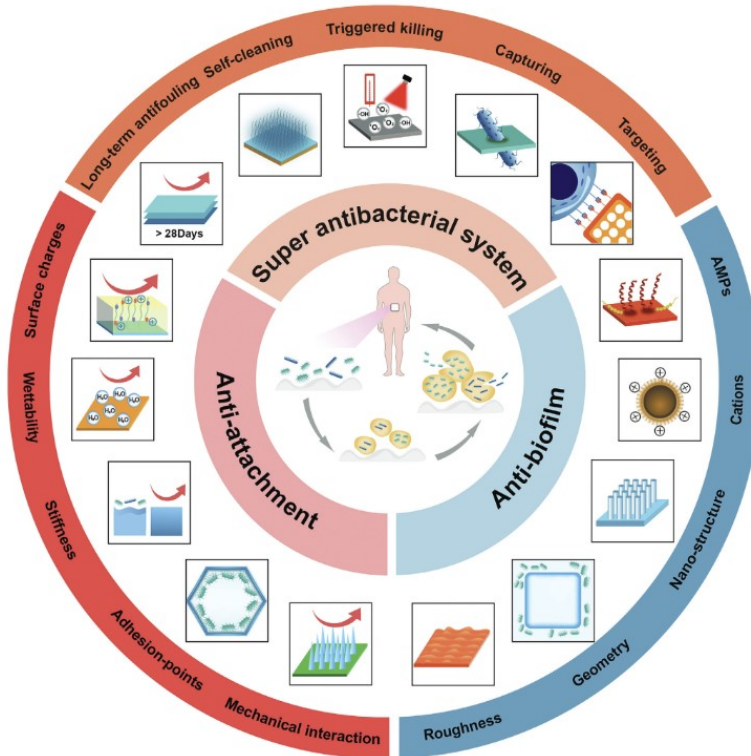


Figure 1.9: Proposed strategies for surface design of antibacterial materials. Reproduced from [161].

The most studied antibacterial alloying elements include Ag [162]–[164], Cu [165], [166], Zn [167]–[169] and Ga [170]–[172]. The exact antibacterial activity of these materials is often unclear but can include several mechanisms such as the generation of reactive oxygen species, actions of metallic ions released by the materials in physiological solutions and interaction between bacteria and the material, especially in the form of

nanoparticles. Metal ions are able to provide strong antibacterial activity, but it is important to consider their potential cytotoxicity.

### 1.4.3 Degradable versus non-degradable biomaterials - infection resistance

Degradable materials have been identified as an effective strategy to reduce infection risk when applicable [173]. The exact mechanism for decreased risk of infection is not yet clear, but a number of hypotheses emerged, such as (i) increased vascularization, (ii) reduction of the local immunological deficit and (iii) influence of degradation on bacterial adhesion, as shown in Fig. 1.10. The last one is of special interest, as it directly translates to the degradation mechanism of biomaterial. The degradation of implant material leads to a reduced area available for bacterial colonization and biofilm formation. As the surface of degradable materials erodes, and thus is unstable, the adhering bacteria are constantly shed from the surface, thus the biofilm can not form as effectively as in the non-degradable material. On the other hand, this also limits the adhesion of desired cells on the surface, which for some applications can be undesired. This is one of the potential challenges tackled in studying antibiofilm degradable alloys.

## 1.5 Antibacterial and antibiofilm Fe-based biodegradable alloys

Fabricating antibacterial or antibiofilm Fe-based alloys is a relatively new concept. Just a few reports examined the effect of antibacterial additions of Cu and Ag in the Fe and Fe-Mn alloys [174]. Ag and Cu, are strong antibacterial agents, with proven action against *E.coli* and *S.aureus*. Up to date, the main approach is to alloy Fe or Fe-Mn with Cu and Ag, which creates precipitates uniformly distributed in the matrix. This approach is not only efficient for the fabrication of Fe-based bacteria-killing materials but also leads to an acceleration of degradation rate due to the formation of microgalvanic cells.

Recently, investigators have examined the effects of Ag and Cu additions on the antibacterial performance of Fe-based alloys. Ma *et al.* [175] showed

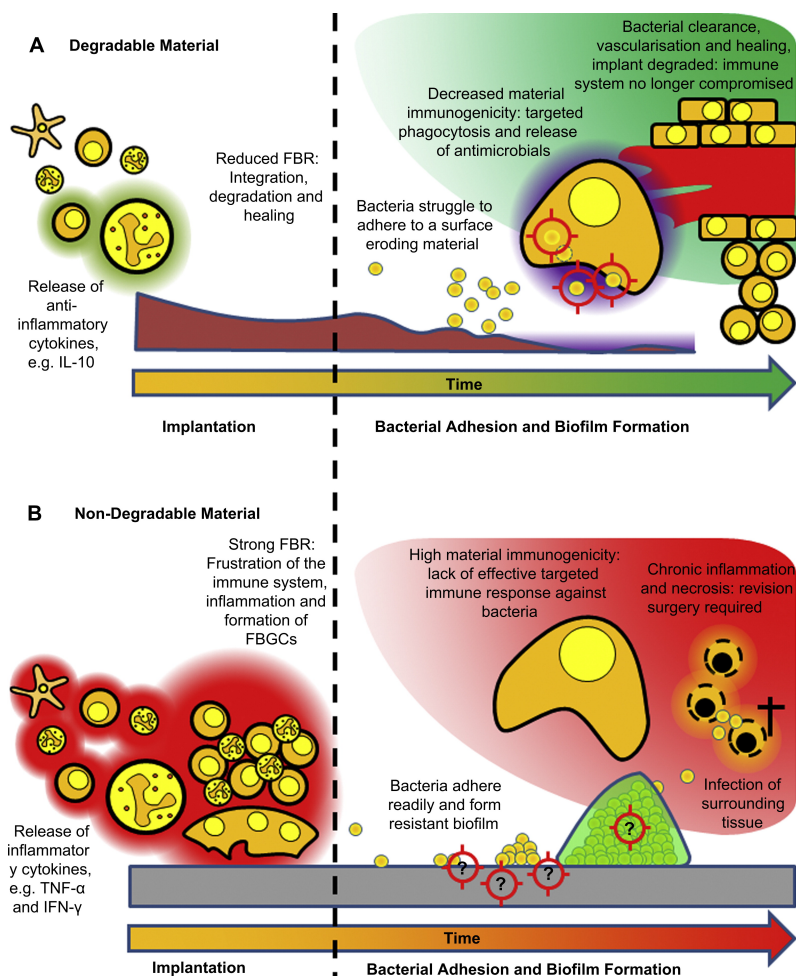


Figure 1.10: Mechanisms responsible for an increased infection resistance of biodegradable *versus* non-biodegradable materials. Reproduced with permission [173]. Copyright 2013, Elsevier.

that the addition of 0.8 wt.% of Cu in the Fe-Mn-C alloy for urinary implant application makes the material antibacterial. Moreover, the prevention of both *S. aureus* biofilm and stone formation was observed. The phenomena were attributed to the continuous release of  $\text{Cu}^{2+}$  ions. The authors, however, have not shown results on cell viability upon the addition of Cu. In studies by Mandal *et al.* [99], [100], the addition of up to 10 wt.% of Cu to Fe-Mn-Cu alloy proved to inhibit the bacterial growth and enhance the degradation rate without compromising the cytocompatibility. However, smaller additions (0.9 wt.%) of Cu did not evoke the antibacterial effect. Guo *et al.* [176] showed that  $\text{Fe}_{1-x}\text{Cu}_x$  ( $x=0, 1.5, 2.3, 7.8$ , and 10.1 wt%)



alloys fabricated by SLM showed antibacterial properties, with a growth inhibition rate of approximately 96.5 % for the addition of 2 wt.% Cu and higher than 99.9 % for higher Cu content. As in the previously mentioned study, additions of Cu also enhanced the degradation rate of Fe, while cell viability of all tested alloys was more than 90% for all compositions.

In a study by Sotoudehbagha *et al.* [137], the effect of Ag addition (1-3 wt.%) to the Fe-35Mn (wt.%) alloy on the bactericidal properties towards *E.coli* and *S.aureus* was examined. The results showed that the addition of 3 wt.% Ag into Fe-35Mn alloy show a significant decrease in the bacterial viability of both *E.coli* and *S.aureus*. The antibacterial effect was attributed to the  $\text{Ag}^+$  ions release, which can penetrate the bacterial membrane and inhibit the bacterial replication ability. A contradictory effect was reported by Liu *et al.* [177], where additions of Ag did not cause any antibacterial effect in Fe70.3-28.9Mn-0.8Ag (wt.%) alloys. However, in both investigations addition of Ag led to an increased degradation rate due to the precipitation of Ag particles in the Fe-Mn matrix, which enabled microgalvanic corrosion.

Additions of Ag and Cu to Fe-based alloys were not only reported to endow the material with antibacterial effect but also to improve the mechanical properties of the alloys, thanks to either solid-state or precipitation strengthening. As Ag and Cu are not fully soluble in the Fe matrix, they will form second-phase precipitates, distributed along grain boundaries, which will increase the hardness of the alloys. Huang *et al.* [178] reported that  $\text{Fe}_{1-x}\text{Ag}_x$  alloys, where  $x = 2, 5, 10$  wt.%, fabricated through powder metallurgy using spark plasma sintering showed increased mechanical properties upon the addition of Ag. Moreover, the corrosion rate of Ag-containing alloys was faster than that of pure Fe and the alloys showed good cytocompatibility, with more than 90% viability for all tested compositions. Additions of Cu have also proved to increase the hardness [176]. Fe-30Mn-3Ag alloys reported by Sotoudehbagha *et al.* [137] also showed improved shear strength with respect to Fe-30Mn alloy. Importantly, as Ag and Cu possess lower mechanical strength than Fe, their content should not be too high, as the strength of Fe-Cu/Ag might finally decrease [174].

Early reports on biodegradable Fe-based alloys with antibacterial and antibiofilm properties show promising results. However, the knowledge is still very limited, as shown in Fig. 1.11. Antibacterial degradable metals are much less studied than permanent implant materials. Moreover, among degradable metals, Fe and Zn are investigated much less than Mg-based alloys. Hence, the knowledge gap gives possibilities to develop new, antibiofilm Fe-based alloys with suitable properties to be used as implants. Moreover, the antibacterial and antibiofilm tests should be accompanied by cytocompatibility tests, as the release level of antimicrobial agents such as Ag, Cu or other elements should be always lower than the cytotoxic level to not affect the cell viability. Up to date, additions of antibacterial elements were conducted through metallurgical approach. Deposition of antibacterial or antibiofilm coatings seems like an interesting approach to be investigated.

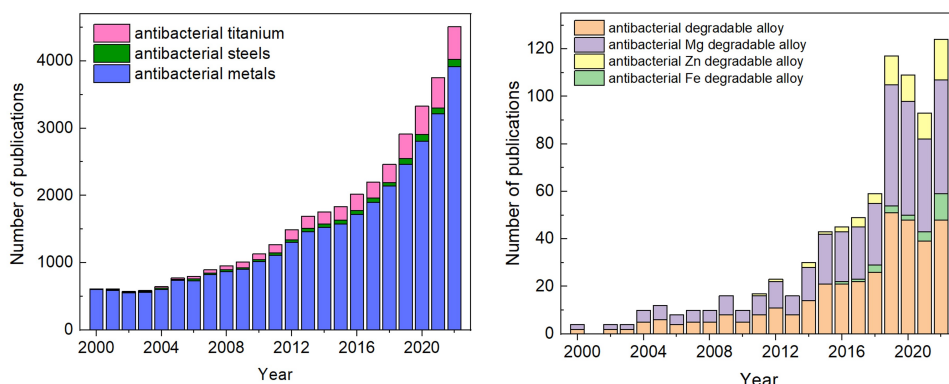


Figure 1.11: Publications on antibacterial materials searched by PubMed. (a) key words used for the search: antibacterial metals, antibacterial titanium, antibacterial steel, (b) keywords used for the search: antibacterial degradable alloy, antibacterial degradable Mg/Zn/Fe alloy. (Updated on 24-04-2023). Publications from 2023 are not included.

## 2 Objectives

The study aims to produce biodegradable equiatomic FeMn alloys with small additions of antibacterial materials *i.e.* Ag and ZnO to obtain a suitable material with antibacterial and/or antibiofilm properties, increased degradation rate and good cytocompatibility. This work is focused mainly on the fabrication of porous FeMn-based alloys with additions of Ag (by alloying) and ZnO (by coating) and shall furthermore highlight their potential use as biodegradable implant materials resistant to the formation of biofilm. Therefore, the work focuses on two main groups of materials, *i.e.* porous FeMn(-xAg) alloys and ZnO-coated FeMn alloys.

The objectives regarding the fabrication and characterization of FeMn(-xAg) porous alloys can be summarised as follows:

- Successful fabrication of porous equiatomic FeMn alloys with additions of homogeneously distributed 1,3, and 5 wt.% Ag by powder metallurgy techniques, *i.e.* ball milling and vacuum sintering;
- Characterisation of the fabricated alloys to reveal their physical characteristics that can affect their properties, *i.e.* phase composition, porosity levels, magnetic and mechanical properties;
- Assessment of their biodegradability rates as a function of alloy composition and microstructure by *in vitro* immersion tests in HBSS;
- Demonstration of good cytocompatibility with Saos-2 cells of the fabricated alloys;
- Determination of the effect of Ag addition on bacterial interactions with *S. aureus*.

The objectives for ZnO-coated porous FeMn alloys can be presented in the following way:

- Establishing the parameters for ZnO deposition by sol-gel methods and coating of FeMn porous alloys with ZnO;

- 
- Characterisation of the deposited coating by SEM and XRD;
  - Evaluation of the ZnO coating effect on the biodegradability of FeMn alloys;
  - Assessment of the effect of ZnO coating on FeMn on cytocompatibility with Saos-2 cells and bacterial interactions with *S. aureus*.

### 3 Experimental techniques

This chapter provides an overview of the experimental techniques used to fabricate and characterize the materials covered in this thesis. The fabrication techniques used to prepare the materials, that is, powder metallurgy and dip coating, are briefly described, with a focus on the specific approach used in this thesis. The evaluation of the physical properties is explained by providing an overview of the techniques used. Moreover, the biodegradability, cytocompatibility and microbial interactions testing are described.

This chapter aims to introduce the reader to the process of sample fabrication and characterization, rather than describing the theoretical principles of the techniques used, as these are widely available in the literature. The specific details of the parameters used in each study are given in the Results section.

## 3.1 Processing techniques

### 3.1.1 Powder metallurgy

Porous FeMn(-xAg) alloys, where  $x = 0, 1, 3$  and  $5 \text{ wt,}\%$  Ag, were fabricated using powder metallurgy. Figure 3.1 shows the schematic of the synthesis process. The first step in the process was the ball milling of commercial Fe, Mn (and Ag) powders. The powders were weighed and placed in a sealed vial in a glove box operating under Ar atmosphere with  $\text{H}_2\text{O}$ ,  $\text{O}_2 < 0.1 \text{ ppm}$ . Subsequently, ball milling was performed with stainless steel balls, with a ball-to-powder weight ratio of 10:1 at 300 rpm for 10h to promote mechanical alloying. Then, polyvinyl alcohol (PVA) powder was added to the metallic powder to act as a binder. The powder mixture was uniaxially pressed at 100 MPa to obtain green pellets with a diameter of 9 mm. The final stage of the synthesis comprised sintering in a vacuum furnace at  $900^\circ\text{C}$  at  $5 \times 10^{-5} \text{ mbar}$  for 4h, at a heating rate of  $1^\circ\text{C}/\text{min}$  and cooling to room temperature at a cooling rate of  $3^\circ\text{C}/\text{min}$ . Due to the low compressive pressure, the produced alloys were inherently porous. The synthesised materials had a diameter of approximately 9 mm and a thickness of 2-3 mm.

Initially, the FeMn powders were milled for 5, 10 and 15h and analyzed by X-ray diffraction (XRD) to determine the time required to obtain the fully austenitic structure. Regarding the FeMn-xAg powders, we first attempted to add Ag powder to the previously milled FeMn mixture and then performed further milling. However, we found out that this way the Ag-rich precipitates are not homogeneously distributed in the matrix, thus we decided to mill initial Fe, Mn and Ag powders for 10h.

In addition, we attempted to fabricate FeMn alloys with additions of Zn and ZnO micro- and nanoparticles using an analogous method, *i.e.* by ball milling and sintering of the powders. However, because of the low melting point of Zn, this approach was unsuccessful. Moreover, as the sintering system used relies on vacuum sintering, we found that ZnO micro/nanoparticles tend to evaporate during the sintering process because of the low partial pressure. Thus, we decided to incorporate ZnO in a different manner, namely by coating deposition.

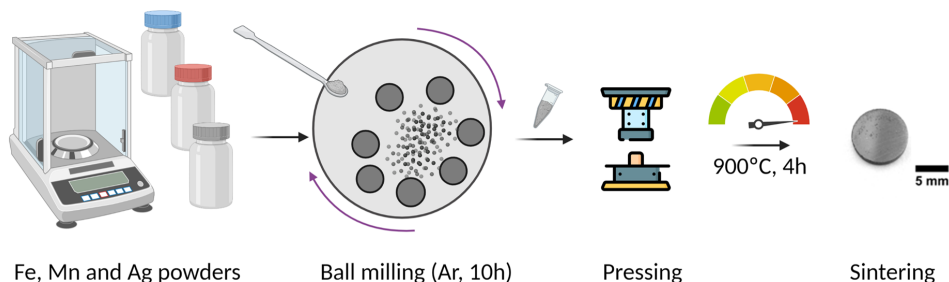


Figure 3.1: Diagram showing the powder metallurgy process leading to synthesis of porous FeMn(-xAg) alloys. Created with BioRender.com

#### 3.1.2 Surface modification of FeMn alloy by dip-coating of ZnO

The equiatomic FeMn alloy was coated with ZnO using the dip-coating method. The coating process is schematically illustrated in Fig. 3.2. The first step involved the preparation of a precursor solution by mixing zinc acetate dihydrate (a precursor of ZnO) with ethanol (a solvent). The solution contained 0.5M zinc acetate and was stirred for 30 min at 60°C. After that monoethanolamine (MEA) which acted as a stabilizer was added to the solution in a zinc acetate dihydrate: MEA 1:1 ratio, and further stirred for 2h. The resulting solution was then kept in the dark for 24 h for aging. Dip coating was then performed using a Coater 5 AC (id Lab) with a withdrawal rate of 300 mm/min. Two layers were deposited on the polished FeMn discs. The solvent was evaporated by drying on a hotplate at 120°C. Subsequently, the coated samples were annealed in a furnace at 500°C to calcinate the aged film.

Varying ZnO precursor concentrations were screened before choosing the final 0.5M concentration, namely 0.1, 0.3 and 1M. However, the 0.5M provided the most homogenous coating, thus we decided to perform further studies using this concentration. Moreover, a mixture of distilled water and ethanol was first tested as a solvent and stabilizer mixture, but it did not led to a homogenous solution and sedimentation was observed even after prolonged mixing. For this reason, we decided to use MEA, which proved to be an efficient stabilizer.

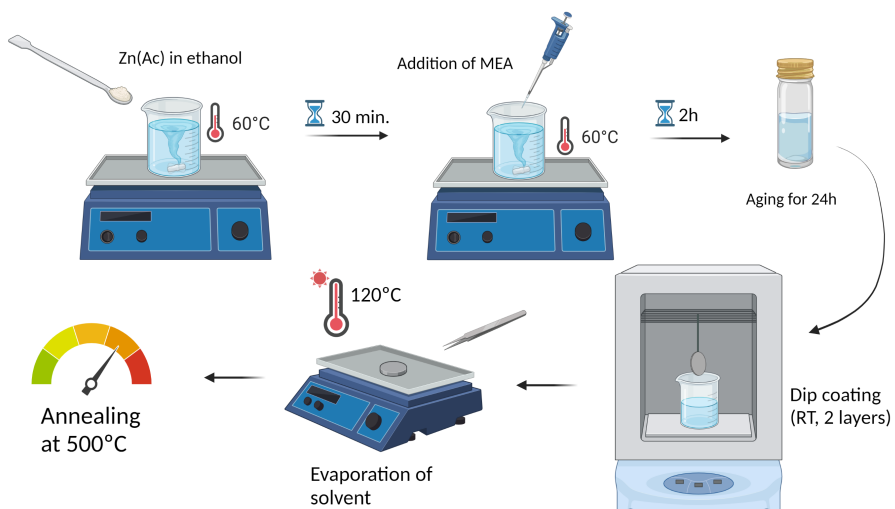


Figure 3.2: Diagram showing the deposition of ZnO coating by dip coating on FeMn polished discs. Created with BioRender.com



## 3.2 Characterization techniques

Various techniques have been used throughout the Thesis to characterize the physical properties of fabricated materials and their biodegradation, cytotoxicity and antibacterial/antibiofilm properties, as shown in Fig. 3.3.

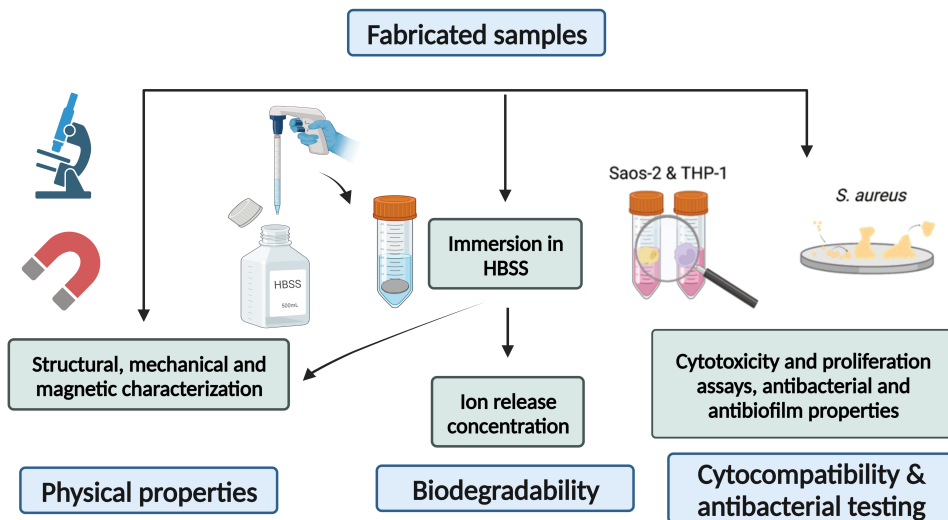


Figure 3.3: Overview on the methodological approach for characterization of fabricated samples. Created with BioRender.com

### 3.2.1 Biodegradability

Biodegradability tests were performed *in vitro* to simulate *in vivo* body conditions, according to the ASTM G31-72 standard, as shown in Fig. 3.4. Before testing, the samples were cleaned and sterilized in ethanol. The surface areas of the samples were measured to determine the required amount of liquid for immersion. Sintered FeMn(-xAg) alloys and ZnO-coated FeMn (FeMn/ZnO) samples with a surface area of approximately  $1.25 \text{ cm}^2$  were immersed in plastic containers containing 30 mL of HBSS solution. The containers were then placed in a water bath at a constant temperature of  $37.5^\circ\text{C}$ . At least three replicas per sample were prepared. The solution was withdrawn and replaced with fresh HBSS after every 1, 3, 7, 14 and 28 days. For the FeMn(-xAg) samples, an extended immersion period of up to 84 days was applied. The withdrawn conditioned solution was subjected to inductively coupled plasma (ICP) analysis to evaluate

the concentration of released ions. Based on this release, the estimated corrosion rate was obtained, according to Eq. 3.1:

$$CR = \frac{cV}{St} \quad (3.1)$$

where  $c$  is the ion release concentration,  $V$  is the volume of the solution used in the immersion test,  $S$  is the initial surface area exposed to the corrosive solution, and  $t$  is the exposure time. Additional samples were prepared for scanning electron microscopy (SEM) and energy dispersive X-ray spectroscopy (EDS) analysis of the degradation products formed on the surface of the samples. This analysis was performed for both in-plane and cross-section observations to analyze the degradation layer as well as the bulk area of the material that was not directly exposed to HBSS. Before SEM/EDS analysis, the samples were coated with an Au/Pt layer to enhance their conductivity.

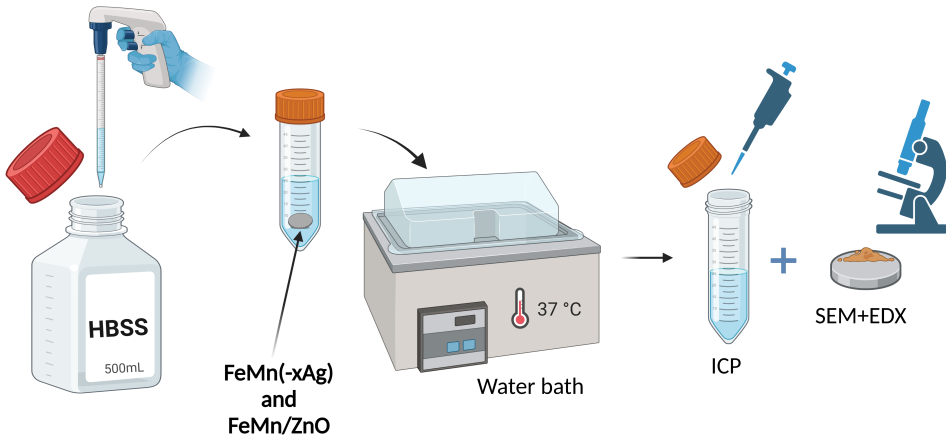


Figure 3.4: Diagram showing the biodegradability testing procedure. Created with BioRender.com

#### 3.2.2 Physical properties

##### Scanning electron microscopy

A Zeiss Merlin field-emission SEM (FE-SEM) equipped with an EDS detector was used for the structural and compositional analysis of the studied materials. A voltage of 1-20 kV was used for imaging purposes, and a voltage of 10-20 kV was used for EDS analysis. Both the secondary electron (SE) and In-lens detectors were used to characterize the morphology and topography. In contrast, a backscattered electron (BSE) detector was used to study the different phases present in the samples. Prior to the analysis, the sintered FeMn(-xAg) discs were embedded in the conductive resin and polished, with a final step of 1  $\mu\text{m}$  diamond particle solution. The FeMn/ZnO samples were observed right after synthesis without any additional preparation.

##### X-ray diffraction

X-ray diffraction was carried out to study the phase composition of powders, sintered alloys, and selected samples after biodegradability testing on a Philips X'Pert diffractometer using Cu  $K\alpha$  radiation ( $\lambda = 0.154178$  nm). The measurements were performed in the angular  $2\theta$  range between 20-100° with a step size of 0.026°.

Grazing-incidence XRD (GIXRD) was performed to structurally characterize the ZnO coating deposited on the FeMn substrate, as it is a more surface-sensitive technique that limits the penetration of X-rays into the bulk. The angular  $2\theta$  range was between 25-75° with a step size of 0.01°. The results were then treated using X'Pert HighScore and MAUD softwares, to analyze the phase composition and perform Rietveld refinement.

##### Nanoindentation

Nanoindentation tests were performed using an Anton Paar NHT<sup>3</sup> nanoindenter. Prior to the tests, the discs were polished to a mirror-like surface, with the final polishing step using a 1  $\mu\text{m}$  diamond particles paste. Maximum applied loads of 100 and 500 mN were used to assess the behaviour of the material during deformation. A series of at least

50 measurements were performed to obtain statistically relevant data. Typical load-displacement curves are shown in Fig. 3.5 together with common parameters.

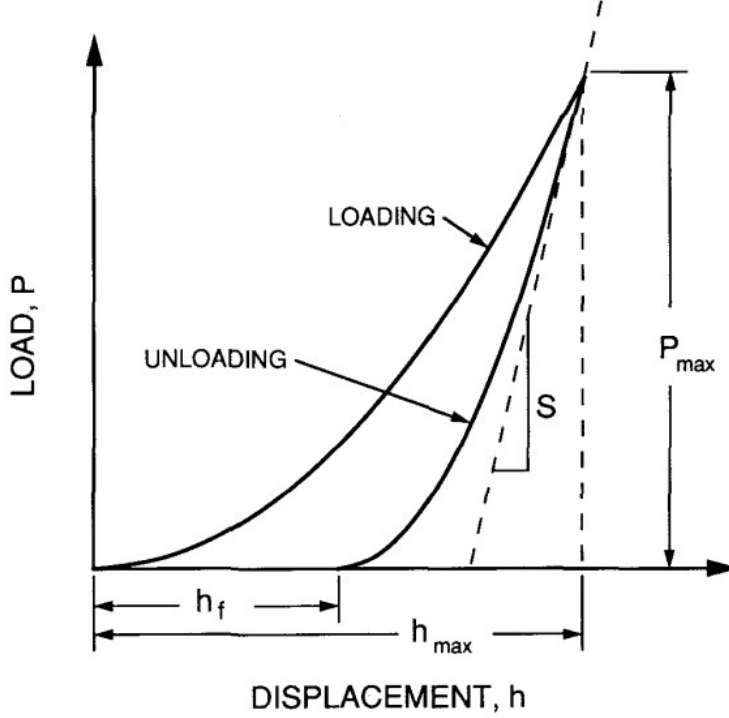


Figure 3.5: Schematic load-displacement curves for nanoindentation experiment.  $P_{max}$  is the maximum applied load,  $h_{max}$  is the indenter displacement at maximum applied load,  $h_f$  is the final depth of the contact impression after unloading and  $S$  is the initial unloading stiffness. Reproduced with permission[179]. Copyright 1992, Springer.

The hardness ( $H$ ) and reduced elastic modulus ( $E_r$ ) were calculated from the load-displacement curves at the beginning of the unloading segments, according to the procedure described by Oliver and Pharr [179]. First, the contact stiffness ( $S$ ) was derived from the initial unloading slope, as described by Eq. 3.2:

$$S = \frac{dP}{dh} \quad (3.2)$$

where  $P$  is the applied load and  $h$  is the penetration depth during nanoindentation. Based on the relation between contact area ( $A$ ) and stiffness,

### 3. Experimental techniques

---

the reduced elastic modulus ( $E_r$ ) was obtained:

$$S = \beta \frac{2}{\sqrt{\pi}} E_r \sqrt{A} \quad (3.3)$$

where  $\beta$  is a correction factor correlated with the indenter geometry (1.034 for the Berkovich indenter). The reduced elastic modulus ( $E_r$ ) can be expressed as:

$$\frac{1}{E_r} = \frac{1 - \nu^2}{E} + \frac{1 + \nu_i^2}{E_i} \quad (3.4)$$

where  $E$  is the elastic modulus of the tested material,  $\nu$  is the Poisson's ratio of the tested material,  $E_i$  is the elastic modulus of the indenter and  $\nu_i$  Poisson's ratio of the indenter. Hardness value was expressed as:

$$H = \frac{P_{max}}{A} \quad (3.5)$$

where  $P_{max}$  is the peak indentation load, and  $A$  is the projected area of the indent. Apart from that, the elastic ( $W_{elast}$ ) and plastic ( $W_{plast}$ ) energies of deformation were obtained from the load-displacement curves by assessing the areas between the unloading curve and displacement axis ( $W_{elast}$ ) and between the loading and unloading curves ( $W_{plast}$ ). Finally, the elastic recovery was calculated as the ratio between elastic ( $W_{elast}$ ) and total ( $W_{elast} + W_{plast}$ ) energies during nanoindentation.

#### Compression tests

Compression tests were performed during the PhD candidate secondments at the IFW Dresden, Germany. Cylindrical samples with a diameter of 2 mm and a height of 4 mm were cut using electrical discharge machining. Prior to the tests, the loading surfaces were ground with silicon carbide paper to become plane-parallel. Uniaxial compression tests were performed at room temperature using an Instron 8562 device at a constant strain rate of  $1 \times 10^{-3} \text{ s}^{-1}$  and at least three specimens per composition were tested. The tests were halted when the sample fractured. The engineering stress-strain compression curves allowed the determination of the following mechanical properties: compressive yield strength (proof offset of 0.2%,  $R_{0.2}$ ) and ultimate compressive strength  $R_m$  according to Eq. 3.6 and 3.7, respectively:

$$R_{0.2} = \frac{F_{0.2}}{S_0} \quad (3.6)$$

where  $F_{0.2}$  is the force applied at 0.2% of deformation (in N) and  $S_0$  is the initial sample area (in  $\text{m}^2$ ). The ultimate compressive strength is expressed by:

$$R_m = \frac{F_m}{S_0} \quad (3.7)$$

where  $F_m$  is the ultimate force causing the sample's fracture and  $S_0$  is the initial sample area.

### Magnetic measurements

The magnetic properties of the synthesized FeMn(-xAg) alloys were investigated to confirm the non-ferromagnetic or weakly ferromagnetic response of the materials. Magnetic measurements were performed on a vibrating sample magnetometer (VSM) from MicroSense, by recording hysteresis loops at room temperature, using a maximum applied field of 20 kOe. The magnetization was normalized over the sample weight to obtain the specific saturation magnetization ( $M_s$  in emu/g). To assess the changes in the magnetic properties upon biodegradation, additional measurements were performed on the FeMn(-xAg) alloys after immersion in HBSS.

### Transmission electron microscopy

Transmission electron microscopy (TEM) was used to get further insights into the microstructure of the FeMn and FeMn-5Ag alloys. Lamellae for TEM observations were obtained using focused ion beam (FIB). Observations were carried out on JEOL JEM-2011 TEM operating at 200 kV. Bright-field images and selected-area electron diffraction (SAED) patterns were obtained from the areas of interest. A scanning transmission electron microscope (STEM, Teknai FEI) operating at 200 kV was used to obtain high-resolution TEM images. The SAED patterns and high-resolution STEM images were used to identify the interplanar distances using the Gatan DigitalMicrograph software.

#### 3.2.3 Cytotoxicity tests and cell proliferation assays

Saos-2 cells (ATCC HTB-85) used in this study were cultured in Dulbecco's modified Eagle's medium (DMEM) with the addition of 10% Fetal

Bovine Serum (FBS) under standard culture conditions (37°C, 5% CO<sub>2</sub>). Cytotoxicity and proliferation assays were performed through indirect tests, as shown in Fig. 3.6. Prior to testing, samples were sterilized using UV light or ethanol and then immersed in DMEM supplemented with FBS. Samples were incubated under standard culture conditions for the desired period. Subsequently, the samples were withdrawn and the conditioned media was used for further study. Two main types of tests were performed: cell viability to assess the cytotoxicity of the material and metabolic activity to observe changes in cell proliferation.

The cell viability study was performed by first culturing Saos-2 cells in fresh media for 24h to allow cells to attach to the wells. The media was then removed and replaced with conditioned media, and cells were cultured for up to 3 days. Afterwards, the media was removed and cells were stained with a Live/Dead Viability/Cytotoxicity kit (Invitrogen), according to the manufacturer's protocol. As a next step, the cells were imaged using the inverted microscope equipped with epifluorescence. At least 10 images per sample were obtained from different randomized regions. After the tests, the images were analyzed using ImageJ to calculate the percentage of Live/Dead cells and a statistical analysis was performed using GraphPad Prism software.

The proliferation assay was performed by seeding cells in standard media for 24h to allow cell adhesion, then replacing it with conditioned media and incubating for 1 and 3 days, as described previously. After 24h, the conditioned media was removed and replaced with fresh media containing 10% Alamar Blue (Invitrogen), and then the cells were incubated for 4h under standard conditions. Afterwards, the supernatant was collected, and fluorescence was analysed at a wavelength of 585 nm after excitation at 560 nm using a Spark multimode microplate reader (Tecan). The cells were then incubated with conditioned media and the procedure was repeated as previously described (day 3).

#### **3.2.4 Assessment of bacterial adhesion and viability**

The bacterial interaction study was partially performed during the PhD candidate secondment at the University of Gothenburg, Sweden. The adhesion and viability of *Staphylococcus aureus* were examined to evaluate

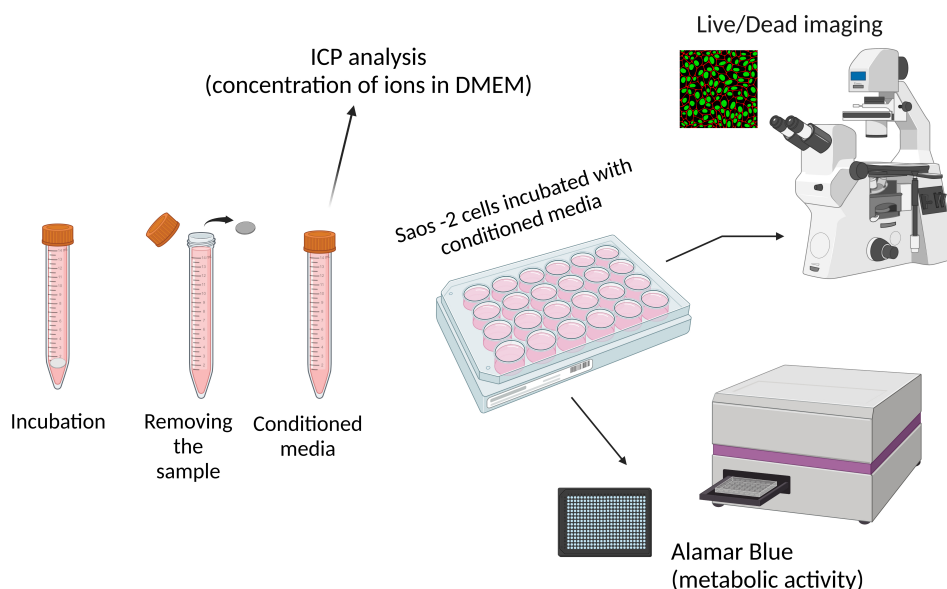


Figure 3.6: Diagram showing the indirect cell viability and proliferation assays experiments. Created with BioRender.com

the potential antimicrobial and/or antibiofilm properties of the tested samples. Prior to the tests, the samples were sterilized, placed in the wells of a 48-well plate, and inoculated with 1 mL of  $10^5$  CFU/mL of a bacterial suspension containing *S.aureus*. Then, the well plate with the samples and the bacterial suspension was incubated at 37°C for 4 and 24h. After 4 and 24h of incubation, the discs were carefully removed from the well plate and rinsed 3 times in sterile saline (0.9% NaCl) solution. The exact details regarding the preparation of bacterial suspension will be described in the Results chapter.

For the adhesion study, after rinsing with saline, the samples were transferred to Falcon Tubes containing saline, then sonicated for 30 seconds and vortexed for 60 seconds at 10000 rpm. Disaggregated biofilm bacterial cells were serially diluted in a mixture of sterile saline and Triton-X. These dilutions were plated on 5 % Horse Blood Agar (HBA) and incubated for 4 and 24h at 37°C. Then, colony-forming unit (CFU) counting was performed.



### 3. Experimental techniques

---

To analyze the *S. aureus* adhered to the disc surface, a confocal laser-scanning microscope Nikon C2+ was used, as shown in Fig. 3.7. To prepare the discs after cleaning with saline solution, the biofilm was stained with a LIVE/DEAD stain, rinsed once more in saline solution to remove the unbound stain and transferred to a petri dish containing saline solution. Then, images were taken using a 100x water-dipping objective, with Z-slices of 3  $\mu\text{m}$  through the adhered *S. aureus* biofilm. The images were analyzed using BiofilmQ software [180] and the total biovolume, and biofilm thickness in both live and dead conditions were examined.

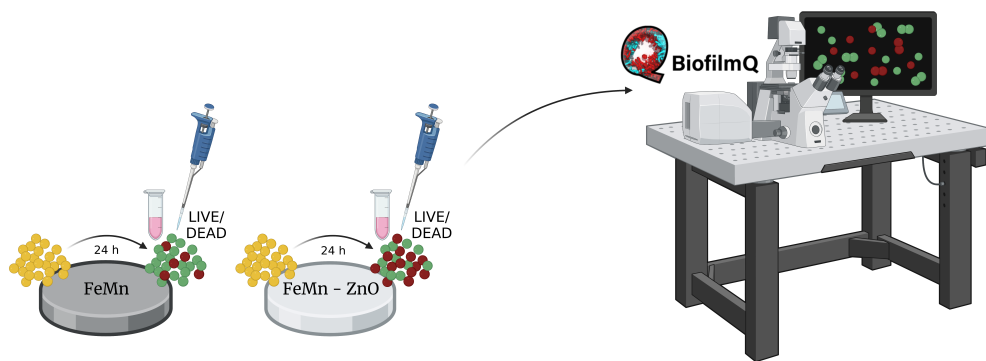


Figure 3.7: Diagram showing the analysis of biofilm on FeMn and FeMn/ZnO samples. Created with BioRender.com. Courtesy of Adam Benedict Turner, University of Gothenburg, Sweden

Selected samples were analyzed using SEM to examine whether the *S. aureus* biofilm adhered to the surface. The procedure was similar to previous cases, where the samples were incubated with the bacterial suspension at 37°C for 24h, and then rinsed with saline solution. The biofilm was then fixed in formaldehyde for 1h and dehydrated in graded ethanol series. Before SEM observations, the samples were gold-sputtered for better conductivity and examined using an SE detector at 5 kV.

# Bibliography

- [1] M. P. Staiger, A. M. Pietak, J. Huadmai, and G. Dias, “Magnesium and its alloys as orthopedic biomaterials: A review,” *Biomaterials*, vol. 27, no. 9, pp. 1728–1734, 2006.
- [2] I. V. Panayotov, V. Orti, F. Cuisinier, and J. Yachouh, “Polyetheretherketone (PEEK) for medical applications,” *Journal of Materials Science: Materials in Medicine*, vol. 27, p. 118, 2016.
- [3] W. Yin, M. Chen, J. Bai, *et al.*, “Recent advances in orthopedic polyetheretherketone biomaterials: Material fabrication and biofunction establishment,” *Smart Materials in Medicine*, vol. 3, pp. 20–36, 2022.
- [4] C. Luo, Y. Liu, B. Peng, *et al.*, “PEEK for Oral Applications: Recent Advances in Mechanical and Adhesive Properties,” *Polymers*, vol. 15, p. 386, 2023.
- [5] C. Shuai, Y. Li, G. Wang, W. Yang, S. Peng, and P. Feng, “Surface modification of nanodiamond: Toward the dispersion of reinforced phase in poly-L-lactic acid scaffolds,” *International Journal of Biological Macromolecules*, vol. 126, pp. 1116–1124, 2019.
- [6] J. S. Bergström and D. Hayman, “An Overview of Mechanical Properties and Material Modeling of Polylactide (PLA) for Medical Applications,” *Annals of Biomedical Engineering*, vol. 44, no. 2, pp. 330–340, 2016.
- [7] K. Polak-Kraśna, A. R. Abaei, R. N. Shirazi, *et al.*, “Physical and mechanical degradation behaviour of semi-crystalline PLLA for bioresorbable stent applications,” *Journal of the Mechanical Behavior of Biomedical Materials*, vol. 118, p. 104 409, 2021.
- [8] P. K. Bowen, E. R. Shearier, S. Zhao, *et al.*, “Biodegradable Metals for Cardiovascular Stents: from Clinical Concerns to Recent Zn-Alloys,” *Advanced Healthcare Materials*, vol. 5, no. 10, pp. 1121–1140, 2016.

- [9] J. M. Seitz, M. Durisin, J. Goldman, and J. W. Drelich, “Recent Advances in Biodegradable Metals for Medical Sutures: A Critical Review,” *Advanced Healthcare Materials*, vol. 4, no. 13, pp. 1915–1936, 2015.
- [10] Y. Sotomi, Y. Onuma, C. Collet, *et al.*, “Bioresorbable scaffold: The emerging reality and future directions,” *Circulation Research*, vol. 120, no. 8, pp. 1341–1352, 2017.
- [11] Y. F. Zheng, X. N. Gu, and F. Witte, “Biodegradable metals,” *Materials Science and Engineering R: Reports*, vol. 77, pp. 1–34, 2014.
- [12] Y. Liu, Y. Zheng, X. H. Chen, *et al.*, “Fundamental Theory of Biodegradable Metals—Definition, Criteria, and Design,” *Advanced Functional Materials*, vol. 29, no. 18, pp. 1–21, 2019.
- [13] ASTM International, “ASTM Standards: G31-72,” *Annual Book of ASTM Standards*, vol. 72, no. Reapproved 2004, 2012.
- [14] A. H. M. Sanchez, B. J. Luthringer, F. Feyerabend, and R. Willumeit, “Mg and Mg alloys: How comparable are in vitro and in vivo corrosion rates? A review,” *Acta Biomaterialia*, vol. 13, pp. 16–31, 2015.
- [15] F. Witte, J. Fischer, J. Nellesen, *et al.*, “In vitro and in vivo corrosion measurements of magnesium alloys,” *Biomaterials*, vol. 27, no. 7, pp. 1013–1018, 2006.
- [16] M. Moravej, A. Purnama, M. Fiset, J. Couet, and D. Mantovani, “Electroformed pure iron as a new biomaterial for degradable stents: In vitro degradation and preliminary cell viability studies,” *Acta Biomaterialia*, vol. 6, no. 5, pp. 1843–1851, 2010.
- [17] R. Tolouei, J. Harrison, C. Paternoster, S. Turgeon, P. Chevalier, and D. Mantovani, “The use of multiple pseudo-physiological solutions to simulate the degradation behavior of pure iron as a metallic resorbable implant: a surface-characterization study,” *Physical Chemistry Chemical Physics*, vol. 18, no. 29, pp. 19637–19646, 2016.

- [18] P. Wlaź, A. Serefko, A. Szopa, and E. Poleszak, “The effect of an acute and 7-day administration of magnesium chloride on magnesium concentration in the serum, erythrocytes, and brain of rats,” *Pharmacological Reports*, vol. 68, no. 2, pp. 289–291, 2016.
- [19] M. K. Kulekci, “Magnesium and its alloys applications in automotive industry,” *International Journal of Advanced Manufacturing Technology*, vol. 39, no. 9-10, pp. 851–865, 2008.
- [20] A. H. Musfirah and A. G. Jaharah, “Magnesium and aluminum alloys in automotive industry,” *Journal of Applied Sciences Research*, vol. 8, no. 10, pp. 4865–4875, 2012.
- [21] A. A. Luo, “Magnesium: Current and potential automotive applications,” *JOM*, vol. 54, no. 2, pp. 42–48, 2002.
- [22] C. Blawert, N. Hort, and K. U. Kainer, “Automotive applications of magnesium and its alloys,” *Transactions of the Indian Institute of Metals*, vol. 57, no. 4, pp. 397–408, 2004.
- [23] T. Kurzynowski, A. Pawlak, and I. Smolina, “The potential of SLM technology for processing magnesium alloys in aerospace industry,” *Archives of Civil and Mechanical Engineering*, vol. 20, no. 1, p. 23, 2020.
- [24] R. Viswanathan, N. Sivashankar, S. Chandrakumar, and R. Karthik, “Improving corrosion resistance of magnesium alloy for aerospace applications,” *International Journal of Mechanical and Production Engineering Research and Development*, vol. 9, no. 3, pp. 769–774, 2019.
- [25] F. Czerwinski, “Controlling the ignition and flammability of magnesium for aerospace applications,” *Corrosion Science*, vol. 86, pp. 1–16, 2014.
- [26] H. Furuya, N. Kogiso, S. Matunaga, and K. Senda, “Applications of magnesium alloys for aerospace structure systems,” *Materials Science Forum*, vol. 350, pp. 341–348, 2000.
- [27] Y. Yang, C. He, Dianyu E, *et al.*, “Mg bone implant: Features, developments and perspectives,” *Materials and Design*, vol. 185, p. 108 259, 2020.

- [28] B. Denkena and A. Lucas, “Biocompatible magnesium alloys as absorbable implant materials adjusted surface and subsurface properties by machining processes,” *CIRP Annals - Manufacturing Technology*, vol. 56, no. 1, pp. 113–116, 2007.
- [29] G. Song and S. Song, “A possible biodegradable magnesium implant material,” *Advanced Engineering Materials*, vol. 9, no. 4, pp. 298–302, 2007.
- [30] “Electrochemical series,” in *CRC Handbook of Chemistry and Physics*, J. Rumble, Ed., 100th ed., 2019, pp. 5–97.
- [31] V. Tsakiris, C. Tardei, and F. M. Clicinschi, “Biodegradable Mg alloys for orthopedic implants – A review,” *Journal of Magnesium and Alloys*, vol. 9, no. 6, pp. 1884–1905, 2021.
- [32] Z. Z. Yin, W. C. Qi, R. C. Zeng, *et al.*, “Advances in coatings on biodegradable magnesium alloys,” *Journal of Magnesium and Alloys*, vol. 8, no. 1, pp. 42–65, 2020.
- [33] H. Hornberger, S. Virtanen, and A. R. Boccaccini, “Biomedical coatings on magnesium alloys - A review,” *Acta Biomaterialia*, vol. 8, no. 7, pp. 2442–2455, 2012.
- [34] P. Tong, Y. Sheng, R. Hou, M. Iqbal, L. Chen, and J. Li, “Recent progress on coatings of biomedical magnesium alloy,” *Smart Materials in Medicine*, vol. 3, pp. 104–116, 2022.
- [35] Z. Yao, L. Li, and Z. Jiang, “Adjustment of the ratio of Ca/P in the ceramic coating on Mg alloy by plasma electrolytic oxidation,” *Applied Surface Science*, vol. 255, no. 13-14, pp. 6724–6728, 2009.
- [36] P. B. Srinivasan, J. Liang, C. Blawert, M. Störmer, and W. Dietzel, “Characterization of calcium containing plasma electrolytic oxidation coatings on AM50 magnesium alloy,” *Applied Surface Science*, vol. 256, no. 12, pp. 4017–4022, 2010.
- [37] S. Shadanbaz and G. J. Dias, “Calcium phosphate coatings on magnesium alloys for biomedical applications: A review,” *Acta Biomaterialia*, vol. 8, no. 1, pp. 20–30, 2012.

- [38] L. Y. Li, L. Y. Cui, R. C. Zeng, *et al.*, “Advances in functionalized polymer coatings on biodegradable magnesium alloys – A review,” *Acta Biomaterialia*, vol. 79, pp. 23–36, 2018.
- [39] S. Heise, S. Virtanen, and A. R. Boccaccini, “Tackling Mg alloy corrosion by natural polymer coatings—A review,” *Journal of Biomedical Materials Research - Part A*, vol. 104, no. 10, pp. 2628–2641, 2016.
- [40] H. M. Wong, K. W. Yeung, K. O. Lam, *et al.*, “A biodegradable polymer-based coating to control the performance of magnesium alloy orthopaedic implants,” *Biomaterials*, vol. 31, no. 8, pp. 2084–2096, 2010.
- [41] H. F. Li, Z. Z. Shi, and L. N. Wang, “Opportunities and challenges of biodegradable Zn-based alloys,” *Journal of Materials Science & Technology*, vol. 46, pp. 136–138, 2020.
- [42] B. Beverskog and I. Puigdomenech, “Revised pourbaix diagrams for zinc at 25–300 °C,” *Corrosion Science*, vol. 39, no. 1, pp. 107–114, 1997.
- [43] J. Hu, S. Sun, W. Zhang, *et al.*, “Softening Behaviors of Severely Deformed Zn Alloy Studied by the Nanoindentation,” *Coatings*, vol. 10, no. 9, p. 803, 2020.
- [44] E. Mostaed, M. Sikora-Jasinska, M. S. Ardakani, *et al.*, “Towards revealing key factors in mechanical instability of bioabsorbable Zn-based alloys for intended vascular stenting,” *Acta Biomaterialia*, vol. 105, pp. 319–335, 2020.
- [45] M. Kawasaki, B. Ahn, and T. G. Langdon, “Microstructural evolution in a two-phase alloy processed by high-pressure torsion,” *Acta Materialia*, vol. 58, no. 3, pp. 919–930, 2010.
- [46] G. R. Edwards, J. C. Shyne, and O. D. Sherby, “Strain softening in powder metallurgy zinc,” *Metallurgical Transactions*, vol. 2, no. 10, pp. 2955–2958, 1971.
- [47] E. Mostaed, M. Sikora-Jasinska, A. Mostaed, *et al.*, “Novel Zn-based alloys for biodegradable stent applications: Design, development and in vitro degradation,” *Journal of the Mechanical Behavior of Biomedical Materials*, vol. 60, pp. 581–602, 2016.

- [48] N. S. Murni, M. S. Dambatta, S. K. Yeap, G. R. Froemming, and H. Hermawan, "Cytotoxicity evaluation of biodegradable Zn–3Mg alloy toward normal human osteoblast cells," *Materials Science and Engineering: C*, vol. 49, pp. 560–566, 2015.
- [49] P. K. Bowen, J. M. Seitz, R. J. Guillory, *et al.*, "Evaluation of wrought Zn–Al alloys (1, 3, and 5 wt % Al) through mechanical and in vivo testing for stent applications," *Journal of Biomedical Materials Research Part B: Applied Biomaterials*, vol. 106, no. 1, pp. 245–258, 2018.
- [50] C. Zhou, H. F. Li, Y. X. Yin, *et al.*, "Long-term in vivo study of biodegradable Zn–Cu stent: A 2-year implantation evaluation in porcine coronary artery," *Acta Biomaterialia*, vol. 97, pp. 657–670, 2019.
- [51] S. Zhao, J. M. Seitz, R. Eifler, *et al.*, "Zn–Li alloy after extrusion and drawing: Structural, mechanical characterization, and biodegradation in abdominal aorta of rat," *Materials Science and Engineering: C*, vol. 76, pp. 301–312, 2017.
- [52] H. F. Li, X. H. Xie, Y. F. Zheng, *et al.*, "Development of biodegradable Zn–1X binary alloys with nutrient alloying elements Mg, Ca and Sr," *Scientific Reports*, vol. 5, pp. 1–14, 2015.
- [53] M. Sikora-Jasinska, E. Mostaed, A. Mostaed, R. Beanland, D. Mantovani, and M. Vedani, "Fabrication, mechanical properties and in vitro degradation behavior of newly developed ZnAg alloys for degradable implant applications," *Materials Science and Engineering: C*, vol. 77, pp. 1170–1181, 2017.
- [54] A. A. Oliver, R. J. Guillory, K. L. Flom, *et al.*, "Analysis of Vascular Inflammation against Bioresorbable Zn–Ag–Based Alloys," *ACS Applied Bio Materials*, vol. 3, no. 10, pp. 6779–6789, 2020.
- [55] B. A. Burgan and M. R. Sansom, "Sustainable steel construction," *Journal of Constructional Steel Research*, vol. 62, no. 11, pp. 1178–1183, 2006.
- [56] N. R. Baddoo, "Stainless steel in construction: A review of research, applications, challenges and opportunities," *Journal of Constructional Steel Research*, vol. 64, no. 11, pp. 1199–1206, 2008.

- [57] J. Galán, L. Samek, P. Verleysen, K. Verbeken, and Y. Houbaert, “Advanced high strength steels for automotive industry,” *Revista de Metalurgia*, vol. 48, no. 2, pp. 118–131, 2012.
- [58] I. Zuazo, B. Hallstedt, B. Lindahl, *et al.*, “Low-Density Steels: Complex Metallurgy for Automotive Applications,” *JOM*, vol. 66, no. 9, pp. 1747–1758, 2014.
- [59] J. H. Schmitt and T. Iung, “New developments of advanced high-strength steels for automotive applications,” *Comptes Rendus Physique*, vol. 19, no. 8, pp. 641–656, 2018.
- [60] B. Beverskog and I. Puigdomenech, “Revised pourbaix diagrams for iron at 25–300 °C,” *Corrosion Science*, vol. 38, no. 12, pp. 2121–2135, 1996.
- [61] N. S. Fagali, C. A. Grillo, S. Puntarulo, and M. A. Fernández Lorenzo de Mele, “Cytotoxicity of corrosion products of degradable Fe-based stents: Relevance of pH and insoluble products,” *Colloids and Surfaces B: Biointerfaces*, vol. 128, pp. 480–488, 2015.
- [62] E. Scarcello, A. Herpain, M. Tomatis, F. Turci, P. J. Jacques, and D. Lison, “Hydroxyl radicals and oxidative stress: the dark side of Fe corrosion,” *Colloids and Surfaces B: Biointerfaces*, vol. 185, p. 110542, 2020.
- [63] N. S. Fagali, C. A. Grillo, S. Puntarulo, and M. A. Fernández Lorenzo de Mele, “Is there any difference in the biological impact of soluble and insoluble degradation products of iron-containing biomaterials?” *Colloids and Surfaces B: Biointerfaces*, vol. 160, pp. 238–246, 2017.
- [64] E. Scarcello, I. Lobysheva, C. Bouzin, P. J. Jacques, D. Lison, and C. Dessy, “Endothelial dysfunction induced by hydroxyl radicals – the hidden face of biodegradable Fe-based materials for coronary stents,” *Materials Science and Engineering: C*, vol. 112, p. 110938, 2020.
- [65] H. Hermawan, A. Purnama, D. Dube, J. Couet, and D. Mantovani, “Fe-Mn alloys for metallic biodegradable stents: Degradation and cell viability studies,” *Acta Biomaterialia*, vol. 6, no. 5, pp. 1852–1860, 2010.



- [66] H. Hermawan, D. Dubé, and D. Mantovani, “Degradable metallic biomaterials: Design and development of Fe-Mn alloys for stents,” *Journal of Biomedical Materials Research - Part A*, vol. 93, no. 1, pp. 1–11, 2010.
- [67] H. Hermawan, H. Alamdari, D. Mantovani, and D. Dubé, “Iron-manganese: New class of metallic degradable biomaterials prepared by powder metallurgy,” *Powder Metallurgy*, vol. 51, no. 1, pp. 38–45, 2008.
- [68] H. Wang, Y. Zheng, J. Liu, C. Jiang, and Y. Li, “In vitro corrosion properties and cytocompatibility of Fe-Ga alloys as potential biodegradable metallic materials,” *Materials Science and Engineering C*, vol. 71, pp. 60–66, 2017.
- [69] A. H. M. Yusop, N. M. Daud, H. Nur, M. R. A. Kadir, and H. Hermawan, “Controlling the degradation kinetics of porous iron by poly(lactic-co-glycolic acid) infiltration for use as temporary medical implants,” *Scientific reports*, vol. 5, p. 11 194, 2015.
- [70] S. Bagherifard, M. F. Molla, D. Kajanek, R. Donnini, B. Hadzima, and M. Guagliano, “Accelerated biodegradation and improved mechanical performance of pure iron through surface grain refinement,” *Acta Biomaterialia*, vol. 98, pp. 88–102, 2019.
- [71] H. Wang, Y. Zheng, Y. Li, and C. Jiang, “Improvement of in vitro corrosion and cytocompatibility of biodegradable Fe surface modified by Zn ion implantation,” *Applied Surface Science*, vol. 403, pp. 168–176, 2017.
- [72] H. Wang, Y. Zheng, C. Jiang, Y. Li, and Y. Fu, “In vitro corrosion behavior and cytocompatibility of pure Fe implanted with Ta,” *Surface and Coatings Technology*, vol. 320, pp. 201–205, 2017.
- [73] T. Huang and Y. Zheng, “Uniform and accelerated degradation of pure iron patterned by Pt disc arrays,” *Scientific Reports*, vol. 6, p. 23 627, 2016.
- [74] J. Cheng, T. Huang, and Y. F. Zheng, “Relatively uniform and accelerated degradation of pure iron coated with micro-patterned Au disc arrays,” *Materials Science and Engineering: C*, vol. 48, pp. 679–687, 2015.

- [75] H. Hermawan, D. Dubé, and D. Mantovani, “Development of degradable Fe-35Mn alloy for biomedical application,” *Advanced Materials Research*, vol. 15-17, pp. 107–112, 2007.
- [76] Y. K. Lee, J. H. Jun, and C. S. Choi, “Damping Capacity in Fe-Mn Binary Alloys,” *ISIJ International*, vol. 37, no. 10, pp. 1023–1030, 1997.
- [77] J. Martínez, S. M. Cotes, A. F. Cabrera, J. Desimoni, and A. Fernández Guillermet, “On the relative fraction of martensite in  $\gamma$ -Fe-Mn alloys,” *Materials Science and Engineering: A*, vol. 408, no. 1-2, pp. 26–32, 2005.
- [78] H. Schumann, “Die martensitischen Umwandlungen in kohlenstoffarmen Manganstählen,” *Archiv für das Eisenhüttenwesen*, vol. 38, no. 8, pp. 647–656, 1967.
- [79] Y. Lü, B. Hutchinson, D. A. Molodov, and G. Gottstein, “Effect of deformation and annealing on the formation and reversion of  $\epsilon$ -martensite in an Fe-Mn-C alloy,” *Acta Materialia*, vol. 58, no. 8, pp. 3079–3090, 2010.
- [80] J. W. Brooks, M. H. Loretto, and R. E. Smallman, “In situ observations of the formation of martensite in stainless steel,” *Acta Metallurgica*, vol. 27, no. 12, pp. 1829–1838, 1979.
- [81] H. Hermawan, “Biodegradable Metals: State of the Art,” in *Biodegradable Metals: From Concept to Applications*, 2012, pp. 13–22.
- [82] H. Hermawan, “Updates on the research and development of absorbable metals for biomedical applications,” *Progress in Biomaterials*, vol. 7, no. 2, pp. 93–110, 2018.
- [83] T. Kraus, F. Moszner, S. Fischerauer, *et al.*, “Biodegradable Fe-based alloys for use in osteosynthesis: Outcome of an in vivo study after 52 weeks,” *Acta Biomaterialia*, vol. 10, no. 7, pp. 3346–3353, 2014.
- [84] J. Venezuela and M. S. Dargusch, “Addressing the slow corrosion rate of biodegradable Fe-Mn: Current approaches and future trends,” *Current Opinion in Solid State and Materials Science*, vol. 24, no. 3, p. 100 822, 2020.

- [85] Č. Donik, A. Kocijan, I. Paulin, M. Hočevár, P. Gregorčič, and M. Godec, “Improved biodegradability of Fe–Mn alloy after modification of surface chemistry and topography by a laser ablation,” *Applied Surface Science*, vol. 453, pp. 383–393, 2018.
- [86] M. Heiden, E. Nauman, and L. Stanciu, “Bioresorbable Fe–Mn and Fe–Mn–HA Materials for Orthopedic Implantation: Enhancing Degradation through Porosity Control,” *Advanced Healthcare Materials*, vol. 6, no. 13, p. 1700120, 2017.
- [87] E. Mouzou, C. Paternoster, R. Tolouei, *et al.*, “CO<sub>2</sub>-rich atmosphere strongly affects the degradation of Fe–21Mn–1C for biodegradable metallic implants,” *Materials Letters*, vol. 181, pp. 362–366, 2016.
- [88] S. Loffredo, C. Paternoster, N. Giguère, G. Barucca, M. Vedani, and D. Mantovani, “The addition of silver affects the deformation mechanism of a twinning-induced plasticity steel: Potential for thinner degradable stents,” *Acta Biomaterialia*, vol. 98, pp. 103–113, 2019.
- [89] M. Schinhammer, C. M. Pecnik, F. Rechberger, A. C. Hänzi, J. F. Löffler, and P. J. Uggowitzer, “Recrystallization behavior, microstructure evolution and mechanical properties of biodegradable Fe–Mn–C(–Pd) TWIP alloys,” *Acta Materialia*, vol. 60, no. 6–7, pp. 2746–2756, 2012.
- [90] E. Mouzou, C. Paternoster, R. Tolouei, *et al.*, “In vitro degradation behavior of Fe–20Mn–1.2C alloy in three different pseudo-physiological solutions,” *Materials Science and Engineering: C*, vol. 61, pp. 564–573, 2016.
- [91] M. Schinhammer, P. Steiger, F. Moszner, J. F. Löffler, and P. J. Uggowitzer, “Degradation performance of biodegradable FeMnC(Pd) alloys,” *Materials Science and Engineering C*, vol. 33, no. 4, pp. 1882–1893, 2013.
- [92] A. Gebert, F. Kochta, A. Voß, *et al.*, “Corrosion studies on Fe–30Mn–1C alloy in chloride-containing solutions with view to biomedical application,” *Materials and Corrosion*, vol. 69, no. 2, pp. 167–177, 2018.

- [93] J. Hufenbach, H. Wendrock, F. Kochta, U. Kühn, and A. Gebert, “Novel biodegradable Fe-Mn-C-S alloy with superior mechanical and corrosion properties,” *Materials Letters*, vol. 186, pp. 330–333, 2017.
- [94] Y. P. Feng, A. Blanquer, J. Fornell, *et al.*, “Novel Fe-Mn-Si-Pd alloys: Insights into mechanical, magnetic, corrosion resistance and biocompatibility performances,” *Journal of Materials Chemistry B*, vol. 4, no. 39, pp. 6402–6412, 2016.
- [95] B. Liu, Y. F. Zheng, and L. Ruan, “In vitro investigation of Fe<sub>30</sub>Mn<sub>6</sub>Si shape memory alloy as potential biodegradable metallic material,” *Materials Letters*, vol. 65, no. 3, pp. 540–543, 2011.
- [96] M. Schinhammer, A. C. Hänzi, J. F. Löffler, and P. J. Uggowitzer, “Design strategy for biodegradable Fe-based alloys for medical applications,” *Acta Biomaterialia*, vol. 6, no. 5, pp. 1705–1713, 2010.
- [97] Y. P. Feng, N. Gaztelumendi, J. Fornell, *et al.*, “Mechanical properties, corrosion performance and cell viability studies on newly developed porous Fe-Mn-Si-Pd alloys,” *Journal of Alloys and Compounds*, vol. 724, pp. 1046–1056, 2017.
- [98] F. Moszner, A. S. Sologubenko, M. Schinhammer, *et al.*, “Precipitation hardening of biodegradable Fe-Mn-Pd alloys,” *Acta Materialia*, vol. 59, no. 3, pp. 981–991, 2011.
- [99] S. Mandal, V. Kishore, M. Bose, S. K. Nandi, and M. Roy, “In vitro and in vivo degradability, biocompatibility and antimicrobial characteristics of Cu added iron-manganese alloy,” *Journal of Materials Science & Technology*, vol. 84, pp. 159–172, 2021.
- [100] S. Mandal, R. Ummadi, M. Bose, V. K. Balla, and M. Roy, “Fe-Mn-Cu alloy as biodegradable material with enhanced antimicrobial properties,” *Materials Letters*, vol. 237, pp. 323–327, 2019.
- [101] P. Sotoudeh Bagha, M. Khakbiz, S. Sheibani, and H. Hermawan, “Design and characterization of nano and bimodal structured biodegradable Fe-Mn-Ag alloy with accelerated corrosion rate,” *Journal of Alloys and Compounds*, vol. 767, pp. 955–965, 2018.

- [102] P. Sotoudeh Bagha, M. Khakbiz, N. Safaie, S. Sheibani, and S. Ebrahimi-Barough, “Effect of high energy ball milling on the properties of biodegradable nanostructured Fe-35wt.% alloy,” *Journal of Alloys and Compounds*, vol. 768, pp. 166–175, 2018.
- [103] M. Caligari Conti, B. Mallia, E. Sinagra, P. Schembri Wismayer, J. Buhagiar, and D. Vella, “The effect of alloying elements on the properties of pressed and non-pressed biodegradable Fe–Mn–Ag powder metallurgy alloys,” *Heliyon*, vol. 5, no. 9, e02522, 2019.
- [104] S. Sivasankaran, H. R. Ammar, B. Almangour, S. A. Elborolossy, A. b. H. Mekky, and A. S. Alaboodi, “Influence of Milling Time and Ball-to-Powder Ratio on Mechanical Behavior of FeMn30Cu5 Biodegradable Alloys Prepared by Mechanical Alloying and Hot-Forging,” *Crystals*, vol. 12, no. 12, p. 1777, 2022.
- [105] J. Kraner, J. Medved, M. Godec, and I. Paulin, “Thermodynamic behavior of Fe-Mn and Fe-Mn-Ag powder mixtures during selective laser melting,” *Metals*, vol. 11, no. 2, pp. 1–12, 2021.
- [106] Č. Donik, J. Kraner, A. Kocijan, I. Paulin, and M. Godec, “Evolution of the  $\epsilon$  and  $\gamma$  phases in biodegradable Fe–Mn alloys produced using laser powder-bed fusion,” *Scientific Reports*, vol. 11, no. 1, pp. 1–10, 2021.
- [107] M. Wiesener, K. Peters, A. Taube, *et al.*, “Corrosion properties of bioresorbable FeMn-Ag alloys prepared by selective laser melting,” *Materials and Corrosion*, vol. 68, no. 10, pp. 1028–1036, 2017.
- [108] T. Niendorf, F. Brenne, P. Hoyer, *et al.*, “Processing of New Materials by Additive Manufacturing: Iron-Based Alloys Containing Silver for Biomedical Applications,” *Metallurgical and Materials Transactions A: Physical Metallurgy and Materials Science*, vol. 46, no. 7, pp. 2829–2833, 2015.
- [109] A. M. Roman, V. Geantă, R. Cimpoeșu, *et al.*, “In-Vitro Analysis of FeMn-Si Smart Biodegradable Alloy,” *Materials*, vol. 15, no. 2, p. 568, 2022.
- [110] S. Loffredo, S. Gambaro, F. Copes, *et al.*, “Effect of silver in thermal treatments of Fe-Mn-C degradable metals: Implications for stent processing,” *Bioactive Materials*, vol. 12, pp. 30–41, 2022.

- [111] A. H. Yusop, A. A. Bakir, N. A. Shaharom, M. R. Abdul Kadir, and H. Hermawan, "Porous biodegradable metals for hard tissue scaffolds: A review," *International Journal of Biomaterials*, vol. 2012, p. 641 430, 2012.
- [112] P. Sharma and P. M. Pandey, "Corrosion rate modelling of biodegradable porous iron scaffold considering the effect of porosity and pore morphology," *Materials Science and Engineering: C*, vol. 103, p. 109 776, 2019.
- [113] V. Raeisdasteh Hokmabad, S. Davaran, A. Ramazani, and R. Salehi, "Design and fabrication of porous biodegradable scaffolds: a strategy for tissue engineering," *Journal of Biomaterials Science, Polymer Edition*, vol. 28, no. 16, pp. 1797–1825, 2017.
- [114] A. H. Aghajanian, B. A. Khazaei, M. Khodaei, and M. Rafienia, "Fabrication of Porous Mg-Zn Scaffold through Modified Replica Method for Bone Tissue Engineering," *Journal of Bionic Engineering*, vol. 15, no. 5, pp. 907–913, 2018.
- [115] P. Liu, D. Zhang, Y. Dai, J. Lin, Y. Li, and C. Wen, "Microstructure, mechanical properties, degradation behavior, and biocompatibility of porous Fe-Mn alloys fabricated by sponge impregnation and sintering techniques," *Acta Biomaterialia*, vol. 114, pp. 485–496, 2020.
- [116] Q. Zhang and P. Cao, "Degradable porous Fe-35wt.%Mn produced via powder sintering from NH<sub>4</sub>HCO<sub>3</sub> porogen," *Materials Chemistry and Physics*, vol. 163, pp. 394–401, 2015.
- [117] J. H. Lee, H. E. Kim, and Y. H. Koh, "Highly porous titanium (Ti) scaffolds with bioactive microporous hydroxyapatite/TiO<sub>2</sub> hybrid coating layer," *Materials Letters*, vol. 63, no. 23, pp. 1995–1998, 2009.
- [118] C. Wang, H. Chen, X. Zhu, Z. Xiao, K. Zhang, and X. Zhang, "An improved polymeric sponge replication method for biomedical porous titanium scaffolds," *Materials Science and Engineering: C*, vol. 70, pp. 1192–1199, 2017.

- [119] H. C. Hsu, S. K. Hsu, S. C. Wua, P. H. Wang, and W. F. Ho, “Design and characterization of highly porous titanium foams with bioactive surface sintering in air,” *Journal of Alloys and Compounds*, vol. 575, pp. 326–332, 2013.
- [120] A. Manonukul, M. Tange, P. Srikudvien, N. Denmud, and P. Wattanapornphan, “Rheological properties of commercially pure titanium slurry for metallic foam production using replica impregnation method,” *Powder Technology*, vol. 266, pp. 129–134, 2014.
- [121] H. Khallok, A. Elouahli, S. Ojala, R. L. Keiski, A. Kheribech, and Z. Hatim, “Preparation of biphasic hydroxyapatite/  $\beta$ -tricalcium phosphate foam using the replication technique,” *Ceramics International*, vol. 46, no. 14, pp. 22 581–22 591, 2020.
- [122] I.-H. Jo, K.-H. Shin, Y.-M. Soon, Y.-H. Koh, J.-H. Lee, and H.-E. Kim, “Highly porous hydroxyapatite scaffolds with elongated pores using stretched polymeric sponges as novel template,” *Materials Letters*, vol. 63, no. 20, pp. 1702–1704, 2009.
- [123] S. Huang, A. Ulloa, E. Nauman, and L. Stanciu, “Collagen Coating Effects on Fe–Mn Bioresorbable Alloys,” *Journal of Orthopaedic Research*, vol. 38, no. 3, pp. 523–535, 2020.
- [124] R. Drevet, Y. Zhukova, P. Kadirov, *et al.*, “Tunable Corrosion Behavior of Calcium Phosphate Coated Fe-Mn-Si Alloys for Bone Implant Applications,” *Metallurgical and Materials Transactions A: Physical Metallurgy and Materials Science*, vol. 49, no. 12, pp. 6553–6560, 2018.
- [125] J. Fornell, Y. P. Feng, E. Pellicer, S. Suriñach, M. D. Baró, and J. Sort, “Mechanical behaviour of brushite and hydroxyapatite coatings electrodeposited on newly developed FeMnSiPd alloys,” *Journal of Alloys and Compounds*, vol. 729, pp. 231–239, 2017.
- [126] M. Heiden, D. Johnson, and L. Stanciu, “Surface modifications through dealloying of Fe–Mn and Fe–Mn–Zn alloys developed to create tailorable, nanoporous, bioresorbable surfaces,” *Acta Materialia*, vol. 103, pp. 115–127, 2016.

- [127] A. Yamamoto, R. Honma, and M. Sumita, “Cytotoxicity evaluation of 43 metal salts using murine fibroblasts and osteoblastic cells,” *Journal of Biomedical Materials Research*, vol. 39, no. 2, pp. 331–340, 1998.
- [128] S. I. Barr, S. P. Murphy, and M. I. Poos, “Interpreting and using the Dietary References Intakes in dietary assessment of individuals and groups,” *Journal of the American Dietetic Association*, vol. 102, no. 6, pp. 780–788, 2002.
- [129] J. Syarif, Y. Pratesa, Y. Prasetyo, and S. Harjanto, “Ball milling effect on corrosion and biocompatibility behavior of femnc alloys produced by powder metallurgy in simulated body fluids environment,” *Metals*, vol. 11, no. 10, p. 1597, 2021.
- [130] A. Przekora, “The summary of the most important cell-biomaterial interactions that need to be considered during in vitro biocompatibility testing of bone scaffolds for tissue engineering applications,” *Materials Science and Engineering: C*, vol. 97, pp. 1036–1051, 2019.
- [131] A. Carnicer-Lombarte, S. T. Chen, G. G. Malliaras, and D. G. Barone, “Foreign Body Reaction to Implanted Biomaterials and Its Impact in Nerve Neuroprosthetics,” *Frontiers in Bioengineering and Biotechnology*, vol. 9, p. 271, 2021.
- [132] C. Xu, Y. Chen, J. Lin, and H. H. Liu, “Direct and Indirect Culture Methods for Studying Biodegradable Implant Materials In Vitro,” *Journal of Visualized Experiments*, vol. 2022, no. 182, e63065, 2022.
- [133] G. Papanikolaou and K. Pantopoulos, “Iron metabolism and toxicity,” *Toxicology and applied pharmacology*, vol. 202, no. 2, pp. 199–211, 2005.
- [134] Y. Hirata, “Manganese-induced apoptosis in PC12 cells,” *Neurotoxicology and Teratology*, vol. 24, no. 5, pp. 639–653, 2002.
- [135] M. Aschner, T. R. Guilarte, J. S. Schneider, and W. Zheng, “Manganese: Recent advances in understanding its transport and neurotoxicity,” *Toxicology and Applied Pharmacology*, vol. 221, no. 2, pp. 131–147, 2007.



- [136] M. Schinhammer, I. Gerber, A. C. Hänzi, and P. J. Uggowitzer, “On the cytocompatibility of biodegradable Fe-based alloys,” *Materials Science and Engineering C*, vol. 33, no. 2, pp. 782–789, 2013.
- [137] P. Sotoudehbagha, S. Sheibani, M. Khakbiz, S. Ebrahimi-Barough, and H. Hermawan, “Novel antibacterial biodegradable Fe-Mn-Ag alloys produced by mechanical alloying,” *Materials Science and Engineering C*, vol. 88, pp. 88–94, 2018.
- [138] P. S. Bagha, M. Khakbiz, S. Sheibani, *et al.*, “In Vitro Degradation, Hemocompatibility, and Cytocompatibility of Nanostructured Absorbable Fe-Mn-Ag Alloys for Biomedical Application,” *ACS Biomaterials Science and Engineering*, vol. 6, no. 4, pp. 2094–2106, 2020.
- [139] M. S. Dargusch, J. Venezuela, A. Dehghan-Manshadi, *et al.*, “In Vivo Evaluation of Bioabsorbable Fe-35Mn-1Ag: First Reports on In Vivo Hydrogen Gas Evolution in Fe-Based Implants,” *Advanced Healthcare Materials*, vol. 10, no. 2, p. 2000667, 2021.
- [140] S. M. Huang, E. A. Nauman, and L. A. Stanciu, “Investigation of porosity on mechanical properties, degradation and in-vitro cytotoxicity limit of Fe30Mn using space holder technique,” *Materials Science and Engineering C*, vol. 99, no. June 2018, pp. 1048–1057, 2019.
- [141] P. Gupta, S. Sarkar, B. Das, S. Bhattacharjee, and P. Tribedi, “Biofilm, pathogenesis and prevention—a journey to break the wall: a review,” *Archives of microbiology*, vol. 198, no. 1, pp. 1–15, 2016.
- [142] R. Mirzaei, R. Mohammadzadeh, M. Y. Alikhani, *et al.*, “The biofilm-associated bacterial infections unrelated to indwelling devices,” *IUBMB Life*, vol. 72, no. 7, pp. 1271–1285, 2020.
- [143] S. Saint and C. E. Chenoweth, “Biofilms and catheter-associated urinary tract infections,” *Infectious Disease Clinics of North America*, vol. 17, no. 2, pp. 411–432, 2003.
- [144] S. Niveditha, S. Pramodhini, S. Umadevi, S. Kumar, and S. Stephen, “The Isolation and the Biofilm Formation of Uropathogens in the Patients with Catheter Associated Urinary Tract Infections (UTIs),”

- Journal of Clinical and Diagnostic Research : JCDR*, vol. 6, no. 9, p. 1478, 2012.
- [145] B. W. Trautner and R. O. Darouiche, "Role of biofilm in catheter-associated urinary tract infection," *American journal of infection control*, vol. 32, no. 3, p. 177, 2004.
- [146] R. Saini, S. Saini, and S. Sharma, "Biofilm: A dental microbial infection," *Journal of Natural Science, Biology, and Medicine*, vol. 2, no. 1, p. 71, 2011.
- [147] T. Larsen and N. E. Fiehn, "Dental biofilm infections - an update," *APMIS : acta pathologica, microbiologica, et immunologica Scandinavica*, vol. 125, no. 4, pp. 376–384, 2017.
- [148] Y. Jiao, F. R. Tay, L. n. Niu, and J. h. Chen, "Advancing antimicrobial strategies for managing oral biofilm infections," *International Journal of Oral Science 2019 11:3*, vol. 11, no. 3, pp. 1–11, 2019.
- [149] M. Kolpen, K. N. Kragh, J. B. Enciso, *et al.*, "Bacterial biofilms predominate in both acute and chronic human lung infections," *Thorax*, vol. 77, no. 10, pp. 1015–1022, 2022.
- [150] A. A. Boisvert, M. P. Cheng, D. C. Sheppard, and D. Nguyen, "Microbial biofilms in pulmonary and critical care diseases," *Annals of the American Thoracic Society*, vol. 13, no. 9, pp. 1615–1623, 2016.
- [151] R. O. Darouiche, "Device-associated infections: a macroproblem that starts with microadherence," *Clinical infectious diseases : an official publication of the Infectious Diseases Society of America*, vol. 33, no. 9, pp. 1567–1572, 2001.
- [152] H. J. Busscher, H. C. v. d. Mei, G. Subbiahdoss, *et al.*, "Biomaterial-Associated Infection: Locating the Finish Line in the Race for the Surface," *Science Translational Medicine*, vol. 4, no. 153, 153rv10, 2012.
- [153] S. Young, S. A. Lie, G. Hallan, L. G. Zirkle, L. B. Engesæter, and L. I. Havelin, "Low infection rates after 34,361 intramedullary nail operations in 55 low- and middle-income countries: validation of the Surgical Implant Generation Network (SIGN) online surgical database," *Acta orthopaedica*, vol. 82, no. 6, pp. 737–743, 2011.

- [154] X. Tian, Z. Lu, C. Ma, *et al.*, “Antimicrobial hydroxyapatite and its composites for the repair of infected femoral condyle,” *Materials Science and Engineering: C*, vol. 121, p. 111 807, 2021.
- [155] J. D. Bryers, “Medical biofilms,” *Biotechnology and Bioengineering*, vol. 100, no. 1, pp. 1–18, 2008.
- [156] A. G. Gristina, P. Naylor, and Q. Myrvik, “Infections from biomaterials and implants: A race for the surface,” *Medical Progress through Technology*, vol. 14, no. 3-4, pp. 205–224, 1988.
- [157] E. Zhang, X. Zhao, J. Hu, R. Wang, S. Fu, and G. Qin, “Antibacterial metals and alloys for potential biomedical implants,” *Bioactive Materials*, vol. 6, no. 8, pp. 2569–2612, 2021.
- [158] D. Campoccia, L. Montanaro, and C. R. Arciola, “A review of the biomaterials technologies for infection-resistant surfaces,” *Biomaterials*, vol. 34, no. 34, pp. 8533–8554, 2013.
- [159] C. R. Arciola, D. Campoccia, and L. Montanaro, “Implant infections: adhesion, biofilm formation and immune evasion,” *Nature Reviews Microbiology*, vol. 16, no. 7, pp. 397–409, 2018.
- [160] K. Sauer, P. Stoodley, D. M. Goeres, *et al.*, “The biofilm life cycle: expanding the conceptual model of biofilm formation,” *Nature Reviews Microbiology*, vol. 20, no. 10, pp. 608–620, 2022.
- [161] W. Li, E. S. Thian, M. Wang, Z. Wang, and L. Ren, “Surface Design for Antibacterial Materials: From Fundamentals to Advanced Strategies,” *Advanced Science*, vol. 8, no. 19, p. 2100368, 2021.
- [162] A. B. Lansdown, “Silver I: its antibacterial properties and mechanism of action,” *Journal of Wound Care*, vol. 11, no. 4, pp. 125–130, 2013.
- [163] J. L. Clement and P. S. Jarrett, “Antibacterial Silver,” *Metal-Based Drugs*, vol. 1, no. 5-6, p. 467, 1994.
- [164] W. Sim, R. T. Barnard, M. A. Blaskovich, and Z. M. Ziora, “Antimicrobial Silver in Medicinal and Consumer Applications: A Patent Review of the Past Decade (2007–2017),” *Antibiotics*, vol. 7, no. 4, p. 93, 2018.

- [165] G. Grass, C. Rensing, and M. Solioz, “Metallic Copper as an Antimicrobial Surface,” *Applied and Environmental Microbiology*, vol. 77, no. 5, p. 1541, 2011.
- [166] I. Salah, I. P. Parkin, and E. Allan, “Copper as an antimicrobial agent: recent advances,” *RSC Advances*, vol. 11, no. 30, pp. 18 179–18 186, 2021.
- [167] M. M. Almoudi, A. S. Hussein, M. I. Abu Hassan, and N. Mohamad Zain, “A systematic review on antibacterial activity of zinc against *Streptococcus mutans*,” *The Saudi Dental Journal*, vol. 30, no. 4, p. 283, 2018.
- [168] S. V. Gudkov, D. E. Burmistrov, D. A. Serov, M. B. Rebezov, A. A. Semenova, and A. B. Lisitsyn, “A Mini Review of Antibacterial Properties of ZnO Nanoparticles,” *Frontiers in Physics*, vol. 9, p. 641 481, 2021.
- [169] J. Pasquet, Y. Chevalier, J. Pelletier, E. Couval, D. Bouvier, and M. A. Bolzinger, “The contribution of zinc ions to the antimicrobial activity of zinc oxide,” *Colloids and Surfaces A: Physicochemical and Engineering Aspects*, vol. 457, no. 1, pp. 263–274, 2014.
- [170] L. Li, H. Chang, N. Yong, M. Li, Y. Hou, and W. Rao, “Superior antibacterial activity of gallium based liquid metals due to Ga<sup>3+</sup> induced intracellular ROS generation,” *Journal of Materials Chemistry B*, vol. 9, no. 1, pp. 85–93, 2021.
- [171] F. Kurtuldu, N. Mutlu, A. R. Boccaccini, and D. Galusek, “Gallium containing bioactive materials: A review of anticancer, antibacterial, and osteogenic properties,” *Bioactive Materials*, vol. 17, pp. 125–146, 2022.
- [172] S. K. Divakarla, T. Das, C. Chatterjee, *et al.*, “Antimicrobial and Anti-inflammatory Gallium-Defensin Surface Coatings for Implantable Devices,” *ACS Applied Materials and Interfaces*, vol. 14, no. 7, pp. 9685–9696, 2022.
- [173] S. Daghighi, J. Sjollem, H. C. van der Mei, H. J. Busscher, and E. T. Rochford, “Infection resistance of degradable versus non-degradable biomaterials: An assessment of the potential mechanisms,” *Biomaterials*, vol. 34, no. 33, pp. 8013–8017, 2013.

- [174] N. Wang, Y. Ma, H. Shi, Y. Song, S. Guo, and S. Yang, “Mg-, Zn-, and Fe-Based Alloys With Antibacterial Properties as Orthopedic Implant Materials,” *Frontiers in Bioengineering and Biotechnology*, vol. 10, p. 684, 2022.
- [175] Z. Ma, M. Gao, D. Na, Y. Li, L. Tan, and K. Yang, “Study on a biodegradable antibacterial Fe-Mn-C-Cu alloy as urinary implant material,” *Materials Science and Engineering C*, vol. 103, p. 109 718, 2019.
- [176] Y. Guo, M. C. Zhao, B. Xie, *et al.*, “In Vitro Corrosion Resistance and Antibacterial Performance of Novel Fe-xCu Biomedical Alloys Prepared by Selective Laser Melting,” *Advanced Engineering Materials*, vol. 23, no. 4, p. 2 001 000, 2021.
- [177] R. Y. Liu, R. G. He, L. Q. Xu, and S. F. Guo, “Design of Fe-Mn-Ag Alloys as Potential Candidates for Biodegradable Metals,” *Acta Metallurgica Sinica (English Letters)*, vol. 31, no. 6, pp. 584–590, 2018.
- [178] T. Huang, J. Cheng, D. Bian, and Y. Zheng, “Fe-Au and Fe-Ag composites as candidates for biodegradable stent materials,” *Journal of Biomedical Materials Research - Part B Applied Biomaterials*, vol. 104, no. 2, pp. 225–240, 2016.
- [179] W. Oliver and G. Pharr, “An improved technique for determining hardness and elastic modulus using load and displacement sensing indentation experiments,” *Journal of Materials Research*, vol. 7, no. 6, pp. 1564–1583, 1992.
- [180] R. Hartmann, H. Jeckel, E. Jelli, *et al.*, “Quantitative image analysis of microbial communities with BiofilmQ,” *Nature Microbiology*, vol. 6, no. 2, pp. 151–156, 2021.

## 4 Results as a compilation of articles

In this chapter, the results obtained in the thesis are structured as a compendium of three peer-reviewed articles. Prior to each publication, a concise overview of its contents is provided. The in-depth analysis and discussion of the achieved results are contained within the individual articles.

#### **4.1 Paper 1: Biodegradable porous FeMn (-xAg) alloys: Assessment of cytocompatibility, mechanical, magnetic and antibiofilm properties**

The first published and initial article focuses on the fabrication of porous FeMn(-xAg) alloys using powder metallurgy techniques. The research investigates the impact of porosity and the silver addition on the alloys' microstructure, biodegradability, as well as on magnetic and mechanical properties. Furthermore, the study delves into cytocompatibility, the inflammatory cytokine response, and the antibacterial/antibiofilm properties.

The resulting alloys exhibit macro- and nanoporous structures with evenly dispersed Ag particles in the FeMn matrix. The fabricated alloys have either a fully austenitic structure or consist of a mixture of austenite and martensite upon addition of 3 and 5 wt.% Ag. In terms of magnetic properties, the as-sintered alloys exhibit consistently low saturation magnetization values, unaffected by the immersion time, which is profitable for MRI imaging. The immersion tests, conducted up to 84 days in HBSS, revealed that the release of Mn is higher than that of Fe. The changes in the structure upon immersion were also observed and showed that the degradation layer forms on the surface, enriched in O, Ca, P and Cl.

Regarding biocompatibility, the alloys were proven to be non-cytotoxic. Moreover, the ions released by the FeMn(-xAg) alloys do not trigger inflammatory responses in macrophages. However, the incorporation of Ag slightly decreases cell proliferation, when compared to FeMn.

This study also investigated the interactions of fabricated alloys with *S.aureus* bacteria. Although no substantial differences in the bactericidal performance are observed between FeMn and FeMn-5Ag alloys, a considerable reduction in total biofilm biomass, encompassing both live and dead bacteria, is noted on the surfaces containing Ag.



# **Biodegradable porous FeMn (-xAg) alloys: Assessment of cytocompatibility, mechanical, magnetic and antibiofilm properties**

Aleksandra Bartkowska<sup>1</sup>, Oriol Careta<sup>2</sup>, Adam Turner<sup>3</sup>, Andreu Blanquer<sup>2</sup>, Elena Ibanez<sup>2</sup>, Margarita Trobos<sup>3</sup>, Carme Nogues<sup>2</sup>, Eva Pellicer<sup>1</sup>, Jordi Sort<sup>1,4</sup>

<sup>1</sup>Departament de Física, Universitat Autònoma de Barcelona, E-08193 Cerdanyola del Vallès, Spain

<sup>2</sup>Departament de Biologia Cel·lular, Fisiologia i Immunologia, Universitat Autònoma de Barcelona, E-08193 Cerdanyola del Vallès, Spain

<sup>3</sup>Department of Biomaterials, Institute of Clinical Sciences, Sahlgrenska Academy, University of Gothenburg, Gothenburg, Sweden

<sup>4</sup>Institució Catalana de Recerca i Estudis Avançats (ICREA), Pg. Lluís Companys 23, E-08010 Barcelona, Spain



## PAPER

[View Article Online](#)  
[View Journal](#) | [View Issue](#)Cite this: *Mater. Adv.*, 2023,  
4, 616**Biodegradable porous FeMn(–xAg) alloys:  
assessment of cytocompatibility, mechanical,  
magnetic and antibiofilm properties†**Aleksandra Bartkowska, <sup>a\*</sup> Oriol Careta, <sup>b</sup> Adam Benedict Turner, <sup>c</sup>  
Andreu Blanquer, <sup>b</sup> Elena Ibañez, <sup>b</sup> Margarita Trobos, <sup>c</sup> Carme Nogués, <sup>b</sup>  
Eva Pellicer <sup>a\*</sup> and Jordi Sort <sup>ad</sup>

In this work, porous FeMn(–xAg) alloys are fabricated through powder metallurgy methods. The effects of porosity and Ag addition on the microstructure, biodegradability, magnetic and mechanical properties of the alloys are investigated. Studies on the cytocompatibility, inflammatory cytokine response and anti-bacterial effect are also conducted. The fabricated alloys exhibit a macro- and nanoporous structure, with uniformly distributed silver particles. The biodegradability tests reveal that the release of Mn to the Hank's solution is higher than that of Fe, without significant differences between the alloys. The degradation products consist mainly of Fe, Mn, O and compounds enriched in Ca, P and Cl. As-sintered alloys show a low saturation magnetization value (below 1 emu g<sup>–1</sup>), which does not increase significantly with immersion time. The results on biocompatibility indicate that all tested alloys are non-cytotoxic, but the addition of Ag might interfere with cell proliferation. However, the ions released by the FeMn(–xAg) alloys do not induce an inflammatory response in macrophages. The obtained results on microbiological interactions reveal that although no significant bactericidal effect is observed at 4 h between FeMn control and FeMn–5Ag, a significant reduction in the total biofilm biomass of both live and dead bacteria is observed after 24 h in Ag containing FeMn–5Ag surfaces.

Received 16th August 2022,  
Accepted 1st December 2022

DOI: 10.1039/d2ma00867j

[rsc.li/materials-advances](https://rsc.li/materials-advances)

## 1 Introduction

In recent years, the application of biodegradable metals (BMs) and polymers as potential candidates for temporary medical implants has been of growing interest.<sup>1–6</sup> This class of materials is expected to corrode gradually *in vivo* once they have fulfilled their role.<sup>2,7</sup> Their main advantage is the possibility of avoiding the implant removal surgery, hence limiting the cost of medical treatment and decreasing the risk of infections, which is

increased during the revision surgery.<sup>8</sup> It has been shown that biodegradable materials are in general less prone to biomaterial-associated infections than non-degradable materials, most probably due to the degradation processes that reduce the area available for bacterial colonization and, therefore, the formation of biofilm.<sup>9</sup> Among various tested alloys, Mg-based and Fe-based alloys are especially attractive due to their very good biocompatibility.<sup>2,7</sup> Mg-based alloys show very low toxicity and their Young's modulus is close to that of the human bone. However, their degradation rate is too rapid for some applications, resulting in H<sub>2</sub> gas evolution and bubbling upon immersion. In addition, they are hard to process, and their strength and ductility are not satisfactory.

Over the past few years, increasing attention has been paid to Fe-based alloys as they show good processability, mechanical strength and low toxicity,<sup>10–13</sup> however, the degradation rate is too slow to be applied as biodegradable implants.<sup>7,14</sup> Moreover, Fe-based alloys tend to be ferromagnetic, which is undesirable for magnetic resonance imaging (MRI) purposes. Thus, several approaches to improve the degradation rate of Fe-based alloys are being explored, such as alloying with different elements (e.g., Mn),<sup>11,13,15</sup> using new fabrication methods to tune the microstructure such as selective laser melting (SLM),<sup>16,17</sup>

<sup>a</sup> Departament de Física, Universitat Autònoma de Barcelona, E-08193, Bellaterra (Cerdanyola del Vallès), Spain. E-mail: [aleksandra.bartkowska@uab.cat](mailto:aleksandra.bartkowska@uab.cat), [eva.pellicer@uab.cat](mailto:eva.pellicer@uab.cat)

<sup>b</sup> Departament de Biologia Cel·lular, Fisiologia i Immunologia, Universitat Autònoma de Barcelona, E-08193, Bellaterra (Cerdanyola del Vallès), Spain. E-mail: [elena.ibanez@uab.cat](mailto:elena.ibanez@uab.cat)

<sup>c</sup> Department of Biomaterials, Institute of Clinical Sciences, Sahlgrenska Academy, University of Gothenburg, Gothenburg, Sweden

<sup>d</sup> Institutió Catalana de Recerca i Estudis Avançats (ICREA), Pg. Lluís Companys 23, E-08010, Barcelona, Spain

† Electronic supplementary information (ESI) available: SEM images of powders and cold-pressed pellets, EDS mappings taken before and after incubation in HBSS solution, XRD patterns after incubation in HBSS, and number of live/dead cells grown on wells cultured with media conditioned. See DOI: <https://doi.org/10.1039/d2ma00867j>

introducing porosity,<sup>17–21</sup> adding small amounts of noble elements,<sup>22–25</sup> or adding C to promote twinning-induced plasticity (TWIP),<sup>7,26–28</sup> amongst others. The addition of elements such as Cu and Ag, which are more noble than Fe or Mn, is being investigated as a way of not only improving corrosion rates (through galvanic pairs) but also because they bring antimicrobial properties to the resulting alloys.<sup>22,25</sup> Powder metallurgy is especially appealing to introduce insoluble elements like Ag to the Fe–Mn matrix in a homogenous manner. However, the effect of adding Ag in terms of its role in the degradation rate remains still controversial: while most authors agree that Ag causes increased degradation rates of Fe-based alloys,<sup>22–24,29</sup> some studies report that Ag additions promote galvanic coupling only in the first stages of degradation and, after formation of the degradation layer, the Ag role is not being fulfilled anymore.<sup>27</sup> Similarly, one can find dissimilar conclusions on the effect of silver on antibacterial activity. In the report by Liu<sup>30</sup> no antimicrobial properties were confirmed in Fe70.3–Mn28.9–Ag0.8 alloy, while in the research published by Sotoudehbagha<sup>22</sup> antibacterial activity in the alloys containing 1 and 3 wt% of Ag was observed.

The main aim of this study is to fabricate and characterize porous Fe–Mn alloys with different additions of Ag in terms of their microstructure, mechanical and magnetic properties, degradation, biocompatibility and antibacterial activity. For this purpose, four different compositions have been investigated: equiatomic FeMn, and FeMn with 1, 3 and 5 wt% of silver. The relatively high content of Mn is proposed to ensure the non-magnetic character of the investigated alloys. Up to date, neither a long-term biodegradability test nor a study of the evolution of magnetic properties upon immersion has been performed in terms of ion release and degradation surface analysis for porous, Ag-containing equiatomic Fe–Mn alloys.

## 2 Materials and methods

### 2.1 Fabrication of alloys

Commercial powders of iron (97% purity, Merck, Germany), manganese ( $\geq 99\%$  purity, Merck, Germany) and silver ( $\geq 99.9\%$  purity, Merck, Germany) were used to prepare four types of samples: FeMn, FeMn–1Ag, FeMn–3Ag and FeMn–5Ag, where the ratio of Fe : Mn was adjusted to 50 : 50 (at%) and the additions of silver are given in wt% (1, 3 and 5 wt%, respectively). Mixtures of powders were alloyed using a planetary ball milling device (Pulverisette 5, Fritsch, Germany) under an Ar atmosphere at a rotation speed of 300 rpm, for 10 h and with a 10 : 1 ball-to-powder weight ratio. The procedure of weighing powders and sealing the container was conducted in a glove box under Ar atmosphere ( $\text{H}_2\text{O} < 0.1$  ppm,  $\text{O}_2 < 0.1$  ppm) to prevent oxidation and atmospheric contamination. The particle size of as-milled powders was measured using the ImageJ software (National Institutes of Health, USA) from scanning electron microscopy (SEM) images. After ball-milling, the powders were further refined in an agate mortar, to avoid leaving large agglomerates. Subsequently, as-prepared powders were uniaxially cold-pressed at 100 MPa to form

cylindrical green pellets (discs) of 10 mm diameter and 2–3 mm in thickness. The green pellets were then loaded in a vacuum furnace and sintered at 900 °C at  $5 \times 10^{-5}$  mbar for 4 h at a heating rate of 1 °C min<sup>−1</sup>. As Mn has a high vapor pressure, higher sintering temperatures and longer dwelling times might lead to significant losses of Mn content due to sublimation,<sup>18,31</sup> therefore the temperature was kept at 900 °C. Moreover, it has been shown that the losses of Mn in ball-milled powders are lower than in powders prepared using other methods.<sup>31</sup>

### 2.2 Structural characterization

The structural and compositional characterization of the fabricated materials was conducted using an SEM microscope (Zeiss Merlin, Zeiss, Germany) operated at 15 kV equipped with an energy-dispersive X-ray spectroscopy (EDS) detector. The phase compositions of ball-milled powders, sintered alloys and alloys after immersion in Hank's balanced salt solution (HBSS) were examined by X-ray diffraction (XRD, Panalytical X'Pert powder diffractometer, Malvern Panalytical, UK) using Cu K $\alpha$  radiation. The measurements were conducted in an angular range from 20° to 100° with a step size of 0.026° in the Bragg-Brentano geometry. The XRD results were analyzed using Rietveld refinement (MAUD software),<sup>32</sup> from which crystallite size and lattice parameters were determined. ImageJ software was used to assess the macroporosity of sintered alloys by analyzing the SEM images. Archimedes' method was used to determine the density of the specimens. Then, the porosity values were estimated by comparing the theoretical (*i.e.*, for the fully dense materials) and experimental densities, according to the formula (eqn (1)):

$$\% \text{ porosity} = \left( 1 - \frac{\text{density}_{\text{experimental}}}{\text{density}_{\text{theoretical}}} \right) \quad (1)$$

### 2.3 Biodegradability tests

Biodegradability tests were conducted by immersing samples of as-fabricated alloy pellets for various periods (7, 14, 28, 56, and 84 days) in HBSS at  $37.5 \pm 1$  °C. Each sample, with a surface area of approximately 100 mm<sup>2</sup>, was immersed in a container containing approximately 30 mL HBSS. The volume of the solution adhered to the ASTM G31-72(2004) standard, using a volume/surface area ratio of 0.3 mL mm<sup>−2</sup>. At least three replicas were prepared at each time point. The HBSS (H8264, Merck, Germany) is a popular physiological solution used to reproduce the conditions in the human body, which contains CaCl<sub>2</sub>, MgSO<sub>4</sub>, KCl, KH<sub>2</sub>PO<sub>4</sub>, NaHCO<sub>3</sub>, NaCl, Na<sub>2</sub>HPO<sub>4</sub> and glucose. After each period, 2 mL of solution from at least three replicas was taken for the ion release concentration analysis, which was conducted using inductively coupled plasma mass spectrometry (ICP-MS, Agilent 7900, Agilent, USA). Before the ICP-MS analysis, the aliquots were diluted with HNO<sub>3</sub>. Samples immersed for 14, 28, 56, and 84 days were withdrawn from the containers for structural analysis of corrosion products formed both on the surface and the cross-section of the pellets. XRD analysis was performed to identify the corrosion products formed on the surface of FeMn and FeMn–5Ag alloys after 7 and 28 days of immersion.



## 2.4 Characterization of mechanical and magnetic properties

The mechanical properties were studied using nanoindentation (Anton Paar NHT<sup>3</sup> nanoindenter, Anton Paar, Austria). Before indentation, the discs were polished to a mirror-like surface, with the final polishing step using 1 µm diamond particles paste. Maximum applied loads of 100 and 500 mN were used to assess the behaviour of the material during deformation. A series of at least 50 measurements were performed on each sample to obtain statistically significant data. The load-displacement curves were used to calculate the hardness ( $H_B$ ) and reduced Young's modulus ( $E_r$ ), using the method of Oliver and Pharr.<sup>33</sup> Apart from that, the elastic ( $W_{\text{elast}}$ ) and plastic ( $W_{\text{plast}}$ ) energies of deformation were obtained from the load-displacement curves by assessing the areas between the unloading curve and displacement axis ( $W_{\text{elast}}$ ) and between the loading and unloading curves ( $W_{\text{plast}}$ ). Finally, the elastic recovery was calculated as the ratio between elastic ( $W_{\text{elast}}$ ) and total ( $W_{\text{elast}} + W_{\text{plast}}$ ) energies during nanoindentation.

A vibrating sample magnetometer (VSM, MicroSense, USA) was used to analyze the magnetic properties of the samples before (as-fabricated) and after incubation in HBSS, at room temperature. The maximum applied magnetic field was 20 kOe. The results were normalized over sample weight to obtain the value of saturation magnetization ( $M_s$ ).

## 2.5 Cell proliferation assays and cytotoxicity tests

For cell proliferation and cytotoxicity experiments, human osteosarcoma Saos-2 cells (ATCC HTB-85) were used. Cells were maintained in Dulbecco's Modified Eagle Medium (DMEM) (Gibco, ThermoFisher Scientific, Waltham, MA, USA) supplemented with 10% fetal bovine serum (FBS; Gibco), under standard conditions (37 °C, 5% CO<sub>2</sub>).

Experiments were conducted in a medium conditioned in the presence of the different FeMn(-xAg) alloys. To prepare the conditioned media, the samples were sterilized with UV light for 3 min and incubated in 15 mL of supplemented DMEM under standard conditions for 7, 14, 28, and 56 days. Then, the alloys were removed, and the conditioned media were kept at 4 °C protected from light until used. In parallel, control media were also prepared following the same incubation times and conditions but without the presence of any alloy (aged media). Osteoblasts (Saos-2 cells) proliferation was determined using Alamar Blue cell viability Reagent (Thermo Fisher Scientific) before (day 0) and after (day 3) cells' exposure to the conditioned media. Briefly,  $5 \times 10^4$  cells were seeded into each well of a 24-well plate with fresh medium. Cells were cultured for 24 h to allow cell attachment, and then the medium was replaced with fresh medium with 10% Alamar Blue, and cells were incubated for 4 h in standard conditions in the dark. Then, the supernatant was collected (day 0), and the fluorescence was measured at 585 nm wavelength after excitation at 560 nm on a Spark multimode microplate reader (Tecan, Männedorf, Switzerland). After supernatant collection, FeMn(-xAg) conditioned media for different incubation times were added to each well. Cells were cultured for 3 more days in a conditioned medium and the

Alamar Blue assay was repeated according to the previously described protocol (day 3). Aged and fresh media were used as controls. Experiments were performed in triplicate.

Immediately after proliferation assays, cytotoxicity was assessed in cells incubated with media conditioned for 7 and 56 days using the live/dead viability/cytotoxicity kit for mammalian cells (Invitrogen), according to the manufacturer's protocol. Images from different regions of the well were captured using an Olympus IX71 inverted microscope equipped with epifluorescence.

## 2.6 Quantification of inflammatory cytokines secretion

THP-1 monocyte cells were used to analyze the potential immunological response induced by the FeMn(-xAg) alloys. Monocytes were grown in RPMI 1640 medium (Gibco) supplemented with 25% FBS (Gibco) under standard conditions. To differentiate monocytes into macrophages,  $4 \times 10^5$  THP-1 cells were seeded into 24-well plates and treated with 0.16 µM phorbol-12-myristate-13-acetate (Sigma-Aldrich, Saint Louis, MO, USA) for 72 h. Then, cells were washed and incubated in a fresh medium for 24 h before carrying out the experiments. The fresh medium was replaced by a conditioned RPMI medium (prepared as explained above) and macrophages were incubated for 5 h and 24 h to allow the secretion of inflammatory cytokines. As a positive control, 1 µg mL<sup>-1</sup> of lipopolysaccharide (LPS) (Sigma-Aldrich) was added to the macrophages culture. As a negative control, macrophages were cultured in a fresh medium. After 5 h and 24 h, supernatants were collected and used to quantify cytokine secretion. Inflammatory cytokines TNF-α, IL-1β and IL-6 were evaluated by flow cytometry using cytometric bead array (CBA) (Becton-Dickinson, East Rutherford, NJ, USA). Cytokine concentrations in the supernatant were analyzed according to the manufacturer's protocol. Negative control was considered as basal secretion level and used for statistical comparisons. Experiments were performed in triplicate.

## 2.7 Assessment of *S. aureus* adhesion and viability

From a frozen stock, *S. aureus* ATCC 25923 was streaked onto a 5% horse blood agar (HBA) plate (Media Department, Clinical Microbiology Laboratory, Sahlgrenska University Hospital, Sweden) and incubated at 37 °C overnight. After incubation, colonies were taken and inoculated into 4 mL tryptic soy broth (TSB) (Scharlau, Barcelona, Spain) to achieve an OD<sub>546</sub> of 0.13, equivalent to 10<sup>8</sup> CFU mL<sup>-1</sup>, which was diluted 1:1000 into 40 mL of TSB to achieve a suspension of 10<sup>5</sup> CFU mL<sup>-1</sup>. One mL of this suspension was then added to each well of a 48-well plate (Nunc Delta-surface; Thermo Fisher Scientific, Waltham, USA) containing 9 mm diameter discs with the test surface (FeMn-5Ag) and controls of FeMn or Ti (Christers Finmekaniska AB, Skövde, Sweden). The discs were then incubated statically at 37 °C for 4 or 24 h to assess bacterial adhesion and biofilm formation as well as bacterial viability.

After each incubation period, each disc was rinsed three times in sterile 0.9% saline to remove non-adhered bacteria. Discs were then stained using LIVE/DEAD<sup>TM</sup> BacLight<sup>TM</sup> Bacterial



Viability Kit, for microscopy & quantitative assays (Invitrogen, Waltham, USA) following the manufacturer's instructions. The discs were rinsed three times to remove any unbound stain and fluorescence was assessed in a plate reader (FluostarOmega, BMG LABTECH, Ortenberg, Germany) and confocal laser-scanning microscope (Nikon C2+, Nikon, Tokyo, Japan) with a 100 $\times$  water dipping objective (CFI Plan 100XC W). Five z-stacks were taken at randomly chosen fields of view on each sample and images were taken at 3  $\mu$ m intervals through the biofilm layers. Biofilm thickness and biomass were analyzed in BiofilmQ.<sup>34</sup> From the plate reader, the average fluorescence intensity of each well scan was taken as the representative live/dead distribution for each disc. Experiments were performed in triplicate with duplicate material samples.

## 2.8 Statistical analysis

All quantitative data were analyzed with GraphPad Prism 9 (GraphPad Software Inc., San Diego, CA, USA) and presented as the mean  $\pm$  standard error of the mean. Statistical differences were assessed by one-way analysis of variance (ANOVA) with a Bonferroni correction for cytocompatibility and inflammatory response analyses and with Fisher's least significant difference post-test for microbiological analyses. A value of  $p < 0.05$  was considered significant.

# 3 Results and discussion

## 3.1 Microstructure and compositional analysis

**3.1.1 Morphology and phase composition of as-sintered alloys.** The SEM images of the initial and ball-milled powders are presented in Fig. S1 (ESI<sup>†</sup>). The initial particle size was less than 50  $\mu$ m for the initial Fe, Mn, and Ag powders. The sizes of the ball-milled powders were in the range of 1–40  $\mu$ m. Fig. 1 shows the XRD patterns of the powders ball-milled for 10 h (Fig. 1a) and the as-sintered FeMn, FeMn-1Ag, FeMn-3Ag and FeMn-5Ag alloys (Fig. 1b). The ball-milled powders have an austenitic structure, which is in accordance with the Fe–Mn phase diagram for this Mn content.<sup>35</sup> XRD patterns of ball-milled powders show wide peaks and a crystallite size which

decreases with increasing the Ag content. Crystallite sizes are 14, 14, 13 and 10 nm for the FeMn, FeMn-1Ag, FeMn-3Ag, FeMn-5Ag, respectively. The lattice constant increases upon the addition of Ag, showing values of 3.625 Å for FeMn, 3.630 Å for FeMn-1Ag, 3.633 Å for FeMn-3Ag and 3.637 Å for FeMn-5Ag.

The FeMn and FeMn-1Ag sintered alloys maintain the austenitic structure, while FeMn-3Ag and FeMn-5Ag alloys consist of a duplex structure, comprising  $\gamma$ -austenite (fcc structure) and  $\epsilon$ -martensite phase (hcp structure). The occurrence of the martensite phase was not expected as alloys containing above 27.3 at% of Mn are known to be mainly austenitic.<sup>13</sup> This phase transition could be caused by the occurrence of discrete inhomogeneities in the element distribution, forming regions of lower Mn content and thus promoting the martensitic transformation. This phenomenon was already observed before by Zhang,<sup>21</sup> but the explanation of martensitic transformation under furnace cooling conditions was not given. In this case, the martensitic transformation could be further enhanced by the presence of Ag. Nevertheless, both  $\gamma$ -austenite and  $\epsilon$ -martensite phases are antiferromagnetic, therefore the occurrence of the martensitic phase should not interfere with MRI. A shift in the diffraction peaks towards higher  $2\theta$  angles is observed in the sintered alloys with higher Ag contents. The crystallite size of the alloys subjected to sintering increases when compared to as-milled powders, and values of 38, 39, 18 and 13 nm for FeMn, FeMn-1Ag, FeMn-3Ag and FeMn-5Ag, respectively, are obtained. Therefore, as in the case of powders, the addition of silver is leading to a decrease in the crystallite size. A peak of low intensity can be observed at  $2\theta = 35^\circ$ , which was attributed to Fe<sub>2</sub>O<sub>3</sub>. The occurrence of the Fe<sub>2</sub>O<sub>3</sub> phase was observed in other studies<sup>35</sup> and it originates from the sintering method, which is always connected with some level of oxidation. Nevertheless, Fe<sub>2</sub>O<sub>3</sub> is also biocompatible,<sup>37,38</sup> therefore its presence should not compromise the biocompatibility of the tested alloys.

Fig. 2 shows SEM micrographs of the morphology of sintered (a–c) FeMn, (d–f) FeMn-1Ag, (g–i) FeMn-3Ag and (j–l) FeMn-5Ag alloys. The SEM images under various magnifications were analyzed using ImageJ software and the % area of macro-porosity and the size of pores were calculated. Manganese is foreseen to diffuse into the iron matrix during sintering and

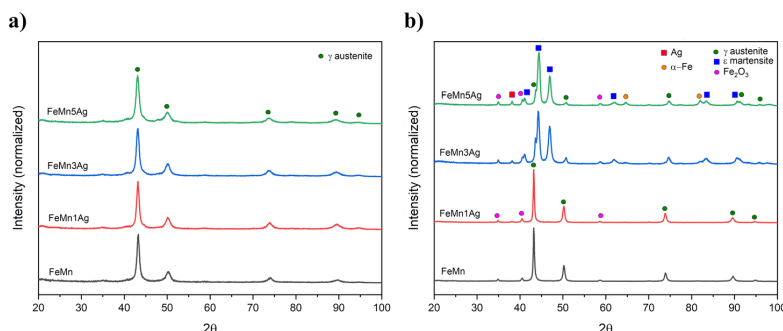


Fig. 1 XRD patterns of (a) ball-milled powders and (b) sintered FeMn(–xAg) alloys.



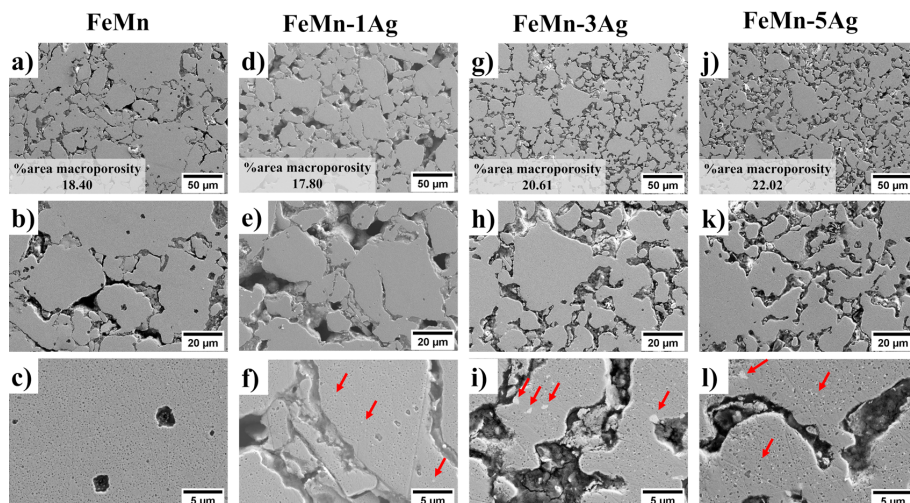


Fig. 2 SEM micrographs of sintered and surface-polished samples of FeMn (a–c), FeMn–1Ag (d–f), FeMn–3Ag (g–i) and FeMn–5Ag (j–l) samples. The % area macroporosity was determined using ImageJ by analyzing SEM images of the regions of macroporosity. The unlabeled red arrows provide reference for the Ag particles.

create a solid solution, while silver may form non-soluble precipitates in the FeMn matrix, as the solubility of Ag in Fe is very low.<sup>39,40</sup> The morphologies of the green pellets, *i.e.* pressed powders before sintering, are shown in Fig. S2 (ESI<sup>†</sup>). All tested alloys show a similar initial porosity in the range of 19–26%, as calculated using ImageJ based on SEM images. The process of sintering typically creates some additional level of porosity resulting from the rearranging of Fe and Mn, *i.e.*, voids are left behind by the metals upon diffusion. Another factor causing porosity is the change in the crystalline structure from bcc-Fe and bcc-Mn to fcc- $\gamma$  (FeMn) and hcp- $\epsilon$  (FeMn). This porosity is expected to have a beneficial impact on the proliferation of cells within the pores and, what is more, it can also improve the degradation rate due to an increased surface area exposed to the bodily environment.<sup>18,41</sup> In the tested materials, two different levels of porosity can be distinguished – namely macroporosity with an average pore size of around 10  $\mu\text{m}$  – and nanoporosity with a pore size of around 100 nm, as presented in Fig. 2(c, f, i and l). The calculated levels of total porosity are presented in Table 1, which shows that porosity increases with Ag content. While the addition of only 1 wt% of Ag does not cause a significant decrease in the density, the addition of 3 and 5 wt% of Ag leads to a higher total porosity (above 30%). This phenomenon is attributed mainly to the

decreased compressibility due to the presence of non-alloyed silver particles in the ball-milled powder.<sup>42</sup>

Silver particles are uniformly distributed within the Fe–Mn matrix, as indicated by red arrows in Fig. 2. To further analyze the distribution of Ag precipitates in the Fe–Mn matrix, EDS compositional maps, presented in Fig. S3 and S4 (ESI<sup>†</sup>), show that Ag precipitates exhibit a polydisperse distribution within a size range of 0.5–3  $\mu\text{m}$ . Larger agglomerates of Ag were observed, particularly in the FeMn–5Ag sintered alloy, as shown in Fig. S4b (ESI<sup>†</sup>). The presence of Ag-rich precipitates could in principle enhance the micro galvanic corrosion, hence inducing faster degradation rate of tested alloys.<sup>22–24</sup>

EDS compositional analysis of the samples furnished the weight percentage of individual elements, as listed in Table 1. The amounts of Ag are close to the nominal values (1, 3 and 5 wt%), while the weight percentages of Fe and Mn are slightly different from the nominal equiatomic composition (50.5 wt% Fe and 49.6 wt% Mn), with a lower amount of Mn than the initial value. Manganese is an element very prone to sublimation under high temperatures;<sup>39</sup> therefore it may be assumed that partial sublimation of Mn occurred, lowering its final amount.

**3.1.2 Surface morphology and chemical composition upon immersion.** The changes in surface morphology of FeMn and

Table 1 Actual chemical composition, macroporosity, density, and total porosity of sintered alloys. Total porosity accounts for both macro- and nanopores. Macroporosity was estimated from ImageJ software processing of SEM images, whereas the total porosity was determined by the Archimedes method

Sample	wt% Fe	wt% Mn	wt% Ag	Macro-porosity (% area)	Density ( $\text{g cm}^{-3}$ )	Total porosity (%)
FeMn	54.3	45.7	0	$18.39 \pm 3.00$	$5.50 \pm 0.16$	$28.2 \pm 2.1$
FeMn–1Ag	56.7	42.0	1.3	$17.80 \pm 1.54$	$5.38 \pm 0.11$	$30.1 \pm 1.4$
FeMn–3Ag	54.9	42.5	2.6	$20.61 \pm 1.34$	$4.94 \pm 0.04$	$36.3 \pm 0.5$
FeMn–5Ag	54.5	41.1	4.4	$22.02 \pm 0.30$	$4.87 \pm 0.12$	$37.7 \pm 0.6$





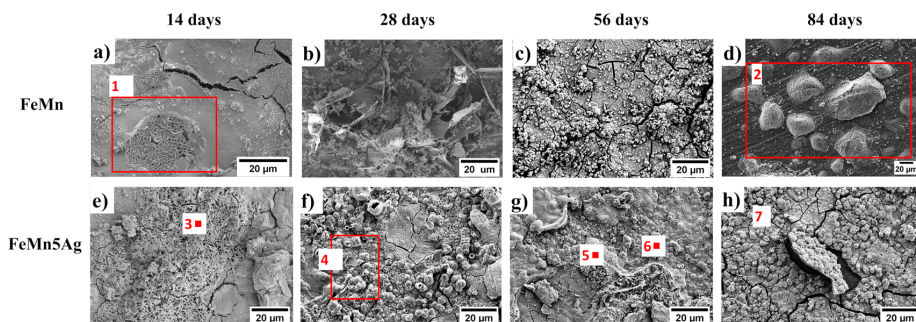


Fig. 3 Top-view SEM images of the degraded surface of FeMn (a–d) and FeMn–5Ag (e–h) incubated for 14 (a and e), 28 (b and f), 56 (c and g) and 84 (d and h) days in HBSS. (EDS analysis on the highlighted areas and locations is presented in Table 2).

FeMn–5Ag alloy upon immersion are presented in Fig. 3. The degradation process of the alloys led to the formation of a degradation layer. The EDS analyses, performed on the areas highlighted in Fig. 3 and summarized in Table 2, reveal that the degradation layer consists not only of Fe, Mn, and O, but also degradation products enriched in Cl, P and Ca, which are elements present in the HBSS, show up. Silver was not detected on the degradation surface, which suggests that it is not prone to be released during incubation in HBSS. In the first stages of degradation, namely after 14 days of immersion the corrosion products formed on the surface are enriched in Ca–P clusters, forming a flaky structure that could be identified as calcium phosphate-based apatite. These clusters tend to disappear at longer immersion periods, being replaced by different corrosion products.

The globular precipitates, shown in Fig. 3f and h mainly consist of O, Mn, Ca and P. Increasing immersion period leads to the formation of a relatively thick oxidation layer, as shown in Fig. 3c and h. Even though the layer has the appearance of compact and homogenous, more detailed analysis (Fig. 3c) reveals a cracked structure caused most probably by dehydration due to air-drying after removal from HBSS.<sup>44,45</sup> The cracked oxide layer is prone to detachment, as shown in Fig. 3h. After detachment, the exposed area allowed HBSS to penetrate further into the pores. As shown in Table 2, the degradation layer of samples incubated for 84 days (Fig. 3d and h) contains high levels of Cl<sup>−</sup>, namely 12.89 and 15.4 wt% for FeMn and FeMn–5Ag, respectively. The Cl<sup>−</sup> ions are aggressive to the surface of

the alloy and they can break the passive oxidation layer, therefore leading to the formation of the pits.<sup>2,23,46</sup> As can be seen in Fig. 3d, Cl-rich precipitates have formed on the exposed surface of FeMn alloys, most probably after Cl<sup>−</sup> ions have broken the oxide layer.

To gain further insight into the degradation products formed on the surfaces upon immersion, XRD analysis was performed on the FeMn and FeMn–5Ag samples after 7 and 28 days of immersion, as presented in Fig. S5 (ESI<sup>†</sup>). The XRD patterns obtained after 7 days did not demonstrate any additional features compared with the as-prepared samples (Fig. 1b). This can be explained by the thin nature of the oxide layer as well as the less abundant presence of other corrosion products. However, after 28 days of immersion, an increase in the intensity of some of the peaks was observed. Corrosion products such as MnPO<sub>4</sub>, MnCO<sub>3</sub>, Fe<sub>2</sub>O<sub>3</sub> and MnO were identified. It is worth noting that some of the oxide peaks can overlap, therefore we might expect more corrosion products on the surface.

To unveil the degradation mechanism, cross-sections of all tested alloys immersed for 14, 28, 56 and 84 days in HBSS were examined (Fig. 4). One can observe the formation of a degradation layer at the utmost sample surface, which is particularly visible in the samples immersed for 14 and 28 days, with a thickness of around 30 μm. This layer was presumably cracked due to dehydration upon air drying or during the curing of the mounting resin, as mentioned before.<sup>11,27</sup> Remarkably, this layer becomes thinner or even disappear for longer immersion periods.

At the same time, an increase of the incubation period favors higher penetration of the HBSS towards the bulk of the material since the HBSS is able to permeate through the open-pore structure of the pellets. As a result, corrosion products formed inside the pores, mainly consisting of iron and manganese oxides, as shown in Fig. S6 (ESI<sup>†</sup>). Brighter contrast (due to charging) is associated with low-conducting corrosion products made of O, Ca, P and Cl. When comparing individual alloys, the degradation layer of Ag-containing alloys seems to be thinner after 56 and 84 days of immersion than that of FeMn. Nevertheless, at the same time, the corrosion products consist mainly of metal hydroxides and carbonates, accompanied by calcium, phosphorus

Table 2 Chemical composition of areas and points indicated in Fig. 3 as measured by EDS

Area/point		Elements (wt%)					
		Fe	Mn	O	Cl	P	Ca
FeMn	1	34.6	22.5	38.3	0.5	3.1	1.0
	2	19.3	20.1	30.9	12.9	8.4	8.4
FeMn–5Ag	3	23.4	—	68.9	0.5	3.8	3.4
	4	12.5	22.3	38.3	—	8.8	18.2
	5	40.5	27.1	31.1	1.4	—	—
	6	27.9	21.1	42.2	0.8	5.8	2.2
	7	6.3	42.9	25.1	15.4	—	10.4



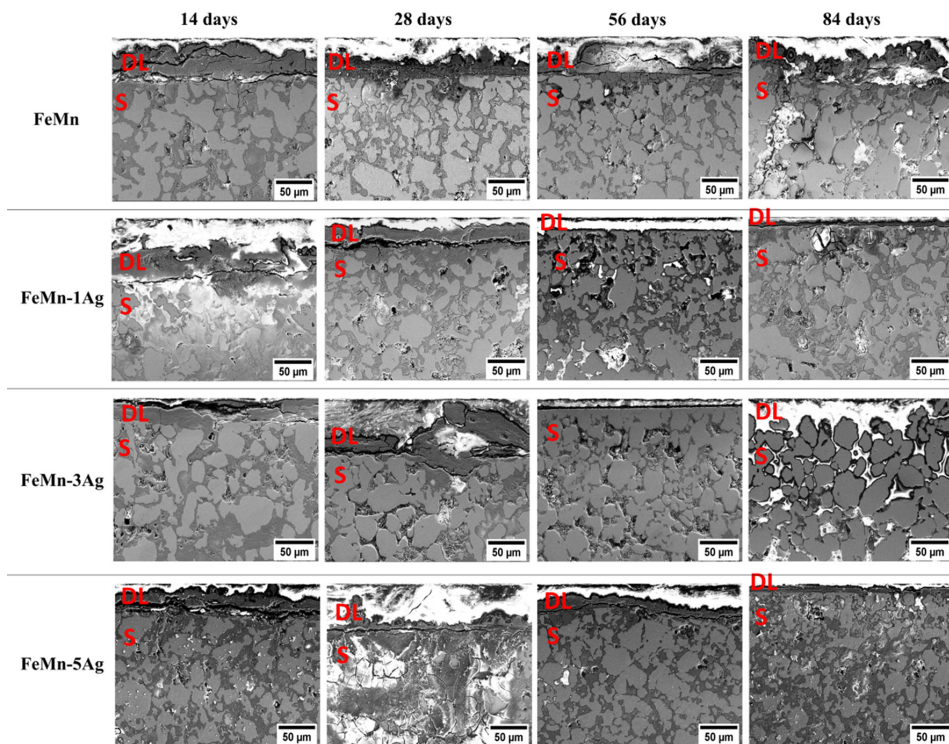


Fig. 4 Cross-section SEM images of FeMn, FeMn-1Ag, FeMn-3Ag and FeMn-5Ag specimens after 14, 28, 56 and 84 days of immersion in HBSS. 'S' stands for sample and 'DL' to the degradation layer formed on top of the sample.

and chlorine elements, as mentioned before.<sup>11,20,47</sup> The amount of Cl is notably higher in the Ag-containing alloys which can be attributed to localized pitting. Since porosity increases with Ag content, the Cl-rich corrosion products are accumulated inside the pores to a larger extent in samples with higher Ag wt%.

The EDS compositional maps of the cross-sections of the alloys immersed for 84 days, presented in Fig. S6 (ESI<sup>†</sup>), show the distribution of Fe and Mn alloying elements as well as of foreign elements that have accumulated inside the pores. Fe and Mn are uniformly distributed in the matrix, but the upper degradation layer shows a lower concentration of those elements than the bulk. The abundant presence of oxygen was observed, both in the degradation layer and the sample, mostly inside the pores. Other elements, such as Ca, Cl and P, were also present, mostly in the degradation layer. The EDS analyses performed in the degradation layer show that its Mn content is lower than that of Fe. For example, in the case of FeMn-5Ag, the content of Fe was around 4–5 times higher than the content of Mn (33.3 wt% of Fe and 8.5 wt% of Mn after 14 days of immersion, and 51.7 wt% of Fe and 11.1 wt% of Mn after 84 days of immersion). This suggests that the release of Mn ions to the HBSS occurs easier than the release of Fe ions.

**3.1.3 Released ion concentration.** It has been shown before that addition of noble elements, such as Pt and Pd,<sup>15,28,42</sup> to the

Fe–Mn matrix can lead to the formation of micro galvanic cells that can cause an accelerated corrosion rate. Additions of Ag particles into the Fe-based alloys have also been tested, but so far mixed results have been reported in the literature. Most of the studies have shown an enhanced corrosion rate<sup>22–24</sup> but a neutral effect has also been observed,<sup>26,27</sup> as well as a decrease in corrosion rate in Fe–Ag alloys.<sup>48</sup> Silver has a more positive standard corrosion potential compared to Fe and Mn, hence it can be assumed that during corrosion the Fe–Mn matrix acts as an anode, and it is therefore oxidized, while the Ag particles act as a cathode and thus accept electrons.<sup>23,30</sup> Another possible mechanism to explain the role of Ag in the acceleration of the corrosion rate is that during corrosion of the Fe–Mn matrix, the Ag particles will form a separate phase, which has the ability to break the Fe oxide layers.<sup>23,43</sup>

The concentration of Fe and Mn ions released from the materials into the HBSS after 7, 14, 28, 56 and 84 days of immersion is presented in Fig. 5a and b. It can be observed that Mn release is higher than Fe release for all tested alloys and that the ion concentration increases with the immersion time, which is in agreement with the previously shown EDS results. Mn is more prone to be released due to a lower standard corrosion potential when compared with Fe (*i.e.*, Mn<sup>2+</sup> ions are more susceptible to be released to the HBSS than Fe<sup>2+</sup> or Fe<sup>3+</sup>).



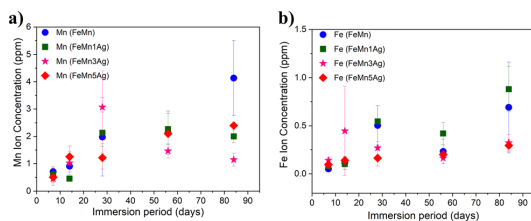


Fig. 5 Concentration of (a) Mn and (b) Fe ions released into the HBSS at different immersion periods as measured with ICP-MS. Please note the different Y-axis scale in panels of Mn (a) and Fe (b) release.

In the first stage, up to 28 days of immersion, a sharp increase in the release is observed, especially in the case of Mn for all tested specimens and it tends to slow down upon further immersion. Nevertheless, an increase in both Mn and Fe release after 84 days of immersion is observed in the case of FeMn and FeMn-5Ag, as well as an increase of Fe release of the FeMn-1Ag sample.

However, no significant differences in the amounts of released ions were observed between the tested alloys. The silver-containing alloys did not show an increase in the ion release of either Fe or Mn when compared to the alloy without Ag. Similar behavior has already been observed in literature with Fe-Mn-C-xAg alloy.<sup>26,27</sup> Apparently, Ag had a negligible influence on the biodegradability of the material. Although Ag could in principle induce microgalvanic corrosion in contact with the less noble FeMn environment, the amounts of leached Fe and Mn ions in FeMn and FeMn-5Ag, as determined by ICP, were similar. This suggests that other effects, likely the porosity, play a major role.

The trend in the curve's shape of the ion concentration indicated a linear dependence up to 28 days and then a more stable increase during a longer immersion period. It can be mainly attributed to the degradation products formed on the surface that are partially blocking the dissolution of Fe and Mn at longer immersion periods. Due to the same reason, the corrosion rate does not increase with the immersion time for the Ag-containing alloys, as the release of silver is being blocked by corrosion products formed on the surface and inside the pores. Nevertheless, the release of silver was also measured, and it was 3 orders-of-magnitude lower than the release of Fe and Mn. Namely, the highest Ag release was observed for the FeMn-5Ag and was  $1.23 \pm 0.21 \mu\text{g L}^{-1}$  after 14 days of immersion, then it decreased to  $0.88 \pm 0.22 \mu\text{g L}^{-1}$  after 56 days of immersion and again increased up to  $6.35 \pm 3.65 \mu\text{g L}^{-1}$  after 84 days in HBSS. In the FeMn-1Ag and FeMn-3Ag, the highest concentration of Ag was also observed after 84 days of immersion and was  $1.65 \pm 0.55 \mu\text{g L}^{-1}$  and  $1.3 \pm 0.34 \mu\text{g L}^{-1}$ , respectively. Thus, as could be suspected, the release of Ag ions increases with the initial Ag content. The increased amount of Ag released after 84 days of immersion, when compared with the amount released after 56 days, can be connected with the increased amounts of Cl-rich precipitates on the degradation surface that can contribute to breaking the degradation layer and, hence, enabling further degradation.

A previous study reported that Fe-Mn alloys (Fe35Mn and Fe25Mn), obtained through powder sintering and cold rolling

and resintering cycles, released around 1.5 ppm and 2 ppm for Mn and Fe ions after 84 days of immersion, respectively.<sup>11</sup> In another report, FeMnSiPd alloys obtained through arc melting,<sup>15</sup> released around 1.5 ppm for both elements up to 120 days of immersion. The release of ions in our tested alloys was higher, presumably due to the higher level of porosity, which enhances the degradation.

### 3.2 Magnetic properties

The magnetic behavior of as-sintered and immersed alloys is presented in Fig. 6a-d. The as-sintered alloys (Fig. 6a) show very low saturation magnetization, with values of 0.019, 0.199, 0.626 and  $1.077 \text{ emu g}^{-1}$  for FeMn, FeMn-1Ag, FeMn-3Ag and FeMn-5Ag, respectively. For comparison, the value of saturation magnetization ( $M_s$ ) of the 304 austenitic stainless steel SS304, commonly used as implant material is  $1.25 \text{ emu g}^{-1}$ .<sup>36,49</sup> On the other hand, the  $M_s$  value of pure iron is as high as  $221.7 \text{ emu g}^{-1}$ .<sup>50</sup> This means that the FeMn-5Ag alloy, which has the highest value of  $M_s$  among the tested alloys, has only 0.49% the magnetization of Fe. In fact, the Fe-based alloys with manganese content above 30 wt% have been reported to be antiferromagnetic as they consist mainly of antiferromagnetic  $\gamma$ -austenite and  $\epsilon$ -martensite phases,<sup>51,52</sup> therefore enhancing the materials' compatibility with MRI imaging. In our case, the  $M_s$  value increased with higher Ag content, which might be attributed to slightly higher porosity of those alloys (which in turn could lead to higher amount of  $\text{Fe}_2\text{O}_3$  after sintering).<sup>53,54</sup>

Following immersion in HBSS, the magnetization of FeMn progressively increased with the immersion time, as shown in Fig. 6c. The alloys incubated for 84 days (Fig. 6b) showed a  $M_s$  value of 2.301, 1.249, 0.0367 and  $0.396 \text{ emu g}^{-1}$  for FeMn, FeMn-1Ag, FeMn-3Ag and FeMn-5Ag, respectively. When comparing the gradual differences in the magnetic properties upon increasing immersion time, a similar trend was noticed in the FeMn alloy – the lowest value of magnetization is shown by the as-sintered material and it increased gradually – after 14 and 28 days the value was similar, around  $0.690 \text{ emu g}^{-1}$ , with an increase up to  $2.290 \text{ emu g}^{-1}$  after 3 months of immersion. This observation can be ascribed to a higher release of Mn than Fe ions, which leads to a higher level of Fe-enriched regions in the material than before immersion. On the contrary, in the case of the FeMn-5Ag, an increase of the incubation time led to a small decrease in the  $M_s$  values, starting from  $1.077 \text{ emu g}^{-1}$  for as-sintered alloy and then decreasing, firstly to around  $0.550 \text{ emu g}^{-1}$  after 14 days of immersion and then to a minimum value of  $0.393 \text{ emu g}^{-1}$  after 3 months of immersion. In any case, even though the  $M_s$  values change upon degradation, the level of  $M_s$  is sufficiently low to assure good compatibility of the alloys with MRI.

### 3.3 Mechanical properties

Nanoindentation was used to analyze the micro/nano-mechanical properties of the tested alloys. The tests were conducted under two different maximum loads, namely 100 and 500 mN. The lower load was used to extract information from the nanoporous regions of the material, while the higher loads may be able to assess the





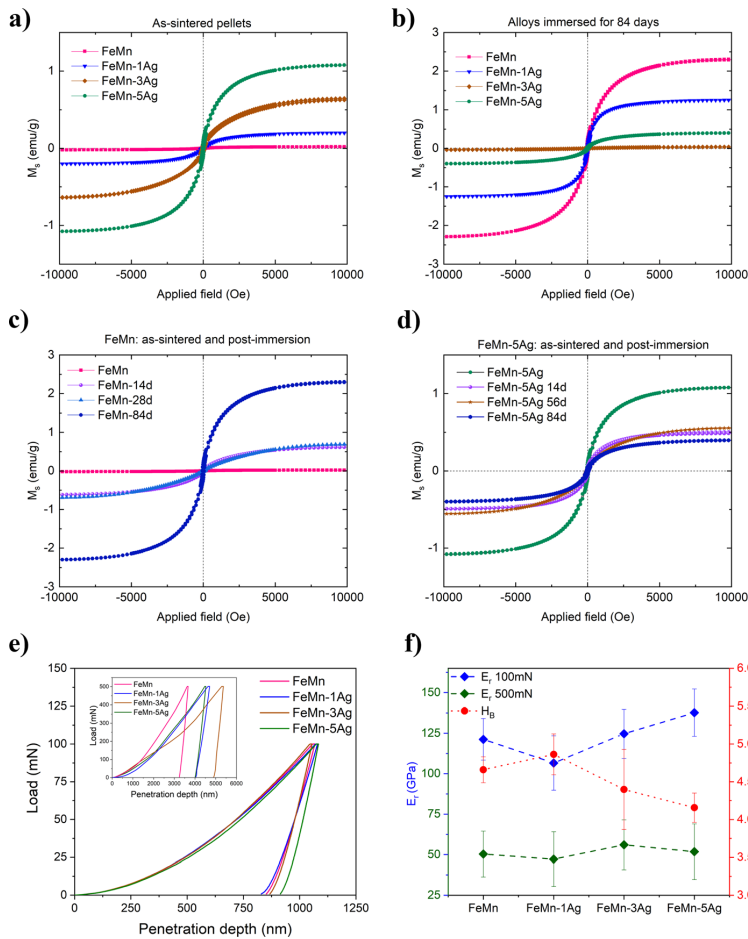


Fig. 6 Magnetization curves (a–d) for (a) as-sintered samples, (b) alloys after immersion in HBSS for 84 days, and detailed changes of magnetization upon immersion for different periods for (c) FeMn and (d) FeMn–5Ag. Load-displacement curves (e) of the FeMn–xAg alloys under 100 and 500 mN (insert) maximum applied loads, and (f) corresponding reduced Young's modulus ( $E_r$ ) under 100 mN (blue) and 500 mN (green) of maximum applied loads, together with hardness ( $H_B$ ) (red). Please note the different Y-axis scales between the panels.

influence of both levels of porosity (macro and nano) on the reduced Young's modulus ( $E_r$ ) and hardness ( $H_B$ ). Representative load-displacement curves of tested alloys, together with calculated values of  $E_r$  and  $H_B$  are presented in Fig. 6e, f and Table 3, respectively. The load-displacement curves (Fig. 6e) show higher variability under higher load, which is mainly due to different levels of macroporosity among the tested alloys. On the other

hand, the curves obtained under 100 mN of maximum load almost overlap and the resulting values of  $E_r$  are more similar among the various samples, as shown in Fig. 6f. The nanoindentation tests conducted under a maximum applied load of 500 mN show that the alloys have a comparable value of  $E_r$ , around 50 GPa, which is relatively close to that of a human bone (cortical bone has Young's modulus value of around 20 GPa).<sup>55</sup> The

Table 3 Values of Young's modulus ( $E_r$ ), hardness ( $H_B$ ),  $H_B/E_r$  ratio and energies of deformation ( $W_{\text{elast}}/W_{\text{total}}$  and  $W_{\text{plast}}/W_{\text{total}}$ ) for FeMn, FeMn–1Ag, FeMn–3Ag and FeMn–5Ag alloys

Sample	$E_r$ (500 mN) GPa	$E_r$ (100 mN) GPa	$H_B$ (GPa)	$H_B/E_r$ (wear resistance)	$W_{\text{elast}}/W_{\text{total}}$	$W_{\text{plast}}/W_{\text{total}}$
FeMn	50.39 ± 14.16	121.24 ± 12.84	4.66 ± 0.17	0.038 ± 0.003	0.22 ± 0.03	0.78 ± 0.03
FeMn–1Ag	47.24 ± 16.86	106.60 ± 16.82	4.86 ± 0.27	0.046 ± 0.008	0.26 ± 0.04	0.74 ± 0.03
FeMn–3Ag	56.09 ± 15.36	124.65 ± 15.13	4.40 ± 0.53	0.035 ± 0.006	0.20 ± 0.03	0.80 ± 0.10
FeMn–5Ag	51.81 ± 17.13	137.67 ± 14.58	4.16 ± 0.19	0.030 ± 0.003	0.18 ± 0.02	0.82 ± 0.04

average value of hardness performed under 500 mN was 1.48 GPa for FeMn, 1.2 GPa for FeMn-3Ag and 1.14 GPa for FeMn-5Ag.

To understand the mechanical properties of the alloys, the results obtained under lower load (100 mN) were used to further calculate  $H_B$ ,  $E_r$ ,  $H_B/E_r$  ratio and energies of deformation, as presented in Table 3. The FeMn-1Ag alloy had the highest hardness and the lowest Young's modulus among all tested alloys, while the FeMn-5Ag had the lowest  $H_B$  and the highest  $E_r$ . The hardness values of all tested alloys are above 4 GPa, which is similar to that of fully dense Fe30Mn6Si1Pd.<sup>15</sup> The values of hardness increase upon small additions of Ag and decrease at higher Ag amounts. As silver does not form an alloy with the Fe-Mn system and stays in a form of precipitates whose hardness is lower than the Fe-Mn matrix, the overall hardness of the material might be lower. The other factor influencing hardness values is the level of porosity (which increases with the Ag content), tending to reduce  $H_B$ .

The  $H_B/E_r$  ratio is an indirect estimation of wear resistance. It has been shown that wear resistance is dependent on the hardness ( $H_B$ ) and the reciprocal value of elastic modulus ( $E_r$ ),<sup>56,57</sup> thus the highest  $H_B/E_r$  ratio of FeMn-1Ag alloys indicates the highest wear resistance for this composition. In Table 3, the ratios of the elastic ( $W_{\text{elast}}$ ) and plastic ( $W_{\text{plast}}$ ) energies *versus* the total ( $W_{\text{total}}$ ) energy of deformation during nanoindentation are presented. All tested alloys demonstrate a higher contribution of plastic energy in the total energy of deformation. It is shown that the contribution of elastic energy is higher for the FeMn-1Ag alloy than for the other alloys, meaning that it possesses a slightly higher elastic recovery, which indicates the ability of the material to recover the initial shape after deformation.

Contrarily, the FeMn-5Ag alloy shows higher contribution of  $W_{\text{plast}}$  to the total energy of deformation. The so-called 'plasticity index' indicates higher plasticity of this alloy when compared to FeMn, FeMn-1Ag and FeMn-3Ag counterparts.

### 3.4 Cytocompatibility of FeMn-(xAg) alloys

To assess the alloys' cytocompatibility, two different analyses were performed *in vitro*: cell proliferation and cytotoxicity. Whilst cell proliferation analysis allows to assess whether cells incubated with conditioned media can proliferate (*i.e.*, increase their number over time), cytotoxicity analysis can determine whether the ions released by the alloys produce a toxic effect (*i.e.*, a decrease in the number of live cells over time).

First, we tried to perform direct cytocompatibility analyses, by growing the cells directly on the surface of the alloys. We observed that the cells did not adhere properly to the alloys (data not shown), probably due to morphological changes that the surface of the alloys experienced upon immersion (see Fig. 3 and 4). It has been described that Fe-based alloys show a relatively high corrosion and degradation rate that preclude cell adhesion.<sup>18</sup> Hence, in order to analyze the effect of the alloys and of the ions released into the medium, we proceeded with the indirect cytocompatibility analyses, by culturing the cells in alloy-conditioned media.

In these experiments, two different control media were used: fresh media prepared just prior the experiment and media that were maintained in the incubator for the same time periods as the conditioned ones (aged medium; see Section 2.5).

We decided to include this aged medium as a control because we reasoned that the medium and serum components could degrade over time during the conditioning of the media with the alloys. Indeed, when comparing cell proliferation in both types of control media, we observed a significant decrease in Saos-2 cells proliferation when the cells were cultured in the 28 and 56 days aged media, the difference being higher in the last timepoint (Fig. 7). It is known that growth factors and other proteins degrade when stored at room temperature or 37 °C. Each protein has a different degradation rate but, to our knowledge, no research studies on serum degradation over time and its effect on cell proliferation have been published. However, the FBS information for users recommends to store the product at -10 to -40 °C, and not to use FBS stored at 2 to 8 °C for more than 4 weeks (Freezing and Thawing FBS and Other Sera). Because of the differences found in cell proliferation when using the two types of control media, the effect of the different conditioned media on cell proliferation was only compared with their corresponding aged medium.

At day 0 (after one day in culture in fresh medium), the intensity of the signal obtained was similar among all samples of the same conditioned time group, with no significant differences (Fig. 7). After 3 days in culture in the conditioned media, cell viability significantly increased in 7 and 14 days conditioned media, regardless of the alloy composition (Fig. 7a and b), meaning that cells were able to proliferate. Nevertheless, cells cultured in the aged control medium showed a higher proliferation rate than in any of the alloys conditioned media tested. Some significant differences were found when comparing all conditioned media: cells cultured in FeMn-3Ag conditioned medium showed the highest proliferation rate among the 7 days conditioned media, and cells cultured in FeMn-5Ag conditioned medium showed the lowest proliferation rate among the 14 days conditioned media (Fig. 7a and b).

After 28 and 56 days of medium conditioning or aging, cell proliferation was similar between conditioned and aged media and among conditioned media, except for a significant decrease in the FeMn-5Ag conditioned medium compared with FeMn-3Ag at 28 days and with FeMn at 56 days (Fig. 7c and d).

Next, the live/dead assay was used to determine the cytotoxicity of the alloy-conditioned media. As shown in Fig. S7 (ESI<sup>†</sup>), the number of cells grown on wells cultured with media conditioned for 7 days with Fe-Mn, FeMn-1Ag, FeMn-3Ag and FeMn-5Ag was similar (A-D), but lower than the number of cells on wells cultured with the aged and the fresh control media (E and F). However, the number of cells grown on wells cultured with medium conditioned for 56 days was much lower. Specifically, cell numbers seemed to decrease as the silver percentage in the alloy increased (G-J). The number of cells growing in culture with the 56 days aged medium was also low (K), whereas cells cultured with fresh media appeared to be in monolayer and in a higher number (L). The number of live cells



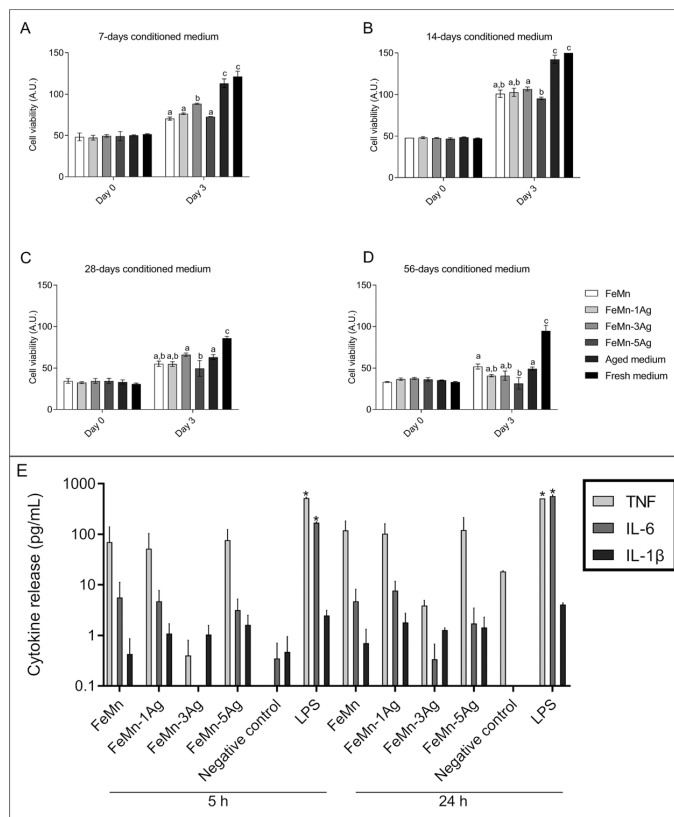


Fig. 7 Cell proliferation of Saos-2 cells before (day 0) and after (day 3) culture with media conditioned for 7 (A), 14 (B), 28 (C) and 56 (D) days with FeMn, FeMn-1Ag, FeMn-3Ag and FeMn-5Ag alloys, measured by Alamar Blue fluorescence. Aged medium, consisting of DMEM medium incubated for the same incubation times and conditions but without any alloy, and fresh medium were used as controls. Bars with different alphabetical superscripts are significantly different from each other ( $p < 0.05$ ), whereas bars with the same alphabetical superscripts are not significantly different from each other. (E) Logarithmic representation of cytokine release by macrophages exposed to 56 days FeMn(-Ag) conditioned media. Secretion was analyzed by the CBA test at 5 and 24 h of culture. LPS: Lipopolysaccharide, positive control. Asterisks above the columns indicate significant differences compared with the negative control.

was higher than 90% in all cases. These results are in agreement with Alamar Blue results, and suggest that, while FeMn(-xAg) materials might interfere with cell proliferation, they are not cytotoxic.

The cytotoxicity of biodegradable metallic alloys is mainly attributed to the released degradation particles<sup>58</sup> and metallic ions<sup>13</sup> which can promote or inhibit both cell proliferation and metabolic activities. In addition, the corrosion of porous alloys can produce a general change in pH and osmolarity that can contribute to a decrease in the cell viability. The results obtained showed that media conditioned with the FeMn-5Ag alloy reduced cell proliferation compared with the other alloys containing less amount of Ag, indicating that certain amount of silver can alter cell proliferation. In fact, the FeMn-5Ag alloy was the one with the highest Ag release after 84 days in Hank's solution ( $6.35 \mu\text{g L}^{-1}$ ).

The effect of Ag on cell viability is controversial and depends on the state of the Ag, *i.e.* whether Ag is present in the culture as

a salt, as nanoparticles, or as part of the alloy. In our case, Ag was incorporated within the FeMn matrix in the form of particles during the fabrication step.

It has been shown that the metal salt  $\text{AgNO}_3$  produces a high cytotoxic effect in mammalian cell cultures,<sup>59,60</sup> with an  $\text{IC}_{50}$  of  $\text{AgNO}_3$  in the range of  $2\text{--}11 \mu\text{M}$  ( $300\text{--}1900 \mu\text{g L}^{-1}$ ) depending on the cell type.<sup>61</sup> On the other hand, studies using nanoparticles concluded that  $6 \mu\text{M}$  silver nanoparticles do not have a significant impact on cytotoxicity of epithelial cells.<sup>62</sup> Similar results were observed specifically using osteoblasts, as the presence of silver nanoparticles coating-alloys did not induce any cytotoxic effect on MG63 osteoblasts.<sup>63,64</sup>

Our results showed values at the  $0.88\text{--}6.35 \mu\text{g L}^{-1}$  range of Ag released from the alloys. The highest values observed for FeMn-5Ag after 84 days were far from the concentrations considered cytotoxic. In this regard, our cytotoxic results are in agreement with those of previous studies (viability higher

than 90%). However, the cell proliferation rate was reduced when osteoblasts were cultured in the presence of the alloy-conditioned media. After culture with 7 and 14 days conditioned medium, a decrease in cell proliferation was observed regardless of the alloy, which indicates that not only Ag can interfere with the cell cycle. The presence of Fe and Mn ions, or the relatively high corrosion rate could be responsible for the reduced proliferation rate. The high corrosion rate could increase the pH and osmolality, as previously observed.<sup>65</sup> The release of Ag from the FeMn-5Ag after 28 and 56 of media conditioning could also contribute to the lowest cell proliferation observed.

### 3.5 Inflammatory cytokine response

To find out whether the ions released by alloys activate the secretion of inflammatory cytokines, 56 days conditioned medium was added to macrophage cultures. We analyzed the pro-inflammatory cytokines IL-1 $\beta$ , IL-6 and TNF, which are commonly produced by macrophages in response to bacterial endotoxin or LPS.<sup>66</sup> According to Chanput *et al.*, stimulating THP-1 macrophages with LPS results in a dramatic increase in the secretion of IL-1 $\beta$ , IL-6, and TNF, which reaches a plateau after 18 h of stimulation.<sup>67</sup>

Results of the CBA showed that ions released by FeMn(-xAg) alloys did not activate the secretion of IL-1 $\beta$ , IL-6 or TNF in macrophages when compared with a non-stimulated control. However, when macrophages were exposed to LPS (positive control), an increase in the concentration of the three cytokines was detected in the culture medium, even though IL-1 $\beta$  increase was not statistically significant (Fig. 7e). Ubanako *et al.* also obtained the same results when using low amounts of LPS to stimulate THP-1 derived macrophages, that is, little or

no secretion of IL-1 $\beta$ , IL-6 and TNF.<sup>68</sup> It has been reported that the presence of metal debris and even low concentrations of metal ions can induce an inflammatory response.<sup>69</sup> In this regard, it has been observed that the release of Fe, Mn and Ag could induce the secretion of inflammatory cytokines; Fe and Mn are considered no allergenic elements, although Ag is.<sup>70</sup> However, the results obtained for cytokine release indicated that concentrations lower than 0.5 mg L<sup>-1</sup> of Fe, 2.3 mg L<sup>-1</sup> of Mn and 0.9  $\mu$ g L<sup>-1</sup> of Ag did not induce the inflammatory response in macrophages.

### 3.6 Microbial interactions with FeMn(-xAg)

In this investigation, the effect of FeMn and FeMn-5Ag alloys on *S. aureus* viability and biofilm formation was tested. The addition of silver was tested due to its widely known antimicrobial capacity.<sup>71,72</sup> Biofilm biomass and thickness were assessed using confocal laser-scanning microscopy (CLSM) (Fig. 8A–D) and fluorescence plate reading (Fig. 8E–H) after 4 and 24 h of growth. Moreover, representative images of the biofilm formed on FeMn and FeMn-5Ag, obtained using CLSM are shown (Fig. 8I and J).

When comparing the FeMn-5Ag to the FeMn material, whilst no significant difference in biofilm viability was observed at 4 h, a significant reduction in the total live and dead biomass was observed at the 24 h time point (Fig. 8A and B). Importantly, the total biofilm thickness on FeMn-5Ag was directly comparable to that of the titanium control (Fig. 8C and D), known for its biocompatibility in bone-implant applications, showing analogous performance of the FeMn-5Ag materials.

According to the fluorescence plate reading data, at 4 h the total biofilm viability was unaffected by the alloying of 5% silver compared to FeMn (Fig. 8E and F). A reduction in biofilm

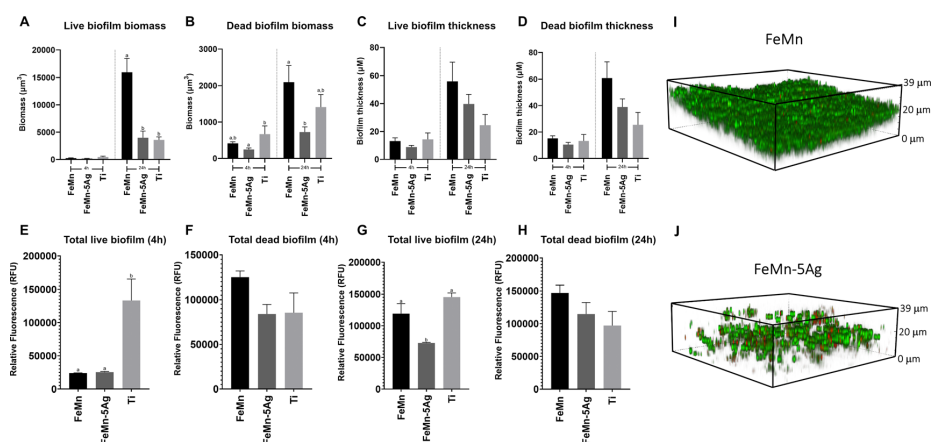


**Fig. 8** *Staphylococcus aureus* ATCC 25923 biofilm morphology on FeMn-5Ag compared to FeMn and machined titanium (Ti) controls after 4 and 24 h incubation, analysed using quantitative confocal laser-scanning microscopy (CLSM) to assess biofilm biomass (A and B) and thickness (C and D). Fluorescence intensity of total live and dead cells in biofilms grown for 4 h (E and F) and 24 h (G and H) on FeMn-5Ag, FeMn and Ti using fluorescence plate reading. Bars with different alphabetical superscripts are significantly different from each other ( $p < 0.05$ ), whereas values with the same alphabetical superscripts are not significantly different from each other. CLSM images of the biofilm formed on the surface of FeMn (I) and FeMn-5Ag (J) alloys (NIS-Elements Viewer, Nikon). Green: Live *S. aureus* cells; Red: Dead *S. aureus* cells.



biomass on FeMn–5Ag compared to FeMn was also observed through fluorescent plate reading at 24 h for live (Fig. 8G) but not for dead (Fig. 8H) bacteria.

The current state of the literature regarding the addition of silver into FeMn alloys as a potential antimicrobial agent is disputed and dissimilar conclusions have been reported.<sup>21,29</sup> The unchanged bacterial viability observed here by the addition of silver to FeMn is in agreement with certain literature,<sup>29</sup> in which no reduction in *S. aureus* viability was observed after incubation with similar silver containing materials. With the concentrations of silver observed in the release assays undertaken in this study, it is likely that the total level of released silver into the culture medium was below the threshold for achieving a significant bactericidal effect.

Therefore, rather than a direct bactericidal activity of Ag, these results show that the FeMn–5Ag material may influence biofilm formation in *S. aureus*. The observed reduction in total biofilm biomass adhered to the FeMn–5Ag surface after 24 h is, to our knowledge, a novel finding (Fig. 8A and B). The potential mechanism for this is unknown but it could be related to the degradability of the bulk material, as seen in Fig. 3 and 4. By limiting the solid surface to which bacteria can adhere to, the ability for biofilm to form may be reduced, a concept also proposed by Daghighi *et al.*<sup>9</sup>

## 4 Conclusions

In this study, porous FeMn alloys with additions of Ag were fabricated through a powder metallurgy route. An in-depth study of the influence of porosity and Ag additions on the microstructure, biodegradability, degradation surface, magnetic and mechanical properties, has been undertaken. Furthermore, studies on cytocompatibility, inflammatory cell response and bacterial interactions have been conducted. The results revealed that:

(a) FeMn and FeMn–1Ag sintered alloys consist mainly of a  $\gamma$ -austenite phase, while FeMn–3Ag and FeMn–5Ag alloys consist of a duplex structure, comprising  $\gamma$ -austenite (fcc structure) and  $\epsilon$ -martensite phase (hcp structure).

(b) The alloys have a porous structure, consisting both of macro- and nanoporosity, with the total level of porosity varying from 28% for FeMn alloy up to 37% for FeMn–5Ag alloy.

(c) The biodegradability experiments, performed in HBSS up to 84 days of immersion, reveal that the release of Mn is higher than the release of Fe, which was attributed to a lower standard corrosion potential of Mn when compared to Fe. The degradation surface changes over time, with corrosion products consisting of Fe, Mn, O and enriched in Ca, P and Cl are present.

(d) The saturation magnetization value of FeMn alloys slightly increases with immersion time, with the highest  $M_s$  value after 84 days of immersion. Nevertheless, the  $M_s$  value even after 84 days is sufficiently low not to interfere with MRI imaging.

(e) No significant differences in the mechanical properties of the different alloys are observed, although the addition of 3% and 5% Ag tends to increase the Young's modulus and the plasticity index.

(f) The cytocompatibility experiments performed using conditioned media revealed that the investigated alloys are non-cytotoxic. Although Ag-containing alloys have shown to be cytocompatible, their cell proliferation is lower than that of FeMn.

(g) The inflammatory cell response experiment, conducted using media conditioned for 56 days, shows that the ions released by FeMn(–xAg) alloys do not induce an inflammatory response in macrophages *in vitro*.

(h) The viability and biofilm formation of *Staphylococcus aureus* with FeMn(–xAg) alloys were tested. The obtained results reveal that whilst no significant increase in bacterial killing is observed at 4 h between the FeMn and the FeMn–5Ag samples, a significant reduction in biofilm biomass of both live and dead cell populations is observed at 24 h.

(i) Overall, these results indicate a potential for a novel material that achieves identical performance compared to the current state of the art, whilst reducing early bacterial adhesion and biofilm formation.

## Author contributions

A. Bartkowska: conceptualization; investigation; data curation; formal analysis; validation, visualization; writing – original draft. O. Careta: investigation; data curation; formal analysis; validation; visualization; writing – original draft. A. Turner: investigation; data curation; formal analysis; validation, visualization; writing – original draft. A. Blanquer: conceptualization; investigation; writing – review & editing; E. Ibáñez: conceptualization; methodology resources; supervision; writing – review & editing. M. Trobos: conceptualization; methodology; resources; supervision; writing – review & editing; funding acquisition C. Nogués: conceptualization; methodology; resources; supervision; writing – review & editing; project administration. E. Pellicer: conceptualization; methodology; resources; supervision; writing – review & editing; project administration. J. Sort: conceptualization; methodology; resources; supervision; writing – review & editing; project administration; funding acquisition.

## Conflicts of interest

There are no conflicts to declare.

## Acknowledgements

This project has received funding from the European Union's Horizon 2020 research and innovation programme under the Marie Skłodowska-Curie grant agreement No. 861046 ('Bioremia' European Training Network), the Spanish Ministry of Economy, Industry and Competitiveness (Grant PID2020-116844RB-C21), the Generalitat de Catalunya (2017-SGR-0292 and 2017-SGR-503), the Swedish Research Council (2022-00853), the Swedish state under the agreement between the Swedish Government and the county councils, the ALF-agreement (ALFGBG-978896), the IngaBritt and Arne Lundberg Foundation (LU2021-0048); the Hjalmar



Svensson Foundation, the Doctor Felix Neuberghs Foundation, and the Adlerbertska Foundation. The authors would like to thank the staff from the Servei de Microscòpia of Universitat Autònoma de Barcelona.

## Notes and references

- 1 Y. Liu, Y. Zheng, X. H. Chen, J. A. Yang, H. Pan, D. Chen, L. Wang, J. Zhang, D. Zhu, S. Wu, K. W. K. Yeung, R. C. Zeng, Y. Han and S. Guan, *Adv. Funct. Mater.*, 2019, **29**, 1–21.
- 2 Y. F. Zheng, X. N. Gu and F. Witte, *Mater. Sci. Eng., R*, 2014, **77**, 1–34.
- 3 H. Li, Y. Zheng and L. Qin, *Prog. Nat. Sci.: Mater. Int.*, 2014, **24**, 414–422.
- 4 J. Cheng, B. Liu, Y. H. Wu and Y. F. Zheng, *J. Mater. Sci. Technol.*, 2013, **29**, 619–627.
- 5 M. Moravej and D. Mantovani, *Int. J. Mol. Sci.*, 2011, **12**, 4250–4270.
- 6 S. Ganguly, S. Mondal, P. Das, P. Bhawal, P. Prasanna Maity, S. Ghosh, S. Dhara and N. C. Das, *Int. J. Biol. Macromol.*, 2018, **111**, 983–998.
- 7 J. Venezuela and M. S. Dargusch, *Curr. Opin. Solid State Mater. Sci.*, 2020, **24**, 100822.
- 8 H. J. Busscher, H. C. van der Mei, G. Subbiahdoss, P. C. Jutte, J. J. A. M. van den Dungen, S. A. J. Zaat, M. J. Schultz and D. W. Grainger, *Sci. Transl. Med.*, 2012, **4**, 153rv10.
- 9 S. Daghighi, J. Sjollem, H. C. van der Mei, H. J. Busscher and E. T. J. Rochford, *Biomaterials*, 2013, **34**, 8013–8017.
- 10 J. He, F. L. He, D. W. Li, Y. L. Liu, Y. Y. Liu, Y. J. Ye and D. C. Yin, *RSC Adv.*, 2016, **6**, 112819–112838.
- 11 H. Hermawan, A. Purnama, D. Dube, J. Couet and D. Mantovani, *Acta Biomater.*, 2010, **6**, 1852–1860.
- 12 R. Gorejová, L. Haverová, R. Oriňáková, A. Oriňák and M. Oriňák, *J. Mater. Sci.*, 2019, **54**, 1913–1947.
- 13 H. Hermawan, D. Dubé and D. Mantovani, *J. Biomed. Mater. Res., Part A*, 2010, **93**, 1–11.
- 14 M. Peuster, C. Hesse, T. Schloo, C. Fink, P. Beerbaum and C. von Schnakenburg, *Biomaterials*, 2006, **27**, 4955–4962.
- 15 Y. P. Feng, A. Blanquer, J. Fornell, H. Zhang, P. Solsona, M. D. Baró, S. Suriñach, E. Ibáñez, E. García-Lecina, X. Wei, R. Li, L. Barrios, E. Pellicer, C. Nogués and J. Sort, *J. Mater. Chem. B*, 2016, **4**, 6402–6412.
- 16 D. T. Chou, D. Wells, D. Hong, B. Lee, H. Kuhn and P. N. Kumta, *Acta Biomater.*, 2013, **9**, 8593–8603.
- 17 P. Liu, D. Zhang, Y. Dai, J. Lin, Y. Li and C. Wen, *Acta Biomater.*, 2020, **114**, 485–496.
- 18 Y. P. Feng, N. Gaztelumendi, J. Fornell, H. Y. Zhang, P. Solsona, M. D. Baró, S. Suriñach, E. Ibáñez, L. Barrios, E. Pellicer, C. Nogués and J. Sort, *J. Alloys Compd.*, 2017, **724**, 1046–1056.
- 19 M. Heiden, E. Nauman and L. Stanciu, *Adv. Healthcare Mater.*, 2017, **6**, 1700120.
- 20 S. M. Huang, E. A. Nauman and L. A. Stanciu, *Mater. Sci. Eng., C*, 2019, **99**, 1048–1057.
- 21 Q. Zhang and P. Cao, *Mater. Chem. Phys.*, 2015, **163**, 394–401.
- 22 P. Sotoudehbagha, S. Sheibani, M. Khakbiz, S. Ebrahimi-Barough and H. Hermawan, *Mater. Sci. Eng., C*, 2018, **88**, 88–94.
- 23 P. S. Bagha, M. Khakbiz, S. Sheibani, S. Ebrahimi-Barough, H. Hermawan, P. Sotoudeh Bagha, M. Khakbiz, S. Sheibani, S. Ebrahimi-Barough and H. Hermawan, *ACS Biomater. Sci. Eng.*, 2020, **6**, 2094–2106.
- 24 P. Sotoudeh Bagha, M. Khakbiz, S. Sheibani and H. Hermawan, *J. Alloys Compd.*, 2018, **767**, 955–965.
- 25 Z. Ma, M. Gao, D. Na, Y. Li, L. Tan and K. Yang, *Mater. Sci. Eng., C*, 2019, **103**, 109718.
- 26 S. Loffredo, C. Paternoster, N. Giguère, M. Vedani and D. Mantovani, *JOM*, 2020, **72**, 1892–1901.
- 27 S. Loffredo, S. Gambaro, L. Marin De Andrade, C. Paternoster, R. Casati, N. Giguère, M. Vedani and D. Mantovani, *ACS Biomater. Sci. Eng.*, 2021, **7**, 3669–3682.
- 28 M. Schinhammer, P. Steiger, F. Moszner, J. F. Löffler and P. J. Uggowitzer, *Mater. Sci. Eng., C*, 2013, **33**, 1882–1893.
- 29 M. S. Dargusch, J. Venezuela, A. Dehghan-Manshadi, S. Johnston, N. Yang, K. Mardon, C. Lau and R. Allavena, *Adv. Healthcare Mater.*, 2021, **10**, 2000667.
- 30 R. Y. Liu, R. G. He, L. Q. Xu and S. F. Guo, *Acta Metall. Sin.*, 2018, **31**, 584–590.
- 31 Z. Xu, M. A. Hodgson and P. Cao, *J. Mater. Res.*, 2017, **32**, 644–655.
- 32 L. Lutterotti, *Nucl. Instrum. Methods Phys. Res., Sect. B*, 2010, **268**, 334–340.
- 33 W. C. Oliver and G. M. Pharr, *J. Mater. Res.*, 1992, **7**, 1564–1583.
- 34 R. Hartmann, H. Jeckel, E. Jelli, P. K. Singh, S. Vaidya, M. Bayer, D. K. H. Rode, L. Vidakovic, F. Díaz-Pascual, J. C. N. Fong, A. Dragoš, O. Lamprecht, J. G. Thöming, N. Netter, S. Häussler, C. D. Nadell, V. Sourjik, Á. T. Kovács, F. H. Yildiz and K. Drescher, *Nat. Microbiol.*, 2021, **6**, 151–156.
- 35 W. Huang, *Calphad*, 1989, **13**, 243–252.
- 36 M. S. Dargusch, A. Dehghan-Manshadi, M. Shahbazi, J. Venezuela, X. Tran, J. Song, N. Liu, C. Xu, Q. Ye and C. Wen, *ACS Biomater. Sci. Eng.*, 2019, **5**, 1686–1702.
- 37 C. R. Ou, C. I. Shen and C. M. Ou, *J. Supercond. Novel Magn.*, 2010, **23**, 1197–1199.
- 38 M. Bhushan, D. Mohapatra, Y. Kumar and A. Kasi Viswanath, *Mater. Sci. Eng. B*, 2021, **268**, 115119.
- 39 L. J. Swartzendruber, *Bull. Alloy Phase Diagrams*, 1984, **5**, 560–564.
- 40 C. G. Fink and V. S. de Marchi, *Trans. Electrochem. Soc.*, 1938, **74**, 271.
- 41 A. H. Yusop, A. A. Bakir, N. A. Shaharom, M. R. Abdul Kadir and H. Hermawan, *Int. J. Biomater.*, 2012, **2012**, 641430.
- 42 C. Tonna, C. Wang, D. Mei, S. V. Lamaka, M. L. Zheludkevich and J. Buhagiar, *Bioact. Mater.*, 2022, **7**, 426–440.
- 43 A. Šalák and M. Selecká, Alloying and sintering of manganese steels in terms of high manganese vapour pressure, in: *Manganese in Powder Metallurgy Steels*, Cambridge International Science Publishing Ltd; 2012, pp. 22–38.





- 44 E. Mouzou, C. Paternoster, R. Tolouei, A. Purnama, P. Chevallier, D. Dubé, F. Prima and D. Mantovani, *Mater. Sci. Eng., C*, 2016, **61**, 564–573.
- 45 M. Moravej, A. Purnama, M. Fiset, J. Couet and D. Mantovani, *Acta Biomater.*, 2010, **6**, 1843–1851.
- 46 Y. Xin, K. Huo, H. Tao, G. Tang and P. K. Chu, *Acta Biomater.*, 2008, **4**, 2008–2015.
- 47 J. Čapek, J. Kubásek, D. Vojtěch, E. Jablonská, J. Lipov and T. Ruml, *Mater. Sci. Eng., C*, 2016, **58**, 900–908.
- 48 J. Čapek, K. Stehliková, A. Michalcová, Š. Msallamová and D. Vojtěch, *Mater. Chem. Phys.*, 2016, **181**, 501–511.
- 49 J. Childress, S. H. Liou and C. L. Chien, *J. Appl. Phys.*, 1998, **64**, 6059.
- 50 H. Danan, A. Herr and A. J. P. Meyer, *J. Appl. Phys.*, 2008, **39**, 669.
- 51 Y. Ishikawa and Y. Endoh, *J. Appl. Phys.*, 2003, **39**, 1318.
- 52 S. Cotes, M. Sade and A. F. Guillermet, *Metall. Mater. Trans. A*, 1995, **26**, 1957–1969.
- 53 M. Tadic, M. Panjan, V. Damjanovic and I. Milosevic, *Appl. Surf. Sci.*, 2014, **320**, 183–187.
- 54 D. Cao, H. Li, L. Pan, J. Li, X. Wang, P. Jing and X. Cheng, *Sci. Rep.*, 2016, **6**, 1–9.
- 55 J. Y. Rho, R. B. Ashman and C. H. Turner, *J. Biomech.*, 1993, **26**, 111–119.
- 56 A. Leyland and A. Matthews, *Wear*, 2000, **246**, 1–11.
- 57 E. Pellicer, S. Pané, K. M. Sivaraman, O. Ergeneman, S. Suriñach, M. D. Baró, B. J. Nelson and J. Sort, *Mater. Chem. Phys.*, 2011, **130**, 1380–1386.
- 58 X. Gu, Y. Zheng, Y. Cheng, S. Zhong and T. Xi, *Biomaterials*, 2009, **30**, 484–498.
- 59 G. Schmalz, D. Arenholt-Bindslev, S. Pfüller and H. Schweikl, *Altern. Lab. Anim.*, 1997, **25**, 323–330.
- 60 A. Yamamoto, R. Honma and M. Sumita, *J. Biomed. Mater. Res.*, 1998, **39**, 331–340.
- 61 D. Tie, F. Feyerabend, W. D. Müller, R. Schade, K. Liefelth, K. U. Kainer and R. Willumeit, *Eur. Cells Mater.*, 2012, **25**, 284–298.
- 62 C. M. Santoro, N. L. Duchsherer and D. W. Grainger, *Nano-biotechnology*, 2007, **3**, 55–65.
- 63 P. Jabłoński, M. Hebda, P. Pytlak, A. Kyzioł, H. Krawiec, Z. Grzesik and K. Kyzioł, *Mater. Chem. Phys.*, 2020, **248**, 122931.
- 64 K. Kleszcz, M. Hebda, A. Kyzioł, H. Krawiec and K. Kyzioł, *Appl. Surf. Sci.*, 2021, **557**, 149795.
- 65 J. Fischer, D. Pröfrock, N. Hort, R. Willumeit and F. Feyerabend, *Mater. Sci. Eng., B*, 2011, **176**, 830–834.
- 66 L. D. Hazlett, *Prog. Retinal Eye Res.*, 2004, **23**, 1–30.
- 67 W. Chanput, J. Mes, R. A. M. Vreeburg, H. F. J. Savelkoul and H. J. Wichers, *Food Funct.*, 2010, **1**, 254–261.
- 68 P. Ubanako, N. Xelwa and M. Ntwasa, *PLoS One*, 2019, **14**, e0222614.
- 69 J. C. Wataha, J. B. Lewis, K. R. Volkmann, P. E. Lockwood, F. L. W. Messer and S. Bouillaguet, *J. Biomed. Mater. Res., Part B*, 2004, **69**, 11–17.
- 70 A. Biesiekierski, J. Wang, M. Abdel-Hady Gepreel and C. Wen, *Acta Biomater.*, 2012, **8**, 1661–1669.
- 71 A. B. Lansdown, *J. Wound Care*, 2013, **11**, 125–130.
- 72 S. Subhadarshini, R. Singh, A. Mandal, S. Roy, S. Mandal, S. Mallik, D. K. Goswami, A. K. Das and N. C. Das, *Langmuir*, 2021, **37**, 9356–9370.



## Supplementary information

### **Biodegradable porous FeMn(-xAg) alloys: assessment of cytocompatibility, mechanical, magnetic and antibiofilm properties**

Aleksandra Bartkowska,<sup>a</sup> Oriol Careta,<sup>b</sup> Adam Benedict Turner,<sup>c</sup> Andreu Blanquer,<sup>b</sup> Elena Ibañez,<sup>b</sup> Margarita Trobos,<sup>c</sup> Carme Nogués,<sup>b</sup> Eva Pellicer,<sup>a</sup> and Jordi Sort<sup>a,d</sup>

<sup>a</sup>Departament de Física, Universitat Autònoma de Barcelona, E-08193 Cerdanyola del Vallès, Spain

<sup>b</sup>Departament de Biologia Cel·lular, Fisiologia i Immunologia, Universitat Autònoma de Barcelona, E-08193 Cerdanyola del Vallès, Spain

<sup>c</sup>Department of Biomaterials, Institute of Clinical Sciences, Sahlgrenska Academy, University of Gothenburg, Gothenburg, Sweden

<sup>d</sup>Institució Catalana de Recerca i Estudis Avançats (ICREA), Pg. Lluís Companys 23, E-08010 Barcelona, Spain



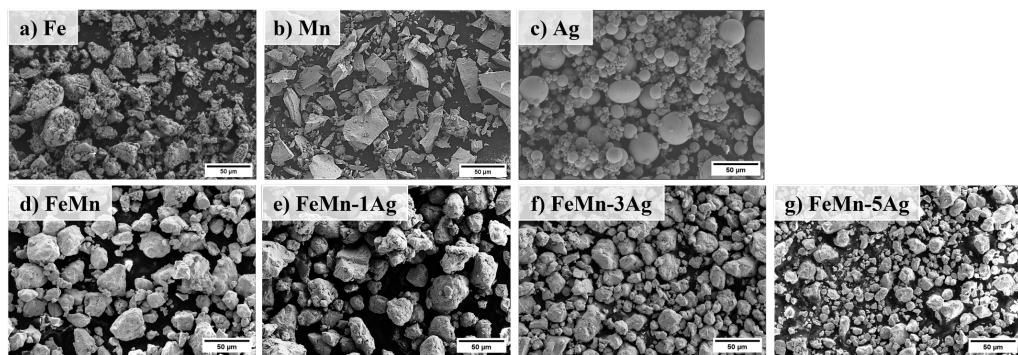


**Fig. S1** SEM images of initial powders of Fe (a), Mn (b) and Ag (c) and of ball-milled FeMn (d), FeMn-1Ag (e), FeMn-3Ag (f) and FeMn-5Ag (g) powders.

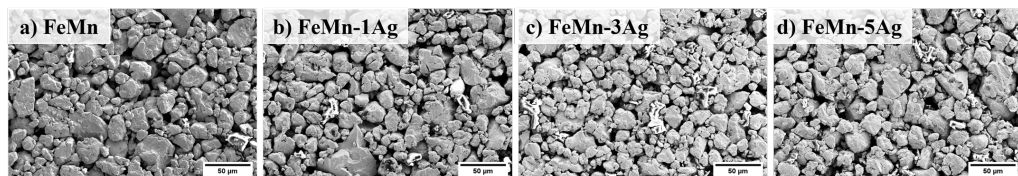


**Fig. S2** SEM images depicting the morphology of cold-pressed pellets of FeMn (a), FeMn-1Ag (b), FeMn-3Ag (c) and FeMn-5Ag (d).

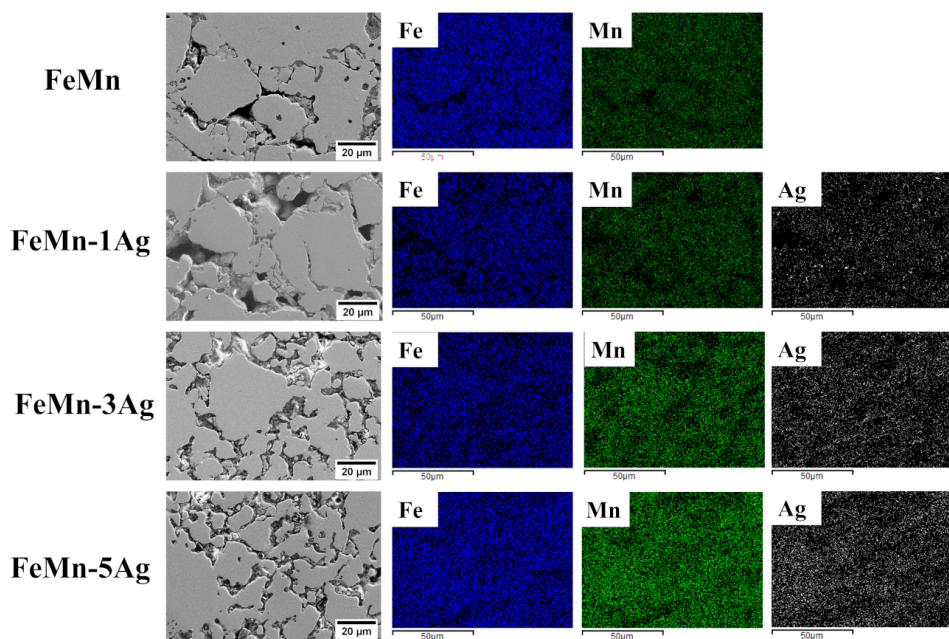


**Fig. S3** EDS elemental maps taken on polished surface of FeMn, FeMn-1Ag, FeMn-3Ag and FeMn-5Ag sintered alloys showing distribution of Fe, Mn and Ag.

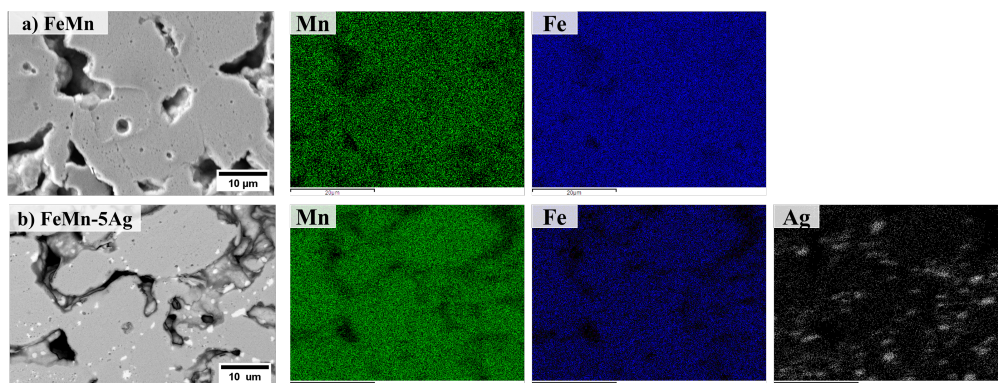


**Fig. S4** EDS elemental maps taken on polished cross-sectional surface of FeMn (a) and FeMn-5Ag (b) sintered alloys showing distribution of Fe, Mn and Ag.

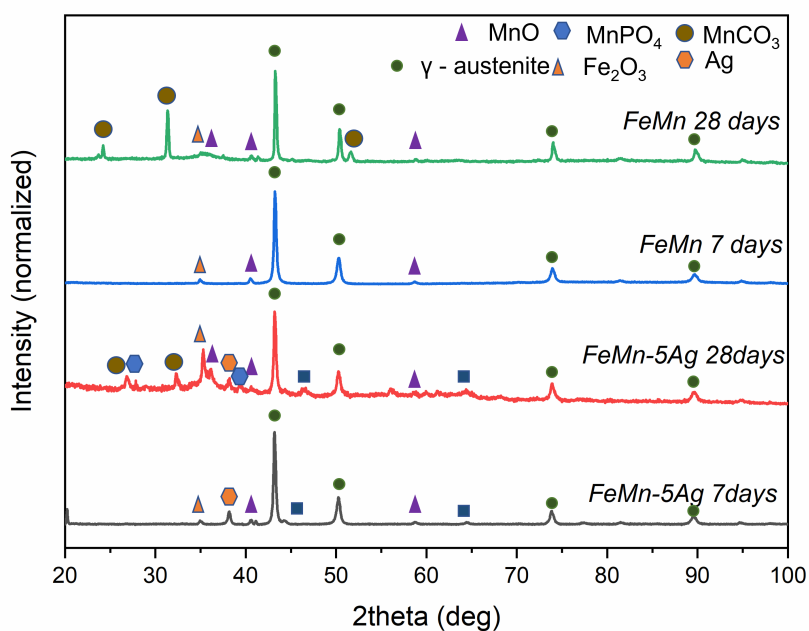


**Fig. S5** X-ray diffraction patterns of the FeMn and FeMn-5Ag alloys after immersion in HBSS for 7 and 28 days.

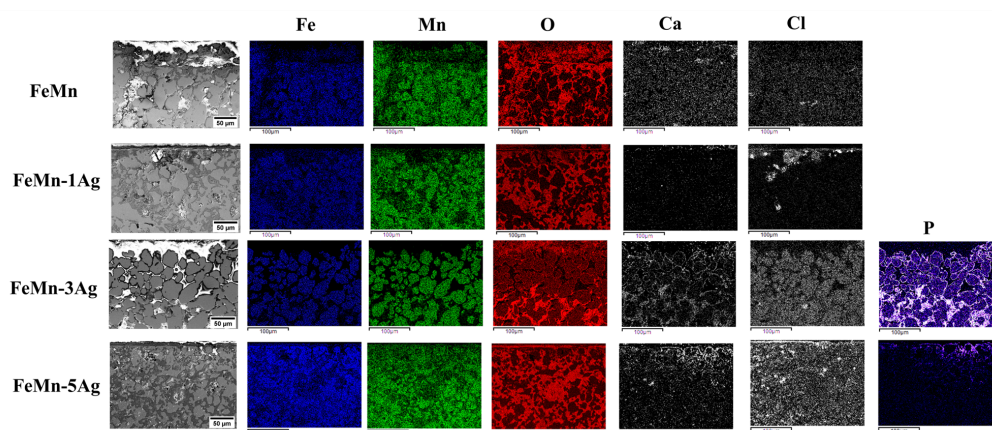


**Fig. S6** EDS maps taken on the cross-sections of FeMn, FeMn-1Ag, FeMn-3Ag and FeMn-5Ag alloys immersed for 84 days in HBSS. EDS maps corresponds to the Fe, Mn, O, Ca, Cl and P distribution for the regions showed in micrographs.

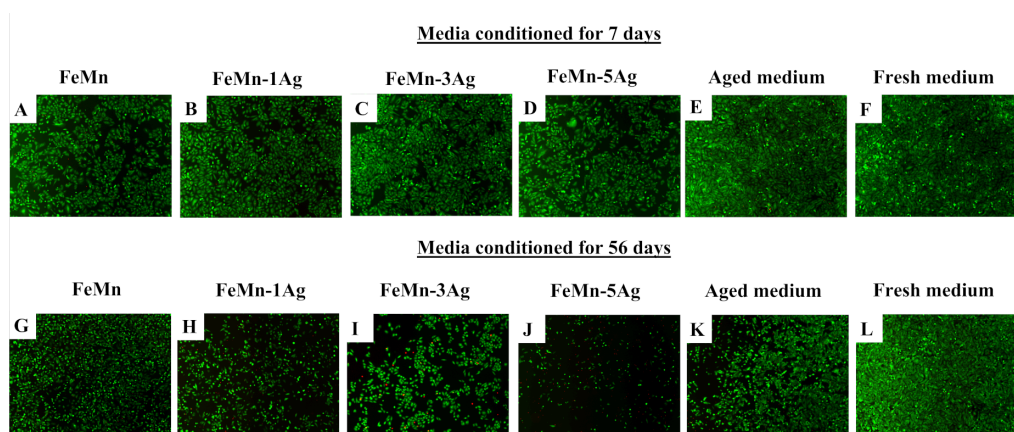


**Fig. S7** Cytotoxicity of medium conditioned during 7 (A-F) and 56 (G-L) days with FeMn (A, G), FeMn-1Ag (B, H), FeMn-3Ag (C, I) and FeMn-5Ag (D, J), measured on Saos-2 cells by live/dead fluorescence staining after 3 days culture. An aged medium consisting of medium prepared following the same incubation times and conditions but without any alloy (E, K) and a fresh medium (F, L) were used as controls. Live and dead cells appear in green and red, respectively.

## 4.2 Paper 2: Silver-induced $\gamma \rightarrow \epsilon$ martensitic transformation in FeMn alloys: An experimental and computational study

In this work, the  $\gamma \rightarrow \epsilon$  martensitic transformation triggered by the addition of Ag in previously described FeMn(-xAg) alloys is studied using experimental and computational techniques. The detailed characterization of phase composition and lattice parameters is conducted using Rietveld refinement on four alloys containing 0, 1, 3 and 5 wt.% Ag. Moreover, detailed microstructural analysis is performed through TEM and STEM on FeMn and FeMn-5Ag specimens. While equiatomic FeMn and FeMn-1Ag alloys exhibited a completely austenitic structure, the introduction of 3% and 5% wt.% Ag induced a phase transformation, resulting in a coexistence of  $\gamma$ -austenite and  $\epsilon$ -martensite phases. The compression tests confirmed that this phase transformation prompted an increase in yield stress.

The evolution of microstructure with varying Ag content can be comprehended through theoretical calculations, which indicate a preference of Ag atoms for intrinsic stacking fault (ISF) sites, revealing a lower energy level for the  $\epsilon$  atomic plane sequence. Consequently, this leads to a local reduction in electronic charge, thereby attenuating interatomic bonds at the ISF plane and facilitating the phase transition. Additionally, the total energy discrepancy between the  $\gamma$  and  $\epsilon$  phases diminishes with the addition of Ag. This permits both phases to coexist within the FeMn-5Ag sample. Both experimental and theoretical data align in confirming a gradual increase in magnetization values following the addition of Ag. This phenomenon arises from local stress introduced by Ag atoms, leading to an expansion of the Ag-Fe and Ag-Mn first neighbour interatomic bonds compared to FeMn. Consequently, this stress promotes electronic charge transfer, inducing localized modifications in the atomic magnetic moments of Fe and Mn.

These findings hold substantial promise for the development of FeMn-based alloys that offer adjustable phase compositions and physical properties, catering to a range of technological applications.



# **Silver-induced $\gamma \rightarrow \epsilon$ martensitic transformation in FeMn alloys: An experimental and computational study**

Aleksandra Bartkowska<sup>a</sup>, Christina Lekka<sup>b</sup>, Ludovico Andrea Alberta<sup>c</sup>, Irena Spasojević<sup>a</sup>, Eva Pellicer<sup>a</sup>, Jordi Sort<sup>a,d</sup>

<sup>a</sup>Departament de Física, Universitat Autònoma de Barcelona, E-08193 Bellaterra (Cerdanyola del Vallès), Spain

<sup>b</sup>Department of Materials Science and Engineering, University of Ioannina, Ioannina 45110 Greece

<sup>c</sup>Leibniz Institute for Solid State and Materials Research Dresden (IFW Dresden), Helmholtzstr. 20, D-01069 Dresden, Germany

<sup>d</sup>Institució Catalana de Recerca i Estudis Avançats (ICREA), Pg. Lluís Companys 23, E-08010 Barcelona, Spain





# Silver-induced $\gamma \rightarrow \epsilon$ martensitic transformation in FeMn alloys: An experimental and computational study

Aleksandra Bartkowska<sup>a,\*</sup>, Christina E. Lekka<sup>b,\*</sup>, Ludovico Andrea Alberta<sup>c</sup>, Irena Spasojevic<sup>a</sup>, Eva Pellicer<sup>a</sup>, Jordi Sort<sup>a,d,\*\*</sup>

<sup>a</sup> Departament de Física, Universitat Autònoma de Barcelona, Bellaterra, E-08193 Cerdanyola del Valles, Spain

<sup>b</sup> Department of Materials Science and Engineering, University of Ioannina, 45110 Ioannina, Greece

<sup>c</sup> Leibniz Institute for Solid State and Materials Research Dresden (IFW Dresden), Helmholtzstr. 20, D-01069 Dresden, Germany

<sup>d</sup> Institució Catalana de Recerca i Estudis Avançats (ICREA), Pg. Lluís Companys 23, E-08010 Barcelona, Spain

## ARTICLE INFO

### Keywords:

Iron-manganese alloys  
Austenite  
Martensite  
Silver  
Magnetic properties  
Phase transformation

## ABSTRACT

Porous FeMn alloys with additions of 0, 1, 3 and 5 wt% of Ag were fabricated using powder metallurgy and sintering. The microstructure of the fabricated alloys was characterized using X-ray diffraction, transmission electron microscopy and selected area electron diffraction. While equiatomic FeMn and FeMn-1Ag alloys possess a fully austenitic structure, a change in the crystallographic structure is observed upon addition of 3 and 5 wt% of Ag, where a mixture of  $\gamma$  austenite and  $\epsilon$  martensite phases is observed. Compression tests reveal that such structural transition causes an increase of the yield stress. The evolution of microstructure with the Ag content can be understood from theoretical calculations which show that Ag atoms prefer the intrinsic stacking fault (ISF) sites, revealing lower energy for the  $\epsilon$  atomic plane sequence. This causes local depletion of the electronic charge, therefore weakening the interatomic bonds at the ISF plane and facilitating the phase transition. In addition, the total energy difference between the  $\gamma$  and  $\epsilon$  phases decreases upon Ag addition. This enables the coexistence of both phases in the sample with 5 wt% Ag. Both experimental and theoretical data agree that the magnetization value gradually increases upon Ag addition. This is due to the local stress that is introduced by Ag atoms, which expand the Ag-Fe and Ag-Mn first neighbour interatomic bonds compared to FeMn. This stress results in electronic charge transfer that locally alters the Fe and Mn atomic magnetic moments. These results are appealing for the design of FeMn-based alloys with tuneable phase composition and physical properties for several technological applications.

## 1. Introduction

Fe-Mn alloys have been studied as versatile materials in widespread applications such as steels for automotive applications [1,2], antiferromagnetic layers in spin valves [3,4], or biodegradable metals for implant applications [5–7], amongst others. The solid solution phases characteristic of the Fe-Mn system are  $\gamma$ -austenite,  $\alpha$ -ferrite,  $\delta$ -Fe,  $\alpha$ -Mn,  $\beta$ -Mn and  $\delta$ -Mn. Moreover, a metastable hexagonally close-packed (hcp)  $\epsilon$  phase can be formed by martensitic transformation in alloys with Mn content above 10 wt%. This transformation can occur owing to prior deformation, high applied pressure or fast cooling from the liquid state by the movement of Shockley partial dislocations between Fe and Mn on the (111) $_{\gamma}$  plane [8]. The  $\gamma \rightarrow \epsilon$  phase transformation is strongly

associated with the stacking fault energy [8,9]. It has been shown that a low stacking fault energy, below 20 mJ m<sup>-2</sup>, facilitates the transformation of fcc  $\gamma$ -austenite into hcp  $\epsilon$ -martensite [10]. The stacking fault energy can be affected by several factors, such as defects or the addition of elements. For example, additions of Al strongly suppress the phase transformation, as they increase the stacking fault energy of  $\gamma$ -austenite [11]. In contrast, the addition of Si lowers the stacking fault energy, favoring the  $\gamma \rightarrow \epsilon$  phase transformation [12]. Several *ab initio* calculations on Fe reveal that the presence of Mn or C causes a minimum in the stacking fault energy (around -450 mJ m<sup>-2</sup> for Fe), thus favoring the  $\epsilon$  phase [13–15].

Depending on the crystallographic phase, Fe-Mn alloys can find potential use in different areas of materials science. For instance,

\* Corresponding authors.

\*\* Corresponding author at: Departament de Física, Universitat Autònoma de Barcelona, Bellaterra, E-08193 Cerdanyola del Vallès, Spain.

E-mail addresses: [Aleksandra.Bartkowska@uab.cat](mailto:Aleksandra.Bartkowska@uab.cat) (A. Bartkowska), [chlekk@uoi.gr](mailto:chlekk@uoi.gr) (C.E. Lekka), [jordi.sort@uab.cat](mailto:jordi.sort@uab.cat) (J. Sort).

<https://doi.org/10.1016/j.jalcom.2023.171640>

Received 7 June 2023; Received in revised form 20 July 2023; Accepted 2 August 2023

Available online 4 August 2023

0925-8388/© 2023 The Authors. Published by Elsevier B.V. This is an open access article under the CC BY license (<http://creativecommons.org/licenses/by/4.0/>).

$\gamma$ -Fe<sub>50</sub>Mn<sub>50</sub> alloys are the basis of antiferromagnetic metallic pinning layers used in spin valves or magnetic tunnel junction devices [16]. High-manganese steels, which show mostly austenitic fcc structure, are known for their high strength and ductility, owing to their high strain hardening capacity [17]. These steels, typically comprising high Mn contents (> 20 wt%) and additions of C (< 1 wt%), Si (< 3 wt%) and Al (< 10 wt%), exhibit various hardening mechanisms, such as twinning-induced plasticity (TWIP) and transformation-induced plasticity (TRIP). The TWIP effect is observed in steels with low stacking fault energy, between 20 and 40 mJ m<sup>-2</sup> [17] and it relies on the transformation of retained austenite into martensite during plastic deformation, which enhances both strength and ductility [2]. Furthermore, in recent years, Fe-based alloys (including Fe-Mn) have emerged as potential candidates for biodegradable materials applications [5,6,18]. Biodegradable alloys are a new class of implantable materials that aim to gradually degrade *in vivo* until their role is fulfilled, without the need for an implant removal operation. This is important to limit the cost of medical treatment and to reduce patients' morbidity. Owing to the high mechanical strength of iron, these alloys surpass the mechanical properties of other biodegradable biomaterials, such as polymers, or Mg- and Zn-based alloys. In the last decade, manganese was established as suitable alloying element in Fe-based biodegradable alloys, since a high content of Mn stabilizes the austenite phase which exhibits antiferromagnetic properties, thus making this material compatible with magnetic resonance imaging (MRI) [7,18–23]. In addition, alloys with various amounts of Mn demonstrate good mechanical properties, a degradation rate higher than in pure Fe, and good cytocompatibility [18,19,23,24].

Due to the extensive use of artificial implant materials, implant-associated bacterial infections have become increasingly common because of biofilm formation, adhesion, and colonization of bacteria on the implant surface [25,26]. Therefore, there is a need to develop materials with antibiofilm and antibacterial properties. Among other strategies, addition of Ag has been extensively tested and proven efficient in promoting antibacterial properties [27,28]. Besides preventing the biofilm formation on the material surface [7], the addition of Ag to the Fe-Mn system has several advantages such as accelerating short-term corrosion [29] or increasing the strength [30]. In fact, the solubility of Ag in  $\gamma$ -austenite is below 0.4 at% [31], therefore the formation of Ag-rich precipitates is expected. These precipitates can act as microgalvanic cells [29], which help increase the corrosion rate of Fe-based alloys.

Interestingly, reports on FeMn-Ag alloys have shown that additions of Ag favor the formation of the martensitic phase, although so far this effect has not been understood or described in detail. For example, in the Fe<sub>30</sub>Mn-Ag alloys reported by Liu et al. [32], the content of the  $\epsilon$  phase increased upon the addition of Ag. In another study by Babacan et al. [33], Ag-bearing alloys showed a higher content of martensite than alloys without Ag. Similar observations were described by Dehghan-Manshadi et al. [34], where additions of Ag increased the intensity of the  $\epsilon$ -martensite peaks in diffraction measurements. Hence, besides providing antibacterial properties, addition of Ag to Fe-Mn can lead to microstructural changes that improve the compressive yield strength of the alloy. However, the effect of added Ag on the structure and the mechanical and magnetic properties of Fe-Mn alloys has been largely overlooked.

In this work, we investigate the phase transformation from austenite to martensite induced in Fe-Mn alloys by the addition of 1–5 wt% Ag. We also correlate the changes in microstructure with the mechanical and magnetic properties of the resulting alloys. Moreover, a theoretical study is conducted to understand the phase transformation and the alterations of the magnetic properties of FeMn due to the presence of Ag, mainly associated to a charge transfer and alterations in the first neighbor's atomic magnetic moments.

## 2. Materials and methods

### 2.1. Sample preparation and characterization

Iron-manganese equiatomic alloys with varying content of Ag (0, 1, 3 and 5 wt%, denoted as FeMn, FeMn-1Ag, FeMn-3Ag and FeMn-5Ag, respectively) were fabricated using powder metallurgy techniques, namely ball milling of commercial Fe (>99% purity), Mn (>99% purity) and Ag (>99.9% purity) powders in a planetary ball mill for 10 h and subsequent sintering under vacuum at 900 °C, as described in our previous report [7]. X-ray diffraction (XRD) was performed on polished surfaces of all tested alloys to assess the phase composition. The experiments were performed on a Panalytical X'Pert powder diffractometer with Cu K $\alpha$  radiation, in the angular range between 20° and 100° and a step size of 0.026° in the Bragg-Brentano geometry.

Thin lamellae of FeMn and FeMn-5Ag samples were prepared for transmission electron microscopy (TEM) observations by focused ion beam (FIB). The microstructure images and selected-area diffraction (SAED) patterns were acquired using a Jeol 2011 TEM operating at 200 kV. High-resolution images were also obtained by scanning-transmission electron microscopy (STEM) utilizing a Teknai Fei instrument operating at 200 kV. The SAED patterns were indexed by the Gatan Digital Micrograph software, which was also employed to analyze the high-resolution images and the corresponding fast Fourier transform (FFT) images. From the SAED patterns and the FFT, the interplanar distances were obtained as well as the lattice constants.

The mechanical properties of the alloys were assessed through compression testing. Specimens of cylindrical shape were prepared according to DIN 50106:2016–11 with a height (4 mm) to diameter (2 mm) ratio of 2. Loading surfaces were ground with silicon carbide papers to become plane parallel. Uniaxial compression tests were performed at room temperature using an Instron 8562 device at a constant strain rate of  $1 \times 10^{-3}$  s<sup>-1</sup> and at least three specimens per composition were tested. The tests were halted at fracture. The following mechanical properties were determined from the engineering stress-strain compression curves: compressive yield strength (proof offset 0.2%,  $R_{0.2}$ ), compressive ultimate strength ( $R_m$ ) and compressive strain ( $A$ ).

To assess magnetic properties, hysteresis loops were recorded at room temperature using a vibrating sample magnetometer (VSM, MicroSense). The maximum applied magnetic field was 20 kOe. The saturation magnetization values were determined from the hysteresis loops. Additional magnetic force microscopy (MFM) measurements were performed using Asylum Research Atomic Force Microscope to map the magnetic field distribution of FeMn-3Ag and FeMn-5Ag samples. MFM measurements were performed in two pass mode; in the first pass topography of the sample surface was obtained, while in the second pass magnetic forces between previously magnetized tip and the sample were sensed at the lift height of 30 nm. All the measurements were performed at remanence state of the as-grown samples.

### 2.2. Computational details

In this work, the Vienna *ab initio* simulation package (VASP) density functional theory (DFT) based on the projector augmented wave method formulated to treat collinear and noncollinear magnetic structures is applied [35–37]. The exchange correlation effect is tuned with the generalized gradient approximation (GGA) by Perdew-Burke-Ernzerhof (PBE) [38]. A minimal basis set is adopted, which includes 3d, 4s and 4p orbitals having a cutoff of 300 eV.

The ordered  $\gamma$ -FeMn austenite is treated using the primitive CuAu-I unit cell [37,39] and a  $2 \times 2 \times 2$  supercell using  $(4 \times 4 \times 4)$  and  $(8 \times 8 \times 8)$  k-points meshed to sample the Brillouin zone. The antiferromagnetic (AFM) spin configurations are notated by 1Q (collinear) and 2Q or 3Q (non-collinear) including several Fe and Mn moments directions in line with previous reports [35,39]. In particular, in 1Q there are several combinations of the atomic moments' alignment in the unit cell e.g.,

antiparallel Fe-Fe ( $\uparrow\downarrow$ ) and Mn-Mn ( $\uparrow\downarrow$ ) moments or parallel Fe-Fe ( $\uparrow\uparrow$ ) and Mn-Mn ( $\uparrow\uparrow$ ) moments [35]. In 2Q the moments in the four-atom CuAu-I unit cell can be along  $[100]$ ,  $[100]$ ,  $[010]$ ,  $[010]$  or along  $[110]$ ,  $[1\bar{1}0]$ ,  $[1\bar{1}0]$ ,  $[110]$  etc. while in 3Q spins can point to the cell center or have any directions in the three axes [35,39]. In addition, in *ab initio* calculations the atomic percent is used, therefore  $\gamma$ -FeMn represents the  $\gamma$ -Fe<sub>50</sub>Mn<sub>50</sub> (at%) or  $\gamma$ -Fe<sub>49.59</sub>Mn<sub>50.41</sub> (wt%) in atomic or weight percent, respectively. The calculations started at the experimental lattice constant of  $\gamma$ -FeMn at zero temperature ( $a = 3.60$  Å) choosing the same spin states with the available theoretical data [37, 39–41] for comparison reasons while cell and atomic relaxation were also employed in several ordered, disordered and Fe- or Mn- rich first neighborhood Ag environments having 16 or 32 atoms, offering in total 58 different configurations. In particular, in the 32 atoms supercell, 1 Fe was replaced by Ag in order to mimic the different Fe-Mn neighborhoods of Ag resulting in system of  $\gamma$ -Fe<sub>46.875</sub>Mn<sub>50</sub>Ag<sub>3.125</sub> (at%) or  $\gamma$ -Fe<sub>45.91</sub>Mn<sub>48.18</sub>Ag<sub>5.91</sub> (wt%) having 15 Fe, 16 Mn and 1 Ag atoms. When replacing 1 Mn, the  $\gamma$ -Fe<sub>50</sub>Mn<sub>46.875</sub>Ag<sub>3.125</sub> (at%) or  $\gamma$ -Fe<sub>48.915</sub>Mn<sub>45.14</sub>Ag<sub>5.91</sub> (wt%) crystal have 16 Fe, 15 Mn and 1 Ag atoms. Moreover, the cases of replacing 1 Fe and 1 Mn atoms by Ag atoms were considered, in order to mimic the cases with Ag first neighbors, resulting in  $\gamma$ -Fe<sub>46.875</sub>Mn<sub>46.875</sub>Ag<sub>6.25</sub> (at%) or  $\gamma$ -Fe<sub>44.62</sub>Mn<sub>43.89</sub>Ag<sub>11.49</sub> (wt%). It should be noted that although the theoretical atomic percentages are not exactly the ones of the experimental weight percentages, they offer a good description of the behaviour of  $\gamma$ -FeMn upon Ag addition. The *ab initio* calculations were performed at FeMn-6Ag (wt%) which is close to FeMn-5Ag (wt%), where the experiments already revealed the appearance of the martensite phase and a slight increase of magnetization. The higher Ag content of  $\gamma$ -Fe<sub>44.62</sub>Mn<sub>43.89</sub>Ag<sub>11.49</sub> (wt%), named FeMn-12Ag (wt%), was also considered to study the cases of having two Ag as first neighbors and to investigate the trends of the structural and magnetic properties upon further increase of the Ag percentage.

Similarly, the  $\epsilon$ -FeMn martensite primitive unit cell and 16 or 32 atoms' supercells were used along with a  $(8 \times 8 \times 8)$  k-point mesh in the suggested collinear AFM spin state having pure Fe or Mn atomic [0001] layers (named herein pure[0001]) [42] and a system with mix Fe-Mn [0001] layers, as expected due to the geometry of ordered  $\gamma$ -FeMn (111) austenite structure, resulting in 26 configurations (named herein FeMn [0001]). In addition,  $\epsilon$ -FeMn represents the  $\epsilon$ -Fe<sub>50</sub>Mn<sub>50</sub> (at%) and  $\epsilon$ -Fe<sub>49.59</sub>Mn<sub>50.41</sub> (wt%) in atomic and weight percent, respectively. The Ag substitution in  $\epsilon$ -FeMn was accounted in a similar way as for  $\gamma$ -FeMn, resulting in  $\epsilon$ -Fe<sub>45.91</sub>Mn<sub>48.18</sub>Ag<sub>5.91</sub> (wt%) or  $\epsilon$ -Fe<sub>48.915</sub>Mn<sub>45.14</sub>Ag<sub>5.91</sub> (wt%) for the different first neighbor environments (when replacing Fe or Mn by Ag) named therefore  $\epsilon$ -FeMn-6Ag. The case of both Fe and Mn atoms' substitution results in  $\epsilon$ -Fe<sub>44.62</sub>Mn<sub>43.89</sub>Ag<sub>11.49</sub> (wt%) and named  $\epsilon$ -FeMn-12Ag in wt% for an easier comparison with the experimental data.

The atomic relaxations were continued until the Hellmann-Feynman forces acting on the atoms were less than  $0.01$  eV/Å and the total energy changes were less than  $10^{-6}$  eV. All the calculations were carried out in spin-polarized mode.

### 3. Results and discussion

#### 3.1. Effect of Ag addition on microstructure of FeMn alloys

The SEM images of the synthesised porous alloys are shown in Supplementary Fig. S1. The alloys show a similar porous microstructure, with macropores of around  $20$   $\mu\text{m}$  for all the investigated compositions. The percentage of macroporosity, calculated from the SEM images, was between 18% and 22% and increased slightly with Ag content. Fig. 1 shows the XRD patterns of the four studied alloys. Equiatomic FeMn and FeMn-1Ag samples mainly possess the face-centered cubic (fcc)  $\gamma$ -austenite phase, which is in accordance with the Fe-Mn phase diagram for this composition [43]. Meanwhile, the FeMn-3Ag and FeMn-5Ag

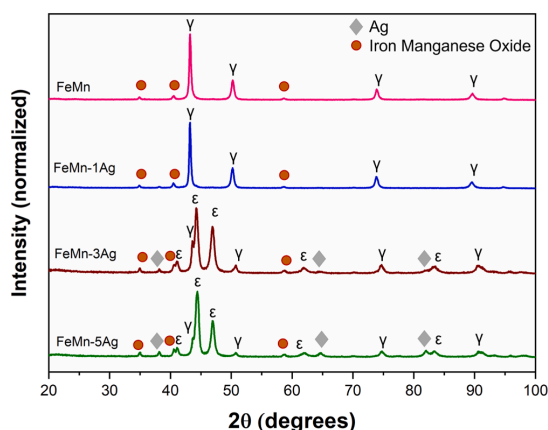


Fig. 1. XRD patterns of FeMn, FeMn-1Ag, FeMn-3Ag and FeMn-5Ag sintered alloys. The symbol  $\gamma$  corresponds to fcc austenite, while  $\epsilon$  denotes the peaks from hcp martensite phase.

samples consist of a mixture of phases, namely fcc  $\gamma$ -austenite and hexagonal close-packed (hcp)  $\epsilon$ -martensite phases. This is a rather surprising result given the small amount of added Ag. In fact, the martensitic phase in FeMn alloys is typical for lower Mn contents, of 15–30 wt% [18,44]. It has been reported that the driving force for the  $\epsilon$ -martensite phase is the low stacking fault energy upon the addition of manganese and other elements to Fe [8]. Our results reveal that the addition of small amounts of Ag may significantly contribute to the  $\gamma$  to  $\epsilon$  phase transformation. Fig. 1 also reveals small amounts of iron-manganese oxides formed during the sintering process. The weight percentage of phases was calculated using X'Pert HighScore Plus software and the results have shown that the percentage of martensite content increases from 0 wt% in FeMn to 71.5% and 77 wt% in FeMn-3Ag and FeMn-5Ag, respectively. Accordingly, the percentage of austenite decreases from 100% in FeMn to 26.5% and 23 wt% for FeMn-3Ag and FeMn-5Ag, respectively.

Figs. 2 and 3 show the bright-field TEM images of the FeMn and FeMn-5Ag samples, respectively, together with their selected area electron diffraction (SAED) patterns. The samples were cut from a dense area to avoid the occurrence of pores. These figures clearly demonstrate the distinct features of the two samples. In Fig. 2(a,b), the FeMn alloy (with no Ag) shows the presence of elongated grains, with a thickness of approximately 20 nm. The microstructure contains a large number of defects, and it is difficult to clearly define the grain boundaries. The SAED pattern, shown in Fig. 2(c), confirms the presence of  $\gamma$ -austenite, where (111), (200), (220) and (311) planes were identified, with a lattice constant of  $3.56 \pm 0.03$  Å. This value is in accordance with the lattice constant of the  $\gamma$ -austenite phase in Fe-40Mn alloy as described in the literature [45]. In Fig. 2(a) we can observe some bright, rounded particles, with a diameter of approximately 200 nm, which can be attributed to iron-manganese oxide, as also detected in the corresponding XRD pattern (Fig. 1).

In the FeMn-5Ag sample presented in Fig. 3, the grains are more equiaxed and larger, with a size of approximately 400 nm. The grain boundaries are very well defined. Apart from austenitic grains, the  $\epsilon$  phase is also present, as shown in Fig. 3(a) (orange) and confirmed by SAED (Fig. 3b). Specifically, the reflections from (111) $_{\gamma}$ , (200) $_{\gamma}$  and (100) $_{\epsilon}$  were identified in Fig. 3(b). Meanwhile, spots attributed to  $\gamma$  austenite are present in Fig. 3(c). The lattice constant of the  $\gamma$  phase was  $3.56 \pm 0.04$  Å. The  $a$  lattice constant of the  $\epsilon$  martensite, calculated based on the (100) interplanar distance, was  $2.53 \pm 0.03$  Å, which agrees with values reported in literature [46]. The high-resolution image in Fig. 3d together with the FFT analysis performed in the region



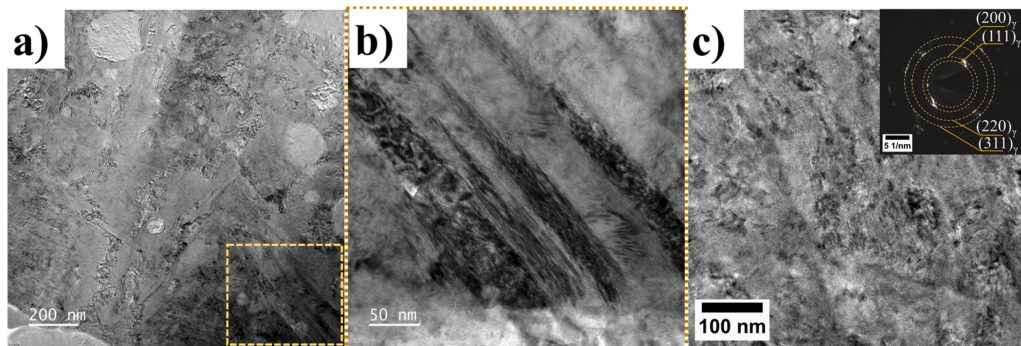


Fig. 2. TEM images of FeMn alloy: (a) low magnification image, (b) magnified detail of the area enclosed within the yellow square in panel a), (c) STEM image together with SAED pattern.

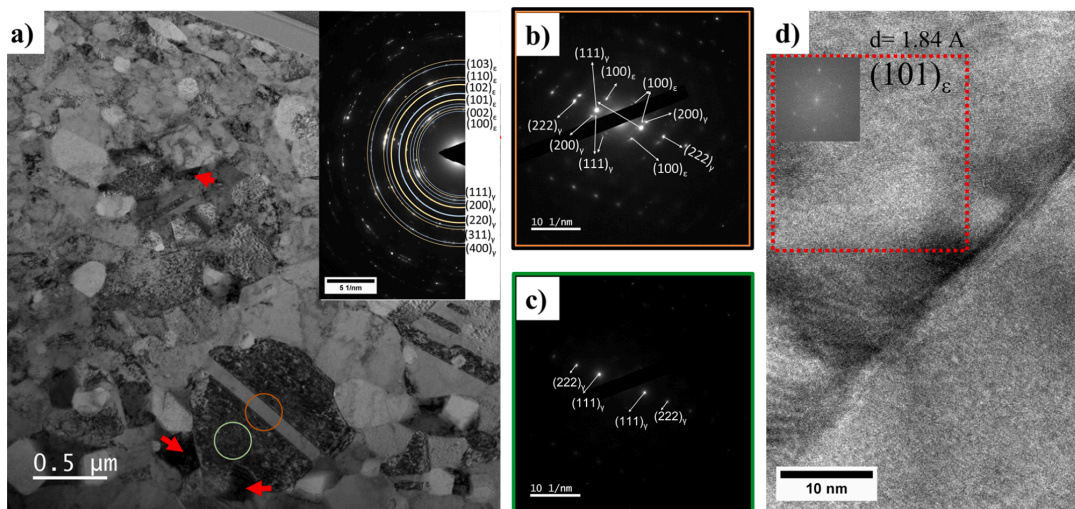


Fig. 3. TEM images of FeMn-5Ag alloy (a) low magnification image with red arrows pointing to Ag particles. The inset shows the corresponding, indexed SAED pattern where blue lines correspond to  $\epsilon$  phase and yellow lines to  $\gamma$  phase. (b) SAED pattern of the region enclosed in the orange circle in panel a) and (c) SAED pattern of the region enclosed in the green circle in panel a), (d) high-resolution STEM image with the FFT performed on the highlighted area in red, indicating the occurrence of  $\epsilon$  phase.

highlighted in red shows the presence of the  $\epsilon$ -martensite (101) plane. Moreover, apart from the austenite and martensite phases, Ag-rich particles were identified and highlighted in Fig. 3(a) with red arrows and confirmed by high-angle annular dark field (HAADF) and EDS analysis, presented in Supplementary Fig. S2. These particles had a diameter of 150–300 nm. As expected, Ag is lowly soluble in the FeMn matrix, and therefore Ag precipitates also form.

A similar morphology of the  $\epsilon$  phase has been observed in the literature [47–49]. This platelet structure of  $\epsilon$  martensite, as shown in Fig. 3 (a), subdivides  $\gamma$  grains by moving from one-grain boundary to the other on the opposite side, which was identified as Type II  $\epsilon$ -martensite [49]. The subdivision of  $\gamma$  grains leads to a dynamic grain refinement, which in turn may lead to an improvement in the mechanical properties of the Ag-containing alloys. The type of martensite formed depends on the initial size of the  $\gamma$  grains and it has been shown that an extensive grain refinement suppresses the  $\gamma$  to  $\epsilon$  transformation [49]. This may be the reason why the martensite phase is observed only in the big grains of the  $\gamma$  phase.

### 3.2. Effect of Ag on atomic structure and spin configurations

Aiming to understand the influence of Ag in the structural properties of FeMn-Ag alloys, DFT calculations were performed for several atomic rearrangements in  $\gamma$ -FeMn and  $\epsilon$ -FeMn and spin states. The starting points were the AFM collinear (1Q) and non-collinear (2Q or 3Q) spin states for the  $\gamma$ -FeMn primitive unit cell available in the literature [37, 39,42] along with the AFM collinear  $\epsilon$ -FeMn phases [42], as shown in Fig. 4(a,b). These DFT studies on  $\gamma$ -FeMn alloys with collinear or non-collinear spin states found for the  $\gamma$ -Fe<sub>50</sub>Mn<sub>50</sub> an energy preference towards the 2Q and 3Q states along with an underestimation of the experimental lattice constant (3.54 Å with GGA and 3.42 Å with local density approximation (LDA) [37,39,42]) except from the introduced frozen core approximation in the exact muffin-tin orbital (EMTO-DFT) method [39]. To this end, most of the previous theoretical studies on  $\gamma$ -Fe<sub>50</sub>Mn<sub>50</sub> were performed at the experimental lattice constant (3.63 Å) or its extrapolation at zero temperature (3.60 Å) [37,39] since it was really interesting to understand the existence of different AFM (1Q, 2Q, 3Q) spin states and verify the related lack of experimental

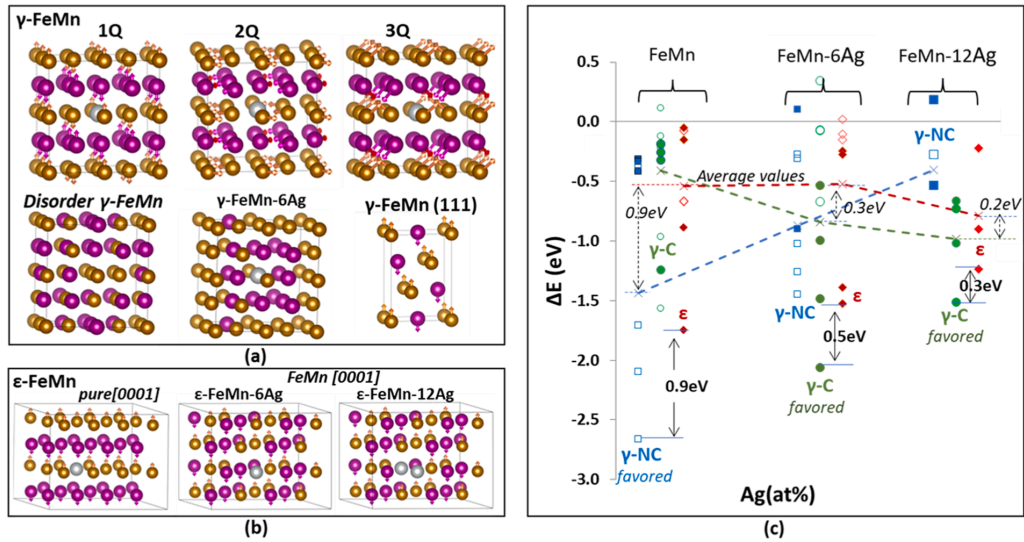


**Fig. 4.** FeMn-Ag alloys' selective atomic structures for (a) austenite and (b) martensite phases along with the main AFM collinear (1Q) and non-collinear (2Q and 3Q) spin states. Fe, Mn and Ag atoms are depicted by gold, magenta and grey spheres. (c) Total energy difference  $\Delta E$  of AFM collinear and non collinear spin states for different atomic rearrangements and crystal structures.  $\Delta E$ 's negative values denote alloy stability against their corresponding pure element phases. Open and filled symbols represent the DFT results on the theoretical and the experimental lattice constants while  $\gamma$ -Collinear ( $\gamma$ -C in green circles),  $\gamma$ -Non-Collinear ( $\gamma$ -NC in blue squares) and  $\epsilon$ -Collinear ( $\epsilon$  in red diamonds) stand for spin states. As a guide to the eye, dashed lines correspond to the average  $\Delta E$  values of all under-study stable ( $\Delta E < 0$ ) configurations for each structure  $\gamma$ -C (green line),  $\gamma$ -NC (blue line) and  $\epsilon$  (red line) that might coexist in the experimental conditions. The difference between the  $\gamma$  and  $\epsilon$  phases' energetically favoured  $\Delta E$  values is denoted by a black vertical arrow while the corresponding deviation between the average values is shown with dashed vertical arrows. The compositions FeMn-6Ag (wt%) describe the  $\gamma$ -Fe<sub>45.91</sub>Mn<sub>48.18</sub>Ag<sub>5.91</sub> (wt%) and  $\gamma$ -Fe<sub>48.915</sub>Mn<sub>45.14</sub>Ag<sub>5.91</sub> (wt%) cases while FeMn-12Ag (wt%) refers to Fe<sub>45.75</sub>Mn<sub>46.51</sub>Ag<sub>11.49</sub> (wt%).

consensus concerning the favoured spin configurations. In line with these previous calculations, the current DFT results also underestimate the  $\gamma$ -FeMn lattice constant (3.53 Å and 3.54 Å for the collinear and non-collinear primitive unit cells) compared with the projected augmented wave (PAW) method (3.53 Å) and simple EMT0 (3.54 Å) [39] and the experimental results of this work, presented in Fig. 1. Therefore, in Fig. 4(c) the current DFT results are presented for both cases: i) at the experimental lattice constant (filled symbols) and ii) for the totally relaxed (unit cell and atomic positions) configurations (open symbols). The total energy difference ( $\Delta E$ ) was estimated for all cases using the  $E_{\text{FeMn-Ag}}$  total energy corresponding to all studied spin states, compositions and atomic environments in order to reveal the energetically favoured structure using the expression (Eq. 1):

$$\Delta E = E_{\text{FeMnAg}} - (N_{\text{Fe}}E_{\text{Fe}} + N_{\text{Mn}}E_{\text{Mn}} + N_{\text{Ag}}E_{\text{Ag}}) \quad (1)$$

where  $E_{\text{Fe}}$ ,  $E_{\text{Mn}}$  and  $E_{\text{Ag}}$  stand for the corresponding austenite or martensite single elements' structure and  $N_{\text{Fe}}$ ,  $N_{\text{Mn}}$  and  $N_{\text{Ag}}$  are the related number of atoms.  $\Delta E$  was calculated in order to be able to compare different phases, Ag contents and cells' sizes. It should be noted that although several units and supercells (ordered or even disorder-like) are chosen in this work, in total 84 configurations, they cannot be directly compared to the experimentally observed solid solution austenite and martensite phases, which sometimes even co-exist. Nevertheless, they might provide an estimation of the FeMn behaviour upon Ag addition.

Starting with the binary alloy, for the  $\gamma$ -FeMn collinear states (1Q) different AFM spin moment combinations on the 4-unit cell's atoms (up or down) have been considered following the spin configurations depicted in [37] and presented in Fig. 4(c) with filled green spheres. Although the energy difference between the several collinear AFM spin states is small (up to 0.05 eV/atom) in line with [37], the results of this work reveal the AFM collinear 1Q of Fig. 4(a) that has antiparallel Fe-Fe

( $\uparrow\downarrow$ ) and Mn-Mn( $\uparrow\downarrow$ ) moments as the most energetically favored [37,39]. Nevertheless, the non-collinear 2Q (having the spins pointing along the  $[110]$ ,  $[\bar{1}\bar{1}0]$ ,  $[1\bar{1}0]$ ,  $[\bar{1}\bar{1}0]$  as in [39]) and 3Q (with spins towards the center of the unit cell, similar to [35,39]) are energetically favored against all collinear configurations, in line with previous studies [37, 39]. It should be noted that the non-collinear energetically favored  $\gamma$ -FeMn of this work has the Fe moments parallel to each other and the Mn moments creating a global anti-parallel magnetization as expected from the approach we have used [37]. The  $\gamma$ -FeMn disorder relaxed supercell also shows a preference towards the non-collinear state ( $-2.09$  eV) compared to the collinear state ( $-0.96$  eV) while the collinear  $\gamma$ -FeMn unit cell of the (111) face ( $-0.22$  eV) has almost the same energy with all collinear  $\gamma$ -FeMn primitive unit cells (oriented along (001)) as expected. Concerning the martensite  $\epsilon$ -FeMn, the experimentally suggested structure having pure [0001] Fe or Mn atomic layer sequence [42] was considered and found to be unfavored ( $-0.88$  eV) compared to mixed FeMn [0001] atomic layers which are related to the  $\gamma$ -FeMn (111) face geometry ( $-1.75$  eV), both calculated at the experimental lattice constants  $a = 2.53$  Å and  $c = 4.079$  Å of  $\epsilon$ -Fe<sub>80</sub>Mn<sub>20</sub> [50], Fig. 4(b). Similar  $\epsilon$ -FeMn mixed structure preference was found when using the present work's  $\epsilon$ -Fe<sub>50</sub>Mn<sub>50</sub> lattice constants  $a = 2.47$  Å and  $c = 3.93$  Å having only a  $\Delta E$  underestimation (the FeMn [0001] shows  $-0.66$  eV against pure [0001]  $\epsilon$ -FeMn  $-0.07$  eV). It should be noted that the AFM collinear and non-collinear  $\epsilon$ -FeMn states reveal equivalent  $\Delta E$  (the difference might be 0.01 eV) and therefore are presented in Fig. 4(c) with the same symbol (diamond).

Turning on the ternary FeMn-Ag system, the same austenite and martensite binary supercells were used to reveal the effect of Ag substitution, as shown in Fig. 4(a,b). In the ordered  $\gamma$ -FeMn-6Ag (wt%), the two available cases of Fe ( $\gamma$ -Fe<sub>46.875</sub>Mn<sub>50</sub>Ag<sub>3.125</sub> (at%) or  $\gamma$ -Fe<sub>45.91</sub>Mn<sub>48.18</sub>Ag<sub>5.91</sub> (wt%)) or Mn ( $\gamma$ -Fe<sub>50</sub>Mn<sub>46.875</sub>Ag<sub>3.125</sub> (at%) or  $\gamma$ -Fe<sub>48.915</sub>Mn<sub>45.14</sub>Ag<sub>5.91</sub> (wt%)) substitution by Ag atoms were considered. In Fig. 4

(a), the energetically favored  $\gamma$ -FeMn-6Ag ( $\gamma$ -Fe<sub>46.875</sub>Mn<sub>50</sub>Ag<sub>3.125</sub> (at%) or  $\gamma$ -Fe<sub>45.91</sub>Mn<sub>48.18</sub>Ag<sub>5.91</sub> (wt%)) atomic and spin configurations are presented where Ag prefers to have as many as possible Mn atoms in the first neighborhood. In particular, the collinear 1Q AFM  $\gamma$ -Fe<sub>45.91</sub>Mn<sub>48.18</sub>Ag<sub>5.91</sub> (wt%) (−2.06 eV) of Fig. 4(a) is favored against the collinear 1Q AFM  $\gamma$ -Fe<sub>48.915</sub>Mn<sub>45.14</sub>Ag<sub>5.91</sub> (wt%) (−1.48 eV) with more Fe atoms as seen in Fig. 4(b). Interestingly, all  $\gamma$ -FeMn-6Ag (wt%) non-collinear states are less preferred compared to the binary FeMn cases while the average  $\Delta E$  (dashed lines) shows equivalent values between  $\gamma$ -NC and  $\gamma$ -C. Furthermore, Ag prefers the FeMn [0001] martensite  $\epsilon$ -FeMn-6Ag (wt%) configuration by 1 eV against the pure [0001] as well as the Fe atomic position (−1.53 eV in Fe site,  $\epsilon$ -Fe<sub>45.91</sub>Mn<sub>48.18</sub>Ag<sub>5.91</sub> (wt%), and −1.39 eV in Mn site,  $\epsilon$ -Fe<sub>48.915</sub>Mn<sub>45.14</sub>Ag<sub>5.91</sub> (wt%)). Fig. 4(c). Similar preference was observed for the austenite phase, revealing the Ag preference towards a ‘rich in Mn’ 1st neighborhood environment.

Upon Ag enrichment, in Fe<sub>45.75</sub>Mn<sub>46.51</sub>Ag<sub>11.49</sub> (wt%) or FeMn-12Ag (wt%), where two Ag atoms might become first neighbours, the austenite collinear states are favored compared to the non-collinear ones while including the martensite cases all  $\Delta E$  values decrease, as shown in Fig. 4(c). Moreover, at much higher Ag compositions, e.g. the FeMn-39Ag (wt%) which describes the four atom primitive  $\gamma$  and  $\epsilon$  unit cells with compositions  $\gamma$ -Fe<sub>40.16</sub>Mn<sub>20.41</sub>Ag<sub>39.43</sub> (wt%) and  $\gamma$ -Fe<sub>20.01</sub>Mn<sub>40.69</sub>Ag<sub>39.30</sub> (wt%) (not included in this figure), the  $\Delta E$  values become positive revealing this system’s instability. Concerning the spin states, the  $\gamma$ -Fe<sub>45.75</sub>Mn<sub>46.51</sub>Ag<sub>11.49</sub> (wt%) or  $\gamma$ -FeMn-12Ag (wt%) AFM 1Q (−1.51 eV) state and the  $\epsilon$ -Fe<sub>45.75</sub>Mn<sub>46.51</sub>Ag<sub>11.49</sub> (wt%) or  $\epsilon$ -FeMn-12Ag (wt%) in the mix FeMn [0001] (−1.23 eV) configuration seem to be the preferred ones (Fig. 4(b, c)).

Overall, the results shown in Fig. 4(c) indicate that the energy difference between the austenite and martensite phase progressively decreases with the increase of Ag content as denoted by continuous black vertical arrows in Fig. 4(c) between the energetically favored structures or with a dashed black vertical arrow between the average  $\Delta E$  values of all stable understudy (dashed blue, green and red lines stand for  $\gamma$ -NC,  $\gamma$ -C and  $\epsilon$  configurations). In particular, for FeMn the energy difference between the favored  $\gamma$ -NC ( $\Delta E = -2.66$  eV) and  $\epsilon$  ( $\Delta E = -1.75$  eV) is 0.9 eV, while for  $\gamma$ -Fe<sub>45.91</sub>Mn<sub>48.18</sub>Ag<sub>5.91</sub> (wt%) or  $\gamma$ -FeMn-6Ag (wt%) the  $\gamma$ -C ( $\Delta E = -2.06$  eV) becomes favored against  $\gamma$ -NC and differs to  $\epsilon$  ( $\Delta E = -1.53$  eV) by 0.5 eV and is further reduced to 0.3 eV at Fe<sub>45.75</sub>Mn<sub>46.51</sub>Ag<sub>11.49</sub> (wt%) or FeMn-12Ag (wt%). Similarly, the difference between the average  $\Delta E$  austenite and martensite values decreases from 0.9 eV (FeMn,  $\gamma$ -NC and  $\epsilon$ ) to 0.3 eV (Fe<sub>45.91</sub>Mn<sub>48.18</sub>Ag<sub>5.91</sub> (wt%) or FeMn-6Ag (wt%),  $\gamma$ -C and  $\epsilon$ ) and 0.2 eV (Fe<sub>45.75</sub>Mn<sub>46.51</sub>Ag<sub>11.49</sub> (wt%) or FeMn-12Ag (wt%),  $\gamma$ -C and  $\epsilon$ ). The small energy difference (0.3 eV on average or 0.5 eV in favoured cases) between these austenite and martensite states in Fe<sub>45.91</sub>Mn<sub>48.18</sub>Ag<sub>5.91</sub> (wt%) or FeMn-6Ag (wt%) explains the experimental results of this work, which found a co-existence of both phases at FeMn-5 wt% Ag (Fig. 1).

### 3.3. Intrinsic stacking fault energy considerations

Aiming to further understand the influence of Ag addition on the FeMn austenite-to-martensite phase transformation, the intrinsic stacking fault energy was evaluated. The pure Fe and FeMn cases were considered first due to the absence of FeMn-xAg stacking fault energy calculations. Concerning the non-magnetic pure Fe at 0 K, previous *ab initio* calculations revealed that the hexagonal close packed stacking is energetically favored with respect to the fcc stacking [13–15]. Therefore, the fcc(111) structure with an intrinsic stacking fault plane (...ABCABCA|CABC...) that locally mimics the hcp stacking plane is more stable than the perfect fcc phase [13–15]. It should be noted that in the fcc phase there might be several stacking faults irregularities in the three ABC (111) atomic planes’ sequence. The perfect ABCABCABC stacking sequence could change to: a) twin boundary that has a twin mirror plane

ABCACBA, b) the intrinsic stacking fault (ISF) that has a ‘missing’ plane due to shear and a sequence ABCABCA|CABC while c) the extrinsic stacking fault ABCACBABC that has an extra plane. This description becomes more complicated in the case of alloys like  $\gamma$ -TiAl or  $\gamma$ -FeMn where the local chemical neighborhood or magnetism are also involved. In this work the intrinsic stacking fault was considered since it is directly related to the generalized stacking fault energy or  $\gamma$  surface that is defined by shearing two parts of the crystal with respect to each other along a certain plane (here in the (111) plane). The intrinsic stacking fault corresponds to a particular shear point ( $\bar{u}/3$  along the  $[1\bar{2}1]$ ) where the existence of a minimum on the  $\gamma$  surface suggests that the transition is favoured [13,14,51–53].

The pure Fe and FeMn supercells having 6 fcc(111) unit cells along the [111] axis and periodic boundary conditions in the in-plane meshed by  $2 \times 4 \times 1$  k-points were firstly considered following Bleskov [13] and Gholizadeh et al. [14]. In Fig. 5(a) the case of FeMn is presented in the perfect austenite  $\gamma$ -phase (oriented along fcc(111)) having the stacking sequence of ABCABC) as well as the ISF which stands for shear of the  $\gamma$ -phase by  $\bar{u}/3$  along the  $[1\bar{2}1]$  resulting the intrinsic stacking fault plane (...ABCABCA|CABC...) presented with a dashed black line. In Fig. 5(a) the  $\gamma$ -FeMn 36 atoms’ supercell represents the  $\gamma$ -Fe<sub>50</sub>Mn<sub>50</sub> (at%) or  $\gamma$ -Fe<sub>49.59</sub>Mn<sub>50.41</sub> (wt%) in atomic or weight percent, respectively while in (b) the refers to  $\gamma$ -Fe<sub>47.2</sub>Mn<sub>50</sub>Ag<sub>2.77</sub> (at%) or  $\gamma$ -Fe<sub>46.41</sub>Mn<sub>48.34</sub>Ag<sub>5.26</sub> (wt%) having 17 Fe, 18 Mn and 1 Ag atoms named for simplicity FeMn-5Ag and in (c) the  $\gamma$ -Fe<sub>47.22</sub>Mn<sub>47.22</sub>Ag<sub>5.55</sub> (at%) or  $\gamma$ -Fe<sub>45.23</sub>Mn<sub>44.50</sub>Ag<sub>10.27</sub> (wt%) having 17 Fe, 17 Mn and 2 Ag atoms named for simplicity FeMn-10Ag. In Fig. 5(b,c) the FeMn-Ag cases were named FeMn-5Ag (wt%) FeMn-10Ag (wt%) for easier comparison with our experimental data.

The intrinsic stacking fault energy ( $\gamma_{ISF}$ ) excess due to the defect formation is given by Eq. (3):

$$\gamma_{ISF} = (G_{def} - G_{ideal})/S \quad (3)$$

where  $G_{def}$  is the energy of the supercell with defects (the  $\epsilon$ -like phase herein),  $G_{ideal}$  is the energy of the ideal fcc(111) (the  $\gamma$ -phase herein) and  $S$  is the interface area over which the defect is extended [13,14]. The  $\gamma_{ISF}$  of non-magnetic Fe,  $-424 \text{ mJ m}^{-2}$  for the optimized  $3.45 \text{ \AA}$  lattice constant, is in line with the previous reports on *ab initio* calculations for this material, i.e.,  $-422 \text{ mJ m}^{-2}$  and  $-451 \text{ mJ m}^{-2}$  [13],  $-464 \text{ mJ m}^{-2}$  [15] and  $-450 \text{ mJ m}^{-2}$  [14].

Similar ISF values were predicted for FeMn ( $-501 \text{ mJ m}^{-2}$ ), as shown in Fig. 5(a), compared to non-magnetic disordered fcc FeMn 22.5 at% ( $-450 \text{ mJ m}^{-2}$ ) alloys and paramagnetic FeMn40at% ( $-325 \text{ mJ m}^{-2}$ ) [51] as well as  $-510 \text{ mJ m}^{-2}$  for Fe<sub>23</sub>Mn<sub>1</sub> [52]. It should be noted that although the *ab initio* values are really far from the experimental values of  $15\text{--}33 \text{ mJ m}^{-2}$  for Fe-Mn alloys [53] due to the tiny and perfect (using periodic boundary conditions) supercell, they already reveal that the ISF structure is favored over the ideal fcc perfect structure.

The next step was to substitute Fe or Mn atoms by Ag starting from the Fe position since Ag prefers the Mn first neighbor atoms, as described in Section 3.2 and observed in Fig. 4.

In Fig. 5(b) the Fe<sub>46.41</sub>Mn<sub>48.34</sub>Ag<sub>5.26</sub> (wt%) or FeMn-5Ag (wt%) case is presented in two atomic AFM configurations having the Ag atom in the stacking fault plane ( $\Delta E = -0.87$  eV) in a Fe position that is less favored compared to a possible Fe ( $\Delta E = -1.04$  eV, Fe<sub>46.41</sub>Mn<sub>48.34</sub>Ag<sub>5.26</sub> (wt%)) or Mn ( $\Delta E = -1.13$  eV, Fe<sub>49.11</sub>Mn<sub>47.22</sub>Ag<sub>5.26</sub> (wt%)) site further from the stacking fault plane. These results suggest that atomic Ag could exist in several positions (close or not to the stacking fault plane) since the difference in  $\Delta E$  between different sites is  $0.1\text{--}0.2$  eV. Similar energies are expected in lower Ag compositions, like FeMn-1Ag (wt%) and FeMn-3Ag (wt%), where the probability of Ag atoms having Fe and Mn neighbor atoms is enhanced compared to Ag-Ag first neighbors.

Nevertheless, using the present supercells, higher Ag compositions



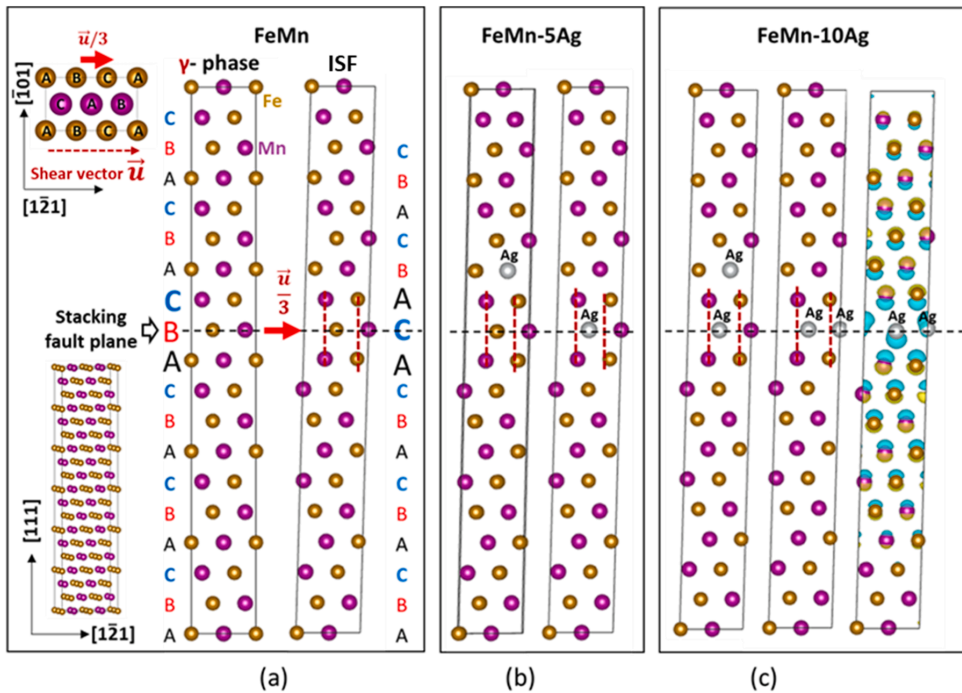


**Fig. 5.** FeMn-xAg(111),  $x = 0, 5, 10$  wt% atomic representation of the intrinsic stacking fault structures for characteristic cases. Fe, Mn and Ag atoms are presented by gold, magenta and grey spheres. Dashed line denotes the stacking fault plane. The compositions FeMn-5Ag (wt%) describe the  $\text{Fe}_{46.41}\text{Mn}_{48.34}\text{Ag}_{5.26}$  (wt%) and  $\text{Fe}_{49.11}\text{Mn}_{47.22}\text{Ag}_{5.26}$  (wt%) cases while FeMn-10Ag (wt%) refers to  $\text{Fe}_{45.23}\text{Mn}_{44.50}\text{Ag}_{10.27}$  (wt%). In Fig. 5(c) the electron charge density difference is also plotted along with atoms where the light blue semicircles denotes depletion of the electron charge that is enhanced close to the stacking plane.

can be achieved where two Ag atoms might be first, second or third neighbors. In Fig. 5(c) for  $\text{Fe}_{45.23}\text{Mn}_{44.50}\text{Ag}_{10.27}$  (wt%) or FeMn-10Ag (wt%) the cases of Ag-Ag atoms being third ( $\Delta E = +0.04$  eV) neighbors (one Ag atom is at the stacking plane and another one two layers further) is unstable while the case where both Ag atoms are neighbors and fully occupy the stacking fault plane ( $\Delta E = -1.22$  eV) is favored occupying. The FeMn-10Ag (wt%) where both Ag atoms are first neighbors but lay two atomic layers further from the stacking fault plane ( $\Delta E = -0.45$  eV) is less favored. Nevertheless, the preference of having in the system Ag-Ag first neighbors with stable configuration ( $\Delta E < 0$ ) is in line with the existence of Ag particles in FeMn-5Ag(wt%) (see Fig. 4). Although, there are several atomic configurations and rearrangements that someone could take into account, the ones presented in Fig. 5(b,c) and described in this paragraph are characteristics and could interpret the Ag behaviour close to the stacking fault plane.

The FeMn-5Ag(wt%) intrinsic stacking fault energies with Ag atom occupying a Fe site at the SF plane (ISF =  $-424 \text{ mJ m}^{-2}$ ) or two layers further from it (ISF =  $-457 \text{ mJ m}^{-2}$ ) increase compared to FeMn (ISF =  $-501 \text{ mJ m}^{-2}$ ) but remain negative denoting the possible existence of both phases in the crystal.

Upon full occupation of the stacking fault plane by Ag in FeMn-10Ag (wt%) ISF decreases to ISF =  $-440 \text{ mJ m}^{-2}$  while a smaller reduction is found for the partial Ag occupation of the stacking plane ISF =  $-413 \text{ mJ m}^{-2}$ , thus showing the tendency of the system towards the martensite structure in both configurations. In Fig. 5(c), the electron charge density difference is presented where depletion of the electron charge (light blue area) close to the stacking plane and the nearest neighboring atomic layers thus weakening the interatomic bonds and allowing therefore an easier slip of atoms and therefore a phase transition from the austenite towards martensite structure.

#### 3.4. Effect of Ag on mechanical and magnetic properties of FeMn alloys

The mechanical and magnetic properties of the samples under study were experimentally determined to assess the impact of the Ag content on these properties. The compressive stress-strain curves of the studied FeMn-xAg samples are presented in Fig. 6. The average values of the compressive yield strength ( $R_{0.2}$ ), compressive ultimate strength ( $R_m$ )

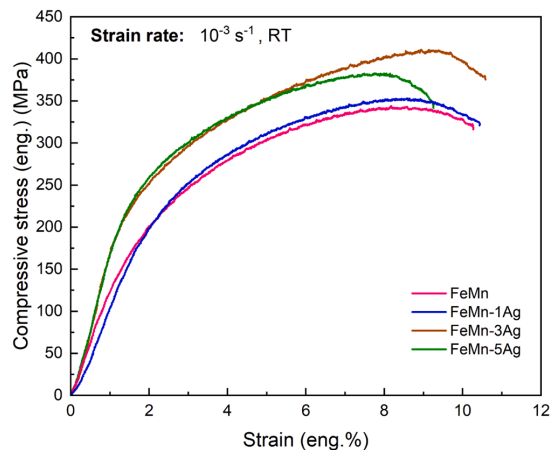


**Fig. 6.** Compression stress-strain curves for FeMn, FeMn-1Ag, FeMn-3Ag and FeMn-5Ag samples. Tests were performed at a strain rate of  $10^{-3} \text{ s}^{-1}$  and halted at fracture.

and compressive strain (A) are presented in Table 1. The shape of the curves indicates the high ductility of the sample, especially considering its high porosity. All tested samples possess a high 0.2% compressive offset yield strength ( $R_{0.2}$ ), above 181 MPa. Among all tested samples, FeMn-3Ag and FeMn-5Ag show the highest compressive strength (430 and 398 MPa, respectively) compared to FeMn and FeMn-1Ag, as presented in Fig. 6. The highest values of  $R_{0.2}$  were obtained for the FeMn-5Ag sample (254 MPa), whereas FeMn-3Ag possesses the highest compressive strength (430 MPa).

FeMn-5Ag and FeMn-3Ag alloys exhibit better mechanical properties at compression than FeMn and FeMn-1Ag alloys, with the maximum 40% increase in  $R_{0.2}$  and 28% increase in  $R_m$ . This increase in mechanical strength is mainly attributed to the different phase compositions of the Ag-containing samples as well as to Ag precipitation at the grain boundaries, which leads to precipitation strengthening. The martensite platelets and Ag precipitates act as planar obstacles and can reduce the mean free path of the dislocation movement, thereby strengthening the material [9,54]. A similar increase in the mechanical properties of Ag-containing FeMn alloys was previously observed by Liu et al. [55], where the addition of 0.8 wt% Ag resulted in an increase in yield strength from 94 to 130 MPa, which was mainly attributed to Ag-rich particles on the grain boundaries. Even a small addition of 1 wt % Ag leads to an improvement in the mechanical properties when compared to the FeMn alloy. Moreover, the addition of Ag does not cause changes in the compressive strain and the values oscillate between 7.7% and 8.8%.

In Table 1, the literature values of  $R_{0.2}$ ,  $R_m$  and A are presented for various porous FeMn alloys. The samples presented in this study show results comparable to the porous, selective-laser-melted (SLM)-fabricated Fe-Mn alloy. At the same time, their strength is higher than that of most other porous alloys formed by sintering of powders. Compared to dense FeMn alloys with similar composition, our materials exhibit lower compression strength because the macropores present in the material act as stress concentration points during deformation.

The magnetic hysteresis loops of the FeMn-xAg alloys, measured by VSM at room temperature, are shown in Fig. 7. The results reveal that the saturation magnetization increases with the Ag content. Among all tested alloys, the highest magnetization value was obtained for the FeMn-5Ag alloy ( $1.075 \text{ emu g}^{-1}$ ), whereas the lowest value was obtained for the FeMn alloy without the addition of Ag ( $0.045 \text{ emu g}^{-1}$ ). MFM analyses were performed to further study the magnetic behaviour of the samples. The results (see Supplementary Fig. S3) reveal that FeMn-5Ag shows a more pronounced ferromagnetic signal than the FeMn-3Ag sample (for which virtually no magnetic contrast is detected). The magnetic contrast observed for the FeMn-5Ag sample indicates a weakly ferromagnetic response, in agreement with the low saturation magnetization observed in the corresponding hysteresis loop (Fig. 7), which is equivalent to approximately 0.5% the value of  $M_s$  of pure Fe ( $M_{s,Fe} = 220 \text{ emu g}^{-1}$ ). Since this was a counterintuitive result, DFT simulations were also run, aiming at finding a plausible explanation, as

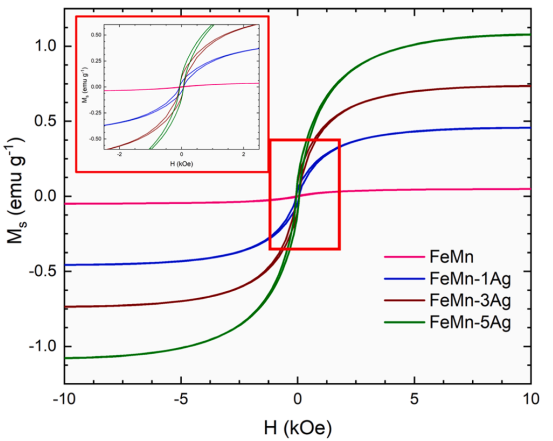


Fig. 7. Magnetization loops of the FeMn, FeMn-1Ag, FeMn-3Ag and FeMn-5Ag samples. Inset shows magnified region between  $-2.5 \text{ kOe}$  and  $2.5 \text{ kOe}$ .

it will be shown below. On the other hand, the fact that  $M_s$  is rather low in all investigated material, makes them compatible with MRI scans.

3.4.1. Ag influences the FeMn magnetization and crystal's magnetic moment

When adding a non-magnetic material like Ag to FeMn, which is well known for its antiferromagnetic properties [59,60], it is not easy to explain the observed increasing magnetization trend of Fig. 7. To this end, the first step is to deeply understand the AFM properties of FeMn. The literature survey reveals many experimental data on  $\text{Fe}_x\text{Mn}_{1-x}$  alloys which do not agree on the type of AFM spin states [42,53,59–64]. For example, neutron diffraction experiments found AFM long-range order in chemically disorder bulk  $\gamma\text{-Fe}_{0.75}\text{Mn}_{0.25}$  [42,59], similar to the 1Q spin state in Fig. 4(a), while Mössbauer neutron diffraction measurements revealed three AFM states depending on the Mn composition named 1Q (the collinear structure for Mn -rich and Fe-rich contents) and 2Q or 3Q (the non-collinear ones for  $\gamma\text{-Fe}_x\text{Mn}_{1-x}$ ,  $0.3 < x < 0.8$  alloys) [59–61]. Moreover, the addition of Mn drastically reduces the magnetic susceptibility of Fe-based alloys [55] while for  $\text{Fe}_x\text{Mn}_{1-x}$ ,  $0.3 < x < 0.8$  alloys, experiments suggested the 1Q state for  $\text{Fe}_{0.66}\text{Mn}_{0.34}$  [62], the 3Q (partially the 2Q) state for  $\text{Fe}_{0.5}\text{Mn}_{0.5}$  [63] and the 3Q for  $\text{Fe}_{0.54}\text{Mn}_{0.46}$  [64], resulting in a lack of experimental consensus. This behaviour could be attributed to bcc Mn which not only undergoes a first-order transition from a low spin state to high spin state in both ferromagnetic (FM) and AFM states, but it is also sensitive to compression or expansion [65]. To this end, earlier calculations revealed a narrow double moment region where low and high spin states co-exist, giving rise to dissimilar lattice constants [66]. Therefore, the introduction of a third element in the system, like Ag, could introduce local stress (compression or expansion in the interatomic distances) which might lead to different behaviour in the magnetic properties, in line with C addition in Fe-Mn-C, which may give rise to spin-glass-like regions [67]. It is worth reminding here the Ag preference towards Mn's first neighbour atoms as depicted in Fig. 4 (Section 3.2), which means that the electronic and magnetic properties of Mn atoms are mainly affected by Ag atoms. Furthermore, in previous reports describing Fe-30Mn-xAg alloys, the authors found a tendency to decrease the magnetization upon the addition of Ag [30]. For example, in the reports by Liu et al. [30,55], the addition of up to 5 wt% Ag led to a slight decrease in magnetic susceptibility. In our case, the FeMn-xAg, as shown in Fig. 8(a), reveals a small increase in magnetization upon Ag addition which can be a result of the higher Mn amount ( $\sim 50 \text{ wt\%}$ ) along with the observed phase transformation and the corresponding co-existence of  $\gamma$  and  $\epsilon$  phases that

Table 1  
Selected parameters calculated from the compression tests: yield strength ( $R_{0.2}$ ), compressive strength ( $R_m$ ) and compressive strain (A) together with literature values on porous and dense Fe-Mn alloys.

Material	$R_{0.2}$ (MPa)	$R_m$ (MPa)	A [%]	Reference
FeMn	$181 \pm 6$	$336 \pm 8$	$8.5 \pm 0.50$	This study
FeMn-1Ag	$205 \pm 26$	$352 \pm 14$	$8.3 \pm 0.3$	This study
FeMn-3Ag	$234 \pm 16$	$430 \pm 7$	$8.8 \pm 0.5$	This study
FeMn-5Ag	$254 \pm 10$	$398 \pm 10$	$7.7 \pm 0.3$	This study
SLM Fe-35Mn scaffold	$89.2 \pm 1.9$	$304.0 \pm 7.4$	-	[56]
Porous PM Fe-35Mn	64	567	-	[24]
10 wt%HA+Fe30Mn	-	$186 \pm 12$	-	[57]
Porous Fe-44Mn	$10 \pm 1$	-	-	[58]
Dense Fe-30Mn-6Si-1.2Ag	$353 \pm 34$	$1849 \pm 39$	-	[33]

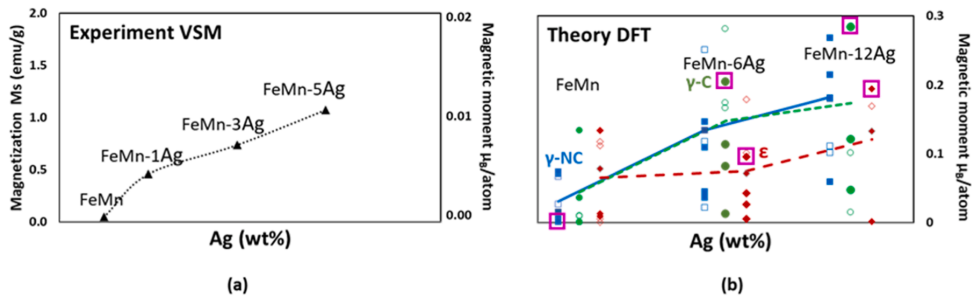


**Fig. 8.** Magnetization of FeMn-xAg by experimental (a) and theoretical (b) data. In (a) the magnetic moment in  $\mu_B/\text{atom}$  is derived from the Magnetization  $M_s$ . The compositions FeMn-6Ag (wt%) describe the  $\gamma\text{-Fe}_{45.91}\text{Mn}_{48.18}\text{Ag}_{5.91}$  (wt%) and  $\gamma\text{-Fe}_{48.915}\text{Mn}_{45.14}\text{Ag}_{5.91}$  (wt%) cases while FeMn-12Ag (wt%) refers to  $\text{Fe}_{45.75}\text{Mn}_{46.51}\text{Ag}_{11.49}$  (wt%). In (b) open and filled symbols represent the DFT results on the theoretical and the experimental lattice constants while  $\gamma$ -Collinear ( $\gamma$ -C in green circles),  $\gamma$ -Non-Collinear ( $\gamma$ -NC in blue squares) and  $\epsilon$ -Collinear ( $\epsilon$  in red diamonds) stand for spin states in line with Fig. 4. As a guide to the eye, the average values of all under-study for each structure  $\gamma$ -C (green line),  $\gamma$ -NC (blue line) and  $\epsilon$  (red line) that might coexist in the experimental conditions are also shown. The energetically favoured  $\gamma$ -NC,  $\gamma$ -C and  $\epsilon$  cases are highlighted by magenta squares. Note that the experimental values of  $M_s$  are a bit lower than the theoretical ones. This can be due, at least in part, to the formation of Ag precipitates (i.e., a fraction of the Ag added to the system does not get introduced into the FeMn crystallographic structures but, instead, remains in the form of Ag precipitates). Also, bear in mind that the calculations were performed at tiny periodic unit cells and 0 K whereas the magnetic measurements are performed at room temperature.

possess different magnetic properties.

Firstly, the total crystal magnetic moment was calculated in order to compare it with the experimental data of this work. In Fig. 8(a, b) both experimental magnetization,  $M_s$ , and DFT crystal magnetic moment are enhanced with Ag content. In Fig. 8(a) the magnetic moment ( $\mu_B/\text{atom}$ ) is also calculated from the experimental magnetization  $M_s$  ( $\text{emu g}^{-1}$ ) and the weighted  $\text{g mol}^{-1}$  percentage for FeMn - x Ag ( $x = 0, 1, 3, 5$ ) %. In Fig. 8(b), the  $\gamma$ -FeMn crystal magnetic moment of the favored non-collinear  $\gamma$ -NC is zero (denoted by blue square), in agreement with previous theoretical and experimental data [35,39]. Nevertheless, the average crystal magnetic moment values of all the under-study cases in Fig. 4 are almost zero. In particular, the energetically favored  $\epsilon$ -FeMn shows an average crystal magnetic moment of  $0.065 \mu_B \text{ atom}^{-1}$  (from 0 up to  $0.13 \mu_B \text{ atom}^{-1}$ ) for several configurations and spin states which might coexist in the experimental conditions.

Concerning the FeMn-6Ag wt% and FeMn-12Ag wt% alloys, the average crystal magnetic moment also depends on the spin states and structural configuration along with compositions showing, nevertheless, a small  $M_s$  increase behaviour upon Ag substitution. Namely, the average crystal magnetic moment of  $\gamma$ -NC and  $\gamma$ -C tends to increase upon Ag substitution, similar to the experimental magnetization, while the  $\epsilon$  magnetic moment is also enhanced in  $\epsilon$ -FeMn-6Ag. The calculated magnetic moment of the energetically favored configurations is presented in Fig. 8(b) showing the enhanced  $\mu_B$  upon Ag substitution. Although there is an agreement between the present experimental data and the theoretical calculations, one should bear in mind that the DFT unit cells are tiny and cannot include dislocations or grain boundaries which might also influence the spin states and the concomitant magnetic moments. The increase of the Fe magnetic moment upon a non-magnetic element like Cu was also observed in the nanocluster cases [68].

### 3.4.2. Ag alters the Fe and Mn atomic magnetic moment

The Fe and Mn atomic magnetic moment of austenite and martensite structures were evaluated with and without Ag atoms. Starting with the  $\gamma$ -FeMn, the atomic magnetic moments stand in the range of  $1.3\text{--}1.8 \mu_B$  for the Fe ( $m_{Fe}$ ) and within  $1.83\text{--}2.4 \mu_B$  for the Mn ( $m_{Mn}$ ) atoms, in line with previous GGA-DFT calculations [37,39]. In particular, the energetically favored 1Q collinear configuration of Fig. 4(a) has  $m_{Fe} = \pm 1.56 \mu_B$  and  $m_{Mn} = \pm 2.20 \mu_B$  compared to  $\pm 1.54 \mu_B$  and  $\pm 2.08 \mu_B$ , respectively, of Ref. 35 while the 3Q non-collinear spin state  $m_{Fe}$  ( $1.87 \mu_B$ ) and  $m_{Mn}$  ( $2.17 \mu_B$ ) are in line with the corresponding  $m_{Fe}$  ( $1.85 \mu_B$ ) and  $m_{Mn}$  ( $2.12 \mu_B$ ) [37]. It should be noted that, like in previous DFT studies, for all under-study cases of  $\gamma$ -FeMn, the atomic

magnetic moment of Mn is always higher than the Fe ones. The average magnetic moment of  $\gamma$ -FeMn is zero for the AFM collinear 1d spin states due to the Fe-Fe and Mn-Mn nearest neighbor antiferromagnetic interactions and  $0.008 \mu_B \text{ atom}^{-1}$  for the noncollinear 3Q configuration while non-zero but relatively small (less than  $0.06 \mu_B \text{ atom}^{-1}$ ) values are found for the other austenite spin states. The Fe and Mn atomic magnetic moments in  $\epsilon$ -FeMn are reduced compared to the  $\gamma$ -FeMn while the  $m_{Mn}$  values might be similar or even smaller than  $m_{Fe}$ . In particular, the favored FeMn [0001] AFM spin state has  $m_{Fe} = 1.42 \mu_B$  and  $m_{Mn} = -1.15 \mu_B$  at the  $\epsilon\text{-Fe}_{50}\text{Mn}_{50}$  and might be lowered to  $m_{Fe} = 0.65 \mu_B$  and  $m_{Mn} = -0.42 \mu_B$  in the relaxed DFT  $\epsilon\text{-Fe}_{50}\text{Mn}_{50}$  lattice. It should be noted that all  $\epsilon$ -FeMn cases prefer the AFM spin states against the FM ones in line with [42]. These DFT results are in agreement with the experimentally observed magnetic moment reduction due to increase of Mn content [60] especially when co-existence of both  $\gamma$  and  $\epsilon$  phases holds.

Concerning the  $\gamma$ -FeMn-6Ag wt%, the collinear AFM spin state becomes favoured along with the Ag preference in Mn-rich 1st neighbour environment shown in Fig. 9. Although the Ag atomic moment is virtually zero, the presence of Ag atom alters the 1Q collinear spin symmetry of the  $\gamma$ -FeMn system influencing the atomic magnetic moment of the Fe and Mn neighbouring atoms compared to the  $\gamma$ -FeMn ( $m_{Fe} = \pm 1.56 \mu_B$  and  $m_{Mn} = \pm 2.20 \mu_B$ ), resulting in a range from  $0.25$  to  $-1.72 \mu_B$  for  $m_{Fe}$  and from  $2.08$  to  $2.62 \mu_B$  for  $m_{Mn}$  which depends on the neighbor distance and the spin direction. In particular, Ag has 12 first neighbors consisting of four Fe and eight Mn atoms. The Fe first neighbors are located in the same (001) plane with Ag and show  $-1.72 \mu_B$  while upon Ag introduction they lose  $-0.02 e^-$  per atom. In addition, due to atomic relaxation, the Ag-Fe first neighbor distance increases to  $2.624 \text{ \AA}$  compared to  $2.546 \text{ \AA}$  (stand for  $a\sqrt{2}/2$ ,  $a = 3.6 \text{ \AA}$  experimental value used in the simulation cell) resulting in 3.1% local expansion of the Ag-Fe bonds and therefore local stress. In the third column of Fig. 9(a) the electron charge density difference is depicted along with the Ag, Fe and Mn atomic balls. The blue sphere around Ag particle denotes the Ag's spherical  $s$  electron charge depletion ( $-0.024 e^-$  per atom) which also affects its first and second neighbourhood. In particular, the second Ag-Fe neighbors retain the  $3.6 \text{ \AA}$  distance but they gain charge  $+0.03 e^-$  per atom which is presented by green hemispheres in the third column. The rest of Fe neighboring atoms' distances are not affected by the Ag presence although they gain charge similar to the second neighbors. The Mn-Ag first neighbor distance is expanded by 3.4%, the atomic magnetic moment is increased to  $2.62 \mu_B$  or  $-2.95 \mu_B$

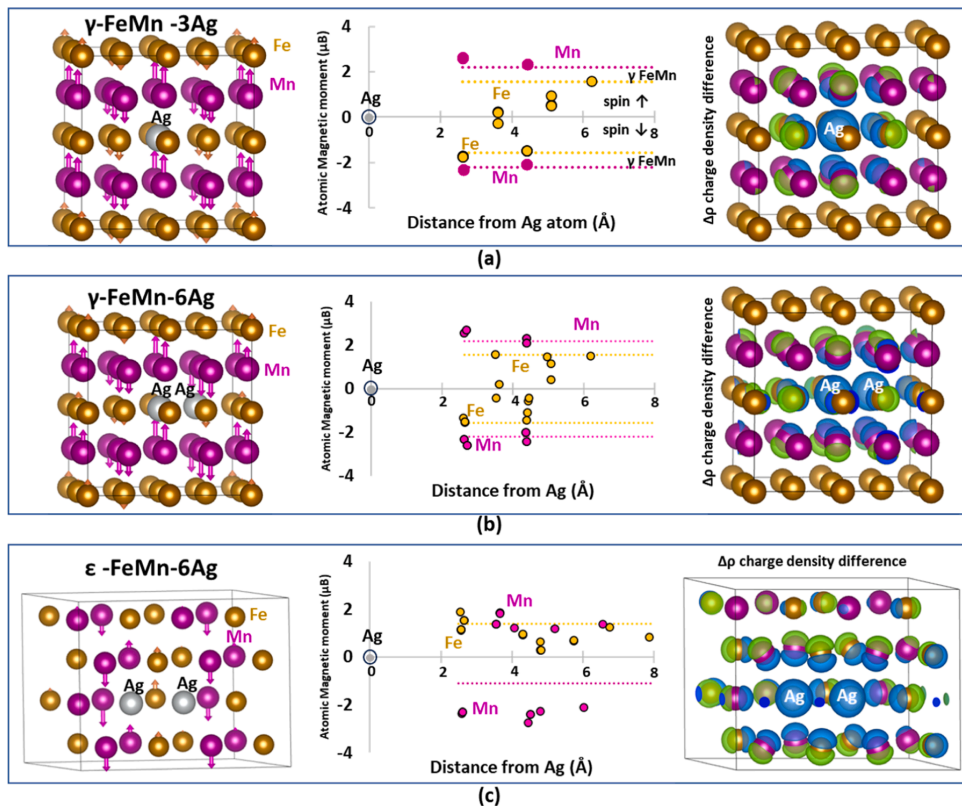


**Fig. 9.** FeMn-Ag atomic representation and spin state, atomic magnetic moment and electronic charge density difference: (a)  $\gamma$ -FeMn-6Ag wt%, (b)  $\gamma$ -FeMn-12Ag wt% and (c)  $\epsilon$ -FeMn-12Ag wt%. Fe, Mn and Ag atoms are presented by gold, magenta and grey spheres. Dashed lines denote the Fe (gold) and Mn (magenta) atomic magnetic moment of  $\gamma$ -FeMn (in a, b) or  $\epsilon$ -FeMn (in c). In the third column the electron charge density difference revealing charge transfer is shown along with the atomic representation, as blue spheres around Ag atoms and blue/green hemispheres with isovalue + 0.1 (for charge gain  $e^-/\text{Bohr}^3$  in green) and  $-0.1e^-/\text{Bohr}^3$  (for charge loss in blue).

compared to  $m_{\text{Mn}} = \pm 2.20 \mu_B$  of the pure  $\gamma$ -FeMn, as shown in Fig. 9 (second column). In line with Fe, the Mn first neighbor atoms of Ag lose charge  $-0.02 e^-/\text{atom}$  (average value on the 8 atoms presented with blue hemispheres in the third column) while the following neighbors gain charge (green hemispheres). This charge loss or gain is also illustrated in the electron charge density difference  $\Delta\rho$  of the third column in Fig. 9 where the blue spherical area around the Ag atom denotes that the 5 s orbital main loss ( $-0.024 e^-$  per atom) also affects the neighbouring atoms. In particular, the electronic charge transfer on the Ag's neighborhood atoms, caused by Ag, reveals electric dipole moment features on the Fe or Mn atoms having charge loss close to Ag (blue hemisphere) and charge gain away from Ag (green hemisphere) in the bond direction between Ag and all neighboring atoms.

Similar behaviour is also depicted in the case of  $\gamma$ -FeMn-12Ag wt% and  $\epsilon$ -FeMn-12Ag wt%, now influencing a higher number of Ag atoms' neighbors. In the case of  $\epsilon$ -FeMn-12Ag wt%, the Fe (from  $1.10\mu_B$  up to  $1.9\mu_B$ ) and Mn ( $-2.30\mu_B$ ) first neighbor atomic magnetic moments increase compared to the pure  $\epsilon$ -FeMn ( $+1.37\mu_B$  for Fe and  $-1.11\mu_B$  for Mn) while the Fe next-next nearest neighbors reveal smaller atomic magnetic moment (from  $0.2\mu_B$  up to  $0.9\mu_B$ ) and slowly converge towards the  $\epsilon$ -FeMn far from Ag atoms. The Ag-Fe first neighbor bonds are expanded from 1% up to 4% along with the Ag-Mn bonds (2%) showing the local stress introduction by Ag that might be responsible for the changes of spin states, in line with bcc Mn spin alterations due to expansion or contraction [65,66]. In addition, charge transfer is

observed in the electronic charge density difference from the Ag atoms and its first neighbors (blue area indicated charge loss) towards the second and third neighbors (green hemispheres show charge gain and blue hemispheres charge loss along the Ag-neighbor atoms directions.). This Ag charge loss ( $0.02 e^-$  per atom), although small, is due to Ag's unpaired 5 s electron resulting in a positively charged Ag ion in the FeMn matrix, revealing the will of Ag to offer electrons to the system. This in turn might be related to its antibacterial properties and its ability to induce generation of reactive oxygen species [69,70]. Charge transfer between Ag and Al has been also found in the case of Ag in AlN matrix affecting the electronic properties and bonding characteristics [71].

#### 4. Conclusions

The present study was devised to determine the effect of Ag on the phase composition and physical properties (mechanical and magnetic) of FeMn alloys. The study consisted of a variety of experimental techniques and was supported by theoretical calculations. The basic structural and magnetic properties of FeMn were reproduced in line with previous data.

This study has experimentally identified the co-existence of  $\gamma$ -FeMn and  $\epsilon$ -FeMn upon Ag addition to equiatomic FeMn alloys, which is related to the decrease of the ISF energy along with the decrease in the  $\Delta E$  between the two phases. The Ag atoms prefer the ISF sites, thus depleting the electron charge at the SF plane and its neighboring atomic



layers, lowering the interatomic bond strength and allowing an easier slip and a possible transition from the austenite towards martensite structure. Small Ag contents in FeMn alter the well-known non-collinear FeMn spin configuration due to the modification of its nearest neighbor Fe and Mn atomic magnetic moment. In addition, Ag prefers the Mn-rich against the Fe-rich first neighborhood, affecting however both Mn and Fe nearest neighbors' atomic magnetic moment, expanding the first neighbor bond length and causing local stress. As a result, although Ag has almost zero magnetic moment, it causes a gradual increase in the FeMn magnetization.

The addition of Ag led to an increased mechanical strength of FeMn alloys at compression, which was attributed to the presence of  $\epsilon$ -martensite as well as to precipitation strengthening. Our results could be used for the design of functionalized FeMn-Ag based alloys with targeted structures and properties, suitable for widespread technological applications.

### CRedit authorship contribution statement

A.B. performed most of the experiments, helped in the interpretation of the data and wrote the first version of the manuscript. C.E.L. performed the DFT calculations. L.A.A. performed part of the experiments. I. S. performed the MFM observations. E.P. and J.S. supervised the work, helped in the interpretation of the data and revised the written manuscript.

### Declaration of Competing Interest

The authors declare the following financial interests/personal relationships which may be considered as potential competing interests: Jordi Sort reports financial support was provided by European Commission. Jordi Sort reports was provided by State Agency of Research. Jordi Sort reports was provided by Government of Catalonia.

### Data Availability

Data will be made available on request.

### Acknowledgements

This project has received funding from the European Union's Horizon 2020 research and innovation programme under the Marie Skłodowska-Curie grant agreement No. 861046 ('Bioremia' European Training Network). Partial financial support from the Spanish Government (PID2020-116844RB-C21) and the Generalitat de Catalunya (2021-SGR-00651) is also acknowledged.

### Appendix A. Supporting information

Supplementary data associated with this article can be found in the online version at [doi:10.1016/j.jallcom.2023.171640](https://doi.org/10.1016/j.jallcom.2023.171640).

### References

- [1] J.H. Schmitt, T. lung, C. R. Phys. 19 (2018) 641–656.
- [2] M. Soleimani, A. Kalhor, H. Mirzadeh, Mater. Sci. Eng. C. 795 (2020), 140023.
- [3] V. Kuncser, M. Valeanu, G. Schinteie, G. Filoti, I. Mustata, C.P. Lungu, A. Anghel, H. Chiriac, R. Vladoiu, J. Bartolome, J. Magn. Magn. Mater. 320 (2008) e226–e230.
- [4] T. Lin, D. Mauri, IEEE Trans. Magn. 35 (1999) 2607–2609.
- [5] Z. Ma, M. Gao, D. Na, Y. Li, L. Tan, K. Yang, Mater. Sci. Eng. C. 103 (2019), 109718.
- [6] H. Hermawan, A. Purnama, D. Dube, J. Couet, D. Mantovani, Acta Biomater. 6 (2010) 1852–1860.
- [7] A. Bartkowska, O. Careta, A.B. Turner, A. Blanquer, E. Ibáñez, M. Trobos, C. Nogués, E. Pellicer, J. Sort, Mater. Adv. 4 (2023) 616–630.
- [8] Y.K. Lee, C.S. Choi, Metall. Mater. Trans. A 31 (2000) 355–360.
- [9] D.T. Pierce, J.A. Jiménez, J. Bentley, D. Raabe, C. Oskay, J.E. Wittig, Acta Mater. 68 (2014) 238–253.
- [10] O. Grässel, L. Krüger, G. Frommeyer, L.W. Meyer, Int. J. Plast. 16 (2000) 1391–1409.
- [11] W.S. Yang, C.M. Wan, J. Mater. Sci. 25 (1990) 1821–1823.
- [12] J. Flocchi, J.N. Lemke, S. Zilio, C.A. Biffi, A. Coda, A. Tuissi, Mater. Today Commun. 27 (2021), 102447.
- [13] I. Bleskov, T. Hickel, J. Neugebauer, A. Ruban, Phys. Rev. B 93 (2016), 214115.
- [14] H. Gholizadeh, C. Draxl, P. Puschnig, Acta Mater. 61 (2013) 341–349.
- [15] A. Abbasi, A. Dick, T. Hickel, J. Neugebauer, Acta Mater. 59 (2011) 3041–3048.
- [16] Y. Hwang, S. Choi, J. Choi, S. Cho, Sci. Rep. 9 (1) (2019) 10.
- [17] I. Gutierrez-Urrutia, D. Raabe, Acta Mater. 59 (2011) 6449–6462.
- [18] H. Hermawan, D. Dubé, D. Mantovani, J. Biomed. Mater. Res. A 93 (2010) 1–11.
- [19] H. Hermawan, Prog. Biomater. 7 (2018) 93–110.
- [20] H. Hermawan, D. Dubé, D. Mantovani, Acta Biomater. 6 (2010) 1693–1697.
- [21] H. Hermawan, D. Dubé, D. Mantovani, Adv. Mat. Res. 15–17 (2007) 107–112.
- [22] H. Hermawan, H. Alamdari, D. Mantovani, D. Dubé, Powder Met. 51 (2008) 38–45.
- [23] Y.P. Feng, A. Blanquer, J. Fornell, H. Zhang, P. Solsona, M.D. Baró, S. Suriñach, E. Ibáñez, E. García-Lecina, X. Wei, R. Li, L. Barrios, E. Pellicer, C. Nogués, J. Sort, J. Mater. Chem. B 4 (2016) 6402–6412.
- [24] M.S. Dargusch, A. Dehghan-Manshadi, M. Shahbazi, J. Venezuela, X. Tran, J. Song, N. Liu, Ch Xu, Q. Ye, C. Wen, ACS Biomater. Sci. Eng. 5 (4) (2019) 1686–1702.
- [25] H.J. Busscher, H.C. van der Mei, G. Subbiahdoss, P.C. Jutte, J.J.A.M. van den Dungen, S.A.J. Zaai, M.J. Schultz, D.W. Grainger, Sci. Transl. Med. 4 (2012) 153rv10.
- [26] S. Daghighi, J. Sjollem, H.C. van der Mei, H.J. Busscher, E.T.J. Rochford, Biomaterials 34 (2013) 8013–8017.
- [27] A.B. Lansdown, J. Wound Care 11 (2013) 125–130.
- [28] S. Chernousova, M. Epple, Angew. Chem. Int. Ed. 52 (2013) 1636–1653.
- [29] P. Sotoudeh Bagha, M. Khakbiz, S. Sheibani, H. Hermawan, J. Alloy. Compd. 767 (2018) 955–965.
- [30] R.Y. Liu, R.G. He, Y.X. Chen, S.F. Guo, Acta Metall. Sin. Engl. Lett. 32 (2019) 1337–1345.
- [31] H.A. Wriedt, W.B. Morrison, W.E. Cole, Metall. Trans. 4 (1973) 1453–1456.
- [32] R.Y. Liu, R.G. He, L.Q. Xu, S.F. Guo, Acta Metall. Sin. Engl. Lett. 31 (2018) 584–590.
- [33] N. Babacan, F. Kochta, V. Hoffmann, T. Gemming, U. Kühn, L. Giebeler, A. Gebert, J. Hufenbach, Mater. Today Commun. 28 (2021), 102689.
- [34] A. Dehghan-Manshadi, J. Venezuela, A.G. Demir, Q. Ye, M.S. Dargusch, J. Manuf. Process. 80 (2022) 642–650.
- [35] G. Kresse, J. Hafner, Phys. Rev. B 48 (1993) 13115–13118.
- [36] G. Kresse, J. Furthmüller, Phys. Rev. B Condens. Matter Mater. Phys. 54 (1996) 11169–11186.
- [37] D. Spisák, J. Hafner, Phys. Rev. B Condens. Matter Mater. Phys. 61 (2000) 11569–11575.
- [38] J.P. Perdew, K. Burke, M. Ernzerhof, Phys. Rev. Lett. 77 (1996) 3865–3868.
- [39] M. Ekholm, I.A. Abrikosov, Phys. Rev. B Condens. Matter Mater. Phys. 84 (2011), 104223.
- [40] H.C. Herper, E. Hoffmann, P. Entel, Phys. Rev. B Condens. Matter Mater. Phys. 60 (1999) 3839–3848.
- [41] D.E. Jiang, E.A. Carter, Phys. Rev. B Condens. Matter Mater. Phys. 67 (2003), 214103.
- [42] J.S. Kovel, J.S. Kasper, J. Phys. Chem. Solids 24 (1963) 529–536.
- [43] V.T. Witusiewicz, F. Sommer, E.J. Mittemeijer, J. Phase Equilibria Diffus. 25 (2004) 346–354.
- [44] Y.K. Lee, J.H. Jun, C.S. Choi, ISIJ Int 37 (1997) 1023–1030.
- [45] C.M. Li, F. Sommer, E.J. Mittemeijer, Mater. Sci. Eng. A 325 (2002) 307–319.
- [46] P. Marinelli, A. Baruj, A. Fernández Guillermet, M. Sade, Z. Metall. 92 (2001) 489–493.
- [47] P. Singh, S. Picak, A. Sharma, Y.I. Chumlyakov, R. Arroyave, I. Karaman, D. Johnson, Phys. Rev. Lett. 127 (2021), 115704.
- [48] J. Dash, H.M. Otte, Acta Met. 11 (1963) 1169–1178.
- [49] S. Takaki, H. Nakatsu, Y. Tokunaga, Mater. Trans. JIM 34 (1993) 489–495.
- [50] G. Parr, J. Iron Steel Inst. 171 (1952) 137–141.
- [51] A. Dick, T. Hickel, J. Neugebauer, Steel Res. Int. 80 (2009) 603–608.
- [52] X. Cui, J. Wang, H. Wang, X.G. Lu, J. Jiang, Met. Mater. Int. 28 (2022) 1215–1223.
- [53] B.C. De Cooman, Y. Estrin, S.K. Kim, Acta Mater. 142 (2018) 283–362.
- [54] D.T. Pierce, J.A. Jiménez, J. Bentley, D. Raabe, J.E. Wittig, Acta Mater. 100 (2015) 178–190.
- [55] R.Y. Liu, R.G. He, L.Q. Xu, S.F. Guo, Acta Metall. Sin. Engl. Lett. 31 (2018) 584–590.
- [56] D. Carluccio, C. Xu, J. Venezuela, Y. Cao, D. Kent, M. Birmingham, A.G. Demir, B. Previtali, Q. Ye, M. Dargusch, Acta Biomater. 103 (2020) 346–360.
- [57] M. Heiden, E. Nauman, L. Stanciu, Adv. Healthc. Mater. 6 (2017) 1700120.
- [58] P. Liu, D. Zhang, Y. Dai, J. Lin, Y. Li, C. Wen, Acta Biomater. 114 (2020) 485–496.
- [59] Y. Ishikawa, Y. Endoh, J. Appl. Phys. 39 (2003) 1318.
- [60] Y. Endoh, Y. Ishikawa, J. Phys. Soc. Jpn. 30 (2013) 1614–1627.
- [61] H. Umebayashi, Y. Ishikawa, J. Phys. Soc. Jpn. 21 (1966) 1281–1294.
- [62] P. Bisanti, G. Mazzone, F. Sacchetti, J. Phys. F 17 (1987) 1425–1435.
- [63] S.J. Kennedy, T.J. Hicks, J. Phys. F 17 (1987) 1599–1604.
- [64] S. Kawarazaki, Y. Sasaki, K. Yasuda, T. Mizusaki, A. Hirai, J. Phys. Condens. Matter 2 (1990) 5747–5752.
- [65] S. Fujii, S. Ishida, S. Asano, J. Phys. Soc. Jpn. 60 (1991) 4300–4310.
- [66] N.E. Brener, G. Fuster, J. Callaway, J.L. Fry, Y.Z. Zhao, J. Appl. Phys. 63 (1988) 4057–4059.
- [67] N.I. Medvedeva, D. van Aken, J.E. Medvedeva, J. Phys. Condens. Matter 22 (2010), 316002.
- [68] C.S. Cutrano, C.E. Lekka, J. Alloy. Compd. 707 (2017) 114–119.



- [69] M. Dhanalakshmi, S. Thenmozhi, K. Manjula Devi, S. Kameshwaran, *Int. J. Pharm. Biol. Arch.* 4 (2013) 819–826.
- [70] T. Ishida, *MOJ Toxicol.* 4 (2018) 345–350.
- [71] Ch.E. Lekka, P. Patsalas, Ph Komninou, G.A. Evangelakis, *J. Appl. Phys.* 109 (2011), 054310.

## **Supplementary information for:**

### **Silver-induced $\gamma \rightarrow \epsilon$ martensitic transformation in FeMn alloys: an experimental and computational study**

Aleksandra Bartkowska<sup>a</sup>, Christina Lekka<sup>b</sup>, Ludovico Andrea Alberta<sup>c</sup>, Irena Spasojevic<sup>a</sup>, Eva Pellicer<sup>a</sup>, Jordi Sort<sup>a,d</sup>

<sup>a</sup>*Departament de Física, Universitat Autònoma de Barcelona, E-08193 Bellaterra (Cerdanyola del Vallès), Spain*

<sup>b</sup>*Department of Materials Science and Engineering, University of Ioannina, Ioannina 45110 Greece*

<sup>c</sup>*Leibniz Institute for Solid State and Materials Research Dresden (IFW Dresden), Helmholtzstr. 20, D-01069 Dresden, Germany*

<sup>d</sup>*Institució Catalana de Recerca i Estudis Avançats (ICREA), Pg. Lluís Companys 23, E-08010 Barcelona, Spain*

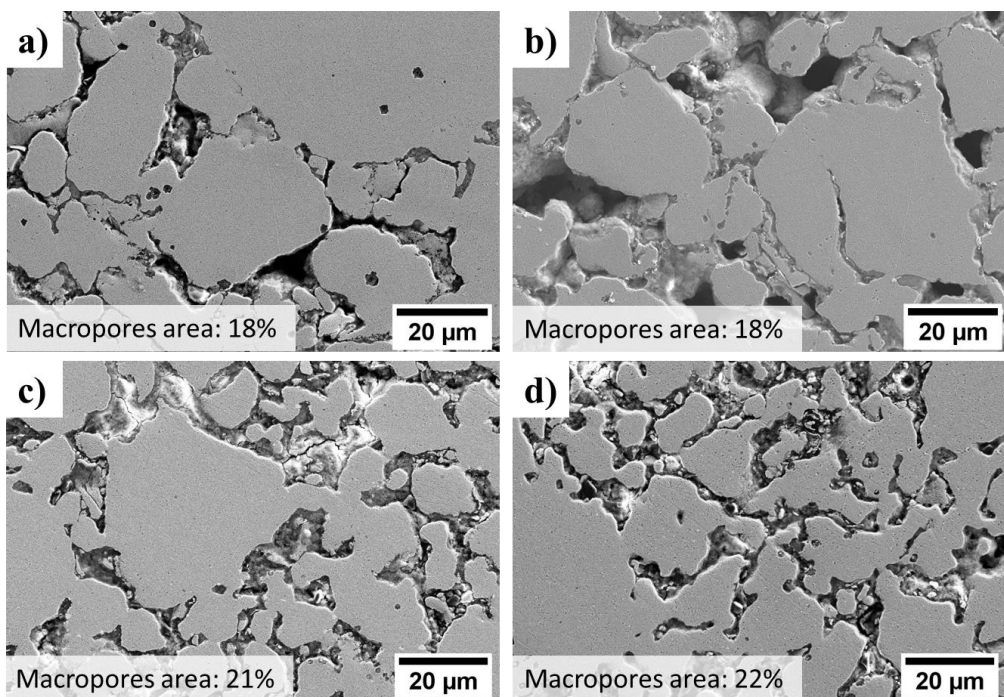


**Fig. S1:** SEM micrographs of the polished surface of (a) FeMn alloy, (b) FeMn-1Ag, (c) FeMn-3Ag and (d) FeMn-5Ag alloys

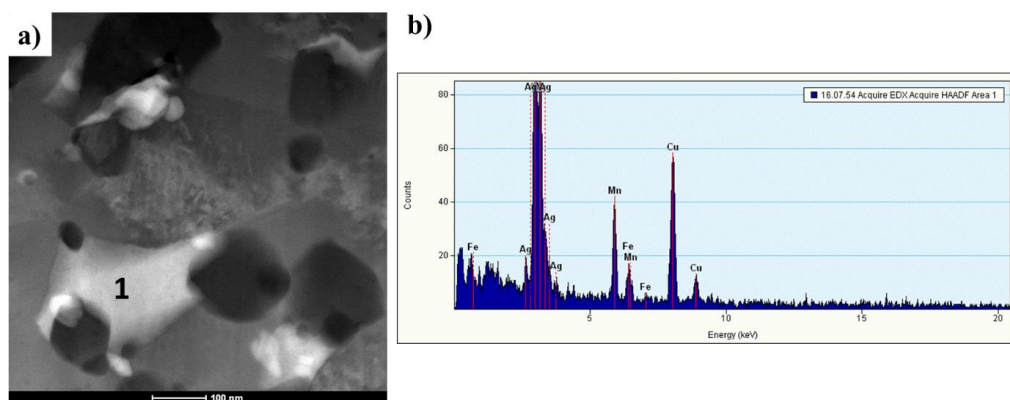


**Fig. S2:** High angle annular dark field (HAADF) image of the region containing Ag-particles (a) together with EDS analysis of particles marked with 1 (b), confirming the Ag-rich precipitates.

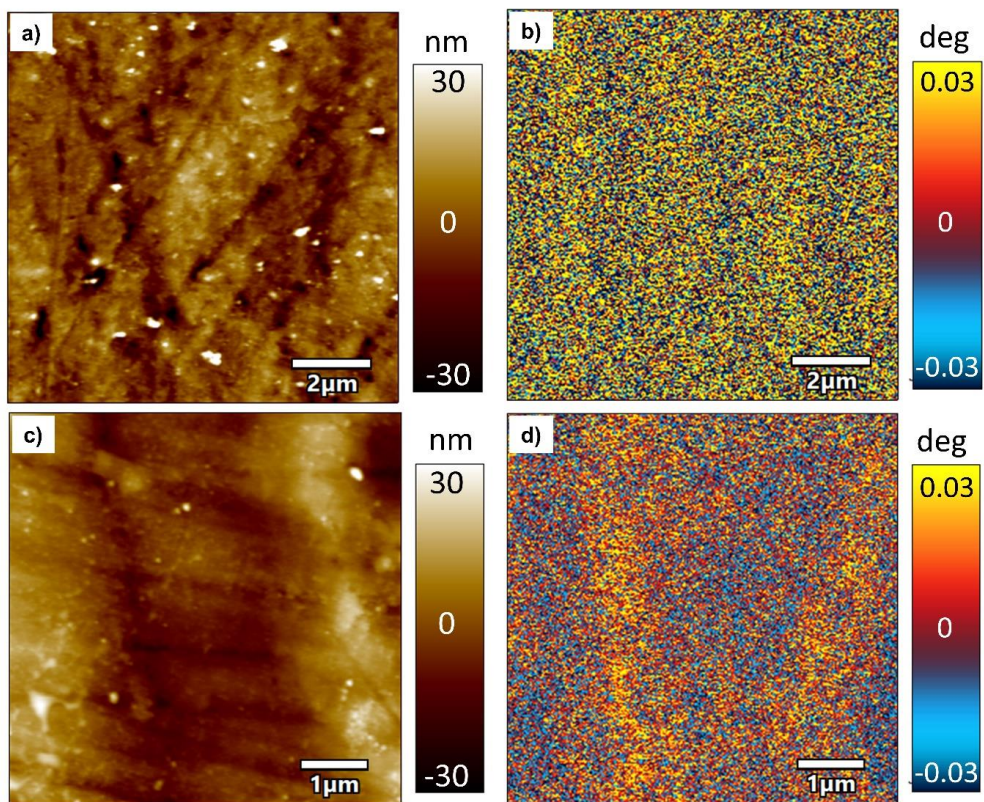


**Fig. S3:** AFM topography images and MFM phase images of FeMn-3Ag alloy (a, b) and FeMn-5Ag alloy (c, d), respectively.

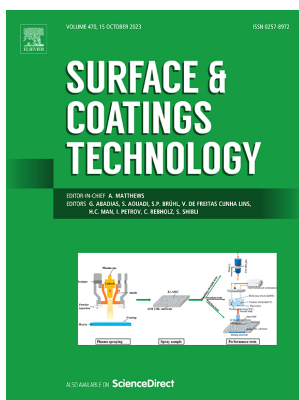
### **4.3 Paper 3: Accelerated biodegradation of FeMn porous alloy coated with ZnO: effect on cytocompatibility and antibiofilm properties**

The third and last study focuses on the deposition of ZnO coating onto previously developed FeMn porous alloy by dip-coating and the evaluation of its effect on biodegradability, cytocompatibility and antibiofilm properties.

The study delved into the impact of the ZnO coating on various aspects such as the material's internal structure, degradation rate, cytocompatibility, and its antibacterial and/or antibiofilm properties. The biodegradability of newly developed materials was analysed through static immersion tests in HBSS performed for up to 28 days. The results revealed that the degradation rate of FeMn/ZnO sample is significantly higher than that of uncoated FeMn. This was attributed to several factors such as the segregation of Fe at grain boundaries, the development of iron-manganese oxide, and the limited formation of degradation products on ZnO.

In addition, the study included indirect cytotoxicity tests using Saos-2 cells cultured in sample-conditioned media and the findings showed no significant cytotoxicity in concentrations equal or below 50%. Furthermore, when assessing the formation of bacterial biofilms by *S. aureus*, the FeMn/ZnO-coated samples exhibited a noticeable reduction in total biofilm volume compared to the uncoated FeMn samples, which was mainly attributed to the accelerated degradation rate.

Overall, the results indicate that depositing a ZnO coating on FeMn alloys significantly enhances the degradation rate of the material, maintains cytocompatibility and diminishes the accumulation of biofilms in comparison to uncoated FeMn alloys.



### **Accelerated biodegradation of FeMn porous alloy coated with ZnO: effect on cytocompatibility and antibiofilm properties**

Aleksandra Bartkowska<sup>1</sup>, Adam Benedict Turner<sup>2,3</sup>, Andreu Blanquer<sup>4</sup>, Aliona Nicolenco<sup>5</sup>, Margarita Trobos<sup>2,3</sup>, Carme Nogues<sup>4</sup>, Eva Pellicer<sup>1</sup>, Jordi Sort<sup>1,6</sup>

<sup>1</sup>Departament de Física, Universitat Autònoma de Barcelona, E-08193 Cerdanyola del Vallès, Spain

<sup>2</sup>Department of Biomaterials, Institute of Clinical Sciences, Sahlgrenska Academy, University of Gothenburg, Gothenburg, Sweden

<sup>3</sup>Centre for Antibiotic Resistance Research in Gothenburg (CARE), University of Gothenburg, Gothenburg, Sweden

<sup>4</sup>Departament de Biologia Cel·lular, Fisiologia i Immunologia, Universitat Autònoma de Barcelona, E-08193 Cerdanyola del Vallès, Spain

<sup>5</sup>CIDETEC Surface Engineering, Basque Research and Technology Alliance (BRTA), Paseo Miramon 196, 20014 Donostia-San Sebastian, Spain

<sup>6</sup>Institució Catalana de Recerca i Estudis Avançats (ICREA), Pg. Lluís Companys 23, E-08010 Barcelona, Spain



# Accelerated biodegradation of FeMn porous alloy coated with ZnO: Effect on cytocompatibility and antibiofilm properties

Aleksandra Bartkowska<sup>a,1</sup>, Adam Benedict Turner<sup>b,c,1</sup>, Andreu Blanquer<sup>d,\*</sup>, Aliona Nicolenco<sup>e</sup>, Margarita Trobos<sup>b,c,\*</sup>, Carme Nogues<sup>d</sup>, Eva Pellicer<sup>a,\*\*</sup>, Jordi Sort<sup>a,f</sup>

<sup>a</sup> Departament de Física, Universitat Autònoma de Barcelona, E-08193 Cerdanyola del Vallès, Spain

<sup>b</sup> Department of Biomaterials, Institute of Clinical Sciences, Sahlgrenska Academy, University of Gothenburg, Gothenburg, Sweden

<sup>c</sup> Centre for Antibiotic Resistance Research in Gothenburg (CARE), University of Gothenburg, Gothenburg, Sweden

<sup>d</sup> Departament de Biologia Cel·lular, Fisiologia i Immunologia, Universitat Autònoma de Barcelona, E-08193 Cerdanyola del Vallès, Spain

<sup>e</sup> CIDETEC Surface Engineering, Basque Research and Technology Alliance (BRTA), Paseo Miramon 196, 20014 Donostia-San Sebastian, Spain

<sup>f</sup> Institució Catalana de Recerca i Estudis Avançats (ICREA), Pg. Lluís Companys 23, E-08010 Barcelona, Spain

## ARTICLE INFO

### Keywords:

Zinc oxide coating  
iron-manganese alloys  
Biofilm  
Cytocompatibility  
*Staphylococcus aureus*  
Saos-2

## ABSTRACT

Fe-based alloys are being studied as potential candidates for biodegradable implants; however, their degradation rates remain too slow. To accelerate biodegradation while simultaneously hindering biofilm formation, a ZnO coating was deposited onto porous equiatomic FeMn alloy discs by sol-gel method using dip coating. The effect of the ZnO coating on the microstructure, biodegradability, cytocompatibility, and antibacterial properties were investigated. Biodegradability experiments were performed by immersing the specimens in Hank's balanced salt solution and measuring ion release after up to 28 days of immersion. The experiments showed an increased degradation of the FeMn/ZnO sample due to Fe segregation towards the grain boundaries, formation of iron-manganese oxide, and limited formation of degradation products on ZnO. Further, indirect Saos-2 cell cytotoxicity testing in 24 h sample-conditioned media showed no significant cytotoxicity in concentrations equal to or below 50 %. In addition, the total biofilm biovolume formed by *Staphylococcus aureus* on the FeMn/ZnO surface was significantly reduced compared to the uncoated FeMn. Taken together, these results show that the ZnO coating on FeMn improves the degradation rate, maintains cytocompatibility, and reduces biofilm accumulation when compared to an uncoated FeMn alloy.

## 1. Introduction

In recent years, metallic bioresorbable or biodegradable metals have emerged as potential candidates for stents and orthopaedic fixation devices such as bone pins, screws, wires, rods, or scaffolds [1–7]. The main idea behind biodegradable metals is to provide mechanical support while gradually degrading over a desired period of time and becoming completely dissolved when their function is fulfilled. Owing to the use of biodegradable materials, implant removal surgery can be avoided and thus the costs of medical treatment and risk of infection can be decreased [8,9]. Fe-based alloys are considered especially promising candidates for biodegradable implant applications due to their excellent mechanical properties and good biocompatibility. However, their degradation rate

is rather slow, limiting their clinical applications [2,3,10,11]. Therefore, the scientific community is currently exploring various solutions to enhance the degradation rate of Fe-based alloys. The common approaches include alloying Fe with other elements (e.g., C, Mn, Si), introducing porosity in the material, or macro-/nano-patterning [3,4,12–17]. In the past decade, surface modification approaches have emerged as an alternative and more efficient way to improve the overall performance of biodegradable metallic materials. These methods often involve ion implantation [18], laser ablation [19] or deposition of coatings [5,20–22]. For instance, zinc ion implantation on the surface of pure iron was found to accelerate the degradation rate by creating galvanic pairs between Fe and Zn clusters [18]. Modification of the Fe-Mn alloys surface by laser ablation increased their biodegradability

\* Corresponding authors.

\*\* Correspondence to: E. Pellicer, Departament de Física, Universitat Autònoma de Barcelona, E-08193 Cerdanyola del Vallès, Spain.

E-mail addresses: [andreu.blanquer@uab.cat](mailto:andreu.blanquer@uab.cat) (A. Blanquer), [margarita.trobos@biomaterials.gu.se](mailto:margarita.trobos@biomaterials.gu.se) (M. Trobos), [eva.pellicer@uab.cat](mailto:eva.pellicer@uab.cat) (E. Pellicer).

<sup>1</sup> A. Bartkowska and A.B. Turner contributed equally to this work as first authors.

<https://doi.org/10.1016/j.surfcoat.2023.129886>

Received 8 June 2023; Received in revised form 1 August 2023; Accepted 2 August 2023

Available online 4 August 2023

0257-8972/© 2023 The Authors. Published by Elsevier B.V. This is an open access article under the CC BY-NC-ND license (<http://creativecommons.org/licenses/by-nc-nd/4.0/>).



thanks to the formation of nanostructured metal oxides [19]. The deposition of coatings offers greater opportunities to adjust the corrosion and other characteristics of the system because the ultimate properties will arise from the interplay between the two components (bulk material and coating).

Recently, several authors have published reports on the improved properties of Fe-based alloys achieved by the deposition of second-phase coatings. For instance, Qi et al. [22] reported the mechanism of acceleration of Fe corrosion by polylactic acid (PLA) coating. A decrease in the local pH due to PLA hydrolysis and the fact that the PLA coating hindered the formation of a passivation layer were behind the observed enhanced degradation. In another report, polyethylene glycol (PEG) coatings were deposited on Fe alloy foam which helped improve its corrosion rate [20,21]. In a study by Huang et al. [23], a collagen coating was applied to the Fe-Mn alloy, and although it did not increase the corrosion rate of the alloy, it helped reduce cytotoxicity and improve osseointegration.

As biomaterial-associated infections are of concern, several approaches have been investigated to decrease the risk of infection [24,25]. One possible solution is the deposition of antibacterial and antibiofilm coatings on the biomaterial surface [26–28]. ZnO has been studied as an antibacterial material, demonstrating its capability to inhibit the growth of *Escherichia coli* [27] and *Staphylococcus aureus* [29,30]. The mechanism of antibacterial activity of ZnO is not yet well understood, but the production of reactive oxygen species on the surface of ZnO that cause oxidative stress to bacterial cells, ultimately causing their death is one of the plausible explanations [31]. Thin ZnO films can be deposited using a wide range of techniques such as sol-gel, spin- and dip-coating, metal-organic chemical vapour deposition, molecular beam epitaxy, pulsed laser deposition, or atomic layer deposition, amongst others [27,32,33]. Sol-gel approaches are especially attractive for their simplicity and ease of tailoring the properties of the synthesised films [33–35]. Several parameters of the sol-gel process can be controlled, such as the type of precursor and its concentration, the type of solvent and additives, the aging time of the mixture, the method of coating the substrate and post-heat treatment of the materials. Sol-gel-derived ZnO coatings have been successfully deposited on degradable Mg alloys [36] to increase cytocompatibility and osseointegration and inhibit bacterial adhesion and growth.

An implanted biodegradable material must be biocompatible (i.e., it must show an appropriate host response upon implantation), it cannot cause a toxic or allergic inflammatory response or be thrombogenic. The biocompatibility of implant materials can be determined by two key factors – the host reaction (caused by implanted material) and the degradation of the material *in vivo* [37]. When studying degradable metals, the second factor is crucial. The abundant degradation products should not cause any inflammatory response. Enhanced biodegradability can influence cell viability and proliferation since the released corrosion products can lead to histological changes in local tissues, due to toxic solutes and also to hypersensitivity to allergens [38].

The objective of this work was to study the effect of ZnO sol-gel-derived coatings deposited on degradable porous FeMn alloys in terms of material biodegradability, cytocompatibility and microbial interactions. The purpose of the ZnO layer deposited on the FeMn alloy is two-fold: to favour the degradation of the alloy, and to confer antibiofilm properties to the material, without compromising its cytocompatibility.

## 2. Materials and methods

### 2.1. Synthesis and characterization of ZnO coating deposited on FeMn alloy

ZnO was deposited on FeMn porous alloy discs by dip-coating. The porous equiatomic FeMn alloys were fabricated by powder metallurgy, namely by ball milling of initial Fe and Mn powders, followed by

pressing and sintering under vacuum at 900 °C. Details regarding the synthesis of the FeMn discs can be found elsewhere [15]. The ZnO precursor solution was prepared by mixing zinc acetate dihydrate (Zn (CH<sub>3</sub>COO)<sub>2</sub>·2H<sub>2</sub>O > 99.0 % purity, Merck, Germany) as a starting material, ethanol as a solvent, and monoethanolamine (C<sub>2</sub>H<sub>7</sub>NO, MEA, >99 % purity, Merck, Germany) as a stabilizer. Zinc acetate and MEA were purchased from Merck and used without further purification. To a solution of 0.5 M zinc acetate, MEA was added, keeping the zinc acetate to MEA ratio of 1:1. The solution was stirred for 2 h at 60 °C using a magnetic stirrer working at 500 rpm to prepare a clear, homogenous solution, and then aged for 24 h at room temperature. Before deposition, the FeMn samples in the form of a flat disc with a diameter of 9 mm and thickness of 2 mm were polished up to #800 grit, ultrasonically cleaned in ethanol and dried using a nitrogen gun.

The ZnO precursor solution was deposited by dip-coating onto FeMn discs at a withdrawal rate of 300 mm/min using a Coater 5 AC (id Lab) operating at room temperature and 50 % relative humidity. To increase the thickness of the ZnO layers and improve surface coverage, the dipping process was repeated two times followed by mild annealing of the deposited layers at 120 °C for 20 min after each cycle. Finally, the coated FeMn substrates were annealed at 500 °C for 3 h in air using a Carbolite furnace. Uncoated FeMn discs were annealed under the same conditions and used as a reference for the ion release study.

The FeMn/ZnO samples were characterized using a scanning electron microscope (SEM, Zeiss Merlin, Zeiss, Germany) coupled with energy-dispersive X-ray spectroscopy (EDS) detector, operating at 5–20 kV. The thickness of the ZnO coating was assessed from SEM images of the discs tilted 60° towards the detector. The phase composition was investigated using grazing incidence X-ray diffractometer (GIXRD) and standard X-ray diffraction (XRD) analyses. The GIXRD patterns were acquired at room temperature using a Malvern Panalytical diffractometer operating at an angular 2θ range of 25°–75°, with a step size of 0.02° and a counting time of 8 s. Standard XRD patterns were performed on a Panalytical X'Pert diffractometer (Malvern Panalytical, UK) with Cu Kα radiation, using an angular range of 20°–100°, with a step size of 0.026°.

### 2.2. Biodegradability test

The biodegradability of FeMn and FeMn/ZnO was studied under static immersion of the samples in Hank's balanced salt solution (HBSS, H8264, Merck, Germany) according to the ASTM-G31–72 standard. Prior to the tests, the samples were cleaned and sterilised in ethanol. Each disc, with a surface area of 1.25 cm<sup>2</sup>, was immersed in plastic containers filled with 30 mL of HBSS solution. The containers were then placed in a water bath and kept at a constant temperature of 37.5 °C. The discs were kept in HBSS for up to 28 days. After 1, 3, 7, 14 and 28 days, the solution was withdrawn, and the containers were refilled with fresh media. The concentration of ions released from the material (Fe, Mn and Zn ions) to the media was measured by inductively coupled plasma-optical emission spectroscopy (ICP-OES, Agilent 7900, Agilent, USA). Prior to analysis, the media was treated with HNO<sub>3</sub> to dissolve the solid corrosion products suspended in the solution. Five replicas of each sample were analysed, and the results are presented as an average ± standard error (SE).

The corrosion rate was estimated according to the release of Fe and Mn after 1 day of sample's immersion [39] (Eq. (1)):

$$C_R = \frac{C \cdot V}{S \cdot T} \quad (1)$$

where  $C_R$  is the corrosion rate given in g/m<sup>2</sup>/day; C is the released ion concentration (g/L), V is the solution volume (L), S is the sample surface area (m<sup>2</sup>), and T is the incubation time (days).

To evaluate the morphological and compositional changes of the samples undergoing biodegradation, additional discs were immersed in



the HBSS. After 3, 7, 14, and 28 days, the specimens were removed from HBSS, rinsed with distilled water, dried using compressed nitrogen, and kept in a desiccator until further examination. Analyses were performed both on the surface and the cross-section of the discs. Once removed from the HBSS, the specimens were not immersed again. The cross sections were prepared by embedding the samples in resin, grinding, and polishing with diamond paste up to 1  $\mu\text{m}$ . Top-down and cross-section SEM observations and EDS determinations were carried out at 10 kV and 20 kV, respectively.

FeMn and FeMn/ZnO samples immersed for 14 and 28 days were also characterized using X-ray diffraction to identify the products formed on the surface. The experiments were carried out on a Bruker diffractometer using Cu K $\alpha$  radiation. The  $2\theta$  region was between  $20^\circ$  and  $100^\circ$  with a step size of  $0.026^\circ$ . The peaks were identified using X'Pert Panalytical software.

### 2.3. Cell proliferation assays and cytotoxicity analyses

*In vitro* cell proliferation and cytotoxicity of FeMn and FeMn/ZnO samples were assessed using human osteosarcoma cells (Saos-2 cell line; ATCC HTB-85). The cells were maintained in Dulbecco's Modified Eagle's medium (DMEM; Gibco, Thermo Fisher Scientific, USA) supplemented with 10 % fetal bovine serum (FBS; Gibco) at a controlled temperature of  $37^\circ\text{C}$  and 5 %  $\text{CO}_2$ .

Samples were ultrasonically cleaned with distilled water and ethanol and then sterilised with pure ethanol. To prepare the conditioned media, the samples were immersed in supplemented DMEM for 24 h under standard conditions. A ratio of  $1.25\text{ cm}^2/\text{mL}$  was used, as recommended by the ISO 10993-5:2009 standard. After 24 h, the samples were removed, and the conditioned media were kept at  $4^\circ\text{C}$  protected from light until use. Next, the conditioned media were diluted to obtain the extract at the following concentrations: 100 % (non-diluted), 50 %, 25 %, and 12.5 % for further analysis. In parallel, control media were prepared by incubating media for 24 h, without any sample to obtain aged media. ICP-OES was used to identify the released ion concentrations of Fe, Mn, and Zn ions in the concentrated conditioned media (100 % extract).

The metabolic activity of osteoblasts was determined using the Alamar Blue reagent (Thermo Fisher Scientific, USA) after 1 and 3 days in order to evaluate the proliferation of cells exposed to the conditioned media. A total amount of  $5 \times 10^4$  osteoblasts were seeded in a 24-well plate using fresh media. After 24 h, the media was replaced with conditioned media at different concentrations (100 %, 50 %, 25 %, and 12.5 %), and the cells were incubated for another 24 h under standard conditions. The conditioned media was then replaced with fresh media containing 10 % Alamar Blue and incubated for 4 h. Afterwards, the supernatant was collected (day 1), and fluorescence was analysed at a wavelength of 585 nm after excitation at 560 nm using a Spark multi-mode microplate reader (Tecan, Männedorf, Switzerland). The cells were then incubated with the same conditioned media previously used and kept in the incubator during the Alamar Blue assay. Cells were cultured for 72 h in this conditioned media and the Alamar Blue assay was repeated as previously described (day 3). Aged and fresh media were used as the controls. The experiments were performed in triplicates.

In parallel, the cytotoxicity of conditioned media was assessed in cells grown for 3 days using the live/dead viability/cytotoxicity kit for mammalian cells (Invitrogen, United States) according to the manufacturer's protocol. Images of randomly selected regions were obtained using an Olympus IX71 inverted microscope equipped with epifluorescence.

### 2.4. Assessment of *S. aureus* adhesion and viability

#### 2.4.1. *Staphylococcus aureus* ATCC 25923 culture conditions

*Staphylococcus aureus* ATCC 25923 (American Type Culture

Collection, Manassas, USA) was streaked from a  $-80^\circ\text{C}$  glycerol stock onto 5 % Horse Blood Columbia Agar (HBA; Media Department, Clinical Microbiology Laboratory, Sahlgrenska University Hospital, Sweden) followed by aerobic incubation at  $37^\circ\text{C}$  overnight. After incubation, isolated single colonies were picked with a flocced nylon swab and inoculated into 4 mL Tryptic Soy Broth (TSB; Scharlau, Barcelona, Spain) to achieve an optical density ( $\text{OD}_{546}$ ) of 0.13, equivalent to  $10^8$  CFU/mL. This suspension was then diluted 1:1000 in TSB to achieve a final working bacterial suspension (inoculum) of  $10^5$  CFU/mL. Prior to inoculation with bacterial suspension, discs were sterilised by dry heat sterilisation at  $180^\circ\text{C}$  for 2 h.

#### 2.4.2. Viability of *S. aureus* after 4 h or 24 h biofilm formation

Dry-heat sterilised FeMn/ZnO and control FeMn discs (9 mm diameter, 2 mm thickness) were added to wells of a 48-well plate, inoculated with 1 mL of  $10^5$  CFU/mL of the previously mentioned *S. aureus* ATCC 25923 working bacterial suspension, and incubated aerobically and statically at  $37^\circ\text{C}$  for either 4 or 24 h.

After each time point, discs were carefully removed from the well plate, rinsed three times in sterile saline (0.9 %), and transferred to a 15 mL Falcon Tube containing 1 mL sterile saline (0.9 %). Discs were then sonicated (42 kHz) in a Branson 3510MT Ultrasonic Cleaner (Branson, Brookfield CT, USA) for 30 s, followed by vortexing for 1 min at 10000 rpm. Disaggregated biofilm cells were then ten-fold serially diluted in a combination of sterile saline (0.9 %) and Triton-X (0.1 %). These dilutions were plated on 5 % HBA plates and incubated at  $37^\circ\text{C}$  overnight and the viable colony-forming units (CFU) were subsequently enumerated. Three independent biological experiments with duplicate samples were performed.

#### 2.4.3. Confocal laser-scanning microscopy and quantitative image analysis of *S. aureus* biofilms

Dry-heat sterilised FeMn/ZnO and control FeMn discs were added to wells of a 48-well plate, inoculated with 1 mL of  $10^5$  CFU/mL of *S. aureus* ATCC 25923 inoculum, and incubated aerobically and statically at  $37^\circ\text{C}$  for either 4 or 24 h. Upon completion of each time-point, discs were carefully removed from the well plate and rinsed 3 times in sterile saline (0.9 %). After which, *S. aureus* adhered to the surface were stained using FilmTracer LIVE/DEAD Biofilm Viability Kit (Invitrogen, Waltham, United States) in the dark at room temperature for 20 min. After staining, discs were rinsed in sterile saline (0.9 %) to remove unbound stain and transferred to a 35 mm petri-dish containing 3 mL sterile saline for imaging on a Nikon C2+ confocal laser-scanning microscope (CLSM; Nikon, Tokyo, Japan) with a  $100\times$  water-dipping objective (CFI Plan 100XC W). Images were taken with Z-slices of  $3\mu\text{m}$  through the *S. aureus* biofilms. Biofilm thickness and biovolume were measured using BiofilmQ [40]. Sections imaged were taken from five randomly selected fields of view on each material sample. Three independent biological experiments were performed with technical duplicates.

#### 2.4.4. SEM imaging of *S. aureus* ATCC 25923

Dry-heat sterilised FeMn/ZnO and FeMn discs were added to wells of a 48-well plate, inoculated with 1 mL of  $10^5$  CFU/mL of *S. aureus* ATCC 25923, and incubated aerobically and statically at  $37^\circ\text{C}$  for 24 h. After incubation, both the control FeMn and FeMn/ZnO samples were carefully removed from the well plate and rinsed 3 times in sterile saline (0.9 %). Following this, *S. aureus* adhered to the surface were fixed in 4 % formaldehyde (HistoLab AB, Sweden) for 1 h at room temperature before dehydration in a graded ethanol series (50-, 70-, 80-, 90-, 95-, 100 %), for 5 min at each concentration, with the final 100 % step being repeated once.

The discs and *S. aureus* biofilms adhered to the surface were gold sputtered (10 nm) using a Leica EM ACE600 Sputter Coater (Leica, Stockholm, Sweden) and imaged in secondary electron mode using an LEO 55 ULTRA FEG SEM (Zeiss, Germany) operating at 5 kV.

## 2.5. Statistical analysis

All quantitative data were analysed using GraphPad Prism 9 and biodegradability and cytocompatibility data is presented as the mean  $\pm$  standard error of the mean. Statistical differences for biodegradability and cytocompatibility studies were obtained by one-way analysis of variance (ANOVA) with a Tukey correction. Microbiological data is presented as the mean  $\pm$  standard deviation. Biofilm viability (CFU/mL) was analysed using an unpaired student's *t*-test. Differences in biofilm biovolume and thickness were analysed by paired Students *t*-test to compare between live and dead groups, and unpaired Students *t*-test for the comparisons between the two biomaterial groups. A value of  $p < 0.05$  was considered significant.

## 3. Results

### 3.1. Morphology of the ZnO coating deposited on FeMn substrate

Fig. 1 displays the topography and morphology of the ZnO coating deposited on the FeMn substrate, together with the elemental distribution of Fe, Mn, Zn and O obtained by SEM + EDS. The porous FeMn substrate contains large pores, with a diameter of around 10  $\mu\text{m}$  and nanopores, with a size around 100 nm, as presented in Fig. S1. The coating has a compact structure and is evenly distributed over the entire surface. However, Fig. 1A, B shows that the regions around the large pores have a distinct morphology. This was attributed to the difference in the wettability between the dense and porous areas of the sample. The regions around the pores were enriched in Mn, O, and Fe, with a very low Zn content, indicating the formation of iron-manganese mixed oxides. The ZnO coating formed a wrinkled network structure consisting of regions of higher thickness (i.e., ganglia-like hills) with a thickness of approximately 2  $\mu\text{m}$ , as well as flat regions with a thickness of approximately 600 nm, as shown in Fig. 1C, D. The flat areas of the ZnO coating possessed a mesoporous structure, as shown in Fig. 1E.

Similar morphologies of ZnO thin films have been previously described in the literature [32,34]. Several explanations have been put forward to explain the morphology of ZnO films, such as stress relaxation and slow cooling conditions. In our case, we attributed the wrinkled morphology to stress relaxation due to the difference in the thermal expansion coefficient between the metallic disc underneath and the thin film, as suggested by Kwon et al. [41]. The sol-gel methods make it

possible to obtain a material using a sol or a gel as an intermediate step with the process being conducted at lower temperatures than traditional methods [33,35]. The sol-gel processes can be divided into the (i) preparation of precursor solution, (ii) sol deposition on the substrate by spin- or dip-coating and (iii) heat treatment of the xerogel film. During the drying process of sol-gel-derived films, when the solvent is removed, compressive stress is generated in the system owing to the difference in the thermal expansion coefficients between the film and the substrate. This likely led to the formation of a wrinkled structure in the gelated ZnO film. In the samples described here, apart from the wrinkled ZnO coating, a layer of Fe-Mn oxide was also present, which was formed during the annealing process.

The GIXRD pattern of the dip-coated ZnO layer on the FeMn substrate is shown in Fig. 2. This pattern confirms the formation of polycrystalline ZnO in the hexagonal wurtzite phase (space group *P63mc*), as

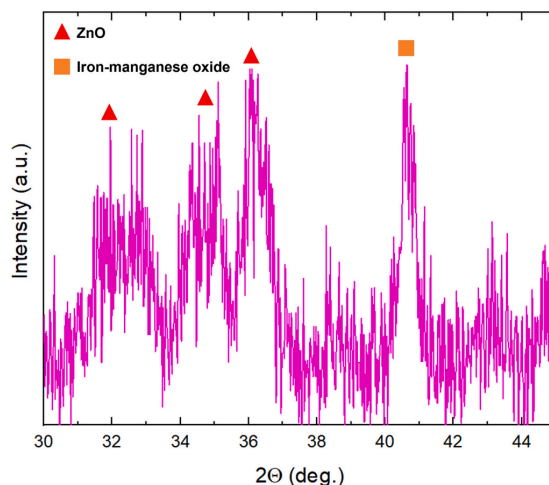


Fig. 2. GIXRD pattern of FeMn/ZnO sample. Triangles correspond to the ZnO hexagonal phase, while squares belong to the iron-manganese oxide phase formed during annealing.

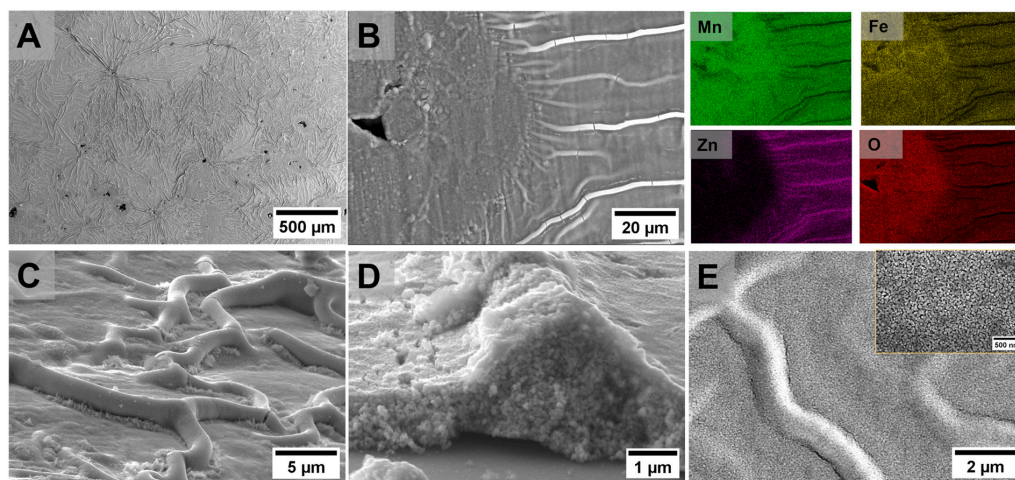


Fig. 1. Morphology of the ZnO film deposited on the FeMn substrate: (a) low-magnification view of the coating, (b) SEM image and EDS map of the area, (c) tilted view of coating' wrinkles, (d) magnified view of a wrinkle and (e) morphology of the coating at the flat areas, showing a detail of the mesoporosity in the inset.

evidenced by the presence of characteristic peaks for this phase at the  $2\theta$  values of  $31.9^\circ$ ,  $34.4^\circ$  and  $36.3^\circ$ , corresponding to (100), (002) and (101) planes, respectively. No preferred orientation was observed; therefore, we can conclude that the ZnO crystallites possess random orientation. Besides the ZnO phase, an additional peak was identified at  $40.6^\circ$ , which is consistent with the (200) plane of iron manganese oxide phase with space group *Fm-3m*. The presence of this oxide is in accordance with the EDS mapping presented in Fig. 1.

### 3.2. Biodegradability of FeMn/ZnO

A first biodegradability test was conducted to assess the changes in the surface morphology and composition of the FeMn/ZnO samples and to measure ion release upon immersion in HBSS. The in-plane views after 3, 7, 14, and 28 days of incubation are presented in Fig. 3. The results of the EDS analysis obtained from the areas highlighted in Fig. 3 (black letters A–D, corresponding to FeMn and numbers 1–4, corresponding to FeMn/ZnO) are shown in Table 1.

The corrosion products formed on the uncoated FeMn alloy after 3, 7, and 14 days of immersion had a size of a few micrometres and mostly consisted of globular precipitates that were not uniformly distributed on the surface. These were identified as Ca, P, and Cl-containing precipitates by EDS. After immersion for 14 and 28 days, the amount of Ca and P precipitates formed on the surface of the FeMn alloys appeared much higher than for the FeMn/ZnO samples (Table 1). After 28 days of immersion, a compact corrosion layer was formed, covering the entire surface. This compact corrosion layer can act as a protective barrier, hindering the progression of corrosion.

The morphologies of the corrosion products formed on the surface of the FeMn/ZnO samples showed different features. Following immersion for a maximum of 14 days, the distinctive morphology of the ZnO coating can be still observed, indicating that it had not been entirely engulfed by corrosion products. The products primarily consist of loosely packed globular precipitates, identified as Ca, P and Cl precipitates. However, following a 28-day immersion period, a denser layer of corrosion products accumulated on the surface of the ZnO coating. This layer included some platelet-like structures that have been recognized as Ca-P apatite-like precipitates [4,14]. The formation of these precipitates is *a priori* positive, since it increases the bioactivity of the surface, eventually leading to a better bone-bonding ability of the material [42].

The XRD patterns of FeMn and FeMn/ZnO samples in the as-prepared state and after 14 and 28 days of degradation in HBSS are displayed in Fig. 4A, B. FeMn specimens (Fig. 4A) in the as-prepared state and after 14 days of immersion in HBSS show the same phase composition ( $\gamma$ -austenite and Fe-Mn oxide phases), while after 28 days

of immersion, new peaks matching the  $\text{MnCO}_3$  phase appear. Indeed, the formation of corrosion products such as carbonates and phosphates resulting from the reaction between samples and the surrounding HBSS environment is common [9]. The HBSS contains  $\text{HCO}_3^-$  and  $\text{HPO}_4^{2-}$  ions which may react with the released metallic ions, thus forming insoluble metal carbonates or phosphates. The latter deposit on the metallic surface, slowing down further degradation. In the case of the FeMn/ZnO sample (Fig. 4B), three characteristic peaks of ZnO, the  $\gamma$ -austenite phase, as well as the iron-manganese oxide phase (identified as well in Fig. 2), are present in all samples. Moreover, one can observe the presence of the  $\alpha$ -Fe in the FeMn/ZnO samples, most probably due to the segregation of Fe on the grain boundaries after the annealing step required to convert the ZnO precursor into ZnO. No peaks ascribed to corrosion products are observed, which would agree with our previous observation that the ZnO might hinder the formation of corrosion products. Hence, the main difference between the uncoated and ZnO-coated discs resides in the phase composition of the FeMn substrate: austenite and ferrite phases coexist in the FeMn/ZnO sample, while the naked substrate has a purely austenitic structure. It is anticipated that the occurrence of the austenite and ferrite phases in the FeMn/ZnO samples might contribute to accelerating their degradation in bodily fluids [3,43].

In addition, having analysed Figs. 3 and 4, it is likely that the ZnO coating acts as a physical barrier in the initial stages of degradation, protecting the surface of FeMn alloy from direct contact with the corrosive environment, therefore, limiting the deposition of insoluble corrosion products from HBSS. In fact, the amounts of Ca- and P-containing products after 7 days of incubation are lower (Table 1). However, over time, the penetration of HBSS through the pores might allow for the initiation of localized corrosion. Moreover, as the ZnO coating is not fully dense, media can easily permeate through the defects and pores and cause micro galvanic corrosion between the semiconductor coating and the metallic substrate.

Fig. 5 shows the cumulative ion release of Fe (A) and Mn (B) in (uncoated) FeMn, annealed FeMn and FeMn/ZnO samples after 1, 3, 7, 14 and 28 days of immersion for both Fe and Mn release after 1 day (C) and 28 days (D) of immersion in HBSS. It can be observed that the release of both Fe and Mn increases over time, with significant differences between FeMn and FeMn/ZnO samples. The release of Fe and Mn ions in FeMn/ZnO samples after 1 day was  $5.50 \pm 0.94$  ppm and  $9.00 \pm 0.86$  ppm, respectively. In uncoated FeMn the release after 1 day in HBSS was much lower and reached  $0.06 \pm 0.02$  ppm for Fe ions and  $0.33 \pm 0.04$  ppm for Mn ions (Fig. 5A). Note that the release of Fe and Mn ions after 1 day is significantly different for FeMn/ZnO sample, while both ions are released in similar amounts from the uncoated FeMn sample. The release after 28 days in HBSS for FeMn/ZnO reached the value of

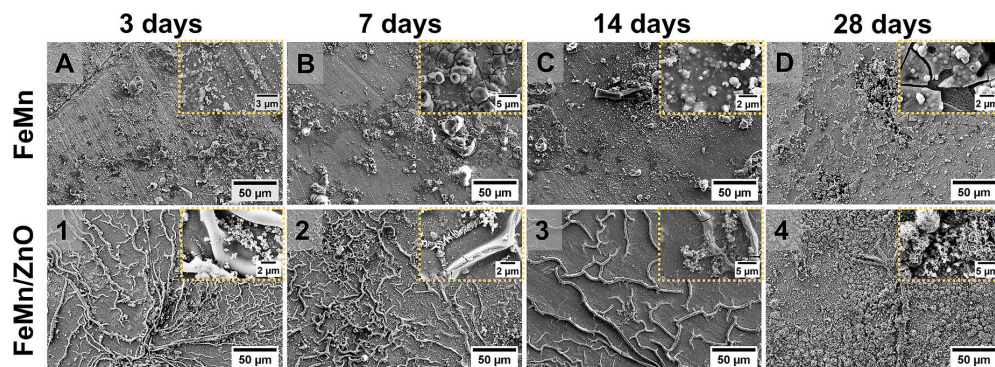


Fig. 3. Top-down SEM micrographs of the surface of FeMn and FeMn/ZnO samples after 3, 7, 14 and 28 days of immersion in HBSS at  $37.5^\circ\text{C}$ . Black letters A–D correspond to FeMn, and numbers 1–4 correspond to FeMn/ZnO immersed for 3, 7, 14, and 28 days, respectively.



Table 1

EDS analysis of the areas presented in Fig. 3. A, B, C, and D correspond to areas of FeMn samples immersed for 3, 7, 14, and 28 days, respectively. Meanwhile, 1, 2, 3, and 4 correspond to areas of FeMn/ZnO samples immersed for 3, 7, 14, and 28 days.

Sample	EDS analysis	Element (wt.%)							
		Fe	Mn	O	Zn	Ca	P	Cl	Mg
FeMn 3d	A	42.9 ± 5.0	35.4 ± 5.4	18.4 ± 2.0	X	X	X	3.3 ± 0.7	X
FeMn/ZnO 3d	1	4.2 ± 0.1	32.1 ± 0.2	19.8 ± 0.2	38.4 ± 0.2	2.6 ± 0.1	1.3 ± 0.1	1.2 ± 0.1	0.5 ± 0.1
FeMn 7d	B	41.9 ± 0.8	36.4 ± 0.8	16.4 ± 0.3	X	1.3 ± 0.1	X	4.1 ± 0.1	X
FeMn/ZnO 7d	2	12.6 ± 0.6	26.5 ± 0.8	25.6 ± 0.4	30.6 ± 0.4	1.4 ± 0.1	2.3 ± 0.1	0.9 ± 0.1	X
FeMn 14d	C	33.6 ± 0.7	31.2 ± 0.9	23.8 ± 0.4	X	2.9 ± 0.1	4.0 ± 0.1	4.6 ± 0.1	X
FeMn/ZnO 14d	3	1.8 ± 0.5	30.7 ± 0.6	22.3 ± 0.3	38.6 ± 0.4	0.7 ± 0.1	0.5 ± 0.1	0.8 ± 0.1	X
FeMn 28d	D	26.3 ± 0.7	29.7 ± 0.9	24.3 ± 0.4	X	9.7 ± 0.2	8.1 ± 0.2	0.9 ± 0.1	1.1 ± 0.1
FeMn/ZnO 28d	4	4.8 ± 0.1	36.1 ± 0.2	27.6 ± 0.2	17.5 ± 0.2	2.0 ± 0.1	3.1 ± 0.1	8.5 ± 0.1	0.3 ± 0.1

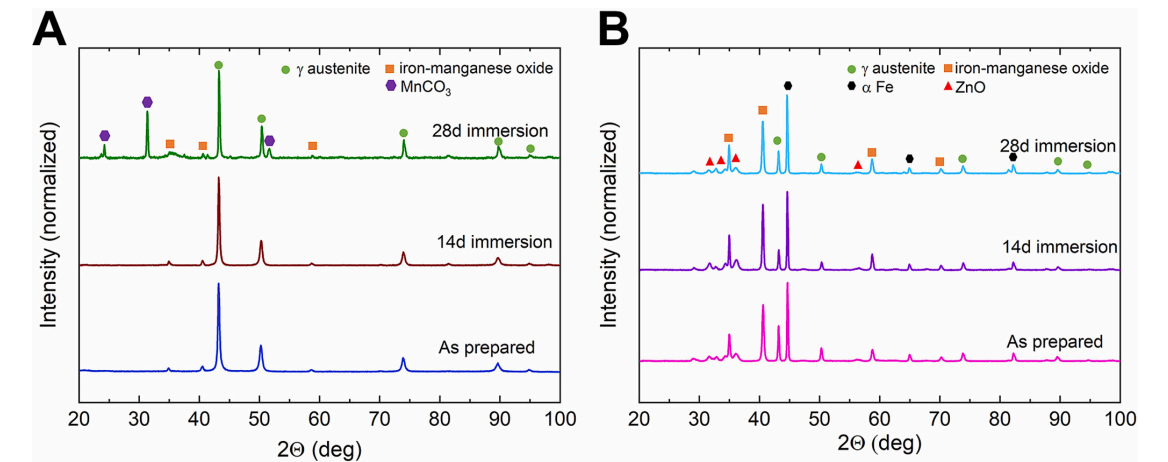


Fig. 4. X-ray diffraction patterns of the as-prepared and immersed for 14 and 28 days in HBSS samples of (A) FeMn and (B) FeMn/ZnO.

14.70 ± 1.55 ppm for Fe and 21.69 ± 1.38 ppm for Mn ions (again, significantly higher), while for FeMn it reached the value of 0.34 ± 0.05 ppm for Fe and 2.9 ± 0.29 ppm for Mn (Fig. 5B). In general, the release of Fe ions is lower than that of Mn. The concentration of Zn<sup>2+</sup> ions in the FeMn/ZnO samples was very low, reaching only 0.15 ppm after 28 days of immersion (not shown).

As a reference, ion release from annealed (uncoated) FeMn discs was tested. An elevated ion release after 1 to 28 days of immersion was observed when compared to the uncoated, non-annealed FeMn disc (Fig. 5C, D). Yet, the release of Fe and Mn ions was lower than for the FeMn/ZnO sample. The release of Mn was also lower when compared to the FeMn/ZnO sample, but it reached the same concentration after 28 days of immersion.

Overall, the release of Fe after 28 days of immersion is 43 times higher (and the release of Mn 7.5 times higher) in FeMn/ZnO sample than in FeMn. The significant differences between FeMn, annealed FeMn and FeMn/ZnO samples indicate that the ZnO coating and the formation of secondary phases stemming from its synthesis would trigger the degradation of FeMn alloys in HBSS.

The concentration of metallic ions after 1 day of immersion in HBSS was used to make a rough estimation of the corrosion rates according to Eq. (1), and the results are shown in Fig. 6. A significant increase in the corrosion rate was observed for the FeMn/ZnO sample when compared to the uncoated FeMn alloy and the annealed (uncoated) FeMn samples. The corrosion rates of FeMn/ZnO were 36 times higher than that of FeMn and 3 times higher than that of annealed FeMn. This indicates that the enhanced degradability can be attributed to both Fe segregation due to annealing and the presence of the ZnO coating.

Fig. 7 presents the SEM images and linear EDS analysis of cross-

sections of FeMn/ZnO discs in the as-prepared state and after 7, 14 and 28 days of immersion in HBSS. Linear EDS analysis was performed on these samples to identify the distribution of Fe, Mn, O, Zn and Ca on the cross-section of the samples. We can observe that already in the as-prepared state, there is a Mn- and O-enriched region, just below the ZnO coating, that can be recognized as the iron-manganese-rich oxide. Just below this layer we can observe a region enriched in Fe with reduced content of Mn, that, likewise, forms due to Mn diffusion towards the surface to form the aforementioned oxide layer. After 28 days we can observe that the Mn-rich region is becoming thicker upon degradation. The outermost layer contains Ca, coming from HBSS-derived precipitates.

Fig. 8 shows cross-section areas of the FeMn and FeMn/ZnO samples in the as-prepared state and after 7, 14 and 28 days of immersion in HBSS. Additional supplementary Fig. S2 presents the EDS mapping performed on the samples immersed for 28 days, where annealed FeMn sample was added as a reference as it has shown an ion release close to that of FeMn/ZnO. Uncoated FeMn and FeMn/ZnO samples present similar microstructural features after 7 days of immersion, with a degradation layer at the upper region. However, after 14 and 28 days of immersion, samples show distinct microstructures. The corrosion layer formed on the FeMn disc becomes thicker and more compact and the macropores are filled with degradation products. Conversely, the FeMn/ZnO sample does not show a thick corrosion layer on the top surface. It does, however, show segregation of Fe around the pores, as highlighted by yellow arrows, and confirmed by EDS mapping in the supplementary information. Moreover, an increase in the size of the nanopores is observed in the denser region, highlighted by red arrows, which would indicate the dissolution of the FeMn matrix.

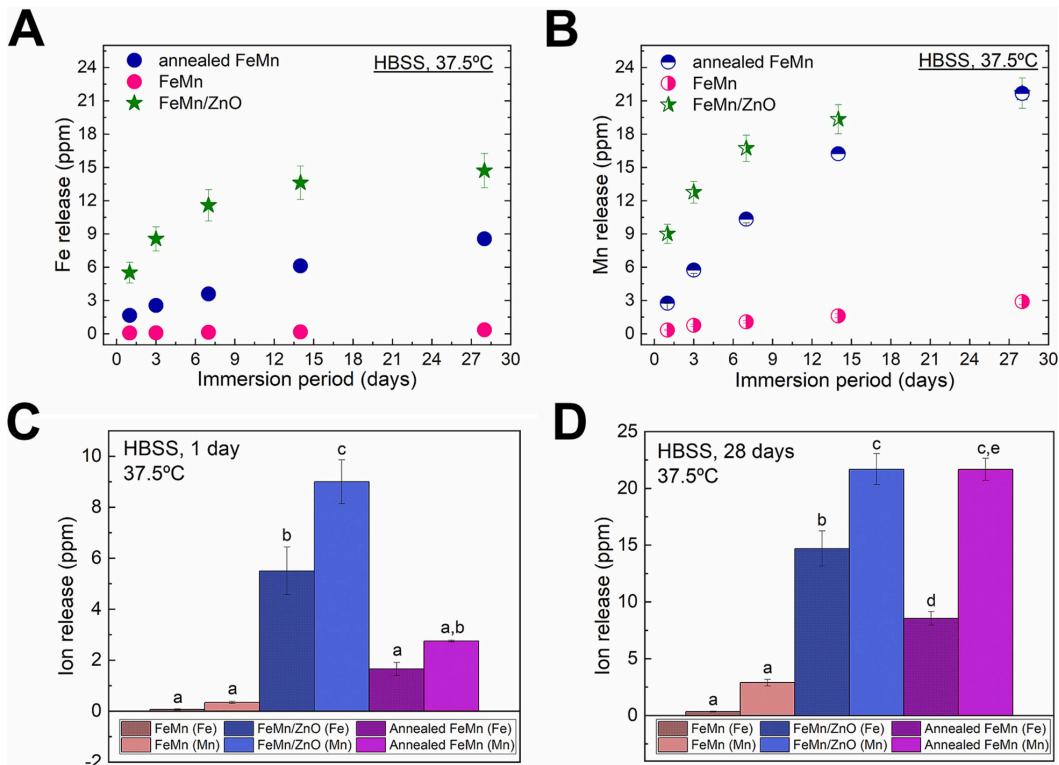


Fig. 5. Released ion concentration of Fe (A) and Mn (B) after 1, 3, 7, 14, and 28 days of immersion in HBSS for FeMn, annealed FeMn, and FeMn/ZnO samples. Analysis of significance for ion release after 1 (C) and 28 (D) days, comparing the release of Fe and Mn for the different samples. Bars marked with different alphabetical superscripts are significantly different from each other, while bars with the same superscript are not significantly different from each other.

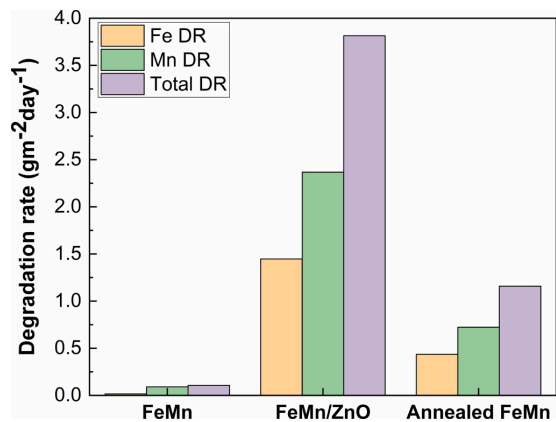


Fig. 6. Calculated corrosion rates of FeMn and FeMn/ZnO samples based on the released ion concentration after 1 day of immersion in HBSS calculated for both Fe and Mn ion release. The total corrosion rate is the sum of Fe and Mn corrosion rates for each sample. 'DR' stands for degradation rate.

### 3.3. In vitro cytocompatibility and cell proliferation

Cytocompatibility of the materials was assessed by cell proliferation and cytotoxicity using an indirect *in vitro* model on Saos-2 cells. The

conditioned media used for the experiments were prepared at 100 %, 50 %, 25 % and 12.5 % concentrations. Similarly, the control media, conditioned for 1 day without any material, was also diluted with fresh media at previously mentioned concentrations.

Fig. 9A shows the ion release concentration after 1 day of incubation in DMEM for 100 % extract. The release of Fe ions was not significantly different for the two samples, whereas the release of Mn was significantly higher for the FeMn/ZnO sample. These results are in line with those previously observed for the ions leaching in HBSS (cf. Figs. 5C and 9A). The release of Zn ions (not shown in the plot) was  $6.2 \pm 0.7$  ppm.

Regarding cell viability (Fig. 9B and C), the percentage of live cells was approximately 75 % for FeMn and 51 % for FeMn/ZnO using the conditioned medium at a concentration of 100 %, which was significantly lower than the control, FeMn and FeMn/ZnO conditioned media. However, the percentage of live cells was 90 % for both samples when the conditioned media was diluted to 50 and 12.5 %, without significant differences between both the samples and the concentrations. Results showed that with an increase in the dilution of the conditioned media, cell viability increased. The fluorescence microscopy images of the live/dead assay (Fig. 9B) for 12.5 % and 50 % conditioned medium showed a similar amount of live Saos-2 cells (green cells), with very few dead cells (red) for both samples. For the concentrated conditioned media (100 %), fewer cells were found for both samples compared to the control and diluted conditioned media. In addition, the conditioned media derived from FeMn/ZnO led to a higher ratio of dead cells than the FeMn sample.

The metabolic activity results after 1 and 3 days of incubation are presented in Fig. 9D–E and Supplementary Fig. S3. The fluorescence intensity of Alamar Blue (which corresponds to metabolic activity of the

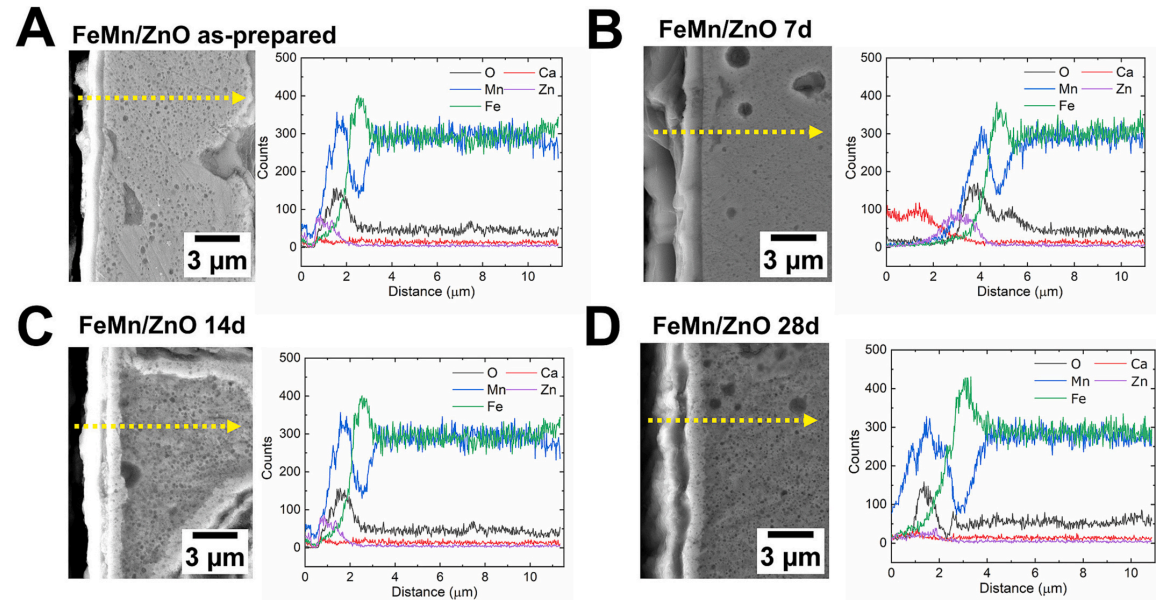


Fig. 7. EDS line scans for O, Mn, Fe, Ca and Zn elements along the cross-section of FeMn/ZnO samples in the as-prepared state (A) and after 7 (B), 14 (C), and 28 (D) days of immersion in HBSS. The yellow arrow indicates the direction of the EDS line scan. (For interpretation of the references to colour in this figure legend, the reader is referred to the web version of this article.)

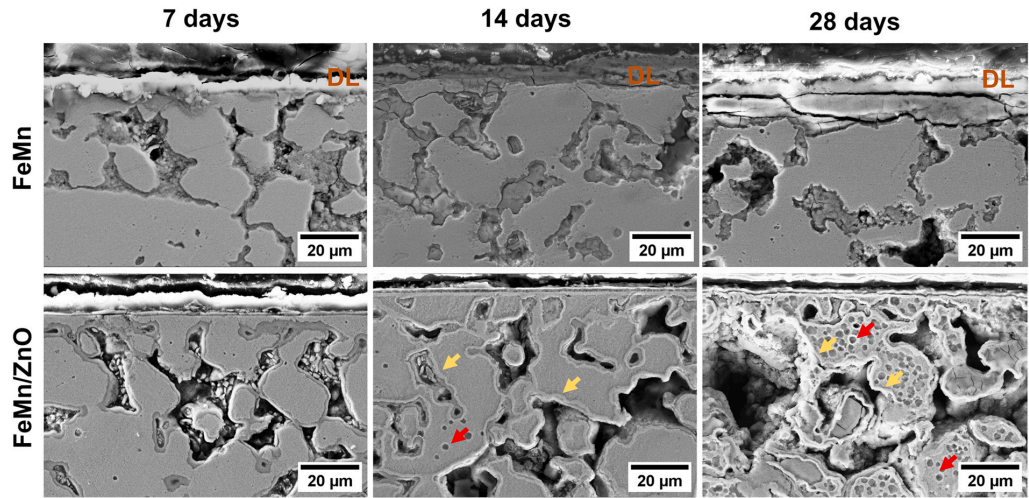
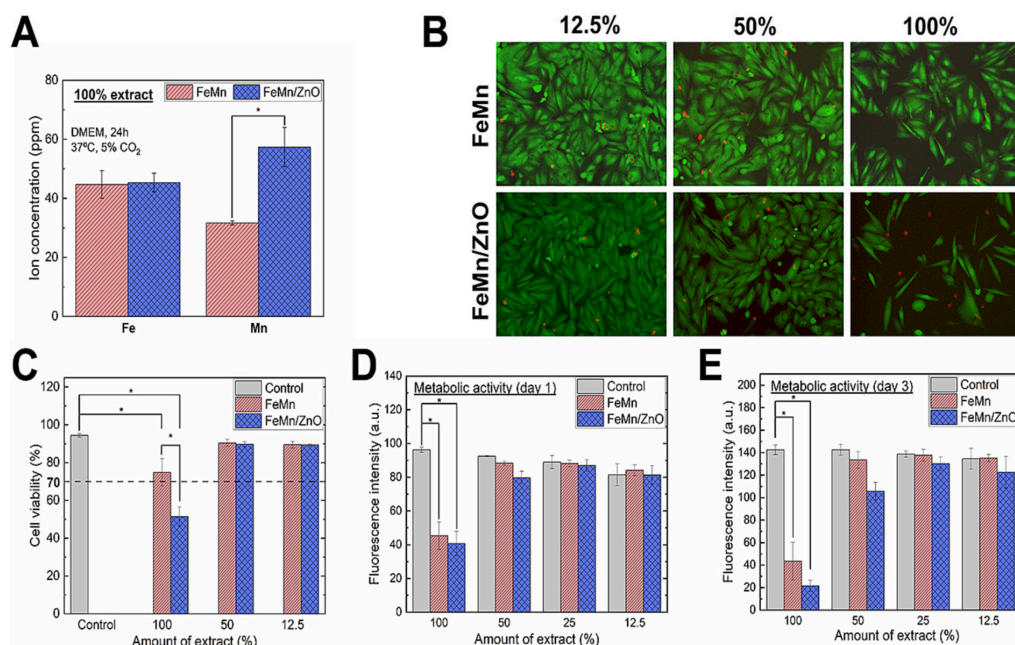


Fig. 8. Cross sections of FeMn and FeMn/ZnO samples immersed for 7, 14 and 28 days in HBSS. 'DL' stands for degradation layer formed on the surface. Yellow arrows indicate the Fe-enriched regions, while red arrows show increased pore size. (For interpretation of the references to colour in this figure legend, the reader is referred to the web version of this article.)

cells) increased with increasing dilution of the conditioned media, although no significant differences were observed amongst the 50 %, 25 % and 12.5 % dilutions. The 100 % concentrated conditioned media led to significant differences between the control, FeMn and FeMn/ZnO samples. A drastic change was observed when comparing the 100 % conditioned media with the diluted conditioned media for both materials in the sense that all materials (FeMn, FeMn/ZnO and control) showed similar metabolic activity. In supplementary Fig. S3, the differences in cell proliferation between days 1 and 3 of culture are

presented. We observed that the metabolic activity in the 100 % conditioned media increased over time for the 24 h-control media, whereas it remained low and without significant differences between the FeMn and FeMn/ZnO samples. On the contrary, no significant differences were observed in cell proliferation between samples on day 1 of culture in the 50 % conditioned media, whereas significant differences arose after 3 days of culture between the 24 h-control media and FeMn conditioned media compared to day 1. The proliferation of the FeMn/ZnO sample after day 3 was not significantly different from that on day





**Fig. 9.** Cytocompatibility assessment of FeMn and FeMn/ZnO samples obtained through indirect assay. The concentration of Fe and Mn ions released to the culture media after 24 h by FeMn and FeMn/ZnO samples (A), Live/Dead images of Saos-2 cells cultured indirectly in conditioned media from FeMn and FeMn/ZnO (B), the viability of Saos-2 cells cultured indirectly in conditioned media from FeMn and FeMn/ZnO (C). Metabolic activity of Saos-2 cells cultured in diluted conditioned media from FeMn and FeMn/ZnO samples after 1 day (D) and 3 days (E). Media conditioned for 1 day without any material was used as a control and diluted with fresh media. Significant differences are marked with (\*). (For interpretation of the references to color in this figure, the reader is referred to the web version of this article.)

1.

### 3.4. Biofilm formation

In this study, the uncoated FeMn substrate was used as a control. *S. aureus* ATCC 25923 was incubated with and directly exposed to the control FeMn and the FeMn/ZnO samples for 4- and 24 h. After both time points, no significant change ( $p > 0.05$ ) in bacterial viability was observed between the FeMn/ZnO specimens and the control FeMn (Fig. 10A).

The live and dead biovolume of *S. aureus* biofilms adhered to the surface were measured by CLSM and quantified using BiofilmQ. After 4 h no differences between the FeMn control and the FeMn/ZnO groups were identified regarding total biovolume or biofilm thickness of both live and dead *S. aureus* cells (Fig. 10B, C). Similarly, after 24 h no significant differences between the two materials were observed regarding the thickness of biofilms composed of live or dead bacterial cells, or the biovolume of dead cells (Fig. 10B, C). However, after 24 h a significant reduction in live biofilm biovolume was observed on the FeMn/ZnO surface when compared to the FeMn surface (Fig. 10B). Further, while an increase in live *S. aureus* biovolume over time was found in both groups, the fold increase in biovolume of live bacteria between 4- and 24 h was noticeably greater on the control FeMn (9.5-fold increase) than on the FeMn/ZnO coated specimen (4.3-fold increase). Moreover, on the FeMn control, an increase in the dead biovolume of biofilms was also observed over time. In addition, after 24 h of growth, significantly more live *S. aureus* cells than dead were found on the FeMn surface, whereas no difference was found between the live/dead cell proportions on the FeMn/ZnO surface (Fig. 10B). Representative CLSM images of *S. aureus* adhered to the FeMn (Fig. 10D) and the FeMn/ZnO surfaces (Fig. 10E) after 24 h reflect these observations.

The morphology of *S. aureus* biofilms adhered to either the control FeMn or the FeMn/ZnO surface after 24 h incubation was visualised by SEM (Fig. 10F–K). In agreement with the obtained data from CLSM, the total biomass adhered to the FeMn control surface (Fig. 10F–H) was noticeably greater than that adhered to the FeMn/ZnO surface (Fig. 10I–K). *S. aureus* biofilm formed on the FeMn control was thicker and more homogeneously distributed across the FeMn surface compared to the FeMn/ZnO surface, where smaller aggregates were common, and the underlying material surface remained visible in many areas. Further, less extracellular polymeric substances (EPS) between bacterial cells were observed on the FeMn/ZnO surface in comparison to the FeMn group (Fig. 10H - red arrows) indicating a less matured and developed biofilm. In combination with this visible reduction in biofilm biomass, more damaged, ruptured and/or dead *S. aureus* cells were observed on the FeMn/ZnO surface (Fig. 10K - blue arrows) when compared to the *S. aureus* cells adhered to the FeMn control.

## 4. Discussion

### 4.1. Effect of the ZnO coating on the degradation of FeMn alloys

Several approaches have been tested to increase the corrosion rate of biodegradable iron-based materials, namely, (i) alloying Fe with other elements, such as Mn to shift the corrosion potential towards more negative values and hence, make it more prone to corrosion (ii) introducing porosity to increase the total area susceptible to corrosion attack and, (iii) introducing noble elements that could act as a cathode and cause the formation of micro-galvanic corrosion cells.

In short, the phenomena taking place when a biodegradable metal is in contact with physiological fluids can be described as follows [4,9]: Once the degradable metal is immersed in the fluid, it undergoes an

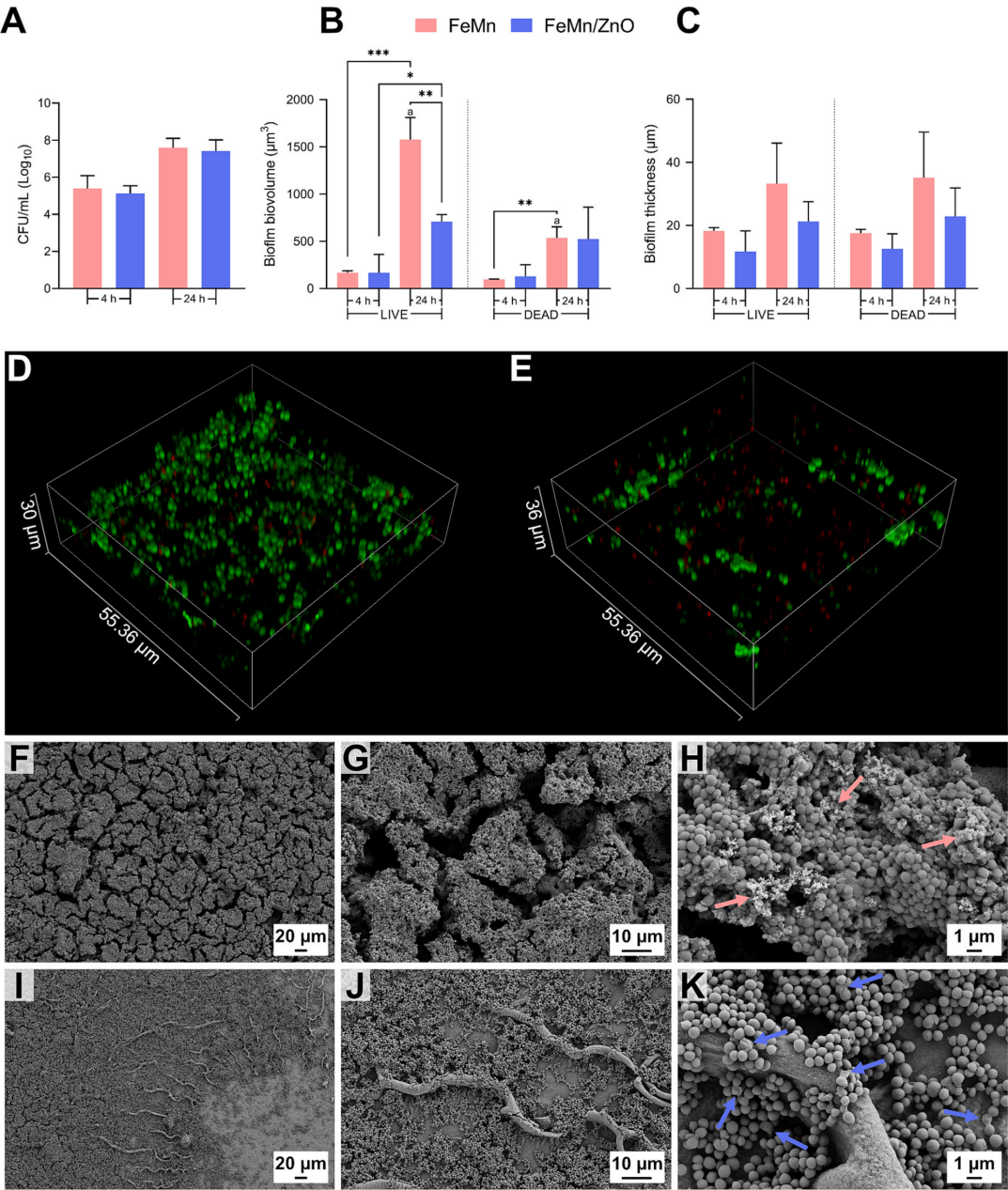
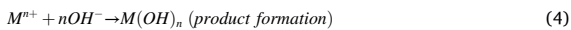
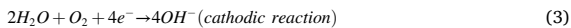
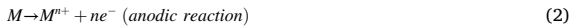


**Fig. 10.** A) Viable *Staphylococcus aureus* ATCC 25923 adhered to the control FeMn and the ZnO-coated material surfaces after 4 h and 24 h. Quantitative confocal laser-scanning microscopy (CLSM) of *S. aureus* biofilms grown on FeMn/ZnO and FeMn surfaces showing the total B) biofilm biovolume and C) biofilm thickness of live and dead bacteria after 4 h and 24 h. Representative CLSM images of live and dead stained *S. aureus* biofilms grown on the D) FeMn control and the E) FeMn/ZnO coated surfaces for 24 h in which live *S. aureus* cells stain green, and dead stain red. Scanning electron micrographs of *S. aureus* adhered to the surface of the control FeMn (F-H) and FeMn/ZnO (I-K) after 24 h of growth, obtained at increasing magnifications (200×, 1000×, 5000×). Red arrows indicate extracellular polymeric substances (EPS) in the biofilm, whereas blue arrows indicate damaged or dead *S. aureus* cells. (For interpretation of the references to colour in this figure, the reader is referred to the web version of this article.)



oxidation reaction, where metallic ions are released (Eq. (2)). The electrons generated by anodic reaction are consumed during the cathodic reaction, which reduces the amount of dissolved oxygen (Eq. (3)). These reactions occur on the entire metallic surface, and the dissolution of the metal can be accelerated by galvanic coupling between metallic matrix and grain boundaries or secondary phases because of their distinct potentials. Moreover,  $M(OH)_n$  corrosion products are deposited on the metal surface (Eq. (4)).



Physiological solutions such as HBSS contain abundant inorganic ions, which can influence the degradation process by either (i) breaking down the passive film and causing pitting corrosion or (ii) passivating the Fe and slowing down corrosion due to the formation of phosphates and carbonates. Ions such as  $Cl^-$  and  $SO_4^{2-}$  can break the passive film and accelerate corrosion, while other ions like  $HPO_4^{2-}/PO_4^{3-}$ ,  $HCO_3^-/CO_3^{2-}$  and  $Ca^{2+}$  might form a protective layer which further delays degradation of the material [9].

Apart from the reaction between the metal and physiological solution, the structural properties of metals themselves can favour or hinder degradation. The segregation of elements is known for enhancing the corrosion rate of alloys [44]. Two grains of different chemical composition and crystal structure can cause corrosion, for example in the case of duplex steels, which consist of austenite and ferrite grains [43]. This can lead to the formation of galvanic couples between them, where one grain acts as anodic site and the other as cathodic site. This galvanic coupling can lead to the selective dissolution of the less corrosion-resistant grain. Similarly, Donik et al. [19] described that the patterning of FeMn surface by laser ablation leads to the formation of high-temperature oxides, that in turn leads to a shift in the ratio of Fe/Mn to Mn, which ultimately enhances biodegradability of the material. In our study, we observe a similar shift, namely, a difference in the Fe to Fe/Mn ratio around the pores, as well as higher Mn content at the surface due to the oxide formation. The layer just below the surface is enriched in Fe that can also influence corrosion.

The standard corrosion potential of Fe and Mn is  $-0.44$  V and  $-1.05$  V, respectively [39]. When mixed, the potential falls in between (around  $-0.7$  V), with the exact value depending on the alloy composition. In this case, apart from the austenitic FeMn phase, the material consists of ZnO coating, iron-manganese oxide, and the  $\alpha$ -Fe phase. This  $\alpha$ -Fe phase formed as a side product of iron-manganese oxide formation during annealing, as the particle boundaries adjacent to the oxide layer were depleted in Mn (Figs. 7–8), thus forming an Fe-rich phase. The  $\alpha$ -Fe zone at the boundaries causes a difference in potential between the inner regions of the grains and the boundary, thus making the material more prone to corrosion. Moreover, the ZnO and iron-manganese oxide phases can form micro-galvanic cells, leading to an increased corrosion rate, when compared to the non-annealed FeMn. Based on the cross-section images presented in Figs. 7 and 8, we suspect that the FeMn austenite phase (with more negative standard corrosion potential) acts as the anode, while the  $\alpha$ -Fe, iron-manganese oxide, and ZnO phases act as the cathode. The pits formed on the cross-sectional area in Fig. 8 indicate that indeed, the austenite matrix may dissolve during the immersion in HBSS. It is important to point out that the pores are not clogged by the ZnO coating and hence the underlying alloy is still exposed to HBSS. The corrosion rate of FeMn/ZnO, presented in Fig. 6, is one order of magnitude higher than corrosion rates given for Fe-based alloys immersed in HBSS under static conditions in the literature while the corrosion rate of FeMn is in accordance with the values found elsewhere [39].

Although previous studies have demonstrated that the deposition of coatings on degradable materials leads to enhanced corrosion resistance,

others have reported higher degradation rates when coatings are deposited on Fe-based alloys. The observed increased corrosion was attributed either to the formation of micro-galvanic cells [45] or increased solubility of Fe corrosion products due to polymer hydrolysis when polymeric coatings were deposited [22]. In our case, we attribute the increased corrosion rate of the FeMn/ZnO composite to the segregation of Fe and the formation of micro-galvanic cells between Fe-rich regions and the FeMn matrix, as well as between the ZnO coating and the FeMn underlying material.

#### 4.2. Effect of the accelerated corrosion on the proliferation and cytotoxicity of Saos-2 cells

Indirect cytocompatibility studies using biodegradable Fe-based alloys have been conducted on various types of cells such as fibroblasts [46], smooth muscle cells (SMC) [47] and osteoblasts [46], depending on the target application. Metallic ions released during corrosion may have harmful effects on cellular functions [9]. Hence, it is important to demonstrate that the degradation products being formed during material dissolution are non-toxic to cells. Here, osteoblastic Saos-2 cells were used to investigate the cytocompatibility of the FeMn-based materials.

Experiments were conducted using conditioned media at concentrations of 100 %, 50 %, 25 % and 12.5 %, showing that only the 100 % extract had a cytotoxic effect. The ionic concentrations of Fe and Mn correlate with cell viability. The maximum concentration of released Fe in 100 % extract was  $45.3 \pm 6.67$  mg/L ( $811 \mu\text{mol/L}$ ), Mn was  $57.3 \pm 3.2$  mg/L ( $1043 \mu\text{mol/L}$ ), while Zn concentration reached  $6.2 \pm 0.7$  mg/L. Our results obtained are in agreement with previous reports. For instance, it has been reported that Fe concentrations above 50 mg/L can result in decreased metabolic activity [38]. Mueller et al. [47] showed that the SMC growth rate was reduced by the addition of soluble ferrous ions to the cell culture medium. The minimum Mn concentration causing cytotoxic effects depends strongly on the type of cells used [48]; for human lung epithelial cells, a concentration above  $20 \mu\text{mol/L}$  was cytotoxic [49], however, for mouse brain cells, the minimum Mn concentration causing cytotoxicity increased to  $200 \mu\text{mol/L}$  [50] and for HUVEC cells it was even higher, reaching  $500 \mu\text{mol/L}$  [51]. For Saos-2 cells cultured with the 50 % extract, containing Mn concentration of approximately  $500 \mu\text{mol/L}$ , cytotoxicity was not observed. The relatively low release of Zn ions should not cause cytotoxicity, as it is below the threshold value.

While discussing the results of *in vitro* cytocompatibility, we should keep in mind that the tests were performed under static conditions, whereas real *in vivo* conditions are more dynamic [52]. As the cell viability presented in this study clearly depends on the level of dilution, it could be presumed that the concentration of ions and degradation products in a dynamic environment is lower than all the dilutions presented here and, therefore, the material should not cause a cytotoxic effect *in vivo*. For instance, in a study by Loffredo et al. [52], the viability of ECs cells treated with a 1 % eluate concentration of media conditioned with Ag-containing TWIP steels was significantly reduced compared to 316 L stainless steel, while the same materials did not show significant differences in the viability towards SMCs. Therefore, the type of cells used also influences the results of *in vitro* cytocompatibility tests.

*In vitro* tests of Fe-based degradable alloys are directly affected by the concentration of ions in the culture media [53]. Manganese, iron, and zinc are essential metals found in tissues. The role of Mn is essential for the immune system, bone growth, adjustment of blood sugar, cofactors in enzymes, and others [54]. However, overexposure to Mn can be hazardous in humans, such as Mn-induced neurotoxicity, which occurs in workers exposed to dust-containing Mn. The toxic level of Mn in our case was above 50 ppm. As the concentration of Fe was not significantly different between the samples, the cytotoxicity of 100 % extract could be attributed to the elevated concentration of Mn or to the release of Zn ions. Nevertheless, as the conditions *in vivo* are more dynamic, the

toxicity of 100 % extract should not be of concern when considering the cytocompatibility of FeMn/ZnO, as aforementioned.

#### 4.3. Effect of the accelerated corrosion on *S. aureus* biofilm formation

Implant-associated infections are an important and debilitating complication of medical implants and have been attributed to the formation of biofilm on the surface of an implant material [24]. A biofilm is a community of bacterial cells irreversibly attached to a substrate and/or each other that are embedded in a self-made matrix of extracellular polymeric substances (polysaccharides, protein, and eDNA) [55]. By adopting a biofilm phenotype, bacterial cells become significantly more resistant to external environmental stresses and challenges, including those from the host-immune system and antibiotic chemotherapy [56]. The stages of bacterial adhesion and biofilm formation are the following: (a) bacterial adhesion, (b) formation of microcolonies, (c) biofilm maturation and (d) biofilm dispersal [26,57]. Many strategies are currently under investigation to avoid or limit the formation of biofilm on the surface of metallic implants such as the incorporation of anti-bacterial agents such as silver, zinc oxide, etc.

Previous research has established that degradable alloys possess better infection resistance than non-degradable ones [25]. One of the potential reasons for their antibacterial/antibiofilm properties can be associated with the effect of degradation on bacterial adhesion [26,58]. This degradation reduces the area available for initial bacterial attachment and colonization and could therefore limit the progression of biofilm formation. Hence, degradable materials with higher corrosion rates should be more resistant to biofilm formation than those with lower corrosion rates. In previous studies on degradable Mg-based alloys, the antibiofilm properties have been associated with an increase in pH and a high release of Mg ions upon degradation [58]. Local pH changes at the material surface were found to limit bacterial attachment. Moreover, bacteria attach preferably to corrosion products and avoid active corrosion sites. In our previous study, Ag-containing Fe-Mn alloys showed an antibiofilm effect higher than in Ag-free Fe-Mn alloys, which could be associated with enhanced corrosion of the former [15]. In this study, a similar effect was observed, as the increased corrosion rate of FeMn/ZnO reduced or delayed the development of biofilm formation more effectively than the slowly corroding uncoated FeMn.

Our results provide more evidence supporting the correlation between enhanced degradation and antibiofilm behaviour. The FeMn/ZnO composite, possessing a higher corrosion rate, has a more pronounced antibiofilm effect than the FeMn sample. As the FeMn/ZnO ion release did not show a bactericidal effect *per se*, the observed antibiofilm properties of FeMn/ZnO may be attributed to the enhanced degradation. It is possible, that the enhanced release of Fe and Mn ions, thus enhanced degradation, limit bacterial attachment and biofilm formation.

## 5. Conclusions

The main goal of the current study was to determine the effect of sol-gel-derived ZnO coating on porous, equiatomic FeMn alloys on the biodegradability, antibacterial/antibiofilm, and cytocompatibility properties. This study demonstrated that ZnO coating on FeMn leads to increased biodegradation in physiological fluids, making the resulting composite a promising candidate for a biodegradable implant. The results showed that annealing applied to convert the ZnO precursors into ZnO film led to the concomitant formation of secondary phases such as iron-manganese oxide and  $\alpha$ -Fe. These secondary phases play a major role in increasing the biodegradability of the FeMn/ZnO samples compared with their uncoated FeMn counterparts. The corrosion rate of FeMn/ZnO, calculated based on ion release, was 36 times higher than that of the uncoated FeMn. Furthermore, FeMn/ZnO showed good cytocompatibility when Saos-2 cells were exposed to diluted conditioned media, for dilutions equal to and below 50 %. The effect of dilution on cytotoxicity strongly correlated with the concentrations of Fe

and Mn ions. Moreover, a significant reduction in the total biofilm biovolume of *S. aureus* was observed at 24 h, indicating antibiofilm properties of the FeMn/ZnO sample. In conclusion, FeMn/ZnO possesses better degradability, and is more resistant to biofilm formation than uncoated FeMn, while maintaining good cytocompatibility.

## CRediT authorship contribution statement

**Aleksandra Bartkowska:** Visualization, Investigation, Formal analysis, Writing – original draft. **Adam Benedict Turner:** Visualization, Investigation, Formal analysis. **Andreu Blanquer:** Methodology, Validation, Writing – review & editing, Supervision. **Aliona Nicolenco:** Investigation. **Margarita Trobos:** Methodology, Resources, Writing – review & editing. **Carne Nogues:** Conceptualization, Resources, Supervision. **Eva Pellicer:** Conceptualization, Writing – review & editing, Supervision. **Jordi Sort:** Conceptualization, Resources, Writing – review & editing, Supervision, Funding acquisition.

## Declaration of competing interest

There is nothing to disclose.

There were no financial or personal relationships with other people or organizations that could inappropriately influence our work.

AI and AI-assisted technologies were not used in the writing process.

## Data availability

Data will be made available on request.

## Acknowledgments

This project has received funding from the European Union's Horizon 2020 research and innovation programme under the Marie Skłodowska-Curie grant agreement No. 861046 ('Bioremia' European Training Network), from the Spanish Government (grants PID2020-116844RB-C21 and PID2020 116844RB-C22), from the Generalitat de Catalunya (2021-SGR-00651 and 2021-SGR-00122), from the Swedish Research Council (2022-00853), the Swedish state under the agreement between the Swedish government and the country councils, the ALF-agreement (ALFGBG-978896), and the Hjalmar Svensson Foundation.

## Appendix A. Supplementary data

Supplementary data to this article can be found online at <https://doi.org/10.1016/j.surfcoat.2023.129886>.

## References

- [1] H. Hermawan, Updates on the research and development of absorbable metals for biomedical applications, *Prog. Biomater.* 7 (2018) 93–110, <https://doi.org/10.1007/s40204-018-0091-4>.
- [2] H. Hermawan, D. Dubé, D. Mantovani, Developments in metallic biodegradable stents, *Acta Biomater.* 6 (2010) 1693–1697, <https://doi.org/10.1016/j.actbio.2009.10.006>.
- [3] H. Hermawan, D. Dubé, D. Mantovani, Degradable metallic biomaterials: design and development of Fe-Mn alloys for stents, *J. Biomed. Mater. Res. A* 93 (2010) 1–11, <https://doi.org/10.1002/jbm.a.32224>.
- [4] H. Hermawan, A. Purnama, D. Dubé, J. Couet, D. Mantovani, Fe-Mn alloys for metallic biodegradable stents: degradation and cell viability studies, *Acta Biomater.* 6 (2010) 1852–1860, <https://doi.org/10.1016/j.actbio.2009.11.025>.
- [5] A.H.M. Yusop, N.M. Daud, H. Nur, M.R.A. Kadir, H. Hermawan, Controlling the degradation kinetics of porous iron by poly(lactic-co-glycolic acid) infiltration for use as temporary medical implants, *Sci. Rep.* 5 (2015) 11194, <https://doi.org/10.1038/SREP11194>.
- [6] A.H. Yusop, A.A. Bakir, N.A. Shaharom, M.R. Abdul Kadir, H. Hermawan, Porous biodegradable metals for hard tissue scaffolds: a review, *Int. J. Biomater.* 2012 (2012), 641430, <https://doi.org/10.1155/2012/641430>.
- [7] M.F. Ulum, A. Arafat, D. Noviana, A.H. Yusop, A.K. Nasution, M.R. Abdul Kadir, H. Hermawan, In vitro and in vivo degradation evaluation of novel iron-bioceramic composites for bone implant applications, *Mater. Sci. Eng. C* 36 (2014) 336–344, <https://doi.org/10.1016/j.msec.2013.12.022>.

- [8] Y. Liu, Y. Zheng, X.-H. Chen, J.-A. Yang, H. Pan, D. Chen, L. Wang, J. Zhang, D. Zhu, S. Wu, K.W.K. Yeung, R.-C. Zeng, Y. Han, S. Guan, Fundamental theory of biodegradable metals—definition, criteria, and design, *Adv. Funct. Mater.* 29 (2019) 1805402, <https://doi.org/10.1002/adfm.201805402>.
- [9] Y.F. Zheng, X.N. Gu, F. Witte, Biodegradable metals, *Mater. Sci. Eng.: R Rep.* 77 (2014) 1–34, <https://doi.org/10.1016/j.mser.2014.01.001>.
- [10] J. Venezuela, M.S. Dargusch, Addressing the slow corrosion rate of biodegradable Fe-Mn: current approaches and future trends, *Curr. Opin. Solid State Mater. Sci.* 24 (2020), 100822, <https://doi.org/10.1016/j.cossms.2020.100822>.
- [11] H. Hermawan, H. Alamdari, D. Mantovani, D. Dubé, Iron-manganese: new class of metallic degradable biomaterials prepared by powder metallurgy, *Powder Metall.* 51 (2008) 38–45, <https://doi.org/10.1179/174329008X284868>.
- [12] F. Moszner, A.S. Sologubenko, M. Schinhammer, C. Lerchbacher, A.C. Hänzli, H. Leitner, P.J. Uggowitzer, J.F. Löffler, Precipitation hardening of biodegradable Fe-Mn-Pd alloys, *Acta Mater.* 59 (2011) 981–991, <https://doi.org/10.1016/j.actamat.2010.10.025>.
- [13] P. Sotoudehbagha, S. Sheibani, M. Khakbiz, S. Ebrahimi-Barough, H. Hermawan, Novel antibacterial biodegradable Fe-Mn-Ag alloys produced by mechanical alloying, *Mater. Sci. Eng. C* 88 (2018) 88–94, <https://doi.org/10.1016/j.msec.2018.03.005>.
- [14] Z. Ma, M. Gao, D. Na, Y. Li, L. Tan, K. Yang, Study on a biodegradable antibacterial Fe-Mn-Cu alloy as urinary implant material, *Mater. Sci. Eng. C* 103 (2019), 109718, <https://doi.org/10.1016/j.msec.2019.05.003>.
- [15] A. Bartkowska, O. Careta, A.B. Turner, A. Blanquer, E. Ibañez, M. Trobos, C. Nogués, E. Pellicer, J. Sort, Biodegradable porous FeMn-(xAg) alloys: assessment of cytocompatibility, mechanical, magnetic and antibiofilm properties, *Mater. Adv.* 4 (2023) 616–630, <https://doi.org/10.1039/D2MA00867J>.
- [16] Q. Zhang, P. Cao, Degradable porous Fe-35wt.%Mn produced via powder sintering from  $\text{NH}_4\text{HCO}_3$  porogen, *Mater. Chem. Phys.* 163 (2015) 394–401, <https://doi.org/10.1016/j.matchemphys.2015.07.056>.
- [17] M. Heiden, E. Nauman, L. Stanciu, Bioresorbable Fe-Mn and Fe-Mn-HA materials for orthopedic implantation: enhancing degradation through porosity control, *Adv. Healthc. Mater.* 6 (2017) 1700120, <https://doi.org/10.1002/adhm.201700120>.
- [18] T. Huang, Y. Zheng, Y. Han, Accelerating degradation rate of pure iron by zinc ion implantation, *Regen. Biomater.* 3 (2016) 205–215, <https://doi.org/10.1093/rb/rbw020>.
- [19] Č. Donik, A. Kocijan, I. Paulin, M. Hočevar, P. Gregorič, M. Godec, Improved biodegradability of Fe-Mn alloy after modification of surface chemistry and topography by a laser ablation, *Appl. Surf. Sci.* 453 (2018) 383–393, <https://doi.org/10.1016/j.apsusc.2018.05.066>.
- [20] R. Orínková, R. Gorejová, J. Macko, A. Orínak, M. Kupková, M. Hrubovčáková, J. Ševc, R.M. Smith, Evaluation of in vitro biocompatibility of open cell iron structures with PEG coating, *Appl. Surf. Sci.* 475 (2019) 515–518, <https://doi.org/10.1016/j.apsusc.2019.01.010>.
- [21] L. Haverová, R. Orínková, A. Orínak, R. Gorejová, M. Baláz, P. Vanýsek, M. Kupková, M. Hrubovčáková, P. Mudron, J. Radoniák, Z.O. Králová, A. M. Turoňová, An in vitro corrosion study of open cell iron structures with PEG coating for bone replacement applications, *Metals* 8 (2018) 499, <https://doi.org/10.3390/met8070499>.
- [22] Y. Qi, X. Li, Y. He, D. Zhang, J. Ding, Mechanism of acceleration of iron corrosion by a polylactide coating, *ACS Appl. Mater. Interfaces* 11 (2019) 202–218, <https://doi.org/10.1021/acsami.8b17125>.
- [23] S. Huang, A. Ulloa, E. Nauman, L. Stanciu, Collagen coating effects on Fe-Mn bioresorbable alloys, *J. Orthop. Res.* 38 (2020) 523–535, <https://doi.org/10.1002/jor.24492>.
- [24] H.J. Busscher, H.C. van der Mei, G. Subbiahdoss, P.C. Jutte, J.J.A.M. van den Dungen, S.A.J. Zaai, M.J. Schultz, D.W. Grainger, Bacterial-associated infection: locating the finish line in the race for the surface, *Sci. Transl. Med.* 4 (2012) 153rv10, <https://doi.org/10.1126/SCITRANSLMED.3004528>.
- [25] S. Daghighi, J. Sjölella, H.C. van der Mei, H.J. Busscher, E.T.J. Rochford, Infection resistance of degradable versus non-degradable biomaterials: an assessment of the potential mechanisms, *Biomaterials* 34 (2013) 8013–8017, <https://doi.org/10.1016/j.biomaterials.2013.07.044>.
- [26] E. Zhang, X. Zhao, J. Hu, R. Wang, S. Fu, G. Qin, Antibacterial metals and alloys for potential biomedical implants, *Bioact. Mater.* 6 (2021) 2569–2612, <https://doi.org/10.1016/j.bioactmat.2021.01.030>.
- [27] M.L. Kääriäinen, C.K. Weiss, S. Ritz, S. Pütz, D.C. Cameron, V. Mailänder, K. Landfester, Zinc release from atomic layer deposited zinc oxide thin films and its antibacterial effect on *Escherichia coli*, *Appl. Surf. Sci.* 287 (2013) 375–380, <https://doi.org/10.1016/j.apsusc.2013.09.162>.
- [28] K. Thongsuriwong, P. Amornpitoksuk, S. Suwanboon, Structure, morphology, photocatalytic and antibacterial activities of ZnO thin films prepared by sol-gel dip-coating method, *Adv. Powder Technol.* 24 (2013) 275–280, <https://doi.org/10.1016/j.apt.2012.07.002>.
- [29] L.C. Ann, S. Mahmud, S.K.M. Bakhori, A. Sirelkhatim, D. Mohamad, H. Hasan, A. Seeni, R.A. Rahman, Antibacterial responses of zinc oxide structures against *Staphylococcus aureus*, *Pseudomonas aeruginosa* and *Streptococcus pyogenes*, *Ceram. Int.* 40 (2014) 2993–3001, <https://doi.org/10.1016/j.ceramint.2013.10.008>.
- [30] A. Abdelghafar, N. Yousef, M. Askoura, Zinc oxide nanoparticles reduce biofilm formation, synergize antibiotics action and attenuate *Staphylococcus aureus* virulence in host; an important message to clinicians, *BMC Microbiol.* 22 (2022) 244, <https://doi.org/10.1186/s12866-022-02658-Z>.
- [31] S. Stoleriu, C. Lungu, C.D. Ghitulica, A. Surdu, G. Voicu, A. Cucuruz, C.S. Turculeț, L.T. Ciocan, Influence of dopant nature on biological properties of ZnO thin-film coatings on Ti alloy substrate, *Nanomaterials* 10 (2020) 129, <https://doi.org/10.3390/NANO10010129>.
- [32] D. Kim, J.-Y. Leem, Crystallization of ZnO thin films via thermal dissipation annealing method for high-performance UV photodetector with ultrahigh response speed, *Sci. Rep.* 11 (2021) 382, <https://doi.org/10.1038/s41598-020-79849-z>.
- [33] L. Znaidi, G.J.A.A. Soler Illia, S. Benyahia, C. Sanchez, A.V. Kanaev, Oriented ZnO thin films synthesis by sol-gel process for laser application, *Thin Solid Films* 428 (2003) 257–262, [https://doi.org/10.1016/S0040-6090\(02\)01219-1](https://doi.org/10.1016/S0040-6090(02)01219-1).
- [34] S.H. Sabeeh, R.H. Jassam, The effect of annealing temperature and Al dopant on characterization of ZnO thin films prepared by sol-gel method, *Results Phys.* 10 (2018) 212–216, <https://doi.org/10.1016/j.rinp.2018.05.033>.
- [35] L. Znaidi, Sol-gel-deposited ZnO thin films: a review, *Mater. Sci. Eng. B* 174 (2010) 18–30, <https://doi.org/10.1016/j.mseb.2010.07.001>.
- [36] Y. Guo, S. Jia, L. Qiao, Y. Su, R. Gu, G. Li, J. Lian, A multifunctional polypyrrole/zinc oxide composite coating on biodegradable magnesium alloys for orthopedic implants, *Colloids Surf. B Biointerfaces* 194 (2020), 111186, <https://doi.org/10.1016/j.colsurfb.2020.111186>.
- [37] N. Eliaz, Corrosion of metallic biomaterials: a review, *Materials* 12 (2019) 407, <https://doi.org/10.3390/MA12030407>.
- [38] S. Zhu, N. Huang, L. Xu, Y. Zhang, H. Liu, H. Sun, Y. Leng, Biocompatibility of pure iron: in vitro assessment of degradation kinetics and cytotoxicity on endothelial cells, *Mater. Sci. Eng. C* 29 (2009) 1589–1592, <https://doi.org/10.1016/j.msec.2008.12.019>.
- [39] B. Liu, Y.F. Zheng, Effects of alloying elements (Mn, Co, Al, W, Sn, B, C and S) on biodegradability and in vitro biocompatibility of pure iron, *Acta Biomater.* 7 (2011) 1407–1420, <https://doi.org/10.1016/j.actbio.2010.11.001>.
- [40] R. Hartmann, H. Jeckel, E. Jelli, P.K. Singh, S. Vaidya, M. Bayer, D.K.H. Rode, L. Vidakovic, F. Díaz-Pascual, J.C.N. Fong, A. Dragoš, O. Lamprecht, J.G. Thöming, N. Netter, S. Häussler, C.D. Nadell, V. Sourjik, Á.T. Kovács, F.H. Yildiz, K. Drescher, Quantitative image analysis of microbial communities with BiofilmQ, *Nat. Microbiol.* 6 (2021) 151–156, <https://doi.org/10.1038/s41564-020-00817-4>.
- [41] S.J. Kwon, J.H. Park, J.G. Park, Wrinkling of a sol-gel-derived thin film, *Phys. Rev. E Stat. Nonlinear Soft Matter Phys.* 71 (2005), 011604, <https://doi.org/10.1103/PhysRevE.71.011604>.
- [42] T. Kokubo, H. Takadama, How useful is SBF in predicting in vivo bone bioactivity? *Biomaterials* 27 (2006) 2907–2915, <https://doi.org/10.1016/j.biomaterials.2006.01.017>.
- [43] J.S. Lee, K. Fushimi, T. Nakanishi, Y. Hasegawa, Y.S. Park, Corrosion behaviour of ferrite and austenite phases on super duplex stainless steel in a modified green-death solution, *Corr. Sci.* 89 (2014) 111–117, <https://doi.org/10.1016/j.corsci.2014.08.014>.
- [44] K.W. Chan, S.C. Tjong, Effect of secondary phase precipitation on the corrosion behavior of duplex stainless steels, *Materials* 7 (2014) 5268–5304, <https://doi.org/10.3390/MA7075268>.
- [45] J. Cheng, T. Huang, Y.F. Zheng, Relatively uniform and accelerated degradation of pure iron coated with micro-patterned Au disc arrays, *Mater. Sci. Eng. C* 48 (2015) 679–687, <https://doi.org/10.1016/j.msec.2014.12.053>.
- [46] A. Yamamoto, R. Honma, M. Sumita, Cytotoxicity evaluation of 43 metal salts using murine fibroblasts and osteoblastic cells, *J. Biomed. Mater. Res.* (1998) 331–340, <https://onlinelibrary.wiley.com/doi/epdf/10.1002/jbm.b.10022>.
- [47] P.P. Mueller, T. May, A. Perz, H. Hauser, M. Peuster, Control of smooth muscle cell proliferation by ferrous iron, *Biomaterials* 27 (2006) 2193–2200, <https://doi.org/10.1016/j.biomaterials.2005.10.042>.
- [48] J. Capek, J. Kubásek, D. Vojtěch, E. Jablonská, J. Lipov, T. Ruml, Microstructural, mechanical, corrosion and cytotoxicity characterization of the hot forged FeMn30 (wt.%) alloy, *Mater. Sci. Eng. C* 58 (2016) 900–908, <https://doi.org/10.1016/j.msec.2015.09.049>.
- [49] L.E. Pascal, D.M. Tessier, Cytotoxicity of chromium and manganese to lung epithelial cells in vitro, *Toxicol. Lett.* 147 (2004) 143–151, <https://doi.org/10.1016/j.toxlet.2003.11.004>.
- [50] N.M. Filipov, R.F. Seegal, D.A. Lawrence, Manganese potentiates in vitro production of proinflammatory cytokines and nitric oxide by microglia through a nuclear factor kappa B-dependent mechanism, *Toxicol. Sci.* 84 (2005) 139–148, <https://doi.org/10.1093/toxsci/kfi055>.
- [51] M. Schinhammer, I. Gerber, A.C. Hänzli, P.J. Uggowitzer, On the cytocompatibility of biodegradable Fe-based alloys, *Mater. Sci. Eng. C* 33 (2013) 782–789, <https://doi.org/10.1016/j.msec.2012.11.002>.
- [52] S. Loffredo, S. Gambaro, F. Copes, C. Paternoster, N. Giguère, M. Vedani, D. Mantovani, Effect of silver in thermal treatments of Fe-Mn-C degradable metals: implications for stent processing, *Bioact. Mater.* 12 (2022) 30–41, <https://doi.org/10.1016/j.bioactmat.2021.10.020>.
- [53] D.T. Chou, D. Wells, D. Hong, B. Lee, H. Kuhn, P.N. Kumta, Novel processing of iron-manganese alloy-based biomaterials by inkjet 3-D printing, *Acta Biomater.* 9 (2013) 8593–8603, <https://doi.org/10.1016/j.actbio.2013.04.016>.
- [54] K.M. Erikson, T. Syversen, J.L. Aschner, M. Aschner, Interactions between excessive manganese exposures and dietary iron-deficiency in neurodegeneration, *Environ. Toxicol. Pharmacol.* 19 (2005) 415–421, <https://doi.org/10.1016/j.etap.2004.12.053>.
- [55] R.M. Donlan, J.W. Costerton, Biofilms: survival mechanisms of clinically relevant microorganisms, *Clin. Microbiol. Rev.* 15 (2002) 167–193, <https://doi.org/10.1128/CMR.15.2.167-193.2002>.
- [56] K. Svensson Malchau, J. Tillander, M. Zaborowska, M. Hoffman, I. Lasa, P. Thomsen, H. Malchau, O. Rolfson, M. Trobos, Biofilm properties in relation to treatment outcome in patients with first-time periprosthetic hip or knee joint

- infection, *J. Orthop. Translat.* 30 (2021) 31–40, <https://doi.org/10.1016/j.jot.2021.05.008>.
- [57] K. Zhang, X. Li, C. Yu, Y. Wang, Promising therapeutic strategies against microbial biofilm challenges, *Front. Infect. Microbiol.* 10 (2020) 359, <https://doi.org/10.3389/FCIMB.2020.00359>.
- [58] N. Wang, Y. Ma, H. Shi, Y. Song, S. Guo, S. Yang, Mg-, Zn-, and Fe-based alloys with antibacterial properties as orthopedic implant materials, *Front. Bioeng. Biotechnol.* 10 (2022) 684, <https://doi.org/10.3389/FBIOE.2022.888084>.

## Supplementary material for:

### **Accelerated biodegradation of FeMn porous alloy coated with ZnO: effect on cytocompatibility and antibiofilm properties**

Aleksandra Bartkowska<sup>1</sup>, Adam Benedict Turner<sup>2,3</sup>, Andreu Blanquer<sup>4</sup>, Aliona Nicolenco<sup>5</sup>, Margarita Trobos<sup>2,3</sup>, Carme Nogues<sup>4</sup>, Eva Pellicer<sup>1</sup>, Jordi Sort<sup>1,6</sup>

<sup>1</sup> Departament de Física, Universitat Autònoma de Barcelona, E-08193 Cerdanyola del Vallès, Spain

<sup>2</sup> Department of Biomaterials, Institute of Clinical Sciences, Sahlgrenska Academy, University of Gothenburg, Gothenburg, Sweden

<sup>3</sup> Centre for Antibiotic Resistance Research in Gothenburg (CARE), University of Gothenburg, Gothenburg, Sweden

<sup>4</sup> Departament de Biologia Cel·lular, Fisiologia i Immunologia, Universitat Autònoma de Barcelona, E-08193 Cerdanyola del Vallès, Spain

<sup>5</sup> CIDETEC Surface Engineering, Basque Research and Technology Alliance (BRTA), Paseo Miramon 196, 20014 Donostia-San Sebastian, Spain

<sup>6</sup> Institució Catalana de Recerca i Estudis Avançats (ICREA), Pg. Lluís Companys 23, E-08010 Barcelona, Spain

---

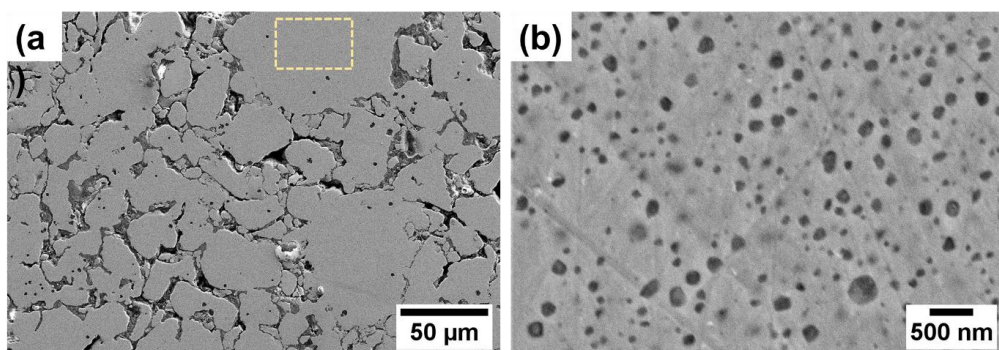


**Fig. S1** SEM micrographs of the polished surface of FeMn substrate (a) low-magnification image showing the macropores, (b) high-magnification view of the area enclosed in the yellow rectangle, showing the nanopores.



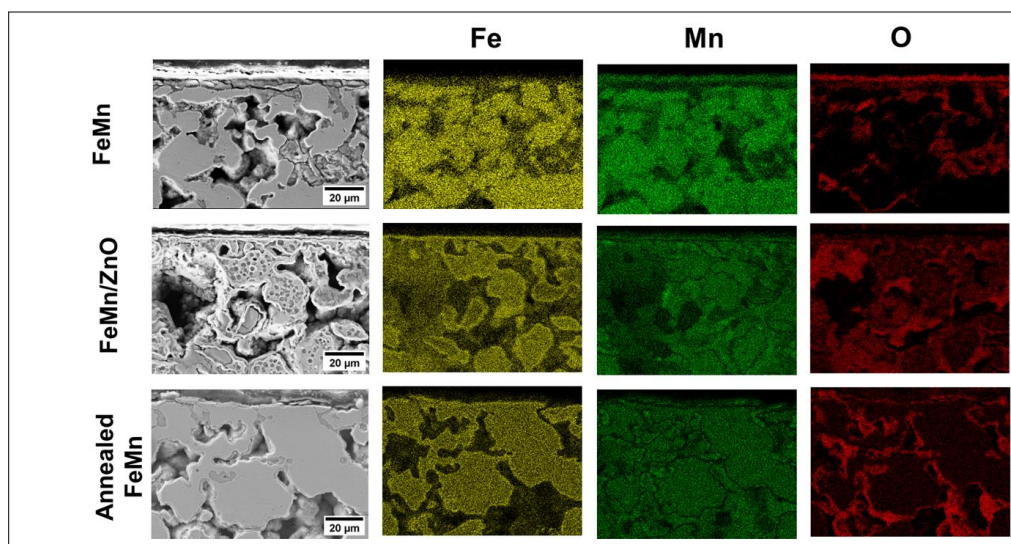


**Fig. S2** EDS mapping obtained on the cross section of uncoated FeMn, FeMn/ZnO and annealed (uncoated) FeMn samples immersed for 28 days in HBSS showing the distribution of Fe, Mn and O.

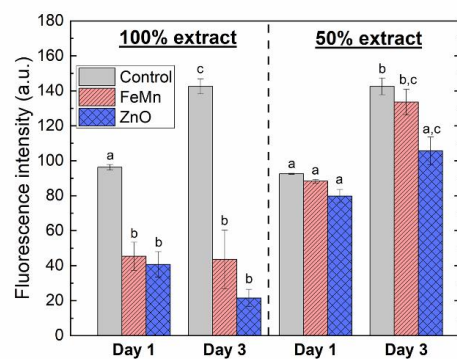


**Fig. S3** Cell proliferation in 100% and 50% conditioned media after 1- and 3-day in culture. Media conditioned for 1 day without any material (24h-control) was used as a control and was also diluted with fresh media. Bars marked with different alphabetical superscripts are significantly different from each other, while bars with the same superscript are not significantly different from each other.



## 5 General discussion

This thesis was designed and developed to fabricate and characterize biodegradable Fe-based alloys with an increased degradation rate and resistance to bacterial adhesion. It was hypothesized that by adding small amounts of Ag and ZnO to the FeMn alloy matrix, both objectives could be fulfilled owing to (a) the creation of micro-galvanic coupling between the matrix and second-phase particles (Ag/ZnO), and (b) antibacterial activity of the second phase (Ag/ZnO). The alloys were designed to contain porosity, as recent reports have shown that it is an efficient method to promote the corrosion of Fe-based biodegradable alloys. Hence, a combined approach of including porosity and second-phase precipitates/coatings has been implemented to obtain advanced composites with optimised properties for use in biodegradable implant applications.

Fe-Mn alloys are promising materials for biodegradable implant applications, such as orthopaedic fixation devices, because of their excellent biocompatibility, non-ferromagnetic character (to not interfere with MRI analyses) for sufficiently large Mn percentages, and high mechanical strength; thus, an equiatomic Fe-Mn porous alloy was chosen as the metallic matrix. The high content of Mn was aimed at eliminating the risk of the ferromagnetic character of the sample while stabilising the austenitic phase. Indeed, the fabricated alloys showed low magnetization even after 84 days of immersion in HBSS. The chosen fabrication path, that is, powder metallurgy, allowed the achievement of a porous architecture. The porosity of implant materials can be beneficial as it may lead to enhanced osseointegration, reduced stress shielding (due to a decreased Young's modulus), and, in the case of biodegradable metals, improved corrosion rate compared with fully dense counterparts. Porous materials have an increased surface area, making the material greatly exposed to the corrosive environment of body fluids, thus increasing its corrosion rate.

In the first stage, the study covered the design, fabrication and characterization of FeMn(-xAg) alloys, where  $x = 1, 3$ , and 5 wt.% Ag. Ag is a well-known antibacterial agent; thus, its addition was aimed at enhancing the antibacterial or antibiofilm effects in the tested alloys. Moreover,

---

the uniformly distributed Ag-rich precipitates are believed to enhance the degradation rate of the tested alloys. The material was prepared by powder metallurgy consisting of ball-milling the initial powders, pressing, and sintering to form disk-shaped specimens. This approach was selected to obtain a homogenous mixing of all metallic elements. The observed microstructure consisted of uniformly distributed Ag precipitates within the FeMn matrix. Biodegradability tests were performed by immersing the samples in HBSS for up to 84 days and measuring the concentration of released Fe, Mn, and Ag ions at selected time points. The results revealed a higher release of Mn than Fe without a significant difference in the leached ion concentrations between the tested alloys. The release of Ag was marginal owing to its higher nobility. However, a decrease in biofilm biomass was observed in the FeMn-5Ag alloys. Although the biodegradability test did not show a significant increase in the degradation of FeMn-xAg alloys and the materials remained intact after 3 months of immersion, it might be hypothesized that the Ag addition limits the formation of degradation layer on its surface, as was observed in the Section 3.1, which can also be attributed to limiting the bacterial adhesion, as the attachment of bacteria prefers more stable surfaces. The biocompatibility study showed no cytotoxic effect in the tested alloys, whereas the Ag-containing alloys might have a slight effect on the decreased cell proliferation. The most striking result for FeMn-xAg alloys was the change in phase composition upon adding 3 and 5 wt.% of Ag, where a formation of martensitic phase was observed, contrary to purely austenitic FeMn alloy. Moreover, the magnetization of FeMn-xAg alloys increased with increasing Ag content. It was, however, still satisfactory low, remaining around 1 emu/g for the FeMn-5Ag sample. When compared to pure Fe, we obtained a 99.5% decrease in the saturation magnetization. Thus, all tested alloys should be compatible with MRI. This phase transformation also contributed to the higher mechanical strength of martensite-containing alloys. This phenomenon was previously mentioned in the literature but never analysed and explained in detail. Thus, we decided to perform theoretical calculations to tackle this phenomenon. The theoretical study proved that Ag addition alters the stacking fault energy and spin configuration of the FeMn system, thus facilitating the martensitic transformation.

Due to the lack of a significant increase in the degradation rate in Ag-containing alloys, another approach has been followed, namely to deposit ZnO coating onto the porous FeMn disks using the dip-coating method. ZnO coating was chosen as the coating material as it has been shown to exhibit antimicrobial properties and good biocompatibility. The formation of ZnO coating included annealing in the furnace, which led to the formation of secondary phases, such as iron-manganese oxide and  $\alpha$  - Fe. These secondary phases, together with ZnO contributed to a significantly enhanced degradation rate compared to that of the uncoated FeMn alloy. The ZnO coating remained on the surface during the biodegradability test, which was conducted for up to 28 days, although the overall corrosion was faster than in the uncoated FeMn. The first signs of corrosion were already visible after 1 day of immersion. Similarly, as in the previous case, Mn release was higher than that of Fe. The fabricated materials have shown to possess antibiofilm properties, significantly limiting the biofilm formation on their surface, which was attributed to an enhanced degradation, and thus, a more active surface. The biocompatibility tests revealed that the material showed good cytocompatibility at dilutions above 50%.

When biodegradable metals are of concern, the big challenge lies in evaluating their degradation over time. The most common tests include electrochemical testing, immersion tests in physiological fluids and *in vivo* tests. The electrochemical tests are rapid and provide a good view of the general corrosion rates for the studied materials. However, they lack information on the evolution of material during degradation and the changes in the corrosive environment in the long term. On the other hand, immersion tests are closer to reality in terms of monitoring the changes in a material upon degradation, as well as in corrosive environment. It is important to monitor the material for a longer period of time as material's degradation is not a linear process, thus several time points should be analyzed. In this study, we performed immersion tests for both long-duration (up to 3 months), and short-term (up to 28 days) tests. HBSS was used as the media, which represents closely the composition of human plasma and is the most widely used solution in the literature on biodegradable Fe-based alloys. After several chosen time points, the ion

---

concentration in HBSS was analyzed and the evolution of material was also examined using SEM and EDS. It has been found that the ion release tends to plateau around 28 days of immersion owing to the formation of corrosion products on the surface. This layer made of degradation products significantly slows down further degradation of the underlying FeMn metallic material. When ZnO layer was deposited on the surface, the degradation layer was forming slower than on the uncoated specimen, which, together with other factors led to an increased degradation rate.

The biodegradability tests performed *in vitro* are a good and efficient way to roughly estimate the corrosion behaviour of biodegradable metals. However, it is important to know that the real, *in vivo* degradation rate is different than that obtained through *in vitro* test. The *in vivo* environment is much more complex, with dynamic interactions among tissues, cells, fluids, *etc.*, which are difficult to mimic in the *in vitro* conditions. Moreover, physical factors such as shear forces, mechanical stresses and physiological movements can have a large influence on the material's performance. This way, to make the material truly applicable, additional *in vivo* studies shall be performed to provide full insights into biodegradability of the tested material.

Biocompatibility tests are crucial for the design of new implant materials. As the *in vivo* tests require long-term evaluation, more resources and ethical considerations, the biocompatibility should be first assessed by the *in vitro* methods that simulate the clinical conditions. Here, the biocompatibility of fabricated Fe-based alloys was assessed using indirect tests, as the trials on direct tests failed because cell adhesion was severely hindered. The fast degradation of porous alloys prevents cell adhesion in the initial phase of cell culture, as the surface state changes dynamically due to degradation and it is not possible to assess the cytotoxicity in cells cultured on the surface of the sample. For this reason, the cytotoxicity was evaluated by an indirect approach and the results of the indirect test did not show any cytotoxic effect of the alloys. It is well known that ion concentration in the media has a crucial effect on biocompatibility - and that exceeding the concentration of potentially non-toxic alloys can have a more harmful effect on cell viability than the low concentration of potentially toxic elements. In the FeMn(-xAg) alloys, described in Section 4.1, the surface-to-media ratio

was established accordingly to biodegradability testing, where a relatively large volume of solution was used, thus the final concentration of Fe and Mn ions in the conditioned media was far below the toxic concentration. In the case of the FeMn(-ZnO) alloys another approach was undertaken, to more precisely identify the level of potentially toxic ion concentration. In detail, a concentrated media was prepared by immersing the fabricated disks in a small amount of media and then diluting that media to lower concentrations, as described in Section 4.3. We found that elevated Mn concentrations can indeed be harmful to cells.

Indirect biocompatibility testing is a good method to initially assess the potential cytotoxicity of newly developed material, however, it lacks comprehensive data. As indirect testing focuses solely on the ion concentration and degradation products, it might not provide a full understanding of the overall biocompatibility of the material. In general, the *in vitro* tests are not able to fully replicate the material's behaviour *in vivo* and thus - to predict the behaviour of material inside the body. It is important to highlight that both *in vitro* and *in vivo* methods have their merits, and thus the less demanding *in vitro* is a valuable approach to initially assess the cytocompatibility of newly developed material.

Biodegradable metals need to possess enough mechanical strength to support the tissue-healing process. The validation of mechanical properties of fabricated FeMn(-xAg) alloys was obtained using nanoindentation and compression tests. The mechanical compression strength, reaching the maximum value above 300 MPa, is sufficiently high to fulfil the requirements of mechanical support during degradation. What's more, due to the introduced porosity, Young's modulus decreased to the value of around 50 MPa. Upon the addition of Ag, an increase in mechanical strength was observed. This was mainly attributed to the phase transformation occurring upon the addition of 3 and 5 wt.% Ag, where a dual phase composition was observed, consisting of both austenitic and martensitic phases. Moreover, the Ag-rich precipitates themselves can contribute to an increased strength through precipitation strengthening. At the same time, the addition of Ag did not contribute to a decrease in the elongation.

The importance of fabricating materials, which prevent biofilm formation on the implant surface is highlighted in Chapter 1. The harmful effect

---

of biofilms can lead to implant failure or, in the worst case, to patient's death. Materials developed in this work have been shown to limit the formation of biofilm, but they did not exhibit direct antimicrobial properties, even in the presence of well-established antimicrobial agents. It can be hypothesized that the added amount of Ag to the FeMn matrix was not high enough to induce the bacteria-killing effect, while at the same time, it formed active corrosion sites preventing biofilm formation. Different results could have been obtained if Ag were accumulated at the surface of the FeMn instead of being finely distributed throughout the entire specimen. Yet, this would have required devising a different synthetic approach. Similarly, the ZnO coating itself did not contribute to enhance the antimicrobial properties but the composite material formed, with a high degradation rate, prevented the biofilm formation on its surface.

In summary, this thesis tackled two approaches for fabricating Fe-based alloys for biomedical applications with enhanced antibiofilm properties. New and unique methods, such as the deposition of coatings, introduction of second-phase noble particles and producing porous alloys have shown to be promising approaches to developing new metallic materials with specifically designed properties.

## 6 Conclusions and future perspectives

This thesis was undertaken to design and develop new biodegradable equiatomic FeMn alloys with additions of antibacterial Ag and ZnO and evaluate their effect on biodegradability, cytocompatibility and biofilm formation. Two main types of porous materials were developed, i.e. FeMn(-xAg) alloys and FeMn alloys with ZnO coating.

For the FeMn(-xAg) alloys, the following conclusions can be extracted from the Thesis:

- FeMn(-xAg) alloys can be successfully fabricated by powder metallurgy, i.e. ball-milling and sintering. The alloys possessed a hierarchically porous structure consisting of both macro- and nanoporosity.
- The sintered FeMn and FeMn-1Ag alloys primarily consisted of  $\gamma$ -austenite phase, whereas the FeMn-3Ag and FeMn-5Ag alloys exhibited a duplex structure comprising  $\gamma$ -austenite (fcc structure) and  $\epsilon$ -martensite phase (hcp structure).
- FeMn-3Ag and FeMn-5Ag had higher compression strength, which was attributed to the presence of the martensitic phase.
- All FeMn-xAg alloys possessed low magnetic character, which makes them potentially compatible with MRI analyses.
- Cytocompatibility experiments demonstrated that the investigated alloys were non-cytotoxic. Although Ag-containing alloys were cytocompatible, their cell proliferation rate was lower than that of pure FeMn. Inflammatory cell response experiments showed that the ions released by FeMn(-xAg) alloys did not induce an inflammatory response in macrophages *in vitro*.
- The viability and biofilm formation of *Staphylococcus aureus* with FeMn(-xAg) alloys were tested. The obtained results revealed a significant reduction in biofilm biomass of both live and dead cell populations at 24h in the FeMn-5Ag sample.

---

The findings regarding the FeMn alloy coated with ZnO led to the following conclusions:

- Dip-coating is an efficient way of depositing ZnO coating onto FeMn porous substrate.
- The ZnO coating process contributed to an accelerated biodegradation rate when compared to uncoated FeMn alloy. This was attributed not only to the ZnO coating itself but also to the formation of secondary phases during the coating fabrication.
- FeMn/ZnO elutions did not show a cytotoxic effect when exposed to Saos-2 cells, as long as the elution concentration remained below 50%.
- The FeMn/ZnO samples displayed effective antibiofilm properties by reducing the overall biofilm biovolume of *S. aureus* at 24h. This suggests that the ZnO coating inhibits biofilm formation on the FeMn alloys, which is advantageous for implant materials.

Overall, the study highlights the potential of FeMn alloys with additions of Ag and ZnO as a biodegradable implant material with improved biodegradability, resistance to biofilm formation and good cytocompatibility. These findings contribute to the development of innovative solutions for biomedical applications and pave the way for further research and optimization in the area of biodegradable metals.

Regarding future perspectives of the research presented here, several steps should be undertaken towards the clinical translation of the developed materials. As a first step, the material should be designed for a specific fixation device or scaffold to tailor the mechanical properties by optimizing the porosity levels. Then, the mechanical properties should be studied in depth by applying different techniques, such as tensile and compression tests, fatigue tests and bending tests. The mechanical properties should be studied as a function of the degradation level to provide enough support for the required period. Complex degradation tests combined with evaluation of mechanical properties after various degradation periods should be assessed. Secondly, a thorough *in vitro* biological study should



## 6. Conclusions and future perspectives

---

be performed, using several cell lines to further assess its cytocompatibility. Similarly as with the mechanical tests, the cell lines should be chosen accordingly to the specific application. As a third step, considering the positive results of the *in vitro* study, a prototype of the implant should be designed, which then could be used for the animal *in vivo* tests to validate the biocompatibility of the material. The biomechanical behaviour of the material upon implantation should be also evaluated to prove its mechanical support for the required period.

## List of Figures

1.1	Schematic mechanism of the degradation process and changes in the mechanical integrity of biodegradable metals during bone healing process. Reproduced from [11]. Copyrights Elsevier 2014. . . . .	4
1.2	Schematic mechanism of the degradation process of biodegradable metals in body fluids. Reproduced with permission [11]. Copyright 2014, Elsevier. . . . .	6
1.3	(a) Phase diagram of Fe-Mn system and (b) volume fraction of phases depending on Mn content in Fe-Mn alloys obtained through casting. Reproduced with permission [76]. . . . .	15
1.4	Schematic of generalized degradation mechanism of Fe-Mn alloys. Reproduced with permission [65]. Copyright 2010, Elsevier. . . . .	16
1.5	Fe-Mn foams fabricated by replica method. Reproduced with permission from [115]. Copyright 2020, Elsevier. . . . .	21
1.6	SEM images of surface topography of laser-textured Fe-Mn samples (a) after 3 days of immersion (b) and (c). Reproduced with permission from [85]. Copyright 2018, Elsevier . . . . .	22
1.7	Risk factors of patients undergoing implant surgery regarding biomaterial-associated infections. From [152]. Reprinted with permission from AAAS. . . . .	30
1.8	The schematic representation of biofilm formation and development. Reproduced from [160]. Copyright 2022, Springer Nature. . . . .	31
1.9	Proposed strategies for surface design of antibacterial materials. Reproduced from [161]. . . . .	33
1.10	Mechanisms responsible for an increased infection resistance of biodegradable <i>versus</i> non-biodegradable materials. Reproduced with permission [173]. Copyright 2013, Elsevier. . . . .	35

1.11	Publications on antibacterial materials searched by PubMed. (a) key words used for the search: antibacterial metals, antibacterial titanium, antibacterial steel, (b) keywords used for the search: antibacterial degradable alloy, antibacterial degradable Mg/Zn/Fe alloy. (Updated on 24-04-2023). Publications from 2023 are not included. . . . .	37
3.1	Diagram showing the powder metallurgy process leading to synthesis of porous FeMn(-xAg) alloys. Created with BioRender.com . . . . .	42
3.2	Diagram showing the deposition of ZnO coating by dip coating on FeMn polished discs. Created with BioRender.com . . . . .	43
3.3	Overview on the methodological approach for characterization of fabricated samples. Created with BioRender.com . . . . .	44
3.4	Diagram showing the biodegradability testing procedure. Created with BioRender.com . . . . .	45
3.5	Schematic load-displacement curves for nanoindentation experiment. $P_{max}$ is the maximum applied load, $h_{max}$ is the indenter displacement at maximum applied load, $h_f$ is the final depth of the contact impression after unloading and $S$ is the initial unloading stiffness. Reproduced with permission[179]. Copyright 1992, Springer. . . . .	47
3.6	Diagram showing the indirect cell viability and proliferation assays experiments. Created with BioRender.com . . . . .	51
3.7	Diagram showing the analysis of biofilm on FeMn and FeMn/ZnO samples. Created with BioRender.com. Courtesy of Adam Benedict Turner, University of Gothenburg, Sweden . . . . .	52

# List of Tables

- 1.1 Comparison of mechanical properties of the most commonly studied biodegradable materials . . . . . 2
- 1.2 Compositions of blood plasma and most commonly used pseudo-physiological solutions [17] . . . . . 7